KU LEUVEN

ARENBERG DOCTORAL SCHOOL
Faculty of Engineering Science

Experimental analysis and numerical modelling of concrete recycling flash-calcined dredging sediments

Céline Van Bunderen

Supervisors:
Prof. dr. ir. Özlem Cizer
Prof. dr. ir. Lucie Vandewalle
Dr. Ruben Snellings

Dissertation presented in partial fulfillment of the requirements for the degree of Doctor of Engineering Science (PhD): Civil Engineering

February 2020

Experimental analysis and numerical modelling of concrete recycling flash-calcined dredging sediments

Céline VAN BUNDEREN

Examination committee:
Prof. em. dr. ir. Omer Van der Biest, chair
Prof. dr. ir. Özlem Cizer, supervisor
Prof. dr. ir. Lucie Vandewalle, supervisor
Dr. Ruben Snellings, supervisor
Dr. ir.-arch. Kristof De Wilder
Prof. dr. ir. Elke Gruyaert
Prof. dr. ir.-arch. Koen Van Balen
Prof. dr. ir. Stéphanie Staquet
(Université Libre de Bruxelles)
Prof. dr. ir. Farid Benboudjema
(ENS Paris-Saclay, France)

Dissertation presented in partial fulfillment of the requirements for the degree of Doctor of Engineering Science (PhD): Civil Engineering

February 2020

© 2020 KU Leuven – Faculty of Engineering Science
Uitgegeven in eigen beheer, Céline Van Bunderen, Kasteelpark Arenberg 40, box 2448, B-3001 Leuven (Belgium)

Alle rechten voorbehouden. Niets uit deze uitgave mag worden vermenigvuldigd en/of openbaar gemaakt worden door middel van druk, fotokopie, microfilm, elektronisch of op welke andere wijze ook zonder voorafgaande schriftelijke toestemming van de uitgever.

All rights reserved. No part of the publication may be reproduced in any form by print, photoprint, microfilm, electronic or any other means without written permission from the publisher.

Voorwoord

Na meer dan vier jaar onderzoek zou ik graag iedereen willen bedanken die heeft bijgedragen tot de voltooiing van dit doctoraat.

First of all, I would like to thank my supervisor, prof. Özlem Cizer, for giving me the opportunity to study this interesting research topic as a part of the BIND-AMOR project. I am grateful for her support and guidance during the past years. I especially appreciate the liberty that was entrusted to me and the many opportunities I have been given.

Daarnaast wil ik ook graag mijn co-promotoren, prof. Lucie Vandewalle en dr. Ruben Snellings bedanken. Bedankt Lucie voor het vertrouwen en de steun gedurende de laatste jaren. Bedankt Ruben voor de zinvolle discussies en de metingen die ik in VITO mocht verrichten. Je was ook steeds bereid een antwoord te bieden op al mijn vragen.

I am also very grateful to prof. Farid Benboudjema. Thank you for the insightful discussions and for giving me the opportunity to perform different tests at LMT (ENS Cachan) during my research stay. I very much enjoyed your hospitality!

Vervolgens wens ik graag de leden van de jury te bedanken voor hun inzet de afgelopen jaren en voor hun nuttige bijdrage tijdens de preliminaire verdediging. Bedankt prof. Koen Van Balen, prof. Elke Gruyaert en dr. Kristof De Wilder, *thank you prof. Stéphanie Staquet and prof. Farid Benboudjema for being a member of the examination committee, and for your interest and constructive comments.* Ook dank aan de voorzitter van de jury, prof. Omer Van der Biest.

De Vlaamse Overheid (Departement Mobiliteit en Openbare Werken - Afdeling Maritieme toegang) wil ik graag bedanken voor de financiële steun. Verder bedank ik ook het Fonds voor Wetenschappelijk Onderzoek (FWO) voor het ter beschikking stellen van een krediet voor een lang verblijf in het buitenland.

Daarnaast wil ik graag alle techniekers oprecht bedanken. Bedankt Bernd, Gerda, Jan, Jimmy, Stephan en Tom voor alle hulp bij het maken van vele betonmengsels en het uitvoeren van vele proeven. Ook mijn thesisstudenten, Josse, Suze, Evert, Tom, Joren, Laurens, Yannick en Emiel, wil ik graag bedanken voor hun inzet en hulp in het labo. *I would also like to thank prof. Stéphanie Staquet for giving me the opportunity to perform different concrete tests at ULB and I want to thank Jérôme for his help in the lab and his help with the treatment of the results. Also thanks to Loic, Olivier, Rémi and Xavier for their help in the lab at LMT Cachan.*

Ik wil ook zeer graag alle collega's bedanken voor de leuke werksfeer. Bedankt Anna, Aziliz, Carolina, Els, Els, Hussein, Kristof, Marcello, Nathalie, Naveen, Pieter, Rita, Shiju, Siva en Youen. Ik heb steeds genoten van de fijne samenwerking, MAT-uitstappen, congressen, loopavonden en Tichu middagen. Ook een welgemeende dankjewel aan Kristine voor alle administratieve taken. *Ahmed, thank you very much for your friendship and support, especially during the last months of writing.* Charlotte, Maure en Rutger, enorm bedankt voor de leuke weekendjes en vele andere activiteiten, zowel binnen als buiten de werkuren. *I would also like to thank my colleagues in Cachan: Pascale, Aya, Nicolas, Livio, Achraf and Melo. Thank you very much for all your help and hospitality during my stay in Cachan.*

Verder wil ik graag mijn vrienden bedanken voor de steun en nodige ontspanning de laatste jaren. In de eerste plaats Helene, bedankt om de voorbije 4 jaar een fantastische huisgenote te zijn. Joke, Evelien, Charlotte, Eline en Sofie, dankjewel voor alle leuke momenten en bedankt om na meer dan 10 jaar nog steeds zo'n geweldige vrienden te zijn. Ook Didier, David, Maxime, Pieter en Brecht, bedankt voor de leuke weekendjes, barbecues en feestjes. Veerle en Tine, dankjewel voor de vele fijne zwemavonden. En ook aan iedereen van de volleybal en de mensen waarmee ik op reis ben geweest: bedankt!

Tot slot wil ik graag nog mijn familie bedanken. Dankjewel mama en papa voor alle goede zorgen, steun en kansen die ik gekregen heb. Ook mijn zus, Dorine, bedankt voor alles!

Céline Van Bunderen
Februari 2020

Abstract

As the world's largest manufactured product by mass, cement is responsible for 10% of the global anthropogenic CO_2 emissions. The share of the cement industry in the total greenhouse gas emissions is only expected to increase due to the population growth and increasing industrialisation and urbanisation in developing countries. The most promising and well-established way to reduce the environmental impact of the cement industry is using supplementary cementitious materials (SCMs) as partial cement replacement in concrete. Considering the limits of the availability and production of the conventional SCMs, such as fly ash (FA) and blast furnace slag, new sources of high-quality SCMs are highly required to further reduce the CO_2 emissions and contribute to achieving the United Nations sustainable development goals.

This thesis investigates the beneficial reuse of dredging sediments from the port of Antwerp as a potential new SCM for the production of sustainable concrete, and is part of the BIND-AMOR project. The dredging material is first processed into filter cakes in a state-of-the-art mechanical dewatering facility. After flash calcination, the filter cakes become pozzolanic reactive, indicating the potential for its use in concrete. The main objective of this thesis is to assess the effect of calcined filter cakes (CFC) as an SCM on early-age properties of concrete, in order to understand its early-age deformation potential and predict its time-dependent deformations at long term. The influence of CFC blended cement on the hydration process, early-age concrete properties, mechanical properties, shrinkage and creep behaviour of concrete is investigated experimentally. Concrete properties are modelled and a cracking prediction tool is developed.

CFC enhances the hydration of ordinary Portland cement (OPC) by the filler effect at early ages and by the formation of additional hydration products at later ages. The hydration products formed in CFC blended cements are similar to those formed in OPC and FA reference mixes. The high specific surface area of CFC increases the water demand of concrete and requires the use of

a superplasticizer, slightly delaying the setting. CFC blended cement reduces the early-age concrete strength, but strongly increases the concrete strength at later ages due to the pozzolanic activity of CFC, reaching strength class C45/55. Both autogenous and drying shrinkage as well as basic creep of concrete are reduced by CFC blended cement. The reduced autogenous shrinkage is, on the one hand, derived from the development of an autogenous swelling as a result of supersaturation of the pore solution towards ettringite, delaying the shrinkage. The dilution effect and formation of different hydration products, on the other hand, reduce the autogenous shrinkage rate. The reduced drying shrinkage is the result of the dilution effect, and altered porosity and pore size distribution of CFC concrete. To explain the reduced basic creep of CFC concrete, the C-S-H phase needs to be further investigated. CFC blended cement shows large similarities with FA blended cement regarding hydration, strength and shrinkage behaviour, proving CFC to behave as a typical SCM in concrete.

The temperature development is modelled using the heat equation and the model of Eurocode 2 is proven to well describe the mechanical properties development of CFC concrete, provided that the cement type dependent parameters are adjusted. Existing empirical autogenous and drying shrinkage models are parametrised to accurately predict concrete shrinkage. Basic creep is modelled using a rheological model and drying creep is modelled using the relationship between drying creep and drying shrinkage. Using these models to describe the concrete properties, a stress-based cracking prediction tool is developed, based on the definition of a cracking index. The viscoelastic behaviour of concrete is taken into account by considering creep/relaxation. It is concluded that the thermal-shrinkage induced cracking risk of concrete is reduced by using CFC blended cement, as a result of the combined effect of the total strains, tensile strength and elastic modulus of CFC concrete on the cracking risk.

The results of this thesis clearly support the use of CFC as a new SCM for the production of sustainable cement and concrete in Flanders. Provided that rheology properties, durability properties, structural behaviour and bond behaviour are further investigated and relevant requirements are fulfilled, application of CFC blended cement for ready-mix concrete is envisaged.

Beknopte samenvatting

De cementindustrie is verantwoordelijk voor 10% van de globale antropogene CO_2-uitstoot. Door de toenemende bevolkingsgroei, industrialisatie en urbanisatie in ontwikkelingslanden, wordt er echter verwacht dat het aandeel van de cementindustrie in de totale broeikasgasemissies enkel maar zal stijgen. Eén van de meest effectieve manieren om de milieu-impact van de cementindustrie te verminderen, is door gebruik te maken van supplementair cementerende materialen (SCMs) als gedeeltelijke vervanging van cement in beton. Door de beperkte beschikbaarheid en verminderde productie van de klassieke SCMs, zoals vliegas en hoogovenslak, is er echter dringend nood aan nieuwe alternatieven, om de CO_2-uitstoot van de cementindustrie verder te reduceren en om bij te dragen aan het bereiken van de klimaatdoelstellingen van de Verenigde Naties.

Dit onderzoek bestudeert het nuttig hergebruik van baggerspecie uit de haven van Antwerpen als potentieel nieuw SCM voor de productie van een duurzaam beton, en is deel van het BIND-AMOR project. De baggerspecie wordt eerst verwerkt tot filterkoeken in een state-of-the-art mechanische ontwateringsinstallatie. Na flash calcinatie worden de filterkoeken puzzolaan reactief, wat het potentieel aantoont voor het gebruik als cementvervanger. Het hoofddoel van deze thesis is het evalueren van het effect van gecalcineerde filterkoeken (CFC) als SCM op de eigenschappen van beton op jonge leeftijd, om zo het vervormingsgedrag op jonge leeftijd te begrijpen en om tijdsafhankelijke vervormingen op latere leeftijd te voorspellen. De invloed van de gedeeltelijke vervanging van cement door CFC wordt enerzijds experimenteel bestudeerd. Zowel het hydratatieproces, de eigenschappen van beton op jonge leeftijd, de mechanische eigenschappen en het krimp- en kruipgedrag van beton worden onderzocht. Anderzijds worden verschillende numerieke modellen gebruikt om de eigenschappen van het beton te beschrijven en wordt er een tool ontwikkeld om het scheurgedrag van het beton te voorspellen.

CFC verbetert de hydratatie van Portland cement (OPC) door het 'filler effect' op jonge leeftijd en door de vorming van extra hydratatieproducten op latere

leeftijd. De hydratatieproducten die gevormd worden in CFC cement zijn gelijkaardig aan deze gevormd in OPC en vliegas mengsels. De hoge specifieke oppervlakte van CFC verhoogt de waterbehoefte van beton en noodzaakt het gebruik van een superplastificeerder, die de binding van het beton enigszins zal vertragen. Het gebruik van CFC cement vermindert de betonsterkte op jonge leeftijd, maar verhoogt de betonsterkte op latere leeftijd significant door de puzzolane activiteit van CFC, en sterkteklasse C45/55 wordt bereikt. Zowel de autogene krimp, uitdrogingskrimp en basis-kruip worden gereduceerd door gebruik van CFC cement. De verminderde autogene krimp is enerzijds het gevolg van de ontwikkeling van een autogene zwelling door supersaturatie van de porieoplossing met betrekking tot ettringiet, die de start van de krimp zal vertragen. Anderzijds zullen het verdunningseffect en de vorming van andere hydratatieproducten de snelheid van de autogene krimp vertragen. De verminderde uitdrogingskrimp is het gevolg van het verdunningseffect en de gewijzigde porositeit en porieverdeling van CFC beton. Om de verminderde basis-kruip te verklaren is echter verder onderzoek met betrekking tot de C-S-H fase noodzakelijk. CFC cement vertoont veel gelijkenissen met vliegas cement, betreffende het hydratatie-, sterkte- en het krimpgedrag. Dit bewijst dat CFC zich gedraagt als een typisch SCM in beton.

De temperatuursontwikkeling in beton wordt gemodelleerd door gebruik te maken van de warmtevergelijking en het model volgens Eurocode 2 is bewezen de ontwikkeling van de mechanische eigenschappen van CFC goed te beschrijven, op voorwaarde dat de parameters afhankelijk van het cementtype worden aangepast. Bestaande empirische krimpmodellen worden geparametriseerd om de krimp van beton accuraat te voorspellen. Basis-kruip wordt gemodelleerd door gebruik te maken van reologische modellen en de uitdrogingskruip wordt gemodelleerd op basis van de relatie tussen de uitdrogingskruip en uitdrogingskrimp. Door gebruik te maken van deze modellen om de eigenschappen van beton te beschrijven, is er een tool ontwikkeld om de scheurvorming in het beton te voorspellen, gebaseerd op de definitie van een scheur-index. Het visco-elastisch gedrag van beton wordt in rekening gebracht door kruip te beschouwen. Er kan besloten worden dat het thermisch-krimp geïnduceerd risico van beton op scheuren gereduceerd wordt door CFC cement te gebruiken, als gevolg van het gecombineerd effect van de totale vervormingen, de treksterkte en de elasticiteitsmodulus van het CFC beton op het risico op scheurvorming.

De resultaten van deze thesis tonen duidelijk het potentieel aan van CFC als nieuw SCM voor de productie van een duurzaam cement en beton in Vlaanderen. Op voorwaarde dat de reologische eigenschappen, duurzaamheidseigenschappen, het structureel gedrag en het hechtgedrag van het beton verder onderzocht worden, en dat aan de relevante eisen wordt voldaan, worden in situ toepassingen beoogd.

Contents

Abstract iii

Beknopte samenvatting v

Contents vii

List of Figures xiii

List of Tables xxiii

List of Symbols xxix

1 Introduction 1

1.1 Problem statement 1

1.2 Research objectives 3

1.3 Outline 4

2 State of the art 7

2.1 Supplementary cementitious materials 7

2.1.1 Definition and classification 7

2.1.2 Use and limitations 9

2.1.3 Calcined dredging sediments as SCM 11

2.2 Influence of SCMs on the hydration process 13
2.2.1 Hydration of OPC 14
2.2.2 Pozzolanic reaction 19
2.2.3 Blended cement hydration 20
2.2.4 Hydration products 21
2.2.5 Conclusion 23
2.3 Influence of SCMs on fresh concrete properties 24
2.3.1 Water demand and workability 24
2.3.2 Setting behaviour 24
2.4 Influence of SCMs on hardened concrete properties 30
2.4.1 Pore structure 30
2.4.2 Strength 30
2.4.3 Elastic properties 31
2.5 Influence of SCMs on volumetric changes 32
2.5.1 Autogenous shrinkage 32
2.5.2 Drying shrinkage 39
2.5.3 Thermal shrinkage 41
2.5.4 Total shrinkage 41
2.5.5 Creep 42
2.6 Modelling time-dependent behaviour 46
2.6.1 Shrinkage modelling 46
2.6.2 Creep modelling 48
2.7 Conclusion 50

3 Materials and methods 53

3.1 Materials 53
3.1.1 Cement 53

3.1.2 Calcined filter cakes (CFC) 54
3.1.3 Aggregates 58
3.1.4 Superplasticizer 59
3.2 Mix compositions and mixing procedure 60
3.2.1 Concrete 60
3.2.2 Cement paste 61
3.3 Methods 61
3.3.1 Early-age characterisation methods 61
3.3.2 Setting time determination 63
3.3.3 Fresh concrete properties 64
3.3.4 Hardened concrete properties 65
3.3.5 Volumetric changes 67
3.4 Conclusion 71

4 Concrete mix design 73

4.1 Cement replacement ratio 73
4.2 Type and dosage of superplasticizer (SP) 77
4.3 W/B ratio 81
4.4 Final concrete mix design 83
4.5 Conclusion 86

5 Early-age development 87

5.1 Hydration process 87
5.1.1 Heat of hydration 89
5.1.2 Hydration products 93
5.1.3 Internal relative humidity development 97
5.2 Setting behaviour 99
5.2.1 Vicat setting time 99

5.2.2 Ultrasonic measurements 100
5.3 Strength and stiffness development 111
5.3.1 Compressive strength 111
5.3.2 Tensile strength 112
5.3.3 Static elastic modulus 114
5.4 Correlations 115
5.4.1 Ultrasonic measurements versus isothermal calorimetry 115
5.4.2 Ultrasonic measurements versus strength measurements 118
5.4.3 Static elastic modulus versus elastic dynamic modulus . 119
5.5 Modelling 121
5.5.1 Temperature development 121
5.5.2 Mechanical properties development 128
5.6 Conclusion 133

6 Shrinkage behaviour 135

6.1 Chemical shrinkage 135
6.2 Autogenous shrinkage 136
6.3 Drying shrinkage 146
6.4 Modelling 150
6.4.1 Empirical shrinkage models 150
6.4.2 Mechanistic shrinkage models 160
6.5 Conclusion 168

7 Creep behaviour 169

7.1 Concrete strains 169
7.2 Creep experiments 170
7.2.1 Instantaneous strain 172
7.2.2 Basic creep strain 173

7.2.3 Drying creep strain 174
7.3 Modelling 176
7.3.1 Basic creep model 176
7.3.2 Drying creep model 181
7.3.3 Total strains 182
7.4 Conclusion 185

8 Cracking risk **187**
8.1 Methodology 187
8.2 Cracking risk 192
8.2.1 Autogenous shrinkage induced cracking risk 192
8.2.2 Drying shrinkage induced cracking risk 193
8.2.3 Thermal strain induced cracking risk 195
8.2.4 Total cracking risk 197
8.2.5 Rate form versus non-rate form 199
8.3 Conclusion 201

9 Conclusion **203**
9.1 General conclusions 203
9.2 Original contributions 209
9.3 Recommendations for future research 210

A Technical datasheets **213**

B Amoras project **237**

C Water absorption aggregates **241**

D Modelling of UPV curves **243**

E Shrinkage modelling **257**

F Drying shrinkage microcracks **263**

G Verification of eccentricity of the creep specimens **265**

Bibliography **269**

Curriculum vitae **291**

List of publications **293**

List of Figures

1.1 Expected cement production in China, India, OECD (Organisation for Economic Cooperation and Development) countries and other countries, according to the IEA (International Energy Agency), adapted from [196]. 1

1.2 Outline of the PhD thesis and interaction between the chapters. 5

2.1 CaO-Al_2O_3-SiO_2 ternary diagram, situating the chemical composition of some commonly used SCMs, adapted from [152]. . . 8

2.2 Global clinker substitution evolution in time, adapted from [196]. 9

2.3 Overview and availability of existing and future SCMs, adapted from [208]. 10

2.4 Heat development during the cement hydration process and corresponding hydration periods, adapted from [110]. 17

2.5 Microstructural development during the hydration of Portland cement, adapted from [194]. 18

2.6 Formation of hydrates in OPC, adapted from [121]. 19

2.7 Hydrate phases in the CaO-Al_2O_3-SiO_2 ternary diagram, adapted from [152]. 22

2.8 Different stages of the setting process, adapted from [49]. . . . 25

2.9 Stages of the P- and S-wave velocity development (I: dormant period, II: acceleration period, III: deceleration period), adapted from [49]. 26

2.10 Development of elastic moduli and Poisson's ratio, calculated from ultrasonic measurements, when considering both P- and S-wave (full lines) and when only considering P-waves (dashed lines). 28

2.11 Stress-strain (ϵ_c-σ_c) relation for concrete with tangent, dynamic (E_d) and secant, static (E_s) modulus of elasticity (f_c: concrete compressive strength), adapted from [225]. 31

2.12 Concrete's compositional changes during hydration, causing autogenous and chemical shrinkage, adapted from [123]. 33

2.13 Surface tension (left) and disjoining pressure (right) mechanisms. 34

2.14 Capillary tension (p_c) mechanism (p_{water}: pressure of water, p_{air}: pressure in air, θ: angle between water surface and pore wall, r: radius of pore). 35

2.15 Nanostructure of C-S-H according to Powers and Brownyard (left) and according to Feldman and Sereda (right), adapted from [231]. 43

2.16 Disjoining pressure and microprestress in a micropore in cement gel, adapted from [17]. 44

2.17 Kelvin-Voigt (left) and Maxwell (right) rheological model. . . . 49

3.1 CaO-Al_2O_3-SiO_2 ternary diagram of some commonly used SCMs and CFC, adapted from [152]. 57

3.2 Particle size distribution of the three different batches of river sand 0/4 and river gravel 4/14. 59

3.3 UPV device (left) and FreshCon system (right). 64

3.4 Corrugated tube method for determination of autogenous shrinkage on cement paste samples. 67

3.5 BTJADE device, adapted from [47]. 68

3.6 Drying shrinkage set-up. 69

3.7 Creep set-up ENS Cachan. 70

4.1 Mechanical properties of the initial concrete mix compositions (n=6 for f_c, E_d and $f_{ct,sp}$ and n=3 for $f_{ct,ft}$). 76

4.2 Slump and flow values of the CFC 30 mix for different types and dosages of superplasticizer (n=1). 78

4.3 Mechanical properties of the CFC 30 mix for different types of superplasticizer (n=3 for f_c and E_d, n=4 for $f_{ct,ft}$ and n=8 for $f_{ct,sp}$). 80

4.4 Mechanical properties of the CFC 30 mix for different W/B ratios (n=3 for f_c and E_d, n=2 for $f_{ct,ft}$ and n=4 for $f_{ct,sp}$). 83

4.5 Average slump values of the different batches of concrete made (n = number of concrete batches). 85

5.1 From hydration to early-age deformations. 88

5.2 Heat flow (left) and cumulative heat (right) of the different cement paste mixes without superplasticizer, normalised to the OPC content (n≥2). 90

5.3 Heat flow (left) and cumulative heat (right) of the different cement paste mixes with (full lines) and without (dashed lines) superplasticizer, normalised to the OPC content. 91

5.4 Heat flow (left) and cumulative heat (right) of the different concrete mixes with superplasticizer, normalised to the OPC content (n=1). 92

5.5 XRD patterns of the RC I cement paste mixes at early ages. The main peaks of ettringite (Ett), portlandite (P), alite (A), belite (B), gypsum (G), anhydrite (Anh), quartz (Q), calcium aluminoferrite (C_4AF) and AFm phases (AFm) are indicated. . 93

5.6 XRD patterns of the RC II cement paste mixes at early ages. The main peaks of ettringite (Ett), portlandite (P), alite (A), belite (B), anhydrite (Anh), quartz (Q), mullite (M), calcium aluminoferrite (C_4AF) and AFm phases (AFm) are indicated. . 94

5.7 XRD patterns of the CFC 30 cement paste mixes at early ages. The main peaks of ettringite (Ett), portlandite (P), alite (A), belite (B), gypsum (G), anhydrite (Anh), quartz (Q), feldspars (F), calcium aluminoferrite (C_4AF) and AFm phases (AFm) are indicated. 94

5.8 Evolution of the consumption of the clinker minerals (C_3S, C_2S, C_3A, C_4AF) and formation of hydration products (portlandite (CH), amorphous phases, ettringite (Ett) and hemicarbonate (Hc)), for RC I, RC II and CFC 30 cement paste mixes at early ages, normalised to the initial OPC content. 96

5.9 Internal RH development of the different cement paste samples, as from final setting: measured RH (left) and RH due to menisci formation (RH_K) (right) (n=2). 98

5.10 Vicat setting times of the different cement paste mixes without (left) (n=1) and with (right) (n≥2) superplasticizer. 99

5.11 General development of the P-wave velocity and derivative of the P-wave velocity (left) and development of the temperature and derivative of the P-wave velocity (right) in cement paste, with corresponding stages (I: dormant period, II: acceleration period, III: deceleration period), P-wave velocity inflection points (δV_P^{min} and δV_P^{max}) and P-wave velocity values in water and air (V_{water} and V_{air}). 100

5.12 Influence of CFC (left) and combined influence of CFC and superplasticizer (right) on the P-wave velocity (n≥2). 102

5.13 Effect of superplasticizer (0 wt.%, 0.35 wt.% and 0.7 wt.% per mass of binder content) on the P-wave velocity and derivative of the P-wave velocity for an OPC reference mix (n≥2). 103

5.14 Elastic properties (ν_d, E_d, K_d and G_d) of the different cement paste mixes with superplasticizer, calculated from the P-wave velocities. 104

5.15 Smooth derivative of the P-wave velocity curves for the cement paste mixes without (left) and with (right) superplasticizer. . . 105

5.16 Overview of the initial setting times according to the standardised Vicat method and the UPV method for the cement paste mixes without (left) and with (right) superplasticizer. 106

5.17 Overview of the final setting times according to different methods for the cement paste mixes without (left) and with (right) superplasticizer. 107

5.18 P-wave velocities (left) and S-wave velocities (right) of the different concrete mixes with superplasticizer (n=1). 108

5.19 Elastic properties (ν_d, E_d, K_d and G_d) of the different concrete mixes with superplasticizer, calculated from the P- and S-wave velocities. 109

5.20 Compressive strength values of the different concrete mixes, from early ages up to 90 days (n=3). 111

5.21 Tensile splitting strength (left) and tensile strength (right) of the different concrete mixes, after 1, 2 and 7 days (n=3). 113

5.22 Static elastic modulus of the different concrete mixes, after 1, 2 and 7 days (n=3). 114

5.23 Correlation between initial setting times derived from ultrasonic measurements and key concrete ages from calorimetry measurements. Trend lines (dashed lines) with equations and errors (R^2) and x=y (black dotted line). 117

5.24 Correlation between the final setting times derived from ultrasonic measurements and key concrete ages from calorimetry measurements. Trend lines (dashed lines) with equations and errors (R^2) and x=y (black dotted line). 118

5.25 Correlations of the compressive strength with the P-wave velocity, S-wave velocity and dynamic elastic modulus at 12, 24 and 48 hours, both for all compositions (orange trendlines) as for only the CFC concrete mixes (blue trendlines). 119

5.26 Correlation of the static and dynamic elastic modulus. 120

5.27 Modelled cumulative heat (dashed lines) versus experiments (full lines) (left) and modelled chemical affinity as a function of the degree of hydration (right). 124

5.28 Geometry of the considered concrete structure in 1D (ϕ: heat flux, T_S: surface temperature, T_{ext}: ambient temperature). . . 125

5.29 Temperature development of the different concrete mixes as a function of time and distance from the center of the specimen (for a concrete structure with thickness of 1.2 m). 126

5.30 Average temperature development of the different concrete mixes as a function of time and thickness of the specimen. 127

5.31 Compressive strength (left) and tensile strength (right) models of the different concrete compositions, compared to the experimental data. 131

5.32 Static E-modulus model of the different concrete compositions, compared to the experimental data. 132

5.33 Relative compressive strength (left) and tensile strength (right) development of the different concrete mixes. 133

5.34 Relative static E-modulus development of the different concrete mixes. 133

6.1 Chemical shrinkage of the different cement paste samples up to 7 days, plotted as from final setting (negative values = shrinkage). 136

6.2 Measured autogenous deformations of the different cement paste samples up to 7 days (negative values = shrinkage). 137

6.3 Autogenous deformation of the different cement paste samples up to 7 days for W/B = 0.42, plotted as from Vicat final setting (upper left), from δV_P^{max} (upper right), from the start of the swelling (bottom left) and from the onset of the RH drop (bottom right) (negative values = shrinkage). 138

6.4 Autogenous deformation of the different cement paste mixes up to 7 days for W/B = 0.5, plotted from the start of swelling (negative values = shrinkage). 139

6.5 Comparison between the autogenous deformations (t_0 = start swelling) and heat flow for the different blended cement paste mixes. 140

6.6 Comparison between the autogenous deformations (black lines) and evolution of the ettringite content (gray dots) for the RC II mix (left) and CFC 30 mix (right) (positive values = swelling). . 141

6.7 Autogenous deformations of the CFC 30 cement paste mix with addition of 5% gypsum, compared to the original CFC 30 cement paste mix (positive values = swelling). 142

6.8 Autogenous deformations as a function of the internal relative humidity development up to 7 days, for the different cement paste mixes. 144

6.9 Autogenous shrinkage development of the different concrete mixes up to 14 days (negative values = shrinkage). 145

6.10 Drying shrinkage of the different concrete mixes up to 90 days, determined by continuous measurements at KU Leuven (left) and by manual measurements at ENS Cachan (right) (negative values = shrinkage). 146

6.11 Drying shrinkage weight loss as a function of time (above) and as a function of the drying shrinkage strains (ENS Cachan) (below) for the different concrete mixes. 148

6.12 Drying shrinkage strains as a function of the drying shrinkage weight loss, with corresponding trendlines, of the different concrete mixes. 149

6.13 Different autogenous shrinkage models for the different concrete mixes, compared with the experimental results. 153

6.14 RMSE of the different autogenous shrinkage models for the different concrete compositions. 154

6.15 Different total shrinkage models for the different concrete mixes, compared with the experimental results. 157

6.16 RMSE of the different total shrinkage models for the different concrete compositions. 158

6.17 Different drying shrinkage models for the different concrete mixes, compared with the experimental results. 159

6.18 RMSE of the different drying shrinkage models for the different concrete compositions. 160

6.19 Capillary tension development of the different cement paste mixes, calculated from internal RH measurements according to the Kelvin-Laplace law. 161

6.20 Bulk modulus development of the different cement paste mixes, calculated from the ultrasonic measurements. 162

6.21 Chemical shrinkage ϵ_{ch} as a function of the advancement of the degree of hydration α (left) and water saturation degree S_w (right) for the different cement paste mixes. 164

6.22 Determination of self-desiccation shrinkage (left) and decoupled self-desiccation shrinkage and swelling as a function of time (right). 165

6.23 Autogenous shrinkage of the cement paste mixes: experimental values (decoupled self-desiccation and swelling) versus Biot-Bischop model. 167

7.1 Strain-time curve of concrete loaded at t_{load} and unloaded at t_{unload} (neglecting thermal and inelastic strains). 170

7.2 Total concrete strains measured in autogenous (left) and drying (right) conditions of the different concrete mixes. 171

7.3 Basic creep strains per MPa of the different concrete mixes. . . 174

7.4 Drying creep strains per MPa of the different concrete mixes. . 175

7.5 Aging Burger model for basic creep. 176

7.6 Basic creep model, with subdivision into the elastic strains (ϵ_e), Kelvin-Voigt strains and Maxwell strains, for the RC I, RC II and CFC 30 concrete compositions. 180

7.7 Evolution of the drying creep strains as a function of the drying shrinkage strains of the different concrete mixes. 181

7.8 Drying creep model of the different concrete compositions. . . . 182

7.9 Total strain model, including elastic strains, drying shrinkage strains, basic and drying creep strains. 183

7.10 Total strain model, including elastic strains, drying shrinkage strains, basic and drying creep strains. 184

8.1 Effect of creep on concrete cracking, considering only shrinkage (left) and considering both shrinkage and swelling (right) (f_{ct}: tensile strength, $\sigma_{elastic}$: elastic stresses (neglecting creep), $\sigma_{viscoelastic}$: viscoelastic stresses (incorporating creep/relaxation)) (positive stresses = tensile stresses), adapted from [65]. 190

8.2 Autogenous shrinkage induced cracking index versus equivalent time (left) and versus autogenous shrinkage (right) for the different concrete mixes: experiments (full line) versus model (dashed line). 192

8.3 Drying shrinkage induced cracking index versus equivalent time (left) and versus drying shrinkage (right) for the different concrete mixes: experiments (full line) versus model (dashed line) (r = 60 mm). 193

8.4 Drying shrinkage induced cracking index versus equivalent time (left) and versus drying shrinkage (right) for three different structure sizes (r = 100 mm, r = 300 mm and r = 600 mm). . . 194

8.5 Temperature induced cracking index versus equivalent time (left) and versus temperature (right) for three different structure sizes (r = 100 mm, r = 300 mm and r = 600 mm). 196

8.6 Total cracking index versus equivalent time for three different structure sizes (r = 100 mm, r = 300 mm and r = 600 mm), considering only elastic stresses (full lines) and considering viscoelastic stresses (dashed lines). 198

8.7 Cracking index versus equivalent time: rate form (full lines) versus non-rate form (dashed lines), for autogenous shrinkage induced (upper left), drying shrinkage induced (upper right), thermal strain induced (bottom left) and total (bottom right) cracking risk (r = 300 mm). 200

9.1 Schematic overview of the methodology for prediction of the cracking risk of concrete structures, using experimentally assessed temperature, mechanical properties, shrinkage and creep models. 208

B.1 AMORAS project with subdivision in different locations (A. location 'Lillobrug', B. location 'Bietenveld', C. location 'Zandwinningsput') and sub-processes ((1) underwater cell, (2) sand separation installation, (3) pressure pipes, (4) consolidation ponds with dredging portico, (5) dewatering installation, (6) water treatment installation, (7) storage location), adapted from [66]. 238

B.2 Storage of the dewatered filter cakes. 239

D.1 Sample curve demonstrating the influence of different parameters on the logistic (left) and power logistic function (right), adapted from [114]. 244

D.2 Comparison of the experimental data with the model fitting of the velocity curves with logistic, power-logistic, bi- and tri-logistic and bi- and tri-exponential functions for the cement paste mixes with superplasticizer up to 7 days. 247

D.3 Comparison of the experimental data with the model fitting of the velocity curves with logistic, power-logistic, bi- and tri-logistic and bi- and tri-exponential functions for the cement paste mixes without superplasticizer up to 7 days. 248

D.4 RMSE of the different model functions for the cement paste mixes with superplasticizer. 249

D.5 RMSE of the different model functions for the cement paste mixes without superplasticizer. 249

D.6 Comparison of the experimental data with the model fitting of the velocity curves with tri-logistic and tri-exponential functions for the cement paste mixes with superplasticizer up to 48 hours. 253

D.7 Comparison of the experimental data with the model fitting of the velocity curves with tri-logistic and tri-exponential functions for the cement paste mixes without superplasticizer up to 24 hours. 254

D.8 Comparison of the experimental data with the 48 hours model fitting of the velocity curves with tri-logistic and tri-exponential functions for the cement paste mixes without superplasticizer. . 255

E.1 Volumetric phase distribution of cement paste as a function of the degree of hydration, according to Powers' model (assuming autogenous conditions, i.e. sealed hydration), adapted from [133]. 258

E.2 Modelled cumulative heat (dashed lines) versus experiments (full lines) for the different cement paste samples. 261

F.1 Microcracks observed on the surfaces of the RC I, RC II and CFC 30 drying shrinkage concrete samples. 263

F.2 Drying shrinkage cracking pattern. 264

G.1 Eccentricity (e_x and e_y) of the creep load resulting in parasitic bending moments (M_x and M_y). 266

List of Tables

2.1 Current research into the use of dredging sediments as clinker substitute or SCM in blended cements and concrete. 12

3.1 Chemical composition [wt.%] of the cements used. 53

3.2 BET specific surface area, Blaine fineness and density of the cements used. 54

3.3 Mineralogical composition [wt.%] of CFC [205]. 55

3.4 Chemical composition [wt.%] of CFC [205]. 56

3.5 Potentially volatile elements [wt.%] of CFC [205]. 57

3.6 BET specific surface area [m^2/g] and Blaine fineness [cm^2/g] of CFC [205]. 58

3.7 Properties of the traditional superplasticizers. 59

3.8 Properties of the PCE superplasticizers. 60

3.9 Mix proportions of the concrete mixtures. 60

4.1 Initial concrete mix compositions. 74

4.2 Dosages of superplasticizer and fresh concrete properties (n=2). 75

4.3 Air content of the CFC 30 mix for different types of superplasticizer. 79

4.4 Final dosages of superplasticizer and fresh concrete properties of the CFC 30 mix for different types of superplasticizer (n=1). . 79

4.5 Final dosages of superplasticizer and fresh concrete properties of the CFC 30 mix for different W/B ratios (n=1). 82

4.6 Final dosages of superplasticizer and fresh concrete properties for the different concrete compositions with W/B = 0.45 (n=2). 84

4.7 Final concrete mix compositions. 86

5.1 Comparison of main calorimetry characteristics between cement paste and concrete samples. 92

5.2 RH drop due to the dissolution of salts (RH_S). 98

5.3 Initial and final setting times of the different cement paste mixes with and without superplasticizer, determined from UPV measurements. 105

5.4 Initial and final setting times of the different concrete mixes with addition of superplasticizer, determined from UPV measurements. 110

5.5 Characteristic cubic compressive strength after 28 days and strength classes of the different concrete mixes. 112

5.6 Difference between the experimentally determined tensile strength and the tensile strength calculated from the compressive strength results at 7 days. 114

5.7 Difference between the experimentally determined static elastic modulus and the static elastic modulus calculated from the compressive strength results at 7 days. 115

5.8 Key concrete ages derived from calorimetry results. 116

5.9 Fitting parameters of the cumulative heat model (left) and fitting parameters of the chemical affinity model (right). 123

5.10 Parameters and boundary conditions of the temperature model. 125

5.11 Different methods for model fitting of the compressive strength results according to Eq. 5.30. 129

5.12 Parameters of the compressive strength development according to Eq. 5.30, using four different fitting methodologies (see Table 5.11). The values in *italic* are fitting parameters. f_{c28} in MPa. 130

5.13 Parameters of the tensile strength and static E-modulus development according to Eq. 5.31-5.32. 131

6.1 Characteristics of the swelling and shrinkage of the autogenous deformation curves for the different cement paste mixes. 139

6.2 Slopes of the relationship between the autogenous shrinkage and RH development for the different cement paste mixes. 144

6.3 Slopes of the relationship between the drying shrinkage strains and weight loss, for the different concrete mixes and compared to the literature. 150

6.4 Volume of chemical shrinkage (ΔV_{cs}) and amount of chemically bound water (w_{cbw}) of the different cement paste mixes. 164

6.5 RMSE of the Biot-Bischop model for the different cement paste mixes. 166

7.1 Load levels of the different concrete mixes. 171

7.2 Instantaneous elastic strains in autogenous and drying conditions, at loading and unloading, for the different concrete mixes. . . . 172

7.3 Instantaneous elastic moduli derived from creep experiments (in autogenous and drying conditions, at loading and unloading) and measured static elastic modulus after 2 days (i.e. t_{load}) of the different concrete mixes. 173

7.4 Average errors of the drying creep strain for all compositions (according to Eq. 7.7). 176

7.5 Fitting parameters of the basic creep model. 179

7.6 Slopes (β_{dc}) of the drying creep versus drying shrinkage curves for the different concrete mixes. 181

7.7 Slopes (β_{dc}) of the drying creep versus drying shrinkage curves for the different concrete mixes, obtained by fitting the total strain model to the total strain results. 184

C.1 Water absorption of the aggregates according to the technical fiches. 241

C.2 Measured water absorption of aggregates. 241

D.1 Parameters of the logistic model fitting for different cement paste mixes with and without addition of superplasticizer. 250

D.2 Parameters of the power-logistic model fitting for different cement paste mixes with and without addition of superplasticizer. . . . 250

D.3 Parameters of the bi-logistic model fitting for different cement paste mixes with and without addition of superplasticizer. 251

D.4 Parameters of the tri-logistic model fitting for different cement paste mixes with and without addition of superplasticizer. 251

D.5 Parameters of the bi-exponential model fitting for different cement paste mixes with and without addition of superplasticizer. . . . 252

D.6 Parameters of the tri-exponential model fitting for different cement paste mixes with and without addition of superplasticizer. 252

D.7 RMSEs of the tri-logistic and tri-exponential 48 hours model fitting for different cement paste mixes without addition of superplasticizer. 255

D.8 Parameters of the tri-logistic 48 hours model fitting for different cement paste mixes without addition of superplasticizer. 256

D.9 Parameters of the tri-exponential model fitting for different cement paste mixes without addition of superplasticizer. 256

D.10 Parameters of the tri-exponential model fitting of the P-wave velocity of the different concrete mixes. 256

D.11 Parameters of the tri-exponential model fitting of the S-wave velocity of the different concrete mixes. 256

E.1 Autogenous shrinkage model parameters (1). 257

E.2 Autogenous shrinkage model parameters (2). 257

E.3 Drying shrinkage model parameters. 258

E.4 Total shrinkage model parameters. 258

E.5 Fitting parameters of the cumulative heat model for cement paste. 260

G.1 Eccentricities and bending moments of the basic creep specimens. 267

G.2 Eccentricities and bending moments of the drying creep specimens. 267

G.3 Impact of the bending moments on the stress level for the basic creep specimens. 268

G.4 Impact of the bending moments on the stress level for the drying creep specimens. 268

List of Symbols

Abbreviations

ASTM	American Society for Testing and Materials
BET	Brunauer-Emmett-Teller
BTJADE	Béton au jeune age, mesure de la déformation endogène
CFC	Calcined filter cakes
EC	Eurocode
EN	European norm
ENS	École Normale Supérieure
FA	Fly ash
GBFS	Granulated blast furnace slag
ICP-OES	Inductive coupled plasma – optical emission spectrometry
IEA	International Energy Agency
ITZ	Interfacial transition zone
LOI	Loss on ignition
LS	Limestone; lignosulphonate
LT-NAT	Low temperature – nitrogen adsorption test
LVDT	Linear variable differential transducer
MC	Model code
MK	Metakaolin
MSWI	Municipal solid waste incinerator
OECD	Organisation for Economic Cooperation and Development
OPC	Ordinary Portland cement
PCE	Polycarboxylate ether
RC	Reference concrete
SCM	Supplementary cementitious material
SF	Silica fume
SNF	Sulphonated naphthalene formaldehyde
SP	Superplasticizer

TOC	Total organic carbon
ULB	Université Libre de Bruxelles
UPV	Ultrasonic pulse velocity
VITO	Vlaamse Instelling voor Technologisch Onderzoek
XRD	X-ray diffraction

Cement chemistry notations and minerals

C	CaO	calcium oxide (free lime)
S	SiO_2	silicon dioxide (silica)
A	Al_2O_3	aluminium oxide (alumina)
F	Fe_2O_3	iron oxide (ferrite)
M	MgO	magnesium oxide (periclase)
N	Na_2O	sodium oxide
K	K_2O	potassium oxide
H	H_2O	water
$\bar{S}$	SO_3	sulfur oxide
$\bar{C}$	CO_2	carbon dioxide
C_3S	Ca_3SiO_5	alite
C_2S	Ca_2SiO_4	belite
C_3A	$Ca_3Al_2O_6$	aluminate
C_4AF	$Ca_4Al_2Fe_2O_{10}$	ferrite phase
CH	$Ca(OH)_2$	portlandite (lime)
$C\bar{S}$	$CaSO_4$	anhydrite
$C\bar{S}H_{0.5}$	$CaSO_4{\cdot}0.5H_2O$	hemihydrate
$C\bar{S}H_2$	$CaSO_4{\cdot}2H_2O$	gypsum
C-S-H	$CaO\text{-}SiO_2\text{-}H_2O$	calcium silicate hydrate
C-A-H	$CaO\text{-}Al_2O_3\text{-}H_2O$	calcium aluminate hydrate
AFm	$Al_2O_3\text{-}Fe_2O_3$-mono	calcium aluminate-ferrite hydrates
$C_4A\bar{S}H_{12}$	$Ca_4Al_2O_7(SO_3){\cdot}12H_2O$	monosulphoaluminate
$C_4A\bar{C}H_{11}$	$Ca_4Al_2O_7(CO_2){\cdot}11H_2O$	monocarboaluminate
$C_4A\bar{S}_{0.5}H_{12}$	$Ca_4Al_2O_7(CO_2)_{0.5}{\cdot}12H_2O$	hemicarboaluminate
C_2ASH_8	$Ca_2Al_2SiO_7{\cdot}8H_2O$	strätlingite (gehlenite hydrate)
C_4AH_{7+x}	$Ca_4Al_2O_7{\cdot}(x+7)H_2O$	hydroxy-AFm
C_3AH_6	$Ca_3Al_2(OH)_{12}$	hydrogarnet
AFt	$Al_2O_3\text{-}Fe_2O_3$-tri	calcium aluminate-ferrite hydrates
$C_6A\bar{S}_3H_{32}$	$Ca_6Al(SO_4)_3(OH)_{12}{\cdot}26H_2O$	ettringite

Symbols *

$\tilde{A}$	[1/s]	Chemical affinity
c_p	[J/kg/K]	Specific heat capacity
C	[J/m^3/K]	Volumetric heat capacity
CTE	[µm/m/K]	Coefficient of thermal expansion
D	[m]	Diameter
E	[GPa]	Elastic modulus; stiffness
E_a	[J/mol]	Activation energy
E_c	[J/mol]	Elastic modulus of concrete
E_d	[GPa]	Dynamic elastic modulus
E_{KV}	[GPa]	Stiffness of the Kelvin-Voigt chain
E_M	[GPa]	Stiffness of the Maxwell chain
E_s	[GPa]	Static elastic modulus
f_c	[MPa]	Compressive strength
f_{ck}	[MPa]	Characteristic compressive strength
f_{cm}	[MPa]	Mean compressive strength
f_{ct}	[MPa]	Tensile strength
$f_{ct,sp}$	[MPa]	Tensile splitting strength
$f_{ct,ft}$	[MPa]	Flexural strength
G_d	[GPa]	Dynamic shear modulus
h	[%]	Relative humidity
h_0	[m]	Notional size
h_p	[W/m^2/K]	Coefficient of heat exchange by convection
I_{cr}	[-]	Cracking index
k	[W/m/K]	Thermal conductivity
K_b	[GPa]	Bulk modulus of porous body
K_d	[GPa]	Dynamic bulk modulus
K_s	[GPa]	Bulk modulus of solid skeleton
L	[m]; [J/m^3]	Length; latent heat of hydration
m	[kg]	Mass
M_w	[kg/mol]	Molecular weight of water
n	[-]; [-]	Number of test specimens; number of moles
n_X	[-]	Aging parameter of material property X
p	[Pa]; [-]	Pressure; initial porosity
p_c	[Pa]	Capillary pressure
q	[W]	Heat flow
Q	[J]	Heat of hydration

*For each symbol, a standard unit is given. The unit used for each of the symbols, however, can deviate from the unit mentioned here and is therefore always indicated in the relevant section.

Q_∞	[J]	Ultimate heat of hydration
r	[mm]	Pore radius
R	[-]	Coefficient of determination
RH	[%]	Relative humidity
RH_K	[%]	Relative humidity due to menisci formation
RH_S	[%]	Relative humidity due to salt dissolution
RMSE		Root mean square error
s	[-]	Cement type dependent parameter
S	[m^2]; [-]	Surface; time function
S_w	[-]	Water saturation degree
t	[s]	Time
t_0	[s]	Time-zero; final setting time
t_{eq}	[s]	Equivalent time
t_s	[s]	Time of start of drying
T	[K]	Temperature
T_0	[K]	Initial temperature
T_{ext}	[K]	Ambient temperature
T_S	[K]	Surface temperature
U	[J]	Interface energy
v	[m/s]	Velocity
V	[m^3]	Volume
V_P	[m/s]	P-wave velocity
V_S	[m/s]	S-wave velocity
V_{cs}	[mL]	Volume of chemical shrinkage
w_{cbw}	[g]	Amount of chemically bound water
W/B	[-]	Water-to-binder ratio
W_{eff}/B	[-]	Effective water-to-binder ratio
W/C	[-]	Water-to-cement ratio
x, y, z	[m]	Cartesian coordinates
X		Material property
X_{28}		Material property after 28 days
α	[-]	Advancement of the degree of hydration
β	[-]	Time function
β_{dc}	[-]	Proportionality factor between drying creep and drying shrinkage
γ_w	[N/m]	Surface tension of water
ϵ	[μm/m]	Strain
ϵ_{as}	[μm/m]	Autogenous shrinkage strain
ϵ_{bc}	[μm/m]	Basic creep strain
ϵ_c	[μm/m]	Concrete strain
ϵ_{ch}	[μm/m]	Chemical shrinkage strain

ϵ_{cr}	[µm/m]	Creep strain
ϵ_{dc}	[µm/m]	Drying creep strain
ϵ_{ds}	[µm/m]	Drying shrinkage strain
ϵ_{e}	[µm/m]	Elastic strain
ϵ_{in}	[µm/m]	Inelastic strain
ϵ_{KV}	[µm/m]	Strain of the Kelvin-Voigt chain
ϵ_{M}	[µm/m]	Strain of the Maxwell chain
ϵ_{sh}	[µm/m]	Shrinkage strain
ϵ_{sd}	[µm/m]	Autogenous self-desiccation shrinkage strain
ϵ_{sw}	[µm/m]	Autogenous swelling strain
ϵ_{th}	[µm/m]	Thermal strain
ϵ_{v}	[µm/m]	Volumetric strain
ϵ_{∞}	[µm/m]	Final/ultimate strain
η	[GPa·s]	Viscosity
η_{KV}	[GPa·s]	Viscosity of the Kelvin-Voigt chain
η_{M}	[GPa·s]	Viscosity of the Maxwell chain
θ	[°]	Contact angle between liquid phase and solid matrix
ν_{d}	[-]	Dynamic Poisson's ratio
ρ	[kg/m^3]	Density
ρ_{c}	[kg/m^3]	Density of cement
ρ_{w}	[kg/m^3]	Density of water
σ	[MPa]	Stress
σ_{c}	[MPa]	Concrete stress
τ_{KV}	[s]	Characteristic/retardation time of the Kelvin-Voigt chain
ϕ	[-]; [W/m^2]	Creep coefficient; heat flux
ξ	[-]	Degree of hydration
ξ_{∞}	[-]	Final degree of hydration

Mathematical symbols

δ	Partial/functional derivative
$\sum$	Sum operator
$\int$	Integral
Δ	Differential operator
∇	Nabla operator
$\nabla\square$	Gradient
$\nabla \cdot \square$	Divergence
$\dot{\square}$	First order time derivative

Constants

R = 8.314 J/mol/K Universal gas constant

Chapter 1

Introduction

1.1 Problem statement

As the world's largest manufactured product by mass, cement is responsible for 10% of the total anthropogenic CO_2 emissions, or about 6% of the total anthropogenic greenhouse gases [196]. Due to the rapid population growth in developing countries and the enormous growth in cement demand associated with it (see Fig. 1.1), the share of the cement production in the global CO_2 emissions is only expected to increase [128, 196].

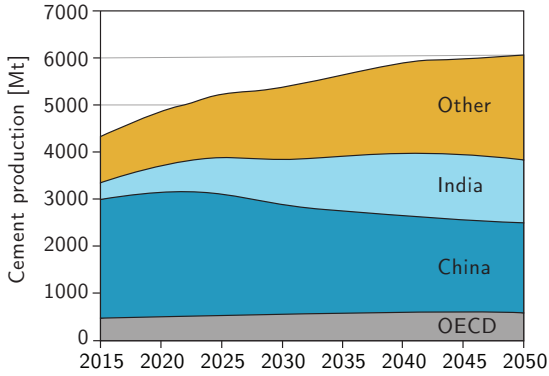

Figure 1.1: Expected cement production in China, India, OECD (Organisation for Economic Cooperation and Development) countries and other countries, according to the IEA (International Energy Agency), adapted from [196].

The biggest challenge of the cement industry nowadays is therefore the reduction of these CO_2 emissions, in order to contribute to achieving the United Nations sustainable development goals [221]. A promising and well-established way to do so, is by using supplementary cementitious materials (SCMs) as partial cement replacement in concrete. The conventional SCMs such as limestone filler, blast furnace slag and coal fly ash, however, will not be able to cover the growing cement demand in future, considering the limits of their availability and production. Therefore, there is a strong need for alternative sources of SCMs [55, 136, 152]. The use of calcined clays as a pozzolanic material in concrete has received considerable interest in recent years [128, 182]. Especially the use of wastes/residues and industrial by-products containing considerable amount of clay minerals (such as calcined clay-rich dredging sediments, calcined excavated waste clays, waste fines from the production of lightweight fine aggregates, etc.) as alternative SCM should be encouraged, contributing in reducing the costs of calcined clay SCMs and limiting the amount of waste streams [137, 196].

In the port of Antwerp, Belgium, each year about 450.000 tonnes (dry matter) of clay-rich dredging material is generated and piled up, maintaining and improving the navigation of ships in the Scheldt river [59, 205]. Until few years back, no suitable or feasible applications existed for the dredging sediments, and the material was disposed of in marine repositories or landfilled, causing a negative impact on the environment. Between 2008 and 2011, a state-of-the-art treatment and storage facility for dredging sediments was realised by the Flemish government, providing a more sustainable solution for treatment and storage of the maintenance dredging material, by processing the sediments to dewatered filter cakes. Nevertheless, the material remains a residue and the current disposal capacity is limited to a period of 30 years. To increase the operational lifetime of the storage facility, new applications for the non-contaminated filter cakes were being considered, and the BIND-AMOR project was launched. The BIND-AMOR project investigates the potential of the filter cakes for production of supplementary cementitious materials and is executed under the authority of the Flemish Government by VITO (Flemish Institute for Technological Research) and KU Leuven. Flash calcination was examined as a means to activate the clay minerals contained in the dredging sediments. The properties, pozzolanic reactivity and hydration process of the calcined dredging sediments, henceforth called CFC (calcined filter cakes), were already extensively investigated in the BIND-AMOR project [205, 207] and has shown the potential of the material for its use as a novel SCM in concrete. The beneficial reuse of this dredging material as SCM could thus provide a sustainable solution, limiting landfilled waste and limiting extraction of natural resources [97].

1.2 Research objectives

The main objective of this research is to assess the effect of CFC as an SCM on the early-age properties of concrete, in order to understand its early-age deformation potential and predict its time-dependent deformations at long term. Detailed analysis of the mechanical properties development and shrinkage behaviour, especially at early ages, and prediction of the time-dependent deformations and cracking risk of concrete are essential to assess the performance and predict the serviceability and durability of a concrete structure.

In order to achieve this main goal and understand the effective role of CFC as an SCM in concrete (at 20, 30 and 40 wt.% replacement ratios), the following objectives are defined:

- Analysis of the influence of CFC on the hydration process and early-age properties of blended cement, which is key to understand concrete properties and performance.
- Characterisation of the impact of CFC on the development of fresh and mechanical concrete properties.
- Identification of the role of CFC on concrete shrinkage and creep, and parametrisation of existing shrinkage and creep models to accurately predict shrinkage and creep of CFC concrete.
- Development of a predictive tool to assess the thermal-shrinkage-creep induced (early-age) cracking risk of concrete with CFC, which aims to provide a general model for comparison of the cracking risk of different concrete mixes and to assess its relevance for realistic structural applications.

With these research objectives, the thesis ultimately aims at understanding main concrete properties and assessing existing models for accurate prediction of early-age and long-term cracking risk of concrete utilising CFC blended cement. The thesis thereby contributes to filling knowledge gaps regarding the influence of potentially new SCMs on early-age and long-term concrete performance. Furthermore, the thesis offers parametrised models for the prediction of shrinkage and creep of SCM blended concrete, and provides a cracking prediction tool applicable to different concrete mixes.

1.3 Outline

The outline of the PhD thesis and the interaction between the different chapters are illustrated in Fig. 1.2.

Chapter 2 provides an overview of the current state of the art regarding the use of supplementary cementitious materials in concrete. The influence of existing, commonly used SCMs on the hydration process and main concrete properties is discussed.

Chapter 3 introduces the different materials and various techniques/methods used. Chemical composition and physical properties of the cementitious materials and aggregates are described. The mix compositions and mixing procedures of both cement paste and concrete mixes are given, and the analytical techniques and test methods are explained.

Chapter 4 describes the concrete mix design optimisation. Three different concrete mix design parameters are examined: cement replacement ratio, type and dosage of superplasticizer, and water-to-binder ratio.

Chapter 5 focusses on the early-age development of CFC blended cement paste and concrete. The influence of CFC on the hydration process is thoroughly studied, by examining the hydration kinetics, hydration products and internal relative humidity development. The setting behaviour is studied by performing traditional Vicat measurements, as well as ultrasonic measurements. Furthermore, the strength and stiffness development is discussed and correlations between different early-age concrete properties are investigated. Finally, the temperature and mechanical properties development is modelled.

Chapter 6 deals with the shrinkage behaviour of CFC blended cement paste and concrete. Both autogenous, chemical and drying shrinkage are studied and different empirical shrinkage models are analysed, in order to provide parameterised models to predict the shrinkage behaviour of CFC concrete.

Chapter 7 describes the creep behaviour of CFC blended cement concrete. Both basic and drying creep are considered and modelled.

Chapter 8 assesses the thermal-shrinkage-creep induced (early-age) cracking risk of concrete with CFC. A macroscopic and stress approach based cracking risk prediction tool, using experimentally assessed model parameters for the prediction of mechanical properties, shrinkage and creep, is developed.

Chapter 9 summarises the main conclusions and provides recommendations for future research.

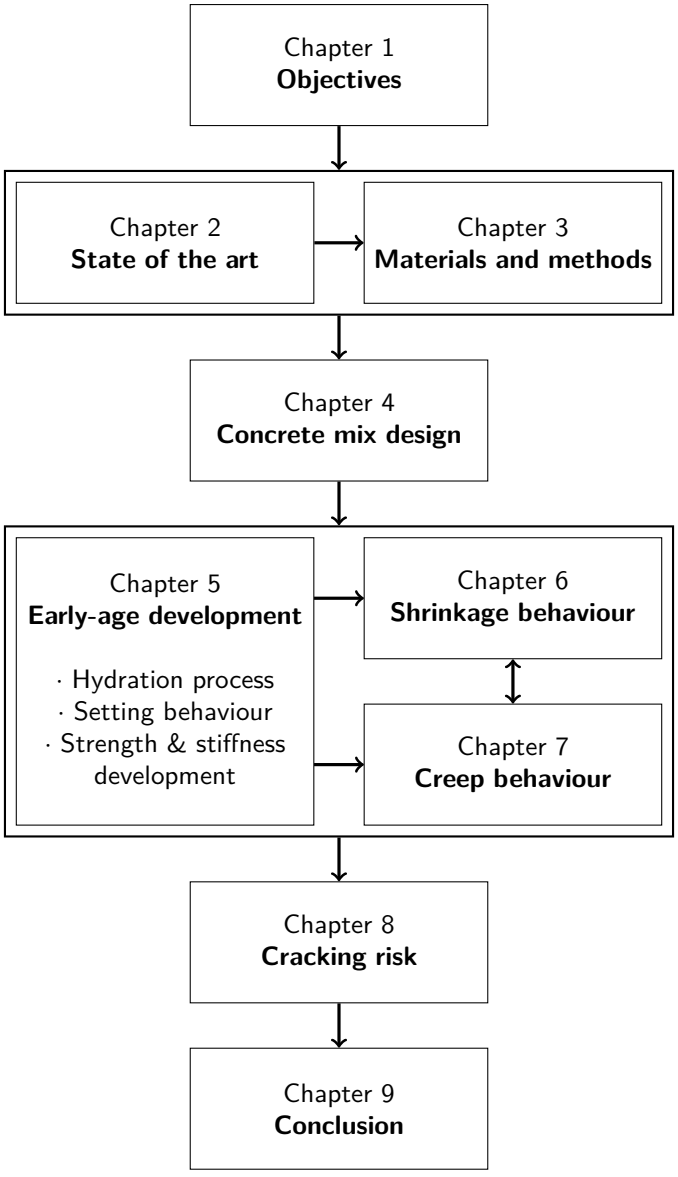

Figure 1.2: Outline of the PhD thesis and interaction between the chapters.

Chapter 2

State of the art

This chapter describes the current state of the art regarding the use of supplementary cementitious materials (SCMs) in concrete and their influence on the hydration process and main concrete properties. First, a general definition of SCMs is given, the limitations regarding their use in concrete are illustrated and the current use of dredging sediments as an SCM is discussed (Section 2.1). Furthermore, the influence of SCMs on the hydration process (Section 2.2), fresh concrete properties (Section 2.3), hardened concrete properties (Section 2.4) and volumetric changes, i.e. shrinkage and creep (Section 2.5) are presented. Finally, the current state of the art regarding shrinkage and creep modelling of (SCM blended) concrete is discussed (Section 2.6). The chapter concludes with a brief summary, highlighting the research gaps and key questions (Section 2.7).

2.1 Supplementary cementitious materials

2.1.1 Definition and classification

SCMs are materials that possess either hydraulic or pozzolanic behaviour and contribute to the properties of hardened concrete in conjunction with ordinary Portland cement (OPC) [209, 216]. Hydraulic binders are materials that are able to set and harden under water by forming cementitious products via hydration reactions. Pozzolanic materials are defined as *"siliceous or siliceous and aluminous materials which, in itself, possess little or no cementitious value, but that will, in finely divided form and in the presence of moisture, react*

chemically with calcium hydroxide at ordinary temperatures to form compounds having cementitious properties" [209, 216].

The definition of SCMs includes a large number of materials, which vary widely in chemical and mineralogical composition, origin and physical properties. Although the hydraulic or pozzolanic reactivity of SCMs largely depends on their physico-chemical properties, SCMs are typically divided according to their origin. Two main categories can be distinguished: SCMs of natural origin and SCMs of artificial origin. Natural SCMs include materials that can be used in their naturally occurring form (after at most a sieving or grinding process), while artificial SCMs are materials that need structural modifications. Artificial SCMs are mostly by-products from high-temperature processes (e.g. fly ash from coal combustion, blast furnace slag from iron extraction in blast furnaces or silica fume from the melting process in the silicon and ferro-silicon industry), but they can also be produced deliberately by thermal activation of natural clays [209, 216].

The chemical composition of some commonly used SCMs is shown in Fig. 2.1 in a CaO-Al_2O_3-SiO_2 ternary diagram. SCMs are generally characterised by a lower calcium content and higher silica and alumina content than OPC, and can also be divided according to their chemical element composition in siliceous, aluminosiliceous and calcium aluminosiliceous SCMs [137, 152]. Considerable variation in chemical composition and physico-chemical properties between different types of SCMs, even within SCM groups of the same origin, demonstrates their large impact on concrete properties [209, 216].

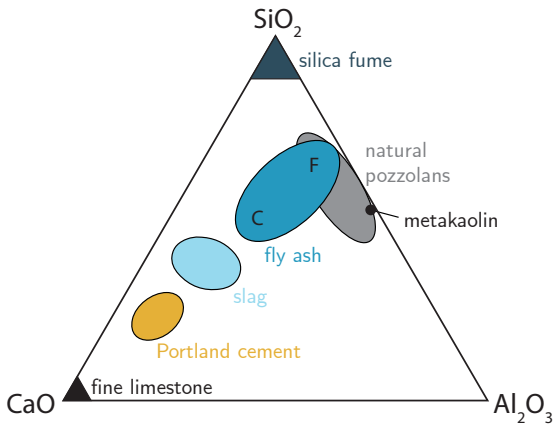

Figure 2.1: CaO-Al_2O_3-SiO_2 ternary diagram, situating the chemical composition of some commonly used SCMs, adapted from [152].

2.1.2 Use and limitations

SCMs are commonly and increasingly used as a partial cement replacement or mineral addition in concrete and are an effective strategy to reduce CO_2 emissions associated with the cement industry. The most commonly used SCM is naturally sourced limestone (LS), mainly acting as an inert filler. The most commonly used 'reacting' SCMs, on the other hand, are granulated blast furnace slag (GBFS) and fly ash (FA), with respective global availability of 330 Mt and 900 Mt per year [196]. The global average clinker-to-cement ratio was 0.65 in 2014. In China, the average clinker factor was 0.65 in 2018, while the European average clinker-to-cement ratio was only 0.74 in 2016 [189]. In Europe, however, there is limited potential for further reduction, considering the decreasing regional availability of the most desirable high-quality SCMs, i.e. fly ash and blast furnace slag [98, 136, 189, 196]. The available amount of GBFS, for example, reduced from 17% of the cement production in 1980 to 8% of the cement production in 2014, due to increased recycling of scrap steel and use of more efficient technologies in the steel production process [196]. Electricity production by burning coal, on the other hand, is being phased out due to its high CO_2 emissions, resulting in closure of coal plants. The UK, for example, plans to close all its coal-fired power plants by 2025 and the Netherlands by 2030, while in the USA already 40% of all coal plants have been closed during the last five years [137]. In Asia, however, the picture is different and FA production will probably remain constant in the following years due to the increasing industrialisation and urbanisation, resulting in a relatively stable coal demand [189]. Fig. 2.2 illustrates the global evolution of the clinker substitutes over the past 25 years, clearly showing the levelling off of the clinker substitution ratio and proving the need for new sources of high-quality SCMs [189, 196].

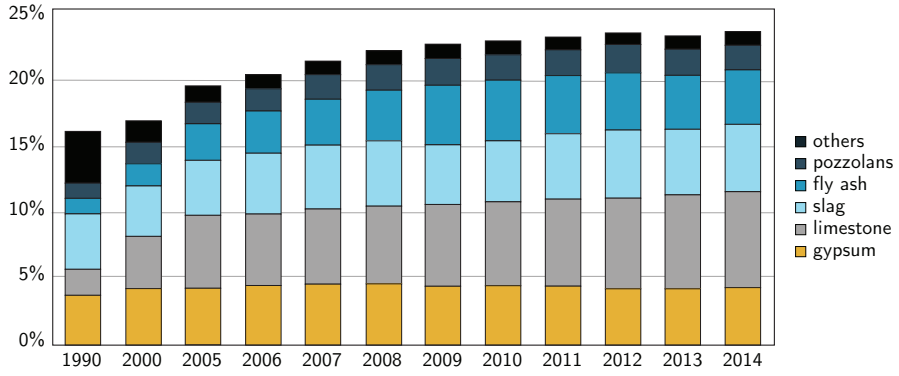

Figure 2.2: Global clinker substitution evolution in time, adapted from [196].

The use of GBFS and FA does not show any potential for further CO_2 reduction. The use of primary sourced SCMs (whether or not calcined) and an expansion of the range of industrial by-products and societal wastes used (see Fig. 2.3), on the other hand, could drastically change the clinker substitution evolution. Calcined clays have received considerable interest in recent years as a pozzolanic material [128, 182] and show the potential to substitute increasing parts of clinker in regions where the global geological availability is high [189]. Metakaolin (MK) is the most commonly used and most reactive calcined clay, however, its availability is limited and its cost is relatively high. Calcination of other clay minerals and impure clays for the use as SCM, should therefore be encouraged. Although the availability of clays can be regionally very limited, vast reserves of clay minerals occur in many parts of the world and exploitation of these reserves could thus significantly increase the global supply of SCMs [137, 196].

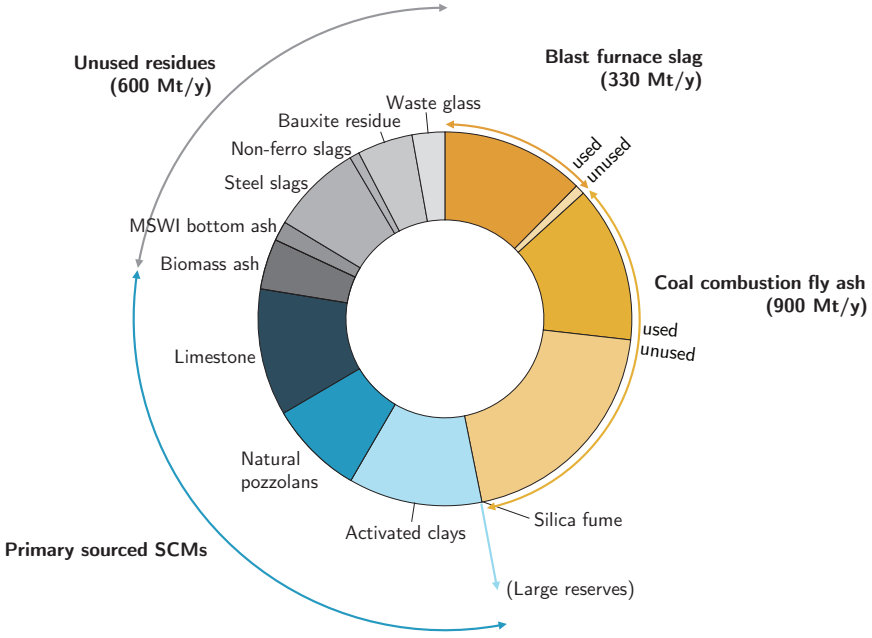

Figure 2.3: Overview and availability of existing and future SCMs, adapted from [208].

Furthermore, unused residues or waste materials, such as biomass ashes, agricultural waste ashes, municipal solid waste incineration (MSWI) ashes, waste glass, etc. (annual production of 600 Mt) should also be considered as alternative pozzolanic or latent hydraulic SCMs [168, 190, 196]. The use of

residues and by-products containing considerable amounts of clay minerals, such as calcined clay-rich dredging sediments, calcined excavated waste clays, waste fines from the production of lightweight fine aggregates, etc. should also receive attention, contributing in reducing the costs of calcined clay SCMs and limiting the amount of waste streams [137, 196]. However, understanding of the early-age and long-term performance and durability of these less frequently used, alternative SCMs in concrete, currently lacks scientific knowledge [168].

2.1.3 Calcined dredging sediments as SCM

Both waterways, marine harbours, estuaries, as well as dams and water reservoirs can be subjected to sedimentation or solid particle accumulation, reducing their capacity [96]. In order to maintain the navigation of ships in waterways and harbours, and to guarantee the lifespan of dams and water reservoirs, dredging is therefore necessary. The volume of dredging material generated annually is huge. In Europe and the United States, the amount of dredging sediments is estimated at respectively 300 million tonnes and 229 million m^3 each year [23, 205]. In France, 50 million m^3 sediments are yearly dredged in five maritime harbours and 17 commercial ports, and in Antwerp port (Belgium), each year 450.000 tonnes of dry matter dredging material is generated and piled up [3, 205]. Dredging sediments are variable in time and space. Geological, topographical and hydro-meteorological features, as well as human interventions, affect spatial and temporal variations [97]. The processing and disposal of dredging sediments has therefore become a major environmental, ecological and economical concern in the world [38, 241]. Competition for resources and space in densely developed areas, such as harbours, is strong and disposal costs are consequently high [207]. Furthermore, dredging sediments can contain variable amounts of inorganic contaminants or organic pollutants [241].

At present, a number of diverse applications for the reuse of dredging sediments as raw material, have been tested at lab, pilot and even industrial scale [207]. The use of dredging sediments as a resource for the production of bricks [116, 146, 184], lightweight aggregates [53], stabilised road-base [201, 233], Portland clinker and SCMs has been explored. Research on the reuse of dredging sediments as clinker substitute or SCM in blended cements is rather limited, but is gaining more attention in recent years. Table 2.1 summarises the current research regarding the use of (calcined) dredging sediments as clinker substitute or as an SCM in blended cements and concretes. Mostly France and Algeria have investigated the use of dredging sediments as an SCM in blended cements in recent years, while research on the use of dredging sediments in concrete is very limited, especially for calcined dredging sediments. Most of the research comprised characterisation of the dredging material and initial tests on

cement pastes or mortar, such as heat of hydration, setting time, mechanical properties, etc. Considering calcined dredging sediments, only Beckstrom et al. [23] and Bouhamou et al. [38] studied concrete properties of calcined dredging sediment blended mixes. The results show the potential of using calcined dredging sediments as an alternative SCM in concrete, by reaching concrete compressive strength equivalent to reference mixes, decreasing concrete shrinkage and reducing CO_2 emissions produced by the cement industry [23, 38].

Table 2.1: Current research into the use of dredging sediments as clinker substitute or SCM in blended cements and concrete.

Author (year)	Origin (country)	Calcined	Reuse as
Achour (2019) [2]	Marine (FR)	✘	SCM in concrete
Agostini (2007) [3]	Harbour (FR)	✘	SCM in mortar
Aouad (2012) [9]	River (FR)	✘	Clinker substitute in cement paste
Beckstrom (2014) [23]	River (USA)	✔	SCM in concrete
Bouhamou (2016) [38]	Dam (ALG)	✔	SCM in concrete
Chikouche (2016) [55]	Dam (ALG)	✔	SCM in cement paste and mortar
Dang (2013) [59]	Marine (FR)	✔	SCM in mortar
Faure (2017) [97]	Reservoir (FR)	✔	Clinker substitute/SCM in cement paste
Rozas (2015) [181]	Harbour (ES)	✘	SCM in concrete
Snellings (2017) [207]	Harbour (BE)	✔	SCM in mortar
Zhao (2018) [241]	Marine (FR)	✘	SCM in mortar and concrete

Flash-calcined dredging sediments from Antwerp port

The potential use of calcined dredging sediments from Antwerp port as SCM in concrete was investigated in the BIND-AMOR project, a collaboration between the Flemish Government, VITO and KU Leuven. Flash calcination was studied as a means to activate the clay minerals present in the dredging sediments and the (flash-calcined) dredging material was characterised in detail [205, 206, 207].

Prior to the dredging operations in the port of Antwerp, extensive sampling campaigns take place to determine the degree of contamination of the sediments in place. Contaminated sediments can thus be strictly separated from non-contaminated sediments. After dredging, treatment of the non-contaminated dredging sediments consists of a separation of the sand fraction and a mechanically dewatering of the fine fraction by membrane filter presses, resulting in filter cakes. After a long term sampling campaign, the final filter cake residue was found to be homogeneous and constant in composition (fluctuations less than 1 wt.%) and granulometry over time [206].

Flash calcination of the dredging sediment filter cakes was considered to be a viable option to produce an alternative SCM for the production of low-CO_2 blended cements [205]. Upon flash calcination, the total organic carbon content

strongly reduces and clay minerals present in the dredging sediments completely dehydroxylate. Furthermore, both melting and sintering occur during flash calcination, resuling in a reduced specific surface area at higher calcination temperatures. Properties and pozzolanic reactivity of the flash-calcined dredging material were studied in detail. The chemical composition of the calcined filter cakes (CFC) is close to the chemical compostion of fly ash and natural pozzolans, and CFC showed a pozzolanic reactivity inferior to metakaolin, but superior to siliceous fly ash [205, 206]. Moreover, the cement hydration was positively affected by the addition of CFC due to the filler effect and the formation of additional cement hydrates. Also, the calcined dredging sediments contributed to the strength development of blended cement mortar, due to the supplemental pozzolanic reaction [207]. More characteristics and material properties of CFC can be found in Chapter 3, subsection 3.1.2.

2.2 Influence of SCMs on the hydration process

Hydration reactions are reactions between anhydrous compounds (e.g. non-hydrated cement) and water, resulting in new compounds, hydrates. The hydration of OPC involves the complex process of a series of individual chemical reactions occurring in parallel or in some complex combination, and is related with both chemical and physico-mechanical changes [44, 121].

SCMs can cause major changes in the hydration kinetics and hydrate assemblages. Firstly, the physical presence of the SCM will enhance the reaction of the clinker phases at early ages by providing additional nucleation sites for hydrates and increasing the effective W/C ratio, i.e. the *filler effect* [197]. Secondly, the hydration reactions are complemented by pozzolanic or hydraulic reactions, forming additional hydration products. SCMs either react with calcium hydroxide, formed during the cement hydration, to form calcium silicate hydrates and other cementitious compounds (i.e. *pozzolanic reaction*) or hydrate with water in the presence of an activator to form hydration products similar to those formed in pure OPC hydration (i.e *hydraulic or latent hydraulic reaction*) [202, 209, 216].

Subsection 2.2.1 discusses the hydration reactions of OPC, while subsection 2.2.2 discusses the pozzolanic reaction. The influence of SCMs on the blended cement hydration is explained in subsection 2.2.3 and in subsection 2.2.4, finally, the different reaction products formed are discussed.

2.2.1 Hydration of OPC

Composition of cement

Ordinary Portland cement comprises Portland clinker and a small amount of calcium sulphate, to control the setting. The raw materials required for the manufacture of Portland clinker are: limestone or chalk (as a source of calcium oxide (CaO)); shales, clays or slates (as a source of aluminium oxide (Al_2O_3) and silica (SiO_2)) and iron and pyrites (as a source of ferric oxide (Fe_2O_3)). Small amounts of other compounds, such as magnesium oxide, alkalis, phosphates, etc. can also appear as pollution in the aforementioned compounds. After crushing, grinding and screening of the raw materials in suitable proportions, and heating the raw mix to a temperature of about 1450°C in a rotary kiln, cement clinker is produced. The main mineral phases of Portland clinker are alite, belite, aluminate and a ferrite phase. Other phases, such as alkali sulphates and calciumoxide, are only present in small quantities [24, 172].

Hydration of individual clinker minerals

Due to the complex interactions between the hydration of the individual clinker minerals in the cement hydration process, the hydration reactions of the individual mineral phases will first be discussed on their own.

Tricalcium silicate Tricalcium silicate or alite (C_3S or $3CaO{\cdot}SiO_2$) is the main and most important clinker mineral in Portland cement. Alite constitutes about 50% to 70% of the cement by mass and dominates the early hydration period, responsible for setting and early strength development. The hydration of C_3S is an exothermic reaction with calcium silicate hydrate (C-S-H) gel and calcium hydroxide or portlandite (CH or $Ca(OH)_2$) as hydration products. Several stages are distinguished in the hydration process: (I) pre-induction period or initial reaction, (II) induction period or period of slow reaction, (III) acceleration period and (IV) deceleration period. The first phase of the hydration begins immediately upon wetting and is the initial reaction of alite with water (see Eq. 2.1), characterised by a large exothermic signal. Both the wetting of cement powder and the dissolution of C_3S contribute to this early heat release [44, 121].

$$C_3S + 3H_2O \rightarrow 3Ca^{2+} + H_2SiO_4^{2-} + 4OH^- \tag{2.1}$$

During the first hour, the C_3S dissolution rate decelerates very quickly and the liberation of hydration heat reduces significantly, while the solution is still undersaturated. This is the start of a dormant period: the induction period.

After several hours, when a certain critical value of calcium and hydroxide ions is reached, a rapid crystallisation of CH and C-S-H takes place, followed by a rapid reaction. During this stage, the hydration reaction (see Eq. 2.2) occurs actively and the rate of hydration increases significantly, reaching a maximum at the end of this acceleration period [44, 121, 172].

$$C_3S + (3+x-y)H_2O \rightarrow C_ySH_x + (3-y)Ca(OH)_2 \tag{2.2}$$

The final stage is the deceleration period, where the formation of hydration products slows down, the rate of reaction decreases and the reaction is diffusion controlled [121, 172].

Dicalcium silicate By constituting 10% to 35% of the cement by mass, dicalcium silicate or belite (β-C_2S or β-$2CaO{\cdot}SiO_2$) is the second most abundant clinker mineral in Portland cement. The hydration of belite (see Eq. 2.3) is similar to the hydration of alite, however, the reaction proceeds slower. Furthermore, significantly less portlandite is formed by the hydration of belite, but the C-S-H phases formed are very similar [121, 172].

$$2C_2S + 5H_2O \rightarrow C_3S_2H_4 + Ca(OH)_2 \tag{2.3}$$

Tricalcium aluminate Although tricalcium aluminate or aluminate (C_3A or $3CaO{\cdot}Al_2O_3$) constitutes only 4% to 11% of Portland cement by mass, it influences the early hydration kinetics significantly. In the absence of soluble calcium sulphate, tricalcium aluminate reacts with water to form hexagonal AFm phases C_2AH_8 and C_4AH_{13}, that are subsequently converted into the thermodynamically more stable C_3AH_6 phase, hydrogarnet (see Eq. 2.4) [44, 121, 172].

$$2C_3A + 21H_2O \rightarrow C_4AH_{13} + C_2AH_8 \rightarrow 2C_3AH_6 + 9H_2O \tag{2.4}$$

This initial reaction of aluminate (the so-called *flash set*) is very rapid and strongly exothermic. In order to slow down the initial reaction rate and control the hydration of aluminate, calcium sulphate in the form of gypsum ($CaSO_4{\cdot}2H_2O$ or $C\bar{S}H_2$), anhydrite ($CaSO_4$ or $C\bar{S}$) or hemihydrate ($CaSO_4{\cdot}0.5H_2O$ or $C\bar{S}H_{0.5}$) is added. In the presence of calcium sulphate, tricalcium aluminate reacts with the calcium sulphate to form a protective layer of ettringite ($C_6A\bar{S}_3H_{32}$) on the surface of the C_3A crystals (see Eq. 2.5) [44, 172].

$$C_3A + 3C\bar{S}H_x + (32-3x)H_2O \rightarrow C_6A\bar{S}_3H_{32} \tag{2.5}$$

where x=0 for anhydrite, x=0.5 for hemihydrate and x=2 for gypsum. The formation of this protective layer reduces the initial reaction rate and introduces

a dormant period in the hydration of tricalcium aluminate. The amount of calcium sulfate added determines the length of this dormant period and ideally for cement hydration, this dormant period lasts until the hydration peak of alite is over. After all available gypsum (SO_4^{-2} ions) is consumed, the dissolution rate increases again and the excess C_3A will react with ettringite to form calcium aluminate monosulfate hydrate ($C_4A\bar{S}H_{12}$), an AFm phase [44, 172].

$$C_6A\bar{S}_3H_{32} + 2C_3A + 4H \rightarrow 3C_4A\bar{S}H_{12} \tag{2.6}$$

Calcium aluminoferrite The hydration of calcium aluminoferrite (C_4AF or $4CaO{\cdot}Al_2O_3{\cdot}Fe_2O_3$) is similar to the hydration of tricalcium aluminate, however, their reaction rates differ. Although the hydration of the ferrite phase is slower than the hydration of the aluminate phase, addition of a calcium carrier is nevertheless necessary to slow down the reaction. In the presence of calcium sulphate, the main hydration product is an AFt phase $C_6(A,F)\bar{S}_3H_{32}$, which will subsequently be converted to AFm $C_4(A,F)\bar{S}H_{12}$ [121, 172].

Hydration of Portland cement

The hydration of OPC is a complex process consisting of multiple reactions between calcium silicates and calcium aluminates (the clinker minerals), calcium sulphate and water. Five different stages can be distinguished during the cement hydration process, based on the heat development, as shown in Fig. 2.4.

Pre-induction period or initial reaction The initial reaction starts immediately upon contact of cement with water and only lasts for a couple of minutes. The calcium and alkali sulphates present in the cement rapidly dissolve, contributing K^+, Na^+, Ca^{2+} and SO_4^{2-} ions. Tricalcium silicate (C_3S) and only a fraction of dicalcium silicate (C_2S) dissolve during the pre-induction period, precipitating a layer of C-S-H gel. Tricalcium aluminate (C_3A) and calcium aluminoferrite (C_4AF) subsequently dissolve and react in a similar way with Ca^{2+} and SO_4^{2-} ions, leading to the formation of an alumina rich amorphous gel around the cement particles and yielding short ettringite (AFt) rods at the edges of the gel layer and in solution (see Fig. 2.5 (b)). This initial reaction is characterised by a significant initial exothermic peak during the first minutes of the cement hydration [110, 121, 212].

Induction period After the pre-induction period of fast reaction, a period of very low heat release, known as the induction period, follows. For a few hours, the hydration of the clinker minerals progresses very slowly [110, 121, 212]. The

exact mechanism behind this slowing down, however, is not yet fully understood and many theories have been proposed to explain these phenomena [138, 212]. The most widely accepted theory is the 'impermeable hydrate layer theory', invoking the formation of a protective layer of (first-stage) hydrates on the surface of the cement particles, limiting the dissolution of the anhydrous phase [138, 212]. A second theory to explain this deceleration period, is the 'double layer theory'. This theory assumes the formation of an electrical double layer, rich in calcium ions close to the surface of the reacting grains, limiting further dissolution [138, 212]. Alternative theories are the 'nucleation of CH theory' and the 'nucleation of C-S-H theory', which hypothesize the length of the induction period to be governed by the nucleation and growth of CH or C-S-H. The 'nucleation of CH theory' suggests that CH is not yet precipitated during the induction period, due to a poisoning of the CH nuclei by silicate ions [138, 212].

Acceleration period During the acceleration period, the hydration reactions and heat release accelerates and this period is characterised by a rapid formation of C-S-H and CH. The calcium silicates hydration rate mainly accelerates, resulting in the formation of a thick layer of 'second-state' or 'outer' C-S-H around the cement particles (see Fig. 2.5 (c)) and the precipitation of portlandite crystals in the originally water-filled space. Towards the end of this acceleration period, ettringite (AFt) crystals start to form (see Fig. 2.5 (d)) and SO_4^{2-} ions start to adsorb on the surface of the formed C-S-H phase, resulting in a decrease in the concentration of sulphate ions [110, 121, 212].

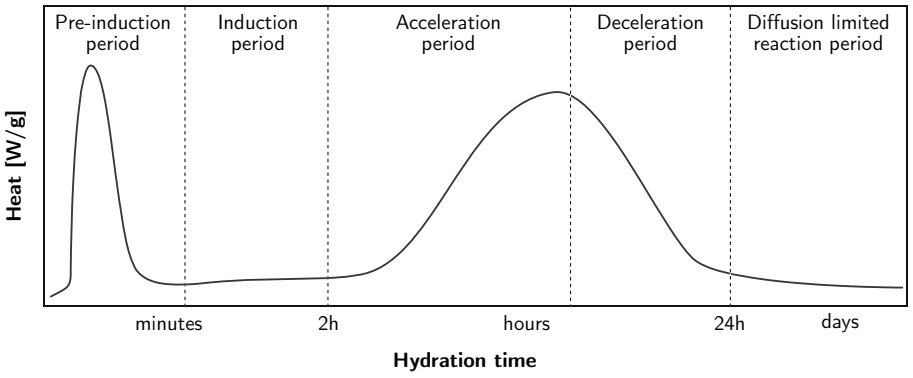

Figure 2.4: Heat development during the cement hydration process and corresponding hydration periods, adapted from [110].

Deceleration period During the deceleration period, the hydration reaction rate gradually slows down and the hydration process becomes diffusion-controlled, resulting in a progressive decrease of the heat release. The hydration of the calcium silicates (C_3S and mainly β-C_2S) continues, leading to the deposition of C-S-H also on the inside of the hydration shells, the 'inner' C-S-H (see Fig. 2.5 (f)). A secondary aluminate (C_3A and C_4AF) hydration starts after about 18 hours, yielding additional AFt crystals, which are more acicular than the ones earlier formed. This reaction can release a significant amount of heat, resulting in a second peak. After consumption of all available calcium sulphate, the AFt phase starts to react with additional C_3A and C_4AF, resulting in the formation of monosulphate (AFm phases) in the shells (see Fig. 2.5 (e)) and possibly also in the formation of a small third hydration peak in the heat release [110, 121, 212].

Diffusion limited reaction period After 1-3 days, the cement hydration reactions significantly decrease. The formation of inner C-S-H continues throughout the years due to the hydration of β-C_2S [110].

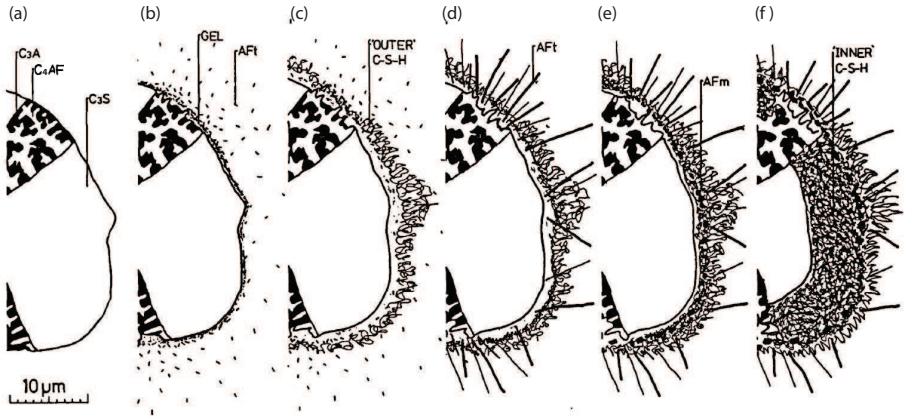

Figure 2.5: Microstructural development during the hydration of Portland cement, adapted from [194].

The evolution of the formation of hydration products is depicted in Fig. 2.6. Starting from the pre-induction period, C-S-H and ettringite (AFt) are formed, due to initial calcium silicates, calcium aluminate and calcium aluminoferrite hydration. During the induction period, the amount of C-S-H increases slowly, while a strong increase is observed during the acceleration period and the formation gradually slows down during the deceleration stage, but still may

continue for years. The formation of portlandite (resulting from C_3S and C_2S hydration) only starts at the end of the induction period and progresses until the deceleration stage. The rate of the AFt formation depends both on the reactivity of C_3A and C_4AF, as well as on the form of calcium sulphate present. At normal sulphate levels, all available calcium sulphate is consumed within 24 hours after mixing, followed by the conversion of AFt to AFm phases [121].

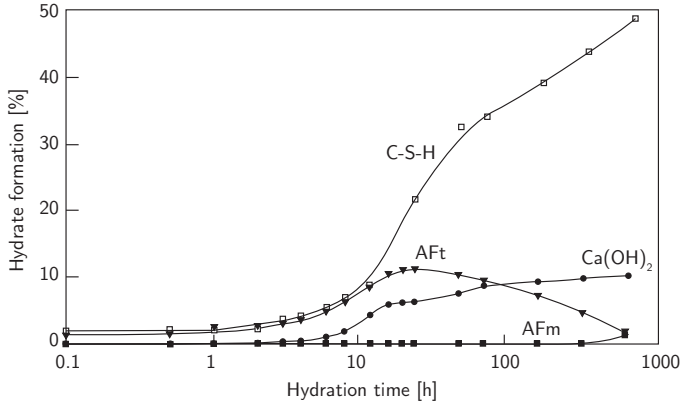

Figure 2.6: Formation of hydrates in OPC, adapted from [121].

2.2.2 Pozzolanic reaction

In the presence of pozzolanic SCMs, portlandite from the hydration reaction of cement will recombine with (alumino-)silicate or aluminate phases from the pozzolanic material, forming additional C-S-H and C-A-H phases [209]:

$$Ca(OH)_2 + SiO_2 \text{ - } Al_2O_3 + H_2O \rightarrow \text{C-S-H} + \text{C-A-H} \tag{2.7}$$

Reaction of mainly siliceous SCMs (e.g. silica fume) results in the formation of additional C-S-H. Reaction of alumino-silicate SCMs (e.g. metakaolin or fly ash), on the other hand, may produce a variety of calcium aluminate hydrates, such as monosulfoaluminate ($C_4A\bar{S}H_{12}$), calcium carboaluminate hydrates ($C_4A\bar{C}H_{11}$ or $C_4A\bar{C}_{0.5}H_{12}$), hydrocalumite (C_4AH_{13}), strätlingite (C_2ASH_8), hydrogarnet (C_3AH_6), etc. [202, 216]. The occurrence and formation of these AFm phases will be discussed more in detail in subsection 2.2.4.

2.2.3 Blended cement hydration

Influence of SCMs on early hydration

The presence of SCMs modifies both the OPC hydration reactions, as well as the reactions of the individual clinker minerals [121]. SCMs influence the early-age hydration of OPC by the *filler effect*, since no or little reaction of the SCM occur at very early ages [191]. Two main mechanisms contribute to the filler effect. Firstly, the presence of the SCM particles provides extra surface for nucleation and growth of hydrates of the clinker phases. Secondly, the increased effective water-to-cement ratio (i.e. the dilution effect) provides additional water available for OPC hydration and more space for the hydration products of the clinker minerals to form [152, 191].

Addition of SCMs generally has an accelerating effect on C_3S hydration, but decreases the C_3A hydration rate [121, 209]. The acceleration of the early alite hydration is thus mainly governed by the fineness and specific surface area of the SCM particles. SCMs of increasing fineness provide additional surfaces for precipitation of C-S-H. SCMs of increasing specific surface area increase the Ca^{2+} adsorption and C-S-H precipitation at the SCM surface. The removal of Ca^{2+} and silicate ions from the pore solution reduces the thickness of the initial impermeable C-S-H layer on the C_3S particles, accelerating its conversion to the more stable and permeable 'second-state' C-S-H [121, 209]. The accelerated alite hydration of natural pozzolan and microsilica blended cements due to increased fineness, is characterised by a shortening of the induction period and a significant increase of the main hydration peak. FA blended cements, however, lengthen the induction period due to their low specific surface are, but their strong increase of the main hydration peak and higher overall heat of hydration also result in an accelerated C_3S hydration [121]. The mechanisms behind the decreased C_3A hydration rate in the presence of SCMs still remain unclear, however, the lower C_3A hydration peak could be related to the specific surface area of the SCM. SCMs with higher specific surface area were found to lower the hydration rate more than SCMs with lower specific surface area. Other causes could be altered solution composition, dissolution of alkalis, surface activity or altered hydration product assemblage [121, 209].

The main component of the blended cement dominates its hydration behaviour. In the presence of pozzolanic SCMs, C_3S is still the main component and the early blended cement hydration is thus accelerated, depending on the fineness and specific surface area of the SCM. Slag blended cements, on the other hand, are known to hydrate more slowly, due to slag being the dominating component [209].

Reactivity of SCMs

At later ages, SCMs take part in the chemical reactions, following the dissolution-precipitation mechanism, to form hydration products [202]. Hydration reactions are complemented by pozzolanic or hydraulic reactions [209]. Both intrinsic SCM properties such as chemical composition and surface area, as well as extrinsic system properties such as temperature and solution composition, control the SCM reaction kinetics. The alkalinity of the pore solution, which is generally built up over the first few days of hydration, strongly influences the reactivity of the SCM. Increasing fineness or specific surface area of the SCM, increases the tendency of aluminosilicates to dissolve and consequently increases the pH of the pore solution and the reactivity of the SCM [152, 202]. The chemical composition and structure of the reactive phases of the SCM, generally glassy or amorphous phases, also largely determine the SCM reactivity.

Metakaolin is known as the SCM with the highest pozzolanic activity, followed by silica fume (SF), both reaching the point of complete CH depletion [202, 216]. The high reactivity of SF is generally due to its small particle size. Most SCMs, however, fail to reach full reaction, even over very long time [202]. The reaction of FA, for example, is very slow at ambient temperatures, and the CH content relative to the OPC content is only reduced after long hydration times [152].

2.2.4 Hydration products

The main hydration products formed during OPC hydration are C-S-H, CH, ettringite and AFm phases. Due to the lower calcium content and higher alumina and silica content of SCMs, different hydrates are formed during blended cement hydration, influencing concrete strength and durability. Fig. 2.7 schematically shows the different hydrate phases formed during blended cement hydration in the CaO-Al_2O_3-SiO_2 ternary diagram. A large field of compositions of the C-S-H phase, the most important phase in cement, is immediately observed in Fig. 2.7. Furthermore, the amount of ettringite and amount and kind of AFm phases in blended cement hydration are also affected, depending on the composition and reactivity of the SCM [152].

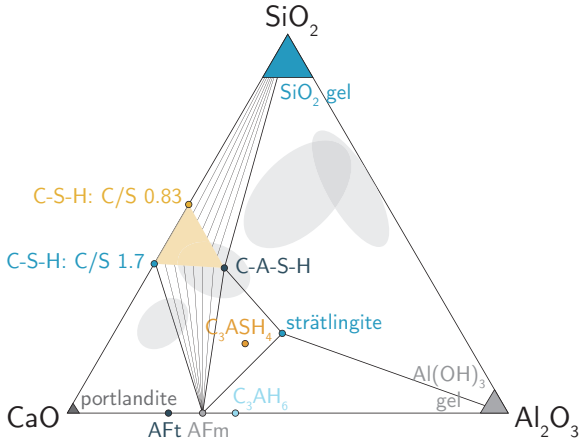

Figure 2.7: Hydrate phases in the CaO-Al_2O_3-SiO_2 ternary diagram, adapted from [152].

C-S-H C-S-H is an amorphous calcium silicate hydrate phase, with general formula $CaO_x{\cdot}SiO_2{\cdot}H_2O_y$, and is the main hydration product in Portland cement hydration. C-S-H constitutes about 60% to 70% of fully hydrated Portland cement paste and is responsible for the strength development. The Ca/Si molar ratio of C-S-H in OPC ranges from 1.2 to 2.1, with a mean value around 1.75. The addition of SCMs, however, generally significantly lowers the Ca/Si ratio of C-S-H, even to below 1. The compositional heterogeneity of C-S-H is denoted by the hyphens in its structural formula and C-S-H gel is generally described by a 14 Å tobermorite-like structure with calcium hydroxide-like regions ($(CaO)_{0.83}SiO_2{\cdot}(H_2O)_{1.5}$ with Ca/Si ratio of 0.83) or a disordered jennite structure ($(CaO)_{1.5-1.9}SiO_2{\cdot}(H_2O)_x$ with Ca/Si ratio of 1.5) or something in between. In blended cement systems containing SCMs with a significant amount of alumina, C-A-S-H (a tobermorite-like structure) is formed due to the uptake of alumina [121, 152, 175, 204].

CH Portlandite ($Ca(OH)_2$) is the second main hydration product in OPC hydration, resulting from the hydration of alite and belite. Portlandite crystals generally have a hexagonal structure and provide an alkaline environment [121]. Due to the pozzolanic reaction consuming CH, the amount of portlandite will decrease in pozzolan blended cements; while for hydraulic blended cements, such as GBFS, the amount of portlandite is barely affected [152].

AFt phases AFt phases (Al_2O_3-Fe_2O_3-tri) are hydrated calcium aluminate-ferrite compounds with general formula $[Ca_3(Al,Fe)(OH)_6{\cdot}12H_2O]_2{\cdot}X_3{\cdot}yH_2O$, where X represents a doubly charged anion such as SO_4^{2-} or CO_3^{2-}. Ettringite ($C_6A\bar{S}_3H_{32}$) is the most common AFt phase found in OPC hydration and has a hexagonal crystal, needle-like, structure [34]. In the presence of carbonates, ettringite tends to stabilise. In the absence of carbonates, ettringite combines further with aluminates upon sulphate depletion, resulting in the formation of AFm phases [8].

AFm phases AFm phases (Al_2O_3-Fe_2O_3-mono) are hydrated calcium aluminate-ferrite compounds, composed of positively charged main layers $[Ca_2(Al,Fe)(OH)_6]^+$ and negatively charged interlayers $[X{\cdot}nH_2O]^-$, where X represents either one monovalent anion (e.g. OH^-, Cl^-, $[AlSi(OH)_8]^-$) or half a divalent anion (e.g. SO_4^{2-}, CO_3^{2-}). For aluminium AFm phases (generally considered in hydrated OPC), the general formula for monovalent anions is $C_4AX_2H_n$, while for divalent anions, the general formula is C_4AXH_n. The cement composition and SCM addition strongly determine the anion content, resulting in different AFm phases. Monosulphoaluminate or monosulphate ($C_4A\bar{S}H_{12}$) is the most common AFm phase formed during OPC hydration, in the presence of calcium sulphate. Other important AFm phases are monocarboaluminate or monocarbonate ($C_4A\bar{C}H_{11}$), hemicarboaluminate or hemicarbonate ($C_4A\bar{C}_{0.5}H_{12}$), strätlingite or gehlenite hydrate (C_2ASH_8) and hydroxy-AFm or OH-AFm (C_4AH_{7+x}) [20]. Monocarbonate and hemicarbonate (AFm-CO_3) can occur in cements blended with SCMs with increased sulphate and carbonate levels, while strätlingite can occur in FA, GBFS or MK blended cements or in hydrated high alumina cements. Hydroxy-AFm, on the other hand, is not likely to occur in hydrated OPC paste and usually decomposes to the thermodynamically more stable hydrogarnet (C_3AH_6) and portlandite [20, 151, 158].

2.2.5 Conclusion

It is thus concluded that SCMs cause major changes in the hydration kinetics and hydration product assemblage. The influence of SCMs on the hydration process is strongly dependent on the physical characteristics and chemical composition of the SCM. The fineness and specific surface area of the SCM mainly determine its contribution to the filler effect, accelerating the early cement hydration, while the chemical composition of the SCM mainly determines its reactivity and type of additional hydration products formed.

2.3 Influence of SCMs on fresh concrete properties

2.3.1 Water demand and workability

The particle size characteristics (i.e. specific surface area, fineness and particle shape) of the SCM and the cement replacement ratio strongly influence the water demand of concrete. Higher specific surface areas and fineness, and more irregular particle shapes of the SCM result in higher amount of water needed for the binder to reach a specified workability. SCMs with high specific surface area, such as SF or MK, therefore typically increase the water requirement of concrete. SCMs with low specific surface area and spherical particle shape, such as FA, on the other hand, substantially lower the water demand of concrete. Higher replacement ratios of cement by SCMs obviously enhance their influence on the workability [209].

2.3.2 Setting behaviour

Setting of concrete is the continuous transition from a workable, plastic state to a stiffer, no longer workable state. Before discussing the influence of SCMs on the setting behaviour, a comprehensive definition of both the initial and final setting time is given and their determination is discussed.

Definition

During hydration, both setting and hardening of the concrete take place. Setting of concrete is the gradual transition from fluid to solid, associated with the development of concrete stiffness and corresponding loss of workability (see Fig. 2.8). The initial setting time is defined as the start of the development of continuous paths of hydration products and corresponds to the initial solid percolation (i.e. the percolation threshold). From practical point of view, initial setting is defined as the point beyond which casting or vibrating will damage the concrete. The final setting time, on the other hand, is defined as the point from which the concrete can be considered as a homogeneous solid viscoelastic material, able to withstand loads, and from which significant mechanical properties can be measured. The final setting time is often related to the time when the formwork can be removed. During the hardening of concrete, the material gains more stiffness and strength [46, 50, 188].

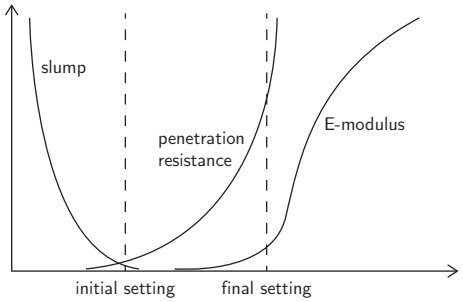

Figure 2.8: Different stages of the setting process, adapted from [49].

Setting and hardening are the result of the continuous development of the microstructure of concrete, responsible for its final mechanical properties, strength development and shrinkage behaviour [46, 50, 188]. Furthermore, knowledge of the initial and final setting times of concrete is of major importance in practice, since it determines the time at which vibrating is no longer allowed and the time at which the formwork can be removed.

Determination

By measuring the penetration resistance of cement paste as a function of time, changes in stiffness of the cement paste can indirectly be studied. This can be done by performing Vicat measurements, according to EN 196-3 [87]. This method allows determination of the initial and final setting time, by observing the penetration of a needle into cement paste (of standard consistency) until a specified value is reached. The traditional Vicat method, however, shows several drawbacks: the method is only applicable to cement paste samples (due to the heterogeneous character of mortar and concrete) and is non-continuous and destructive.

A more accurate method for determination of the setting behaviour is the ultrasonic pulse velocity (UPV) method. Since the solid percolation of cement-based materials causes big changes in the ultrasonic wave behaviour, the UPV method is extremely suitable for continuous monitoring of the solid phase transition. Ultrasonic wave measurement is a non-destructive and continuous (however, not standardised) method, whose results can be correlated with the early-age evolution of cement-based materials, such as initial and final setting time and mechanical properties [46]. Both compressive waves (P-waves), as well as shear waves (S-waves) can be used. The use of P-waves is the easiest and the most established method for correlation with early-age properties. S-waves, on

the other hand, are better indicators of the setting process and their velocity development is less dependent on the air content [46, 50]. A detailed overview of the UPV method and corresponding determination of elastic properties and setting times is given in the next paragraph.

Ultrasonic pulse velocity method

General development of UPV curves A schematic overview of the development of P-waves and S-waves is given in Fig. 2.9. Generally, both P- and S-wave velocity curves follow an S-shape. The P-wave velocity starts to develop almost from the time of mixing and initial values of around 250 m/s are typically measured. The S-wave velocity, on the other hand, is still undefined right after mixing and the onset can only be detected when reaching values of around 30 m/s [49].

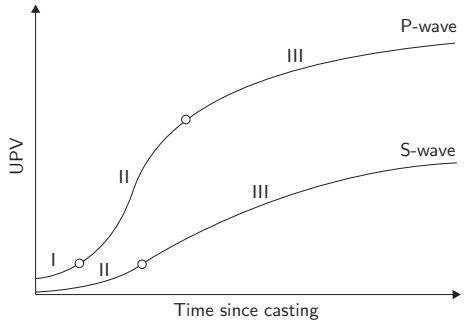

Figure 2.9: Stages of the P- and S-wave velocity development (I: dormant period, II: acceleration period, III: deceleration period), adapted from [49].

Three different stages can be distinguished in the development of the P-wave. During the first stage, the dormant period (I), the P-wave velocity is relatively low, due to the cementitious phase acting as a water-like viscous suspension [238, 240]. A small increase in the P-wave velocity is observed, caused by internal settling and initial formation of hydration products with no or little influence on the penetration resistance (e.g. ettringite) [49, 54, 218]. Initial densification of the microstructure takes place, however, the cementitious phase not yet gains any stiffness. The P-wave velocity during the dormant stage is also strongly affected by the presence of entrapped air in the sample [49]. After the dormant period, the P-wave velocity significantly increases, announcing the start of the acceleration period (II). During this stage, a great amount of hydration products is formed, filling up the pore space and creating a denser structure, resulting in a higher bulk modulus [49]. The P-wave velocity inflection point corresponds

to the moment when solid phases are connected and a solid percolation path is formed (i.e. the percolation threshold) or the start of initial penetration resistance development [49, 238]. During the third stage, the deceleration stage (III), the rate of P-wave velocity decreases. Progressive densification of the material takes place, most of the hydration has been completed and pores has been filled up by hydration products [49, 238].

While P-waves are sensitive to the build-up of solid paths and solid percolation, S-wave are more sensitive to stiffening of the solid matrix [46]. As observed in Fig. 2.9, the S-wave velocity develops slower than the P-wave velocity and only two different phases can be distinguished (no dormant period). During the acceleration period (II), the S-wave velocity increases with increasing rate. This stage corresponds to a period of intense hydration and is characterised by the rapid formation of CH, C-S-H and ettringite. Complete pathways of interconnected particles start to form and the shear modulus starts to develop [49, 50]. An advantage of using S-waves is that the early S-wave velocity development is not depending on the air content of the mixture, while P-waves are strongly affected by the entrainment and removal of air at early ages until final setting. During the deceleration stage (III), the S-wave velocity increases with decreasing rate and progressive stiffening of the material takes place [50].

Derivation of elastic properties For linear homogenous isotropic media, dynamic elastic properties can be derived from the ultrasonic measurements. Both the dynamic Poisson's ratio (ν_d), the dynamic elastic modulus (E_d), the dynamic bulk modulus (K_d) and the dynamic shear modulus (G_d) can be derived using the following formulas [46]:

$$\nu_d = \frac{V_P^2 - 2 \cdot V_S^2}{2 \cdot V_P^2 - 2 \cdot V_S^2} \tag{2.8}$$

$$E_d = V_P^2 \cdot \rho \cdot \frac{(1 + \nu_d) \cdot (1 - 2 \cdot \nu_d)}{(1 - \nu_d)} \tag{2.9}$$

$$K_d = \frac{E_d}{3 \cdot (1 - 2 \cdot \nu_d)} \tag{2.10}$$

$$G_d = V_S^2 \cdot \rho = \frac{E_d}{2 \cdot (1 + \nu_d)} \tag{2.11}$$

with V_P and V_S respectively the P- and S-wave velocity and ρ the density of the cementitious material. When only P-waves are available, the Poisson's ratio cannot be calculated from the ultrasonic results and the dynamic elastic and shear modulus can only be derived when assuming a specific value for the Poisson's ratio. The assumption of a constant Poisson's ratio, however,

underestimates its actual value at early ages, resulting in an overestimation of the dynamic elastic modulus and shear modulus, and an underestimation of the dynamic bulk modulus during the first day (see Fig. 2.10).

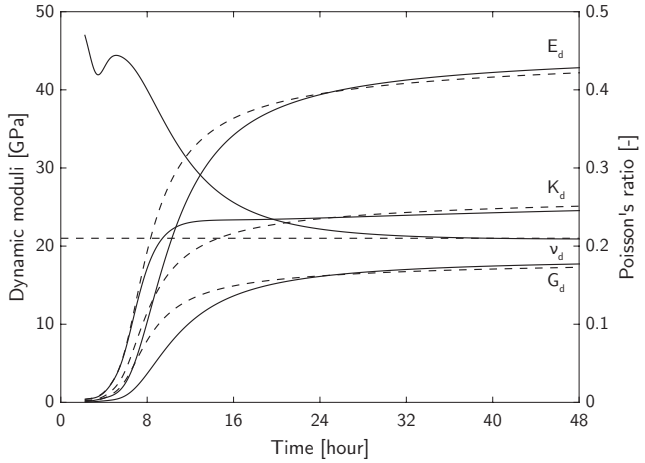

Figure 2.10: Development of elastic moduli and Poisson's ratio, calculated from ultrasonic measurements, when considering both P- and S-wave (full lines) and when only considering P-waves (dashed lines).

Setting determination In the literature, different methods exist to derive the initial and final setting time from UPV results. However, none of them has been standardised. The different criteria, as found in the literature, are summarised below. The correlations are generally based on threshold velocity or velocity gradient values and therefore care must be taken when applying them to blended concrete mixes [46].

Initial setting time:

- Time of the first inflection point of the V_P curve, $t(\delta V_P^{min})$, for cement paste, according to Trtnik et al. [218] and Zhang et al. [240].
- Time when V_P reaches a value between 1400 and 1450 m/s for cement paste, according to Trtnik et al. [218].
- Time when V_P reaches 1430 m/s (P-wave velocity in water) for cement paste, according to Trtnik et al. [218].
- Time when V_P reaches 1500 m/s (approximately the P-wave velocity in water) for mortar, according to Desmet et al. [68].

- Time of the inflection point of the V_P curve multiplied by 1.45, $1.45 \cdot t(\delta V_P^{max})$, for mortar and concrete, according to Desmet et al. [68].
- Time of the inflection point of the V_S curve, $t(\delta V_S^{max})$, for mortar and concrete, according to Carette et al. [49, 50].

Final setting time:

- Time when V_P reaches 1650 m/s for cement paste, according to Trtnik et al. [219].
- Time of the inflection point of the V_P curve, $t(\delta V_P^{max})$, for cement paste, according to Zhang et al. [240].
- Time when the rate of V_P has descended to 20% of its maximum value, $t(0.2 \cdot \delta V_P^{max})$, for concrete, according to Desmet et al. [68].
- Time of the inflection point of the E_d curve, $t(\delta E_d^{max})$, for mortar and concrete, according to Carette et al. [49, 50] and for cement paste, according to Mohamed et al. [163].

The use of dynamic elastic properties to predict the setting of cement-based materials is suggested by many authors. This because of the fact that the elastic properties are closely related to the yield stress development and because they allow accurate capturing of microstructural evolutions [46].

Influence of SCMs on setting behaviour

The addition of SCMs can both accelerate or delay the setting of blended cements. The accelerated C_3S hydration in blended cements decreases the setting time. Higher replacement ratios of SCMs, on the other hand, could neutralise this acceleration effect and might result in a delayed setting. For MK blended cements, the setting time is generally accelerated at low cement replacement ratios [209]. For FA blended cements, on the other hand, the influence on the setting strongly depends on the characteristics and amount of fly ash used. Low-calcium fly ashes were found to delay the setting, while high-calcium fly ashes generally accelerate the setting. Higher replacement ratios of cement by FA ($> 50\%$) obviously result in delayed setting times [200]. The use of GBFS results in a delay of the setting time, with increasing setting time for increasing amount of GBFS [200, 210]. In SF blended cements, the setting is accelerated, due to the increased hydration of the fine and reactive SF particles [32, 200, 238].

2.4 Influence of SCMs on hardened concrete properties

2.4.1 Pore structure

Pores, which range from nm to mm and vary in shape and distribution, are an inherent part of concrete. Pores in concrete include gel pores (C-S-H gel, < 0.01 μm), capillary pores (< 10 μm), hollow-shell pores and air voids forming in the cement paste matrix, pores in the aggregates, pores associated with the interface between aggregates and cement paste, water voids, and internal discontinuities in the cement paste due to dimensional instability induced by humidity and temperature changes [6]. The amount, size and distribution of the pores have a significant effect on the properties and durability of concrete [6].

Improvement of mechanical properties and durability of concrete by SCMs is mainly due to the refinement of the pore structure by the filler effect and pozzolanic or hydraulic reaction of the SCM, forming additional hydrates. In general, blended cements have higher total porosity at early ages compared to Portland cement, due to the dilution effect (lower clinker content) and the slow reaction of SCMs [31]. At later ages, however, the total pore volume decreases and the pore size distribution shifts to the smaller pore diameter. Typically, the capillary porosity is reduced, while the gel porosity is increased by the addition of SCMs [70, 209]. Moreover, each SCM behaves differently in filling the porosity. The reaction of GBFS has been found to be more reactive and therefore more efficient than that of FA in reducing the porosity in the blended cement systems [31].

2.4.2 Strength

Strength of concrete is related to the structure of the hydrated cement paste and gives an overall picture of the quality of the concrete. Strength is commonly considered as the most valuable concrete property. However, in practice, other properties, such as volumetric changes or durability, may be more important [166].

The strength development of concrete including SCMs is controlled by several factors: the dilution effect, the filler effect, the hydration acceleration effect and the pozzolanic or hydraulic reaction. The first three effects mainly dominate the early-age strength, where for the large majority of blended cement concretes (e.g. fly ash, silica fume or blast furnace slag) lower initial strengths are observed,

compared to OPC. At later ages, the pozzolanic or hydraulic reactions typically cause the formation of additional hydration products, resulting in higher rates of strength development and compressive strength values equivalent to that of reference mixes [61, 106, 209]. Metakaolin blended cement concretes, on the other hand, behave differently and can cause considerable enhancement in strength, particularly at early ages. This is mainly the result of the filler effect and acceleration effect, which are for MK more effective at early age [109, 169, 171, 182].

2.4.3 Elastic properties

With any stress applied to concrete, there is always an associated strain. Fig. 2.11 shows the general stress-strain relationship of concrete. Concrete is elastic to a certain degree. However, when concrete is subjected to sustained loading, the strain increases with time and concrete exhibits creep [166]. The elastic modulus of concrete (E_c) is defined as the ratio of the compressive stresses (σ_c) and corresponding strains (ϵ_c) [225]:

$$E_c = \frac{\sigma_c}{\epsilon_c} \tag{2.12}$$

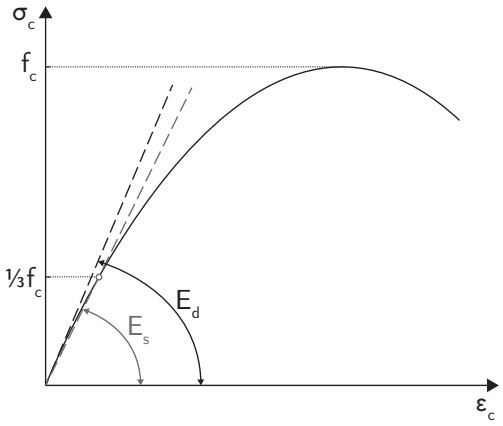

Figure 2.11: Stress-strain (ϵ_c-σ_c) relation for concrete with tangent, dynamic (E_d) and secant, static (E_s) modulus of elasticity (f_c: concrete compressive strength), adapted from [225].

Two different elastic moduli can be distinguished: the dynamic elastic modulus and the static elastic modulus. The tangent modulus or dynamic modulus of

elasticity (E_d) corresponds to the tangent to the curve at the origin. The secant modulus or static modulus of elasticity (E_s) corresponds to the gradient of the straight line between the strain at 0.5 MPa and the strain at around 1/3 of the ultimate stress. The value of the dynamic elastic modulus is easy to determine by performing ultrasonic tests, while the value of the static elastic modulus, which is required in structural design, should be determined from experimental stress-strain curves [110, 166].

The influence of SCMs on the development of the modulus of elasticity is almost similar to their influence on the strength development. Lower elastic moduli at early ages and higher stiffness values at later ages (equivalent to that of reference mixes) are noticed for FA and GBFS blended cement concretes [30, 200]. A reduction in the elastic modulus, however, was reported by Gonçalves et al. [109] for MK blended cement mortars. The continuous decrease in elastic modulus for increasing replacement levels of cement by calcined clays was attributed to the lamellar structure of clays, which are more deformable under loading [109, 200].

2.5 Influence of SCMs on volumetric changes

Volumetric changes in concrete comprise both shrinkage and creep deformations. Shrinkage strains are independent of stress, while creep deformations are produced by sustained stresses [203]. The total shrinkage of concrete is usually considered as the sum of the drying shrinkage and autogenous/chemical shrinkage (plus carbonation and thermal deformations). As the water-to-cement ratio becomes smaller, the total amount of shrinkage is composed of more autogenous shrinkage rather than drying shrinkage [123, 145]. Creep deformations are defined as continuous, time-dependent deformations under sustained loading and comprise both basic creep and drying creep (and eventual transient thermal creep). The different types of shrinkage and creep, their mechanisms and the influence of SCMs on their behaviour is discussed in the following subsections.

2.5.1 Autogenous shrinkage

Autogenous shrinkage of concrete is defined as the external volume change of concrete, occurring without any moisture loss to the surrounding environment. The main driving mechanisms behind this macroscopically observed autogenous shrinkage are chemical shrinkage and self-desiccation. Chemical shrinkage is defined as the internal volume reduction of concrete, as a result of the cement

hydration reactions. Self-desiccation is the progressive desaturation of the concrete porosity, i.e. the reduction of internal relative humidity (RH), while generating empty pores [123, 160].

Autogenous shrinkage mechanisms

Fig. 2.12 shows the reactions causing external autogenous and internal chemical shrinkage, and their relationship. When the concrete is still fresh and liquid, all capillary actions can be neglected and all *chemical shrinkage* is converted into an external volume change (i.e. autogenous shrinkage). This is a result of the fact that the cementitious system is not yet able to sustain internal voids created by chemical shrinkage, because of the very low stiffness of the concrete at that moment. At this stage, all volume changes will result in plastic settlement, i.e. lateral swelling and top shrinkage. The chemical shrinkage only contributes to the autogenous shrinkage during the first hours of hydration. However, it was found that during the first 12 hours after mixing, the major part of the autogenous shrinkage takes place [21, 37, 47, 123, 160, 235]. During the setting of the concrete, however, the concrete gains early stiffness by the formation of a skeletal frame as a result of the percolation of the hydrates and the particle interference. This rigid skeleton enables the concrete to support its own weight. The concrete skeleton can resist some of the stresses and the chemical volume changes due to hydration will manifest in the formation of a large number of fine pores in the cement matrix [46, 123, 145, 160, 234]. This results in the formation of water-air menisci, when the relative humidity inside the pores drops. These water-air menisci give rise to the development of a capillary pressure in the pore fluid, accompanied by changes in the surface tension of the cement particles and a disjoining pressure between solid surfaces, resulting in autogenous *self-desiccation* deformations [153].

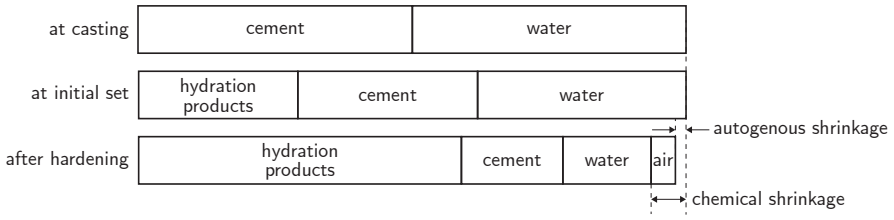

Figure 2.12: Concrete's compositional changes during hydration, causing autogenous and chemical shrinkage, adapted from [123].

Chemical shrinkage The chemical shrinkage, also called Le Chatelier contraction, is the volume change which results from various chemical reactions within the cement paste, and the immediate result of the fact that the hydration products occupy less space than the unhydrated cement and water [46]. The cement hydration and equivalent chemical shrinkage are complex phenomena, since many different reactions occur, each with its own volume stoichiometry [145]. Chemical shrinkage results both from the hydration of the main clinker minerals, as well as from secondary reactions, such as ettringite formation [153]. By using the densities and molecular weights of the reactants (clinker minerals) and reaction products (hydrates), the chemical shrinkage can be estimated [123, 237]. Holt [123] calculated the chemical shrinkage values for the four individual clinker phases. C_3A and C_4AF were found to develop/encounter the highest chemical shrinkage upon hydration, while C_3S and C_2S contributed the least to the chemical shrinkage [123, 237]. High aluminate cements are thus more susceptible to chemical shrinkage, while the chemical shrinkage of siliceous SCM blended cements generally will be lower.

Self-desiccation shrinkage Three mechanisms can explain the self-desiccation shrinkage: changes in the surface tension of the solids, a disjoining pressure of adsorbed water between solid surfaces and the development of tensile stresses in the pore solution [153]. Each of these mechanisms will shortly be discussed below.

- Surface tension Changes in the surface tension of the cement gel particles could result in shrinkage or expansion of the cement paste (see Fig. 2.13 (left)). Adsorption of water on the pore walls lowers the surface tension of the cement gel particles, resulting in expansion; while removal of the adsorbed water results in shrinkage. This self-desiccation mechanism is only important in cases of low internal relative humidity and can be neglected for RH $> 75\%$, since only the first three adsorbed water layers are of significance for changes in the surface tension [21, 153].

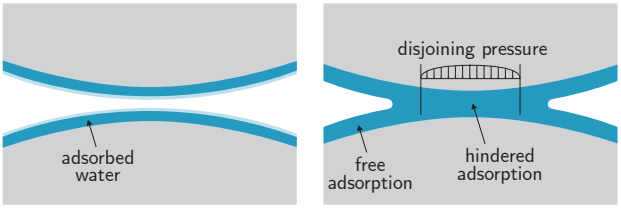

Figure 2.13: Surface tension (left) and disjoining pressure (right) mechanisms.

- Disjoining pressure When the diameter of the pores is smaller than two times the thickness of the water layer in the pores, a disjoining pressure between C-S-H gel particles develops in the hindered adsorption areas (see Fig. 2.13 (right)). This disjoining pressure is of major importance at high RH. The adsorbed water layers push apart the pore surfaces, resulting in an early-age swelling. This phenomena is the combined effect of molecular Van der Waals forces, overlapping electrostatic fields, double layer repulsion and structural forces. When the hydration continues and the relative humidity inside the pores drops, the disjoining pressure is reduced, causing shrinkage [153, 160].

- Capillary tension The capillary tension is related to the formation of water-air menisci in partly emptied pores [153]. Due to self-desiccation, the relative humidity in the pores drops, forming water-air menisci (see Fig. 2.14) and resulting in a pressure difference between the water (pore fluid) and air. This pressure difference (i.e. the tensile stresses developed in the pore solution) is balanced by compressive stresses in the solid, and can be described by the Laplace's law [95, 123]:

$$\Delta p = p_{air} - p_{water} = p_c = \frac{2 \cdot \gamma_w \cdot \cos\theta}{r} \tag{2.13}$$

with γ_w the surface tension of water, θ the angle between the water surface and the pore wall and r the radius of the capillary pore. When the meniscus thus appears in smaller pores, the pressure in water decreases, showing that self-desiccation is the viscoelastic response of the material [21].

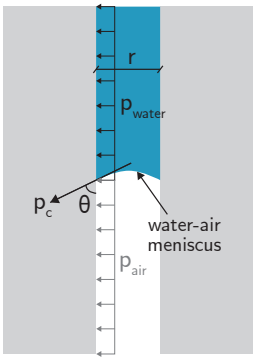

Figure 2.14: Capillary tension (p_c) mechanism (p_{water}: pressure of water, p_{air}: pressure in air, θ: angle between water surface and pore wall, r: radius of pore).

The size of the capillary pores and internal relative humidity of the matrix are related by the Kelvin's law:

$$\ln(\mathrm{RH}) = -\frac{2 \cdot \gamma_w \cdot M_w \cdot \cos\theta}{\rho_w \cdot r \cdot RT} \tag{2.14}$$

where M_w is the molecular weight of water, ρ_w is the density of water, R is the ideal gas constant and T is the temperature. This equation assumes menisci formation in circular cylindrical pores (see Fig. 2.14) and assumes that the biggest pores empty first. Combining both equations results in the Kelvin-Laplace equation, showing the relationship between the capillary tension and the internal relative humidity development [123, 153]:

$$\Delta p = -\frac{RT \cdot \rho_w}{M_w} \cdot \ln(\mathrm{RH}) \tag{2.15}$$

According to the Kelvin's and Laplace's law, there is an access radius r (the Kelvin radius) such that all pores with radius smaller than r are filled with water and all pores with radius bigger than r are empty, introducing a tension in the liquid phase (p_{water}). Lura et al. [153] therefore state that the capillary tension mechanism is only important for RH $>$ 45% [153], since at lower internal relative humidities, the radius of the pores filled with water decreases below a critical value, resulting in a strong decrease of the tension in the pore solution, which is physically impossible. However, discussion exists in the literature about the value of the critical Kelvin radius. Opposite to Lura et al. [153], Hua et al. [126] state that the capillary tension mechanism is only valid for a RH above 80%.

The capillary tension approach is mostly used for modelling autogenous shrinkage. Once the capillary pressure of the pore fluid is calculated, the autogenous shrinkage can easily be predicted by only knowing the degree of saturation and deformability of the paste [153].

Autogenous swelling Autogenous swelling peaks, not attributed to thermal deformations, may occur in concrete at early ages and can be the result of several phenomena. Firstly, autogenous swelling peaks can be attributed to the reabsorption of bleeding water or water kept in the aggregates, cancelling the self-desiccation shrinkage [46, 95]. Secondly, the presence of fillers or fine particles can promote the adsorption of water by the filler, resulting in a disjoining pressure and inducing swelling [58]. Thirdly, autogenous swelling peaks can be the result of the formation and growth of hydration products, such as portlandite crystals (also AFt needles or AFm crystals) [22] or ettringite [95]. From chemical point of view, the formation of hydration products leads to a decrease in volume, known as chemical shrinkage. However, crystal growth can generate a crystallisation pressure on the pore walls, inducing expansion [58].

Time-zero definition Time-zero (t_0) is defined as the moment when cement paste transforms from fluid to solid, when a stable solid skeleton is formed and residual stresses can start to develop. This moment corresponds to the moment when the autogenous shrinkage starts to diverge from the chemical shrinkage and when self-desiccation occurs. It is thus important to accurately define this time-zero, since it determines the initialisation of the autogenous shrinkage and will therefore strongly affect the early-age autogenous shrinkage behaviour. Different approaches exist in literature to determine this time-zero: the final setting time, the change of slope of the autogenous deformation curve (the start of the swelling peak) or the onset of the internal relative humidity drop [21, 58, 61, 71, 127, 186].

Influence of SCMs on autogenous shrinkage

The rate and amplitude of the autogenous deformations are both dependent on micro-physico-chemical properties, such as hydration rate, chemical shrinkage and pore structure, as well as on macro-mechanical properties, such as strength and stiffness development. These properties are, on their turn, influenced by the mix design of the concrete and thus, among others, by the water-to-binder ratio, the replacement of cement by SCMs or the addition of admixtures [211].

The influence of SCMs on the early-age deformations is strongly dependent on their physical, chemical and mineralogical properties. These properties namely affect the key parameters determining the autogenous shrinkage: the pore structure, hydration rate, chemical shrinkage and mechanical properties of the cement paste or concrete [36, 106]. Most existing SCMs ensure an acceleration of the cement hydration and a refinement of the pore size distribution, increasing the capillary pressure, escalating self-desiccation and increasing the autogenous shrinkage. Furthermore, the lower Young's modulus of SCM blended cement pastes and concretes also induces greater self-desiccation and higher capacity of the concrete to deform under self-induced stresses. The dilution effect, on the other hand, lowers the shrinkage, due to less available amount of cement. [43, 108, 193]. The influence of a specific SCM on the deformation potential thus depends on different factors and the influence of the most commonly used SCMs on the autogenous shrinkage behaviour is discussed below.

Fly ash The addition of fly ash leads to a decrease in the autogenous shrinkage [5, 211, 215]. Tangtermsirikul [211] attributed this lower autogenous shrinkage to the larger free water content of FA blended cement mixes, since fly ash particles retain less water than cement particles due to their spherical shape. Termkhajornkit et al. [215], on the other hand, explained the lower autogenous

shrinkage of fly ash blended cement by their lower C_3A content, reducing the chemical shrinkage. The dilution effect was also attributed as a cause of the lower autogenous shrinkage by several researchers [177, 211, 227].

Blast furnace slag Blast furnace slag generally increases the autogenous shrinkage [61, 165, 147, 150]. Darquennes et al. [61] attributed the higher autogenous shrinkage of slag cement concretes to the finer and larger porosity, leading to larger capillary depression. An expansion of the cement matrix, as a result of the formation of hydration products, was also observed, delaying the occurrence of the autogenous shrinkage. Mounanga et al. [165] explained the higher autogenous shrinkage of the slag blended cement concretes by their greater chemical shrinkage, higher fineness and slower evolution of the mechanical properties (in particular the elastic modulus).

Silica fume Presence of silica fume also increases the autogenous shrinkage of blended cement paste or concrete and increasing SF content increases the autogenous shrinkage. The refinement of the pore size distribution, resulting in increased capillary tension, and the pozzolanic reaction of SF are mainly responsible for the higher autogenous deformations [159, 200].

Metakaolin In literature, both an increase and decrease of the autogenous shrinkage of metakaolin blended cements are reported. Wild et al. [228] reported increased autogenous shrinkage for blended cement pastes containing up to 10% MK, while at higher replacement levels, a decreased autogenous shrinkage was noticed. Brooks et al. [43] also reported higher autogenous shrinkage values for MK blended cement concrete at low replacement levels and lower autogenous shrinkage for MK blended cement concrete high replacement levels. The higher autogenous shrinkage for lower replacement levels was attributed to the accelerating effect of MK on the cement hydration and pozzolanic reaction [43], and the higher chemical shrinkage for lower cement replacement ratios [182]. The lower autogenous shrinkage for higher replacement levels, on the other hand, was attributed to the increased formation of low-density strätlingite and reduced formation of C_4AH_{13}, the lower chemical shrinkage and an observed swelling for high replacement ratios [108, 182].

Calcined dredging sediments Research on the autogenous shrinkage behaviour of concrete with the addition of calcined dredging sediments is very limited. Bouhamou et al. [38] investigated the evolution of the autogenous deformations of concrete with partial replacement of the cement by calcined

mud up to 90 days. It was concluded that the addition of the calcined mud decreased the autogenous shrinkage and this was attributed to the formation of some expansive calcium aluminate hydrates (due to the pozzolanic reaction), compensating for the shrinkage.

2.5.2 Drying shrinkage

Drying shrinkage of concrete is defined as the volume reduction caused by the loss of water from the hardened concrete to the surrounding environment [123, 160]. Loss of water from the concrete surface by evaporation can occur while the concrete is still fresh and fluid, and this phenomenon is called plastic shrinkage. Plastic shrinkage only occurs during the very first hours after mixing of the concrete, when the concrete is still in its plastic state [160].

Drying shrinkage mechanisms

Water that can be removed from concrete by drying is called evaporable water and is defined as the sum of physically adsorbed water and free water. Physically adsorbed water occupies the gel pores and is adsorbed at the surfaces of the gel particles. Free water occupies the capillary pores. A third type of water that exists in cement paste is chemically bound water. This water reacts with cement to form the cement paste and is an integral part of the cement gel, which cannot be removed by drying [33]. During the first stages of drying shrinkage, the free water from the capillary pores evaporates and little shrinkage occurs. As drying continues, the physically adsorbed water from the surfaces of C-S-H gel particles is removed and finally drying shrinkage results from loss of water contributing to the structure of C-S-H gel [33]. Due to the dense pore structure, drying of concrete is a slow process. Typically a moisture gradient will develop across the material, since concrete dries non-uniformly. Depending on the size of the specimen, ambient temperature and relative humidity, and concrete mix design, it can take months or years before drying equilibrium is reached [33].

The mechanisms causing drying shrinkage mainly depend on the porosity of the concrete and four phenomena are believed to contribute to drying shrinkage of cement paste: capillary tension, movement of interlayer water, disjoining pressure and surface tension or surface free energy [33, 117, 145]. The capillary tension, disjoining pressure and surface tension mechanisms were already discussed in detail in subsection 2.5.1, as being the main mechanisms causing autogenous shrinkage. The only difference is that with drying shrinkage, water is removed by evaporation to the environment, while with autogenous

shrinkage, water is removed by self-dessication. The mechanism of movement of interlayer water is discussed below.

- Movement of interlayer water C-S-H particles of the cement gel form a layered microstructure and highly attract polarized water molecules at the interface. As water moves in and out the structure of the layered C-S-H particles, volume changes occur. Most researches attribute drying shrinkage at internal RH between 35% and 40% to this mechanism [145].

Influence of SCMs on drying shrinkage

Drying shrinkage of concrete is mainly depending on the water-to-binder ratio, the volume of paste in the concrete and the rate of hydration. The influence of different types of SCMs on the drying shrinkage is discussed below.

Fly ash A decrease in drying shrinkage for FA blended cement concretes was reported by most researchers. Abdalhmid et al. [1] and Saha [183] both reported significantly reduced drying shrinkage when OPC was replaced by FA and attributed this decrease due to the reduced hydration rate of FA blended cement concrete, due to their lower lime content. Wang et al. [227] and Hu et al. [124] also reported lower drying shrinkage for FA blended cements, due to the pore refinement and improved resistance to shrinkage because of the pozzolanic reaction of FA. Akkaya et al. [5], however, reported increased drying shrinkage by incorporation of fly ash.

Blast furnace slag Both an increased and decreased drying shrinkage of GBFS blended cement concretes were reported in literature. Darquennes et al. [62] observed higher drying shrinkage for GBFS mixes due to the lower reaction of GBFS, leading to a larger free water content. Shariq et al. [199] also reported higher drying shrinkage for higher replacement ratios of cement by GBFS. Gedam et al. [106] and Jianyong and Yan [200], however, reported lower drying shrinkage values for GBFS blended cement concretes.

Silica fume SF blended cement concretes were observed to have similar drying shrinkage behaviour as OPC concrete at long term [161, 173]. Rao et al. [173], however, reported higher drying shrinkage values at early ages, due to the pozzolanic reaction and pore size refinement of SF.

Metakaolin MK blended cements generally reduce the drying shrinkage of concrete. Brooks et al. [43] and Guneyesi et al. [115] reported reduced drying shrinkage for increasing amount of MK, attributed to the lower amounts of evaporable water, due to the hydration and pozzolanic reactions, consuming water.

Calcined dredging sediments Research on the drying shrinkage of concrete with addition of calcined dredging sediments is limited. Bouhamou et al. [38] reported lower drying shrinkage for concrete blended with calcined mud, with decreasing shrinkage for increasing amount of dredged mud.

2.5.3 Thermal shrinkage

As a result of the exothermic hydration reactions of cement, a certain degree of heat is liberated at early ages, which can cause thermal swelling. The development of a thermal gradient, results in generation of stresses, possibly causing cracking. As the rate of hydration declines, on the other hand, the temperature decreases and the concrete shrinks. At this moment, the concrete skeleton is already completely formed and thermal shrinkage can, therefore, cause serious cracking. Thermal dilation may also occur at later ages, as a result of temperature fluctuations in the surrounding environment [123, 145].

Pozzolanic SCMs generally accelerate the hydration at early ages, increasing the amount of heat liberated and therefore increasing the risk of thermal cracking. However, due to the dilution effect, the hydration heat will be low at higher replacement ratios, lowering the risk of thermal cracking. Slag blended cements are known to lower the heat of hydration and are therefore suitable for mass concrete, since the risk of thermal cracking is significantly reduced.

2.5.4 Total shrinkage

Total shrinkage is considered to be the sum of autogenous, drying, thermal and carbonation deformations. Considering only autogenous and drying deformations, the total shrinkage in a concrete element depends on the competition between hydration, causing autogenous shrinkage, and drying, causing drying shrinkage, which are strongly influenced by the concrete mix design and environmental conditions [95, 123]. At low W/B ratio's, the drying shrinkage will be low (since less water is available for evaporation), while the autogenous shrinkage will be high (since the internal relative humidity decreases significantly, resulting in increased self-desiccation). At high W/B ratio's, on

the other hand, the drying shrinkage will be higher, while the autogenous shrinkage will be lower. Furthermore, a decrease in the W/B ratio also results in a refinement of the pore structure and a reduction of the total pore volume, increasing the autogenous shrinkage [95, 229]. The environmental conditions also play a significant role in the competition between hydration and drying. Considering low ambient RH (drying conditions), drying shrinkage increases, while the autogenous shrinkage will be reduced, since less water is available for hydration, resulting in a delayed and less complete hydration, decreasing autogenous shrinkage [229]. Furthermore, also the temperature strongly affects the autogenous and drying shrinkage. Both self-desiccation and autogenous swelling deformations are highly affected by temperature. Increased curing temperatures accelerate cement hydration, resulting in a faster development of water consumption and an increased early-age autogenous shrinkage [51, 154]. Coarser porosity at higher curing temperatures and high RH for constant water content, however, strongly reduces the self-desiccation shrinkage at later ages [51]. Moreover, the influence of the temperature on the autogenous deformation is strongly influenced by the type of cement and use of mineral additions and SCMs [46, 134].

2.5.5 Creep

Creep of concrete is the time-dependent deformation under sustained loading. Basic creep is defined as the continuous deformation under autogenous conditions (i.e. no moisture exchange with the environment), while drying creep is defined as the additional acquired deformation under decreasing water content (i.e. drying conditions) [231]. Furthermore, additional creep due to temperature changes may occur, named transient thermal creep or load-induced thermal strain [95].

Creep mechanisms

Despite extensive research conducted over decades, no single creep mechanism has been universally accepted and the origin of creep is not yet fully understood. Nevertheless, there is agreement that creep involves water, is associated with the viscous nature of C-S-H and interacts with micro-cracking and debonding of the cement paste-aggregate interface [95, 231]. However, discrepancy still exists regarding the nanostructure of C-S-H and regarding the function of water at various scales in C-S-H [231]. The different nanostructure models of C-S-H and the different creep theories proposed over the years are discussed below.

The first nanostructure model of C-S-H was proposed by Powers and Brownyard (1946), assuming C-S-H to be a colloidal material with crystalline phases (see

Fig. 2.15 (left)). Feldman and Sereda (1968) modified the model proposed by Powers and Brownyard, by resembling C-S-H as a layered tobermorite-like crystal and incorporating the structural function of interlayer water in the C-S-H (see Fig. 2.15 (right)). Jennings et al. (2000), in the end, represented C-S-H as a combination of a layer model and colloid model [231].

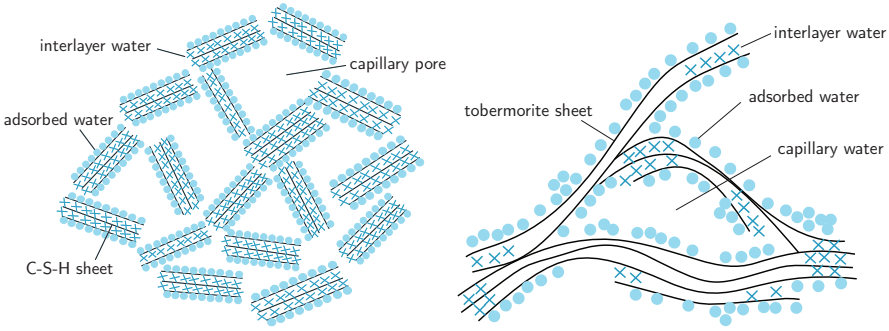

Figure 2.15: Nanostructure of C-S-H according to Powers and Brownyard (left) and according to Feldman and Sereda (right), adapted from [231].

Water in C-S-H is generally divided into capillary water, adsorbed water and interlayer water, and each of these types of water has a different role in different creep mechanisms [231]. The capillary water, which is not chemically or physically bound, is expelled from the concrete under long-term static loads. When an external load is applied, water diffuses from high to low pressure areas and the load gradually transfers from the water to the solid phase, increasing the stress in the solid phase and resulting in a gradual volume reduction, i.e. creep. The role of the capillary water, however, is mainly inessential to creep, since it cannot account for the irreversible creep [231]. Different theories regarding the role of the adsorbed water in basic creep mechanisms are proposed over recent years and are discussed below:

- Seepage theory The seepage theory was proposed by Powers (1968) and ascribes creep to the expulsion and decomposition of gel water within the cement paste. The water in the hindered adsorption region (or the load-bearing water) is easiest to be squeezed out [107, 231].
- Microprestress-solidification theory The microprestress-solidification theory, proposed by Bazant (1972), is an extension of the seepage theory. The existing disjoining pressure in the hindered adsorption region of a pore must be balanced by tensile forces, which are carried partly by the solid framework around the pore and partly by bridges or bonds between opposite walls of the pore. The solid part of the microstructure is thus

permanently in a pretensioned state. Reduction of the hindered adsorbed water results in a decrease of the disjoining pressure. Relaxation of this pre-existing disjoining pressure in micropores generates micro-prestress in the bridges or bonds between opposite walls of the same pore (see Fig. 2.16) and layers of hindered adsorbed water are then slip planes giving rise to creep. The shear slip of these overstressed bonds, as a result of breakage and restoration of atomic bonds (called quasi-dislocations), is then postulated to be the source of creep [17, 25, 231].

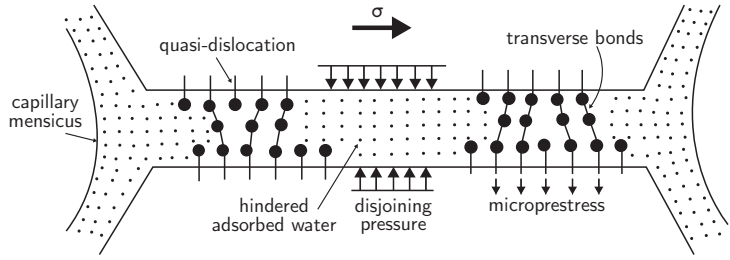

Figure 2.16: Disjoining pressure and microprestress in a micropore in cement gel, adapted from [17].

- Viscous shear theory The viscous shear theory or viscous flow theory, proposed by Ruetz (1968), ascribes creep to sliding of the colloidal C-S-H sheets in the cement gel between the layers of adsorbed water. Under shear force, the overall C-S-H particles are rearranged. Different to the seepage theory, which assumes gel water being squeezed out, the viscous shear theory assumes gel water acting as a lubricator, promoting C-S-H slip [25, 107, 231].

- Thermal activation energy theory The thermal activation theory, proposed by Wittmann (1973), hypothesizes creep to be a result of a thermally activated process, rearranging and redistributing C-S-H particles to evolve towards lower energy. The absorbed water is also considered as a lubricant, weakening the C-S-H interparticle bonds [231].

- Nanoparticle rearrangement This theory, proposed by Jennings (2006), assumes creep to occur as a rearrangement of C-S-H globules under stress, reducing gel porosity and enhancing bonds by silicate polymerisation. Recent studies have shown that this nanoparticle rearrangement can also be a result of dissolution-diffusion-reprecipitation process [231].

Feldman and Sereda (1972), however, stated that interlayer water in C-S-H is responsible for the major part of creep by attributing creep to a gradual

crystallisation or aging of layered C-S-H. Alizadeh et al. (2010) supported this theory by ascribing creep to sliding and translation of C-S-H sheets under stress and interlayer water acting as a lubricator [231].

Upon drying, additional strains are observed under loading, i.e. drying creep. This behaviour is also called the Picket effect and two main mechanisms are hypothesised to contribute to this effect:

- Microcracking effect Microcracking corresponds to the additional (delayed) strain, on top of drying shrinkage and basic creep strains, since upon loading, drying-induced microcracking is less pronounced compared to a non-loaded specimen [19, 26].
- Stress-induced shrinkage The stress-induced shrinkage theory, proposed by Bazant and Chern, ascribes drying creep to micro-diffusion of water molecules between micro- and macropores, upon simultaneous drying and loading. Micro-diffusion disrupts the microstructure of solid cement gel by enhancing debonding and rebonding of particles forming C-S-H [16, 19, 26].

In a nutshell, there is still no consensus on the mechanisms at the origin of creep. However, distinction has been recently made between short-term (a few days) and long-term components of creep. Short term basic creep, is mainly attributed to migration (micro-diffusion) of adsorbed water, occurring due to changes in the hygral equilibrium in the gas-filled space, generating stresses, strains and microcracking, and is generally associated with the reversible part of creep. Creep at long term, on the other hand, is mainly governed by sliding of C-S-H sheets and micro-prestress, and is associated with the reversible part of creep [25, 95].

Influence of SCMs on creep

Basic creep of concrete is mostly dependent on the age at loading and the concrete mix design, e.g. water-to-binder ratio, addition of SCMs, etc. The older the concrete specimen, the lower the amplitude and rate of basic creep. Low water-to-binder ratios result in decreased basic creep. The addition of both silica fume and fly ash, as well as slag results in a reduction of the basic creep, as was reported by many researchers [25, 42, 106, 148, 141, 159, 216]. The exact mechanisms of reduced creep upon SCM addition, however, are not yet clear, but are most likely due to altered porosity and pore size distribution and due to formation of different hydration products.

2.6 Modelling time-dependent behaviour

2.6.1 Shrinkage modelling

Different concrete shrinkage models have been developed during the past years, estimating the amplitude and rate of the time-dependent deformations. Two main categories can be distinguished: the empirical/phenomenological models, recommended by design codes, and the mechanistic models, based on the theory of poromechanics [69].

Empirical shrinkage models

Empirical or phenomenological shrinkage models are generally used in civil engineering practice to predict the time-dependent behaviour of concrete. The most popular prediction models are: the CEB-FIP Model Code 2010 model [129], the Eurocode 2 model [77], the ACI 209 model [7], the JSCE 2007 model [130] (all design code models), the Gardner/Lockman GL2000 model [102] and the Bazant B4 model [18] (academic models). These empirical models are all obtained through best-fit analysis of experimental data and generally describe shrinkage as the product of two terms: the final/ultimate shrinkage ϵ_∞ (a magnitude function) and the shrinkage rate β or S (a time function). Several mathematical forms of the time function are given in literature, such as hyperbolic, square root hyperbolic, tangent hyperbolic or exponential expressions [69, 119, 185].

The empirical shrinkage models all vary in precision, complexity and parameters necessary for the calculation, and are all primarily based on pure Portland cement concrete. However, the considerable amount of input parameters, excessive amount of experimental data necessary for validation and limited application to non-standardised materials (e.g. SCM blended cement mixes) are the main drawbacks of these models [69]. In order to take the SCM inclusion effect into account, the existing shrinkage prediction models should be parameterised, requiring experimental data. Mokarem et al. (2005) [164] assessed the accuracy of existing shrinkage prediction models for concrete including various SCMs. Li (2016) [149] modified two existing drying shrinkage prediction models to take the inclusion of metakaolin and fly ash in the cement matrix into account, based on a regression equation for predicting the ultimate drying shrinkage. Abdalhmid et al. (2019) [1] assessed the robustness of the existing shrinkage prediction models by studying the influence of different parameters on the drying shrinkage strain of concrete with addition of fly ash.

Mechanistic shrinkage models

Changes in the pore fluid pressure acting on the solid skeleton, associated with capillary pressure, is one of the main driving mechanisms of concrete shrinkage. Poromechanics (the study of porous materials whose mechanical behaviour is significantly influenced by the pore fluid [56]) and poroelasticity (in which the solid skeleton of the porous material is considered to behave elastically [69]) could therefore be used to model the shrinkage deformations caused by pore fluid pressure changes. Fundamental understanding of the mechanisms and physical properties involved in the process, are accordingly necessary to accurately predict the concrete deformations [69, 112, 230].

An extensive review of the different mechanistic shrinkage models, developed during the past years, is given in Wyrzykowski et al. (2017) [230] and the main conclusions are summarised. A first approach was proposed by Biot and Bischop, based on the concept of effective stress and theory of poroelasticity to describe the consolidation process of a porous material. Partial saturation of the pores was taken into account and the volumetric deformations (ϵ_v) could subsequently be described as:

$$\epsilon_v = -S_w \cdot p_c \cdot \left(\frac{1}{K_b} - \frac{1}{K_s}\right) \tag{2.16}$$

with S_w the water saturation degree, p_c the capillary pressure in the pores, which can be calculated according to the Kelvin-Laplace equation (Eq. 2.15), K_b the bulk modulus of the drained porous body and K_s the bulk modulus of the solid skeleton. Bentz et al. [29] used the Biot-Bischop approach to predict the drying shrinkage of porous glass and found good agreement at high internal relative humidity levels. For lower levels of saturation, on the other hand, the model underestimated the real drying shrinkage. In order to address this underestimation, Coussy et al. [57] proposed an alternative approach, introducing an equivalent pore pressure, to take the contribution of interface energy (U) into account.

$$\epsilon_v = -\left(S_w \cdot p_c + U\right) \cdot \left(\frac{1}{K_b} - \frac{1}{K_s}\right) \tag{2.17}$$

Alternative to the Biot-Bischop and Coussy approaches, Vlahinić et al. [226] and Rougelot et al. [180] incorporated the effect of (partial) saturation in the mechanical properties (bulk modulus) of the matrix by considering the partial saturated material as a saturated material and accounting for desaturation by reducing the effective bulk modulus of the solid skeleton [69, 230]. Maruyama [157], on the other hand, developed an approach assuming disjoining pressure to be the main driving mechanism for concrete shrinkage.

Lura et al. [153] used the Biot-Bischop approach to model the autogenous shrinkage of cement pastes and obtained good predictions in the high RH range. At lower RH, however, the model underpredicted autogenous shrinkage, which was attributed to the influence of viscoelastic effects (i.e. creep), that was not considered in the model. Aili et al. [4] confirmed that long-term autogenous shrinkage is due to creep under the action of capillary forces due to self-desiccation. Grasley and Leung [112] proposed a new approach incorporating these viscoelastic effects, by using aging poroviscoelasticity for prediction of desiccation shrinkage (both drying and autogenous). Hu et al. [125] used the fundamental principle as proposed by Grasley and Leung [112] for studying the autogenous shrinkage prediction of different compositions and expressed the autogenous shrinkage (ϵ_{as}) as:

$$\epsilon_{as} = \epsilon_{e} + \epsilon_{cr} \tag{2.18}$$

with ϵ_{e} the poroelastic deformation and ϵ_{cr} the viscoelastic deformation (contribution of creep). It was concluded that sole poroelastic calculations underestimated the measured autogenous shrinkage, while predictions with inclusion of the viscoelastic response overestimated the shrinkage.

In conclusion, prediction of concrete shrinkage using mechanistic models requires understanding of the fundamental mechanisms causing shrinkage, and knowledge of the moisture state and elastic properties of the porous material. It has been recently explored that creep (or the viscoelastic response) of cementitious materials accounts for long-term autogenous deformations and should be also considered in the poroelastic shrinkage models, yielding poroviscoelastic models.

2.6.2 Creep modelling

Empirical creep models

Empirical creep models are (same as empirical shrinkage models) based on regression analysis of experimental data. The most popular creep prediction models are: the Eurocode 2 model [77], the ACI 209 model [7], the Model Code 2010 model [129] and the Bazant B3 model. These empirical creep models all describe the development of creep as:

$$\epsilon_{cr}\left(t, t_0\right) = \phi\left(t, t_0\right) \cdot \frac{\sigma_c}{E_c} \tag{2.19}$$

with σ_c the sustained stresses in concrete, E_c the elastic modulus of concrete and $\phi\left(t, t_0\right)$ the creep coefficient, defined as the ratio of the creep strain to the instantaneous elastic strain under constant stress. The evolution of the

creep coefficient in time can be described using both logaritmic, power law, exponential as well as hyperbolic functions. Empirical creep prediction models can predict creep deformations for a specific set of experimental results and most of the models distinguish between basic and drying creep. However, empirical creep models experience the same drawbacks as the empirical shrinkage models and are less general than rheological or viscoelastic models, since they assume a constant stress level [15].

Rheological/viscoelastic models

Viscoelastic models are usually used for basic creep modelling and are based on rheological elements: springs and dashpots. The main basic models are the Kelvin-Voigt model and the Maxwell model (see Fig. 2.17), combined in series or in parallel.

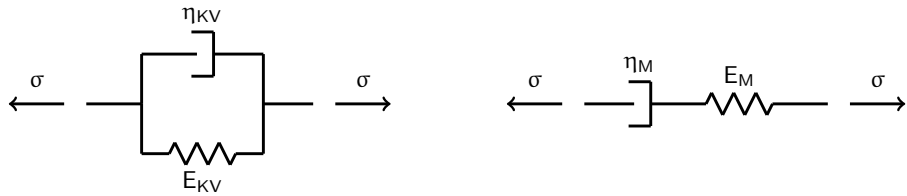

Figure 2.17: Kelvin-Voigt (left) and Maxwell (right) rheological model.

Different combinations of these basic rheological models have been investigated over the years to accurately model the creep behaviour of concrete. De Schutter (1999) [63] and Hauggaard et al. (1999) [118] used one Kelvin-Voigt chain for modelling of the early-age basic creep. Bazant et al. (1997) [17] developed a rheological model based on the solidification theory, which was improved by also considering the relaxation of microprestress. Gawin et al. (2006) [103, 104], on the other hand, developed a rheological creep model by using a Kelvin chain with a proper number of elements, and modelled the basic creep strain based on the solidification theory, and the long-term and drying creep strain based on the microprestress theory. Sciume et al. (2013) [192] adapted the model developed by Gawin and separated the aging elasticity, non-aging creep and microprestress development by defining a rheological model composed of a Kelvin-Voigt chain and two dashpots in series. Sellier et al. (2016) [198] developed a poro-mechanical creep model, consisting of two branches in parallel. The first branch representing the solid behaviour (containing an elastic part to model the instantaneous behaviour, a Kelvin chain to model the reversible creep and a Maxwell chain to model the irreversible creep) and the second branch representing the effects of hydric forces, i.e. capillary pressure and variation of

disjoining pressure. Benboudjema and Torrenti (2008) [27] used several Kelvin-Voigt chains for prediction of the basic creep strains. Briffaut et al. (2012) [40] added a dashpot in series to three Kelvin-Voigt chains to more accurately predict the irreversible creep [65].

Several rheological model approaches were thus proposed in the literature by different researchers, however, none of them have tried to include the influence of SCMs in the rheological creep models.

Coupling between drying creep and drying shrinkage

Since drying creep and drying shrinkage are coupled phenomena, drying creep strains are often predicted using the linear relationship between drying creep (ϵ_{dc}) and drying shrinkage (ϵ_{ds}) [101, 122]:

$$\dot{\epsilon}_{dc} = \beta_{dc} \cdot \sigma \cdot \dot{\epsilon}_{ds} \tag{2.20}$$

with β_{dc} a constant and σ the applied stress level. Other authors [16] propose to link drying creep with the evolution of the internal relative humidity (h):

$$\dot{\epsilon}_{dc} = \lambda_{dc} \cdot |\dot{h}| \cdot \sigma \tag{2.21}$$

with λ_{dc} a constant. Both relationships, however, are similar, since at low drying rate, there exists an almost linear relationship between the drying shrinkage and internal relative humidity development [122].

2.7 Conclusion

In this chapter, the current state of the art regarding the use of SCMs in concrete was discussed. Firstly, the use and limitations of existing SCMs were addressed. The use of SCMs can significantly reduce the clinker content of cement. However, the conventional SCMs will not be able to cover the growing cement demand in future, considering the limits of their availability and production. Therefore, there is a strong need for new sources of alternative high-quality SCMs. The use of primary sourced SCMs and unused residues and waste materials should thereby be encouraged and the use of calcined dredging sediments appears to be a promising alternative. Knowledge gaps, however, currently exist regarding the myriad of potential alternative SCMs and understanding of their influence on early-age properties, as well as on long-term durability and performance of concrete.

Secondly, the influence of SCMs on the hydration process and main concrete properties was discussed. At early ages, SCMs contribute to the cement

hydration by the filler effect. At later ages, SCMs contribute to refinement of the porosity by formation of additional hydration products (C-S-H and AFm phases) as a result of the pozzolanic or hydraulic reaction. Influence of SCMs on mechanical properties is strongly controlled by their influence on the hydration process, i.e. the filler effect, the dilution effect, the cement hydration acceleration effect (determining the early-age strength) and the pozzolanic and hydraulic reaction (determining the long-term strength). The influence of SCMs on the volumetric changes, on the other hand, is significantly affected by the hydration process (hydration rate, pore structure, etc.) and the macro-mechanical properties (strength and stiffness development). In order to understand and explain the influence of SCMs on the volumetric changes, it is therefore of major importance to first understand the influence of SCMs on the hydration process and mechanical development.

Thirdly, the current state of the art regarding the modelling of shrinkage and creep of SCM blended cement concretes was discussed. Incorporation of SCMs in empirical shrinkage models can (easily) be done by parametrisation of existing shrinkage models, provided that sufficient experimental data is available for validation. The considerable amount of input/fitting parameters, however, can cause large uncertainties. Incorporation of SCMs in mechanistic shrinkage models is more difficult, since understanding of the fundamental mechanisms causing shrinkage, which are affected by incorporation of SCMs, is required and creep should be taken into account. Rheological models are mostly used for basic creep prediction and an infinite combination of the basic rheological elements can be considered. Since there is still no consensus on the mechanisms at the origin of creep, different creep models have been developed over decades, based on different creep mechanisms. Research on incorporating SCMs in these models is therefore limited/non-existent.

Considering the state of the art and the research objectives set, the main key question asked is: *"Can we use CFC blended cement for structural concrete applications and how can we understand the influence of CFC on the early-age and long-term performance of concrete structures?"*. In order to answer this main question, following sub-questions can be asked:

- What is the influence of CFC on the hydration process and how does this affect the strength development of CFC concrete?
- How do changes in hydration kinetics and products, and changes in strength and stiffness development influence the shrinkage and creep behaviour of CFC concrete? And, thus, how does CFC contribute in the volumetric changes?

- How can we integrate CFC as an SCM in the existing shrinkage and creep models in order to predict the early-age and long-term cracking risk, and durability and performance of concrete structures?

The next chapters try to provide answers to these research questions.

Chapter 3

Materials and methods

This chapter introduces the different materials and various methods/techniques used. The first part describes the material properties (Section 3.1), the second part describes the mix compositions and mixing procedures (Section 3.2) and the third part includes the different analytical techniques and test methods (Section 3.3). Finally some conclusions are summarised (Section 3.4).

3.1 Materials

3.1.1 Cement

Ordinary Portland cement CEM I 52.5 N and Portland fly ash cement CEM II/B-V 42.5 N, complying with the European standard EN 197-1 [73], are used as two reference cements. The chemical composition of both cements, determined with the inductively coupled plasma - optical emission spectometry (ICP-OES) technique, and the loss on ignition (LOI), determined according to EN 196-2 [84], is shown in Table 3.1.

Table 3.1: Chemical composition [wt.%] of the cements used.

	Al_2O_3	SiO_2*	Fe_2O_3	CaO*	MgO	Na_2O	K_2O	P_2O_5	LOI
CEM I	4.9	14.0	2.8	57.4	1.6	0.5	0.9	0.3	2.7
CEM II	11.3	22.0	4.0	45.2	1.8	0.9	1.5	0.6	2.2

* The SiO_2 and CaO content are underestimated due to the limitations of the ICP-OES measurement technique and sample preparation.

The BET (Brunauer-Emmett-Teller) specific surface area and Blaine fineness of both cements are also determined, respectively by performing a low temperature nitrogen adsorption test (LT-NAT) and through the European standard EN 196-6 [80] (including a determination of the density using a pyknometer). The results are shown in Table 3.2 and the specific surface area of the Portland fly ash cement is slightly higher than the specific surface area of the ordinary Portland cement. The Portland fly ash cement also shows slightly lower density due to the lower specific gravity of FA [209].

Table 3.2: BET specific surface area, Blaine fineness and density of the cements used.

	BET [m^2/g]	Blaine [cm^2/g]	Density [kg/m^3]
CEM I	0.934	3418.4	2928.5
CEM II	2.199	3884.5	2665.0

Technical information about the cements is given in the technical datasheets in Appendix A.

3.1.2 Calcined filter cakes (CFC)

Two different batches of CFC are used in this study. This subsection describes the treatment of the dredging sediments before they can be used as SCM (including a mechanical dewatering and flash calcination) and their resulting chemical and physical properties.

Treatment

Each year 450.000 tons dry matter of dredging sediments are processed in a mechanical dewatering installation in the Port of Antwerp. Prior to the dewatering process, carried out by membrane filter presses, sand is removed by hydrocyclones. Lime (2-5 wt.%) is added to enhance solid-liquid separation in the filter presses. A detailed description of the dewatering installation can be found in Appendix B. The produced fine grained (< 63 μm) filter cakes contain at least 60 wt.% dry matter and occupy a significant lower volume than the original sludge [207].

A first batch of filter cakes with representative composition was flash calcined at three different calcination temperatures (820°C, 865°C and 905°C), in order to evaluate the potential of flash calcination as a means to activate the clay minerals in the filter cakes. The design and operation of the pilot-scale gas

suspension flash calciner are described in [214]. Before calcination, the filter cakes were first dried at 110°C until constant mass and subsequently ground in a vertical roller mill to below 0.5 mm. After calcination, the material was cooled down by a counter flow of cold gas and further ball milled to reach the targeted fineness (< 34 wt.% on a 45 µm sieve) and particle size distribution ($d_{50} < 25$ µm). The resulting calcined filter cakes are henceforth called CFC 820, CFC 865 and CFC 905.

After positive evaluation of the first batches, another batch of filter cakes with representative composition was flash calcined in a different pilot-scale flash calciner at 865°C, in order to confirm the technical feasibility of the flash calcination process. The calcined filter cakes of this batch are henceforth called CFC 865*.

Properties

The effect of flash calcination on the physico-chemical characteristics, mineralogy and pozzolanic reactivity of the dredging sediments was investigated in detail in [205]. The mineralogical composition of the first batches of filter cakes before and after calcination is given in Table 3.3.

Table 3.3: Mineralogical composition [wt.%] of CFC [205].

	Untreated	CFC 820	CFC 865	CFC 905
Quartz	22	26	27	25
Plagioclase	3	5	5	6
Alkali feldspar	2	2	3	3
Calcite	12	4	4	3
Aragonite	5	-	-	-
Pyrite	1	-	-	-
2:1 clays (illite, smectite)	34	12	6	6
Kaolinite	3	-	-	-
Fe-oxides (hem/mag)	-	2	3	3
Free lime	-	2	1	1
Anhydrite	-	2	2	2
Unidentified/amorphous	18	45	49	51

The major mineral phases of the dredging sediments comprise clays (2:1 clays and kaolinite), quartz, calcite and an amorphous phase. Flash calcination results in dehydroxylation of the clay minerals and decarbonation of the calcite. The dehydroxylated clay minerals react with part of the free lime, released in the decomposition of the calcium carbonates, to form an amorphous reactive

phase (± 50 wt.%), responsible for the pozzolanic reactivity. Higher calcination temperatures result in a more complete structural decomposition of the clay minerals and slightly increase the amorphous fraction. However, the pozzolanic reactivity of CFC was not influenced by the calcination temperature and CFC was found to be less reactive than metakaolin, but more reactive than siliceous fly ash [205].

The chemical composition of CFC was determined by ICP-OES and the results are shown in Table 3.4. CFC is mainly composed of SiO_2, besides other major components of CaO, Al_2O_3 and Fe_2O_3. The effect of the calcination temperature on the chemical composition is mostly insignificant in terms of major elements. The element composition of the first batches and the second batch are slightly different, especially for the silica content. Two possible explanations can be found for the differences in silica content:

- The limitations of the ICP-OES technique for SiO_2 determination (overlap of optical emission lines) and the different sample preparation of both batches. The samples of the first batches were microwave digested in acid ($HCl/HNO_3/HF/H_3BO_3$) before measurement, while the samples of the second batch were digested in HNO_3 after muffle oven incineration.
- Small variations in the sampling of the filter cakes. A lower sand content in the CFC 865* batch, for instance, could explain the lower SiO_2 and higher Al_2O_3 and Fe_2O_3 contents, due to quartz (SiO_2) being the main component of the sand fraction and clay minerals (aluminosilicates) and Fe-(oxy)hydroxides being the main components of the fine fraction.

Table 3.4: Chemical composition [wt.%] of CFC [205].

	Al_2O_3	SiO_2	Fe_2O_3	CaO	MgO	Na_2O	K_2O	P_2O_5	LOI
CFC 820	10.4	53.7	8.7	12.5	1.7	0.8	2.1	0.9	2.9
CFC 865	10.2	54.3	8.3	12.2	1.7	0.8	1.9	1.0	2.1
CFC 905	10.7	54.1	8.7	13.3	1.8	0.8	2.1	1.0	2.4
CFC 865*	13.0	42.0	9.7	12.5	2.2	1.4	3.4	0.8	1.7

Compared to other existing and commonly used SCMs, the chemical composition of CFC is close to the chemical composition of siliceous - class F - fly ash and natural pozzolans (see Fig. 3.1).

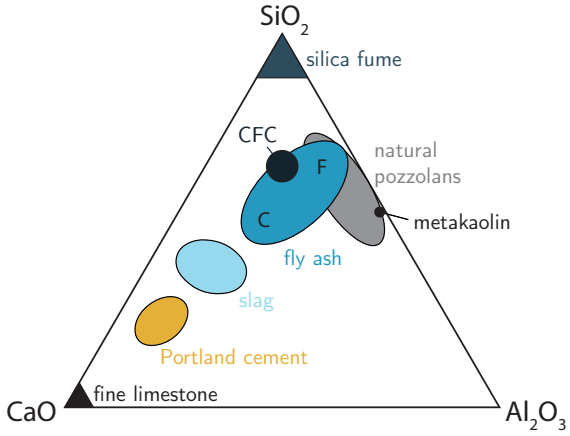

Figure 3.1: CaO-Al_2O_3-SiO_2 ternary diagram of some commonly used SCMs and CFC, adapted from [152].

Potentially volatile components, such as sulphur, organic carbon compounds and chlorine were also quantified for the first batches of CFC [205], respectively by anion chromatography on the digested solutions, by ignition and CO_2 detection by IR spectrometry after acid dissolution of inorganic carbonates, and by anion chromatography according to ASTM C1218 [11]. The results are shown in Table 3.5. Sulphur and chlorine contents were relatively low and comply with the regulations for use in non-reinforced and normal reinforced concrete according to EN 206 [74]. Furthermore, the total organic carbon (TOC) level was strongly reduced upon calcination (2.49 wt.% on ignited base before calcination) [205].

Table 3.5: Potentially volatile elements [wt.%] of CFC [205].

	SO_3	Cl	TOC
CFC 820	1.50	0.14	0.31
CFC 865	1.52	0.16	0.25
CFC 905	1.57	0.19	0.18

The BET specific surface area and Blaine fineness of CFC are shown in Table 3.6. The specific surface area of CFC is much higher than the specific surface area of the two reference cements, negatively influencing its water demand. Furthermore, the calcination temperature significantly affects the BET specific surface area, with decreasing specific surface area for increasing calcination temperature. Given that the particle size distributions of CFC are practically identical [205], the observed decrease in BET specific surface area indicates a strong reduction

in particle surface roughness due to sintering and melting of some CFC particles at higher calcination temperatures [205]. The measured density of CFC, finally, is also lower than the density of both reference cements.

Table 3.6: BET specific surface area [m^2/g] and Blaine fineness [cm^2/g] of CFC [205].

	BET [m^2/g]	Blaine [cm^2/g]	Density [kg/m^3]
CFC 820	8.945	-	-
CFC 865	4.938	-	-
CFC 905	3.345	-	-
CFC 865*	4.018	6477.6	2403.8

Blaine fineness and density were not measured for CFC 820, 865 and 905.

In conclusion, the calcination temperature has no influence on the pozzolanic reactivity or chemical composition of CFC, however, lower calcination temperatures result in higher specific surface areas. Higher calcination temperatures, on the other hand, result in higher energy costs and more decomposition of $CaCO_3$. The choice of calcination temperature 865°C for the second batch of CFC, was therefore a compromise between all these factors. Both batches CFC 865 and CFC 865* were used for further testing. Batch CFC 905 was only used to a limited extent (after batch CFC 865 was finished and before batch CFC 865* was delivered).

3.1.3 Aggregates

The aggregates used in this study are river sand 0/4 and river gravel 4/14. Three different batches from three different suppliers are used, all complying with the European standard EN 12620 [83]. The particle size distribution of the different batches of aggregates was determined according to EN 933-1 [81] and the results are shown in Fig. 3.2. There is almost no difference between the particle size distributions of the three batches of sand; while for the gravel, the second batch is a bit coarser and has a smaller particle size range than the other two batches. However, the influence of these differences on the studied concrete properties is negligible.

More characteristics and physical properties of the aggregates can be found on the technical datasheets in Appendix A.

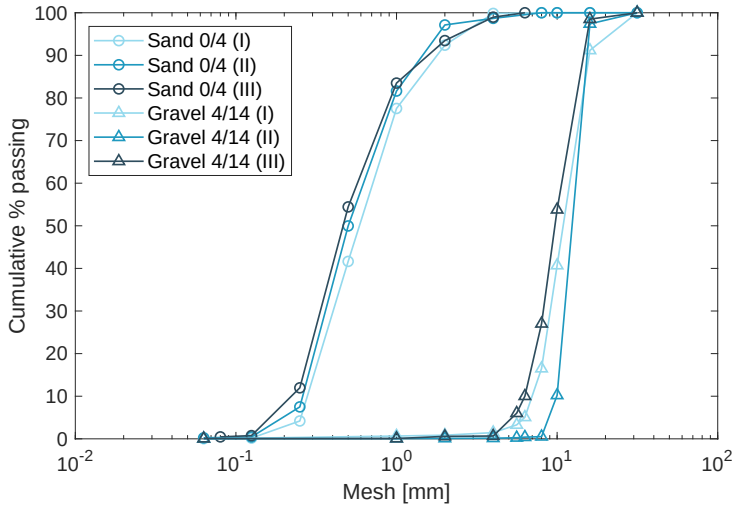

Figure 3.2: Particle size distribution of the three different batches of river sand 0/4 and river gravel 4/14.

3.1.4 Superplasticizer

Five commercial superplasticizers, from three different generations, are examined: a modified lignosulphonate (LS), a sulphonated naphthalene-based superplasticizer (SNF) and three different polycarboxylate ethers (PCE). The physical and chemical characteristics of the admixtures used can be found in Tables 3.7 and 3.8 and they all comply with the European standard EN 934-2 [78]. The technical datasheets of the superplasticizers can be found in Appendix A.

Table 3.7: Properties of the traditional superplasticizers.

	LS	SNF
Commercial name	MasterPozzolith 390N	MasterRheobuild 1100
Producer	BASF	BASF
Effective component	Lignin sulphonate	Sulphonated naphthalene formaldehyde condensate
Dry matter content [%]	38 ± 1.9	40
Density [kg/l]	1.22	1.20
pH [-]	6-9	6-9
Chloride content [%]	$\leq$ 0.1	$\leq$ 0.1
Dosage [wt.%/binder]	0.2-0.6	0.5-1.2

Table 3.8: Properties of the PCE superplasticizers.

	PCE 1	PCE 2	PCE 3
Commercial name	MasterGlenium 51	Tixo®	ViscoCrete® 4035
Producer	BASF	Sika	Sika
Effective component	Polycarboxylate ether	Water-based polymer solution	Modified polycarboxylate
Dry matter content [%]	35	25 ± 1.5	35 ± 1.0
Density [kg/l]	1.10	1.09 ± 0.02	1.08 ± 0.01
pH [-]	5-8	4.6 ± 1.5	4.5 ± 1.0
Chloride content [%]	≤ 0.1	≤ 0.1	≤ 0.1
Dosage [wt.%/binder]	0.4-1.3	0.5-2.0	0.4-1.5

3.2 Mix compositions and mixing procedure

3.2.1 Concrete

Five different concrete compositions, including two reference mixes and three CFC blended cement mixes, are investigated. The reference mixes (RC I and RC II) are produced by using respectively CEM I 52.5 N and CEM II/B-V 42.5 N. OPC was used as a reference cement in order to determine the pozzolanic and filler effect of CFC, replacing cement in concrete. Portland fly ash cement was used for benchmarking. By comparing CFC with FA, an existing, commonly used SCM, the quality of CFC can be measured. Three blended cement mixtures (CFC 20, CFC 30 and CFC 40) were made by replacing OPC with respectively 20, 30 and 40 wt.% CFC (assuming a constant cementitious materials content) and assuming a constant aggregate content for all mixes. The final mix compositions of the studied concretes are shown in Table 3.9. Chapter 4 describes the initial mix compositions and mix design optimisation in detail.

Table 3.9: Mix proportions of the concrete mixtures.

		RC I	RC II	CFC 20	CFC 30	CFC 40
Sand 0/4	[kg]	640	640	640	640	640
Gravel 4/14	[kg]	1225	1225	1225	1225	1225
CEM I 52.5N	[kg]	360	-	288	252	216
CEM II/B-V 42.5N	[kg]	-	360	-	-	-
CFC	[kg]	-	-	72	108	144
Water	[l]	162	162	162	162	162
ViscoCrete® (PCE 3)	[wt.%/B]	0.35	0.20	0.55	0.70	0.75
W/B	[-]	0.45	0.45	0.45	0.45	0.45
W_{eff}/B	[-]	0.42	0.42	0.42	0.42	0.42

Table 3.9 shows both the total water-to-binder (W/B) ratio and the effective water-to-binder (W_{eff}/B) ratio. The W_{eff}/B ratio takes into acount the water absorption by the aggregates. For commonly used aggregates in Belgium, a value of 10 litres of water per m^3 of concrete can be used [24]. Justification of this assumption can be found in Appendix C. According to EN 206-1 [74], the water content of the superplasticizer should not be taken into account for calculating the W/B (and W_{eff}/B) ratio, since less than 3 litres of superplasticizer per m^3 of concrete is added.

A strict concrete mixing procedure was followed, with a total mixing time of 6 minutes. Materials were added in the following order: sand and gravel (60 s mixing), half of the water (120 s mixing), rest (120 s), cement and CFC (30 s mixing) and finally the remaining water and superplasticizer (150 s mixing). Four different intensive EIRICH concrete mixers were used with different volumes: a 40 litres concrete mixer (ULB, type R05T), a 50 litres concrete mixer (KU Leuven, type SKG1), a 75 litres concrete mixer (ENS Cachan, type R08W) and a 250 litres concrete mixer (KU Leuven, type EB36).

3.2.2 Cement paste

The mix compositions of the cement paste mixes are derived from the concrete mix compositions in Table 3.9. The same W_{eff}/B ratio and amount of superplasticizer are used.

Cement paste mixes were prepared according to EN 196-3 [87], using a HOBART cement mixer, with a rotational speed of 140±5 min^{-1} according to EN 196-1 [86]. After pouring water (+ superplasticizer) and cement (+ CFC) in the mixing bowl, two mixing periods of 90 s followed. In between the two mixing periods the paste adhering to the walls and bottom part of the bowl was removed (during max. 30 s). When only small amounts of cement paste were needed (e.g. for calorimetry and XRD), a hand mixer with adjustable speed was used.

3.3 Methods

3.3.1 Early-age characterisation methods

In order to characterise the early-age behaviour of CFC in cement paste and concrete and in order to study the influence of CFC on the cement hydration process, three different analytical techniques were used: isothermal calorimetry, X-ray diffraction and internal relative humidity measurement.

Isothermal calorimetry

Isothermal calorimetry is a commonly used technique to measure the heat release rate (heat flow) of small cement paste, mortar or concrete samples, in order to study the reaction kinetics of cement hydration [193]. The heat flow of cement paste samples was measured using an isothermal heat conduction calorimeter (8 channel TAM AIR) at 20°C. Samples of 8.4 ± 0.2 g were taken at the end of mixing and the first measurements were acquired within less than 5 minutes after the first contact between the cementitious materials and the water. Calorimetry measurements were performed up to 7 days and the reported results are the average values of at least two measurements ($n \geq 2$).

The heat flow of the concrete mixtures was measured using an isothermal heat conduction calorimeter (3 channel TAM AIR) at 20°C. Samples of 140 ± 5 g of concrete were taken at the end of mixing and the first measurements were acquired less than 10 minutes after the first contact between water and cement. One measurement up to 7 days was done for each concrete composition ($n=1$).

X-ray diffraction (XRD)

XRD is a prominent analytical technique to characterise crystalline, fine-grained materials, such as cement [193]. In combination with Rietveld quantitative phase analysis, XRD allows to identify and quantify the crystalline phases in complex reacting systems. XRD measurements were carried out on cement paste samples after hydration stoppage by solvent exchange at very early ages (10, 20, 30, 40, 50 and 60 hours of hydration). The samples were first crushed to below 1 mm and submerged in isopropanol for 15 minutes. Then, the residue was rinsed once with isopropanol and twice with di-ethylether over a Büchner filter. Finally, the filter residue was dried for about 15 minutes in a ventilated oven at 40°C. The powders were finely ground just before XRD analysis and the measurements were carried out within two days after the hydration stoppage. The XRD analysis was performed at VITO using an Empyrean X-ray Diffractometer (PAN analytical) with CoKα radiation.

Internal relative humidity (RH) measurement

The development of the relative humidity inside cement paste samples was measured using a Rotronic device with HC2-AW-USB probe (accuracy of 1%). The probes were calibrated in the 65-95% RH range, using standard salt solutions of known constant RH. The stations were placed in a thermostatically controlled room (± 20°C), and RH and temperature in the sample were continuously

measured, from final setting up to 7 days. The reported results are the average values of two measurements (n=2).

3.3.2 Setting time determination

Vicat setting time

The Vicat test, according to EN 196-3 [87], was used for determination of the cement paste setting times. By measuring the penetration depth of the Vicat needle as a function of time, the initial and final setting times can be determined. The initial setting time is defined as the time measured from time zero (first contact between water and cement) at which the distance between the needle and the base-plate is 6 ± 3 mm. The time (measured from time zero) at which the needle first penetrates only 0.5 mm into the sample, is defined as the final setting time of the binder. The reported results are the average values of at least two measurements (n≥2).

Ultrasonic pulse velocity (UPV) measurements

The use of ultrasonic waves through cement-based materials is a well-established non-destructive method to detect setting time in cement pastes, mortars and concretes, and to monitor the development of mechanical properties. An ultrasonic P-wave analysis device (multichannel IP-8, from UltraTest), equipped with a 30 kHz transducer, was used for cement paste samples (see Fig. 3.3 (left)). Each measuring cell was composed of a cylindrical silicone mould, with an ultrasonic sender and receiver and a temperature sensor. The volume of the cement paste samples was equal to 95 mL and all tests were performed with a sender-receiver distance of 40 ± 0.5 mm. The reported results are the average values of at least two measurements (n≥2).

Measurement of the ultrasonic pulse velocity through concrete samples, on the other hand, was done at ULB with a FreshCon device (see Fig. 3.3 (right)), developed at the university of Stuttgart [174]. Both P- and S-waves were simultaneously measured on separate moulds. A 5 μm pulse was sent every minute through the concrete sample, with a distance of 7.8 cm between the sensors. The P-wave sensors had a frequency of 0.5 MHz and the frequency of the S-wave sensors was 0.25 MHz. Detailed information about this equipment is provided in [49]. Only one continuous measurement of P- and S-waves was done for each concrete composition (n=1).

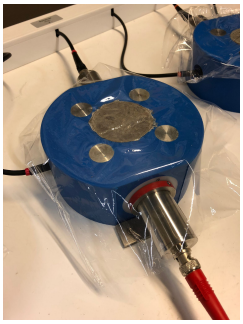
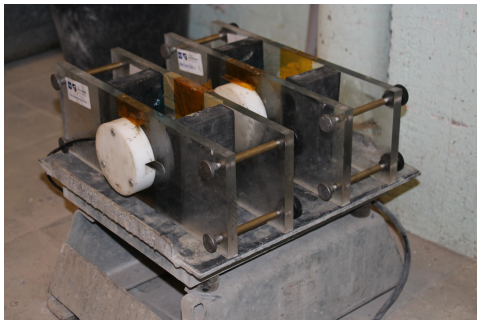

Figure 3.3: UPV device (left) and FreshCon system (right).

3.3.3 Fresh concrete properties

Fresh concrete properties were measured on fresh concrete immediately after mixing and all tests were performed according to the European standards.

Bulk density

The bulk density of fresh concrete was determined according to EN 12350-6 [90]. Fresh concrete was compacted into a rigid container of a known volume (V) and mass ($m_{containter}$), and was then weighed (m_{total}). The density (ρ) was then calculated as:

$$\rho = \frac{m_{total} - m_{containter}}{V} \tag{3.1}$$

Workability

To evaluate the workability of the fresh concrete, both flow and slump tests were carried out, respectively according to EN 12350-5 [89] and EN 12350-2 [88]. The flow test determines the consistency of the fresh concrete by measuring the spread of the concrete on a flat plate, subjected to jolting. The slump test determines the consistency of fresh concrete by compacting the fresh concrete into a truncated cone shaped mold and measuring the distance between the height of the cone and the highest point of the slumped test specimen, after withdrawing the cone upwards.

Air content

The air content was determined according to EN 12350-7 [91], by using the 'water column method'. Water is introduced into a sealed container, filled with compacted concrete, to a predetermined height above the concrete. A predetermined air pressure is applied over the water and the reduction in volume of air in the concrete samples is then measured by observing the amount by which the water level is lowered.

3.3.4 Hardened concrete properties

Hardened concrete properties were determined on hardened concrete samples after curing in a climate room at 20 ± 2°C and > 90% RH. All tests were performed according to the European standards and three samples were used per test (n=3).

Bulk density

The bulk density of hardened concrete was determined in according to EN 12390-7 [94]. The mass and volume of cubic samples (150 x 150 x 150 mm) were determined precisely and the density was then calculated as the ratio of the mass over the volume.

Compressive strength

Compression strength tests were carried out on cubic specimens (150 x 150 x 150 mm) according to EN 12390-3 [92], by means of a 5000 kN capacity testing machine. The applied rate of loading was equal to 15 kN/s, corresponding to a stress rate of 0.67 MPa/s.

Flexural strength

Flexural strength tests were conducted on prismatic test specimens (150 x 150 x 600 mm) according to EN 12390-5 [93], three-point bending test. The applied loading rate was 0.3 kN/s, corresponding to a stress rate of 0.04 MPa/s.

Tensile splitting strength

Tensile splitting strength tests were carried out on both prismatic (150 x 150 x 300 mm) and cylindrical (ϕ 150 mm x 300 mm) test specimens, according to EN 12390-6 [79]. The tensile splitting strength results reported in Chapter 4 were carried out on prismatic test specimens. Since the standard deviations of these results were quite high, there was switched to cylindrical test specimens for the tensile splitting strength tests reported in Chapter 5. The applied loading rate was similar to the loading rate of the flexural strength test, i.e. 0.3 kN/s. Teflon packing strips were used between the concrete and testing machine surface in order to limit the influence of the rough concrete surface. According to Eurocode 2 [77], the tensile strength (f_{ct}) can be derived from the tensile splitting strength ($f_{ct,sp}$) as:

$$f_{ct} = 0.9 \cdot f_{ct,sp} \tag{3.2}$$

It should be remarked that Model Code 2010 [129], however, suggests a value of 1 instead of 0.9 in Eq. 3.2.

Dynamic elastic modulus

The dynamic modulus of elasticity was evaluated by determination of the ultrasonic pulse velocity (v), according to B 15-229 [72] and EN 12504-4 [76]. An ultrasonic wave of 55 kHz was transmitted through a cubic concrete specimen. Based on the path length, the time taken by the pulse to transverse the path length and the density (ρ) of the concrete, the dynamic E-modulus (E_d) is calculated as:

$$E_d = 0.9 \cdot \rho \cdot v^2 \tag{3.3}$$

assuming a Poisson's ratio of 0.2 for concrete.

Static elastic modulus

The static elastic modulus was determined according to EN 12390-13 [85] on cylindrical test specimens (ϕ 150 mm x 300 mm). Three loading cycles, in which the concrete specimens were loaded until 1/3 of their compressive strength, were carried out with a loading rate of 10.52 kN/s or stress rate of 0.6 MPa/s. The corresponding deformations were measured by means of three Linear Variable Differential Transducers (LVDTs), symmetrically arranged around the specimen. The static modulus of elasticity (E_s) was then calculated as:

$$E_s = \frac{\Delta\sigma}{\Delta\epsilon} \tag{3.4}$$

with $\Delta\sigma$ the difference in applied stress between the start and the end of the cycle and $\Delta\epsilon$ the difference in measured strain.

3.3.5 Volumetric changes

Autogenous shrinkage

The corrugated tube method (see Fig. 3.4) was used to determine the linear autogenous deformations of cement paste samples, according to ASTM C1698-09 [12]. Fresh paste was placed into a corrugated plastic mould immediately after preparation, permitting measurements to start less then 30 minutes after the first contact between the water and the cementitious materials. This method allows the specimen to shrink freely and prevents moisture loss to the environment. After casting, the corrugated tubes were placed in a dilatometer and by means of LVDTs, the unrestrained autogenous deformations of the specimens were measured continuously up to 7 days [186]. The reported results are the average values of at least two individual measurements, obtained on different specimens ($n \geq 2$).

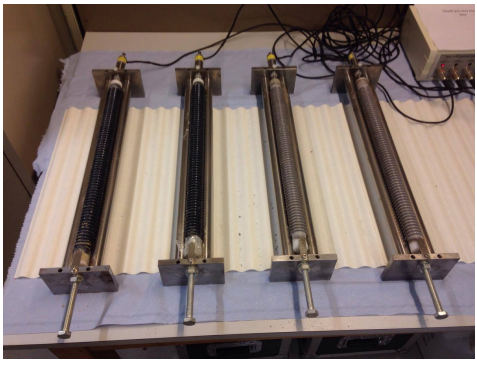

Figure 3.4: Corrugated tube method for determination of autogenous shrinkage on cement paste samples.

The autogenous deformations of concretes samples were measured using a BTJADE device (see Fig. 3.5) at ULB. This device is developed by Boulay [39] and is specially designed for autogenous shrinkage measurements of concrete at early ages. The test rig is composed of a flexible corrugated PVC mould - in which the concrete is casted - and a steel frame with fixed metallic parts. The whole frame is placed in a thermo-controlled bad to ensure a constant temperature of $\pm$ 20°C and a stress free state. A thermocouple is inserted into the concrete specimen to continuously measure the temperature inside

the sample and the deformations are measured by an external LVDT. The water temperature and temperature of the air above the cover of the tank are also continuously monitored. This allows calculating the 'actual' autogenous deformations (ϵ_{au}) as the measured deformations (ϵ_{meas}) minus the thermal deformations (ϵ_{th}), minus the deformations as a result of the temperature variation around the sensor (ϵ_{ts}), minus the deformations resulting from the reaction of the frame (ϵ_{tm}):

$$\epsilon_{au} = \epsilon_{meas} - \epsilon_{th} - \epsilon_{ts} - \epsilon_{tm} \tag{3.5}$$

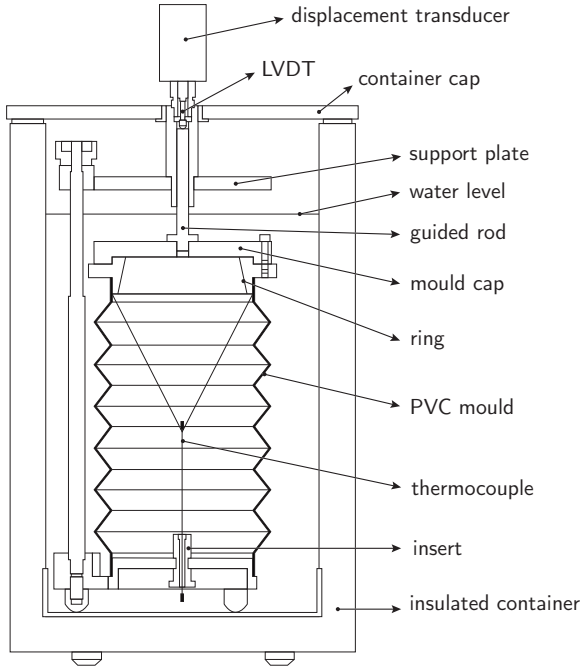

Figure 3.5: BTJADE device, adapted from [47].

Autogenous shrinkage measurements on concrete samples were performed up to 14 days. The reported results are the average values of four individual measurements, obtained on two different batches of concrete (n=4). Only for the RC II and CFC 40 mix, only one batch of concrete was made (n=2).

Chemical shrinkage

The chemical shrinkage of cement paste samples was determined using the dilatometry method according to ASTM C1608-17 [14]. This method measures the drop in water level in a hydrating cement paste system by means of a pipette. About 20 ± 0.05 g of cement paste was placed in a glass jar and this corresponds to a thickness of 20 mm cement paste. Demineralised water was added carefully to fill the glass jar to the top and the volume change of the water in the pipette is then considered as the chemical shrinkage [237]. The specimens were stored at 20°C and measurements were taken every 15 minutes, starting from after final setting up to 7 days. The reported results are the average values of two individual measurements (n=2).

Drying shrinkage

Concrete drying shrinkage measurements were performed on cylindrical specimens with diameter 120 mm and height 300 mm. The specimens were installed in a frame made of brass (see Fig. 3.6), where a bottom ring is immovably fixed to the concrete specimen by means of three points, while an upper ring is only fixed in two opposite points, allowing the ring to rotate around the axis formed by the two fixation points. The two rings are connected to each other at two sides. At one side by a small bar and a spring (to keep the bar under pressure), in order to provide a fixed distance between the two rings at this side. At the other side by a second small bar, holding at one end the core of an LVDT, to measure the relative displacement between the two rings.

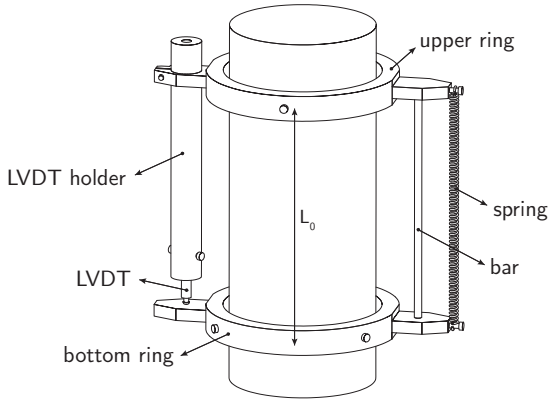

Figure 3.6: Drying shrinkage set-up.

The time-dependent deformations were then continuously measured by means of LVDTs and the concrete shrinkage strains (ϵ_{sh}) are then calculated as:

$$\epsilon_{sh} = \frac{1}{2} \cdot \frac{\delta_t - \delta_0}{L_0} \tag{3.6}$$

with L_0 the LVDT measuring base (= 200 mm) and δ_t and δ_0 respectively the LVDT reading at time t and at the start of drying (= 1 day) [120]. Drying took place in a climate room at a temperature of 20°C and relative humidity of 60%, and measurements were performed up to 90 days. The reported results are the average values of measurements on three different concrete cylinders (n=3).

Creep

Compressive creep experiments were performed at ENS Cachan, according to ASTM C512/C512M-15 [13], both in autogenous and drying conditions. Simultaneously also autogenous and drying shrinkage measurements were done (using specimens of the same size as for the creep measurements), in order to calculate the creep strains (ϵ_{cr}) as:

$$\epsilon_{cr} = \epsilon_{measured} - \epsilon_{sh} \tag{3.7}$$

Both creep and shrinkage measurements were performed on prismatic test specimens of 70 x 70 x 280 mm. Four creep frames (see Fig. 3.7) were available, so per composition, two specimens were used for basic creep measurements and two specimens were used for autogenous creep measurements (n=2). For shrinkage, three specimens were used for drying shrinkage measurements and three specimens were used for autogenous shrinkage measurements (n=3).

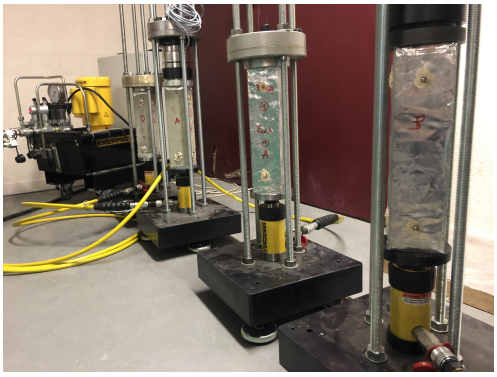

Figure 3.7: Creep set-up ENS Cachan.

Autogenous conditions were obtained by sealing the test specimens with a plastic foil and three layers of aluminium tape. Drying conditions were obtained by putting the specimens in a temperature and relative humidity controlled room, ensuring a temperature of 23°C and relative humidity of 50%. The drying shrinkage weight loss was also measured simultaneously on the drying shrinkage specimens.

A creep load of 30% of the concrete compressive strength was applied two days after casting and the specimens were unloaded after 14 days. The compressive creep load was applied using a compressor and the applied pressure working on the jack (with a surface area of 1450 mm^2) was recalculated to the applied pressure on the specimen (surface area: 4900 mm^2). Shrinkage and creep deformations were monitored by measuring the length change between two steel balls, which were stuck on every side of the concrete specimen (see Fig. 3.7), with a base length of 200 mm. The shrinkage and creep strains were then calculated as follows:

$$\epsilon = \frac{\Delta L}{L_0} \tag{3.8}$$

where ΔL is the difference in length between two measurements and L_0 is the initial length between the two steel balls ('zero'-measurement).

3.4 Conclusion

In this chapter, the different materials and various methods/techniques used were described in detail, in order to allow meaningful interpretation of the experimental results in the following chapters.

The main material properties of the reference cements and CFC were discussed thoroughly. CFC mainly consists of silica, and its chemical composition is close to the chemical composition of siliceous fly ash. The specific surface area of CFC is much higher than the specific surface area of the reference cements, negatively influencing its water demand. Furthermore the specific gravity of CFC is lower than the specific gravity of the reference cements, slightly reducing the concrete density.

A lot of standardised methods are used to investigate the behaviour of CFC in cement paste and concrete, since these methods have already been used for very long time and their efficiency is already proven long ago. However, in some cases and especially when using new blended cements, these standardised methods show some drawbacks, since the early-age behaviour is not continuously captured. Therefore also some non-standardised techniques were used. Measurement of ultrasonic waves (UPV method) was done with the UltraTest and FreshCon

device as a continuous, non-destructive method for setting determination and mechanical properties correlation, and the BTJADE device was used for early-age autogenous shrinkage measurement.

The final mix compositions of the concrete mixes were also given, however, a detailed design and optimisation of the concrete mix compositions can be found in Chapter 4.

Chapter 4

Concrete mix design

This chapter describes the concrete mix proportions design and optimisation. The influence of different concrete mix design parameters on fresh and hardened concrete properties is investigated, in order to find an appropriate/suitable mix design for CFC blended cement concretes. Three different mix design parameters are studied: cement replacement ratio (Section 4.1), type and dosage of superplasticizer (Section 4.2) and water-to-binder ratio (Section 4.3). Furthermore, a summary of the final mix compositions used for further testing is given (Section 4.4) and the chapter ends with a conclusion (Section 4.5). *

4.1 Cement replacement ratio

The aim of the initial test series was to upscale the mortar mix design [207] to concrete and to face the initial challenges associated with it. The influence of the cement replacement ratio and the influence of the addition of a superplasticizer (in order to contribute to the higher water demand due to the higher specific surface area of CFC) on fresh and hardened concrete properties are investigated.

*Parts of this chapter have already been published in Van Bunderen, C. et al. Mixture proportions of concrete with dredging sediments as novel SCM. In *Proceedings of the 10th ACI/RILEM International Conference on Cementitious Materials and Alternative Binders for Sustainable Concrete*, A. Tagnit-Hamou, Ed., vol. 1, pp. 27.1-27.10 [223].

Experimental program

Starting from a reference concrete mix design (RC I), four different concrete compositions, including one other reference mix (RC II) and three CFC blended cement mixes (CFC 20, CFC 30 and CFC 40), were defined/derived (see Table 4.1). Constant aggregate content (sand: 640 kg and gravel: 1225 kg), constant cementitious materials content (360 kg) and constant water-to-binder ratio (W/B = 0.5) were used. The reference mixes were produced by using respectively ordinary Portland cement (OPC) and Portland fly ash cement, while the three blended cement mixtures were made by replacing OPC with respectively 20, 30 and 40 wt.% of CFC.

Table 4.1: Initial concrete mix compositions.

		RC I	RC II	CFC 20	CFC 30	CFC 40
Sand 0/4	[kg]	640	640	640	640	640
Gravel 4/14	[kg]	1225	1225	1225	1225	1225
CEM I 52.5N	[kg]	360	-	288	252	216
CEM II/B-V 42.5N	[kg]	-	360	-	-	-
CFC	[kg]	-	-	72	108	144
Water	[l]	180	180	180	180	180
W/B	[-]	0.5	0.5	0.5	0.5	0.5
W_{eff}/B	[-]	0.47	0.47	0.47	0.47	0.47

Since CFC was already known to negatively influence the flowability of cement paste and mortar mixes [207] and since in practice the workability of a concrete mix is an important issue, strongly determining its applicability, the workability of the concrete mixes was also targeted to be constant. This was done by adding a superplasticizing admixture, and slump class S2 (50-90 mm) and flow class F2 (350-410 mm) were pursued for all mixes. The dosage of superplasticizer was determined experimentally by means of fresh concrete properties testing, using batches of 25 litres of concrete. Later on, mechanical properties were investigated, using batches of 140 litres of concrete.

Fresh concrete properties

Commercial PCE superplasticizer 2 (Tixo®) was added to the initial concrete mixes in order to reach the intended workability. Table 4.2 shows the final dosages of superplasticizer - obtained after trial and error - and their corresponding fresh concrete properties. The values of the workability and air

content are the average values of two measurements on two different batches of concrete. The standard deviations are also shown in Table 4.2.

Table 4.2: Dosages of superplasticizer and fresh concrete properties (n=2).

		RC I	RC II	CFC 20	CFC 30	CFC 40
PCE 2	[wt.%/B]	0.1	0	0.3	0.6	0.9
Slump	[mm]	50 ± 0	50 ± 0	40 ± 10	40 ± 30	50 ± 40
Flow	[mm]	380 ± 0	400 ± 10	370 ± 10	350 ± 20	350 ± 40
Air content	[%]	2.7 ± 0.2	1.5 ± 0.1	2.5 ± 0.4	2.2 ± 0.2	2.4 ± 0.1

No superplasticizer was needed for the reference mix with fly ash (RC II), since the spherical shape and glassy surface of the fly ash particles permit sufficient workability [200, 209]. The amount of superplasticizer of the CFC blended cement mixes, on the other hand, had to be increased for increasing amount of CFC, due to the high specific surface area of the CFC particles.

The slump values of all mixes are on the transition of slump class S1 (10-40 mm) to slump class S2 (50-90 mm). Although slump class S2 was targeted, the goal of reaching the same workability for all mixes has been achieved, since all mixes have similar slump values. For the flow, all values obtained are within the range of flow class F2 (350-390 mm). It should be noted that the standard deviations of the slump and flow values of the CFC mixes are remarkably higher than the standard deviations of the slump and flow values of the reference mixes. This is most probably due to the less 'stable' CFC mixes, due to higher dosages of superplasticizer compared to the reference mixes. Furthermore, the air content is almost constant for all mixes, except for the RC II mix with FA, which shows a significantly lower air content. This is the result of FA particles being finer than OPC particles [200] and the fact that no superplasticizer was added to RC II mix. After all, PCE superplasticizers are known to slightly contribute to the formation of air bubbles in fresh concrete [155, 172].

Hardened concrete properties

The results of compressive strength (f_c), dynamic E-modulus (E_d), flexural strength ($f_{ct,ft}$) and tensile splitting strength ($f_{ct,sp}$) after 7, 28, and 90 days, are shown in Fig. 4.1. After 7 days, the CFC blended cement mixes show a lower compressive strength compared to the OPC reference mix, with a decreasing strength for increasing amount of CFC. Compared to the Portland fly ash cement concrete, on the other hand, slightly higher compressive strength values are observed for the CFC 20 and CFC 30 mixes. After 28 days, the lower early-age strength of the RC II and CFC mixes is compensated by the pozzolanic

reactions taking place and the compressive strengths of blended cement mixes approximately reach the compressive strength of the OPC reference mix. Up to 90 days, compressive strength values further increase.

The results of the dynamic elastic modulus show a slightly lower stiffness for the CFC blended cement concretes, with decreasing E-modulus for increasing amount of CFC. The flexural and tensile splitting strength results show some inexplicable abnormalities. Furthermore, large standard deviations are observed in the results of the tensile splitting strength. These deviations can be explained by the difficulties associated with the test method, the indirect character of the flexural and tensile splitting strength tests, and the heterogeneity of the concrete specimens. Since the tests only considered initial testing, the batches were not remade. Overall, the results show trends similar to the compressive strength development.

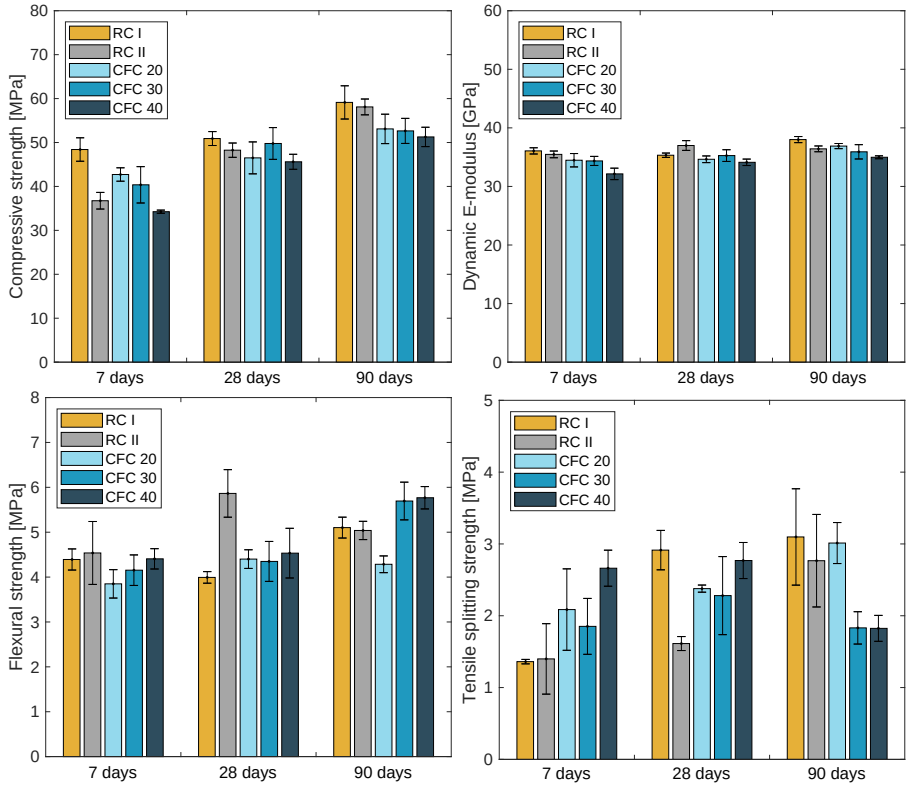

Figure 4.1: Mechanical properties of the initial concrete mix compositions (n=6 for f_c, E_d and $f_{ct,sp}$ and n=3 for $f_{ct,ft}$).

Conclusion

It is concluded that the addition of a superplasticizing admixture is needed in the CFC mixes, in order to compensate for the higher specific surface area of CFC and in order to meet predetermined workability requirements. Higher dosages of superplasticizer are needed for higher replacement ratios of CFC. Furthermore, the early-age strength development of CFC blended cement mixes is slower than the strength development of an OPC reference mix, but faster than the one of a Portland fly ash cement concrete. At later ages, the strength values of the CFC mixes catch up with those of the OPC reference mix and a strength class C30/37 is reached for the CFC blended cement mixes [75, 77]. The cement replacement ratio only had a minor impact on the strength and stiffness development, with slightly lower strength and stiffness values for higher replacement levels of CFC, especially at early ages.

4.2 Type and dosage of superplasticizer (SP)

In a next step, the influence of the type and dosage of superplasticizer was investigated. Since SCMs may affect the interaction between the superplasticizer and the cement [45], the compatibility of CFC with different types of superplasticizing admixtures was determined, in order to find the most optimal type of superplasticizer in combination with CFC.

Experimental program

Three different generations of superplasticizers were examined: modified lignosulfonates (LS), sulfonated naphthalene-based superplasticizers (SNF) and polycarboxylate ethers (PCE). Conventional superplasticizers such as LS (first generation) and SNF (second generation) disperse the cement particles due to electrostatic forces. The third and newest generation of superplasticizers (PCEs), on the other hand, disperse the cement particles partly due to electro-static repulsion, but primarily due to steric repulsion, by forming a steric obstacle to any direct inter-particle contact. The latter type of superplasticizer is therefore known to have higher efficiency than LS-based or SNF-based superplasticizers [170, 172].

Five commercial superplasticizers were examined and their chemical and physical properties were summarised in Tables 3.7-3.8. In order to check the compatibility of these superplasticizers with CFC, only the CFC 30 mix (see Table 4.1) was retained. The influence of the different types of superplasticizer on the

workability of the CFC 30 mix was examined by means of slump and flow tests, using batches of 25 litres of concrete. Later on, mechanical concrete properties were investigated, using batches of 140 litres of concrete.

Fresh concrete properties

The results of the workability tests, i.e. slump and flow, for different types and dosages of superplasticizer are shown in Fig. 4.2. Since all types of superplasticizer had a different dry matter content, the dosage of superplasticizer in Fig. 4.2 is expressed as wt.% solid content by mass of the binder.

For both traditional superplasticizers (LS and SNF), the targeted slump (S2) and flow (F2) class could not be reached without exceeding the maximal allowed dosage of superplasticizer recommended by the producer. In both cases, flow class F2 was reached once; however, in these cases, segregation has occurred and the concrete spread was not homogeneous. These results are therefore not further taken into account. The SNF superplasticizer appears to have an optimal working point at a dosage of 0.32 wt.% solid content by mass of the binder. At higher dosages, the workability again decreased.

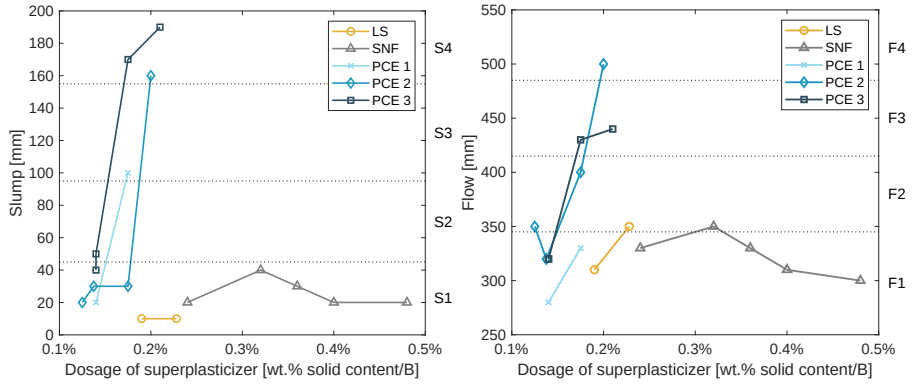

Figure 4.2: Slump and flow values of the CFC 30 mix for different types and dosages of superplasticizer (n=1).

For the PCE types of superplasticizer, the required slump (S2) and flow (F2) class could be reached in all cases, after some trial and error testing. It is observed from Fig. 4.2 that much lower dosages (solid content by mass of the binder) of superplasticizer were needed to reach the desired workability, compared to the traditional superplasticizers (LS and SNF). This strongly proves the higher efficiency of PCE superplasticizers, due to both electrostatic and steric repulsion mechanism. The fluidizing effect of the three different types

of PCE superplasticizers was slightly different; PCE 2 needed a higher dosage of superplasticizer in order to obtain the same workability in comparison with the two other PCE superplasticizers.

The results of the air content obtained on the 25 liter batches are summarised in Table 4.3. The results are the average values of the different batches made for the different types and dosages of superplasticizer. It can be concluded that the air content was quite constant for all types of superplasticizer, except for the SNF type superplasticizer, which shows a significantly lower air content. Superplasticizers based on naphthalene are known to slightly reduce the air content of a fresh concrete mix, while LS and PCE superplasticizers both promote the air bubble formation in concrete [155, 172].

Table 4.3: Air content of the CFC 30 mix for different types of superplasticizer.

		SNF (n=5)	LS (n=2)	PCE 1 (n=2)	PCE 2 (n=4)	PCE 3 (n=4)
Air content	[%]	1.9 ± 0.1	2.7 ± 0.1	2.0 ± 0.6	2.6 ± 0.4	2.5 ± 0.3

Due to the low workability achieved with the two traditional superplasticizers (LS and SNF), it was decided to only select one of these two types for mechanical testing. Since the concrete mixture with the SNF superplasticizer showed a low air content and almost reached the required workability, this composition was chosen for further testing. The final dosages of superplasticizer used for further mechanical testing are summarised in Table 4.4, together with their fresh concrete properties obtained on big batches of concrete (140 liters). Slump class S2 was reached for all mixes, except for the SNF concrete mix, as expected. However, only the PCE 2 concrete mix reached the required flow class F2, while for the other mixes, only flow class F1 was reached. The air reduction effect of SNF superplasticizers is also confirmed on the big batch of concrete.

Table 4.4: Final dosages of superplasticizer and fresh concrete properties of the CFC 30 mix for different types of superplasticizer (n=1).

		SNF	PCE 1	PCE 2	PCE 3
Dosage SP	[wt.% solid content/B]	0.32	0.18	0.15	0.16
Slump	[mm]	30	60	40	70
Flow	[mm]	310	340	350	330
Air content	[%]	1.5	2.6	2.2	2.3

Hardened concrete properties

The results of the mechanical properties testing of the concrete mixes with different types of superplasticizer are shown in Fig. 4.3. After 7 days, all PCE concrete mixes show almost equivalent compressive strengths and moduli of elasticity, while the concrete mix with the SNF superplasticizer shows lower strength. After 28 days, the compressive strength increases due to the pozzolanic reactions induced by CFC. The SNF concrete mix still shows significantly lower strength, while the PCE 1 concrete mix shows the highest compressive strength. This clearly shows that the SNF superplasticizer is less efficient. The targeted workability was not reached and, despite the lower air content, strength values could not catch up with those of the PCE concrete mixes. The lower compressive strength of the SNF concrete mix may be the result of an overdose of the

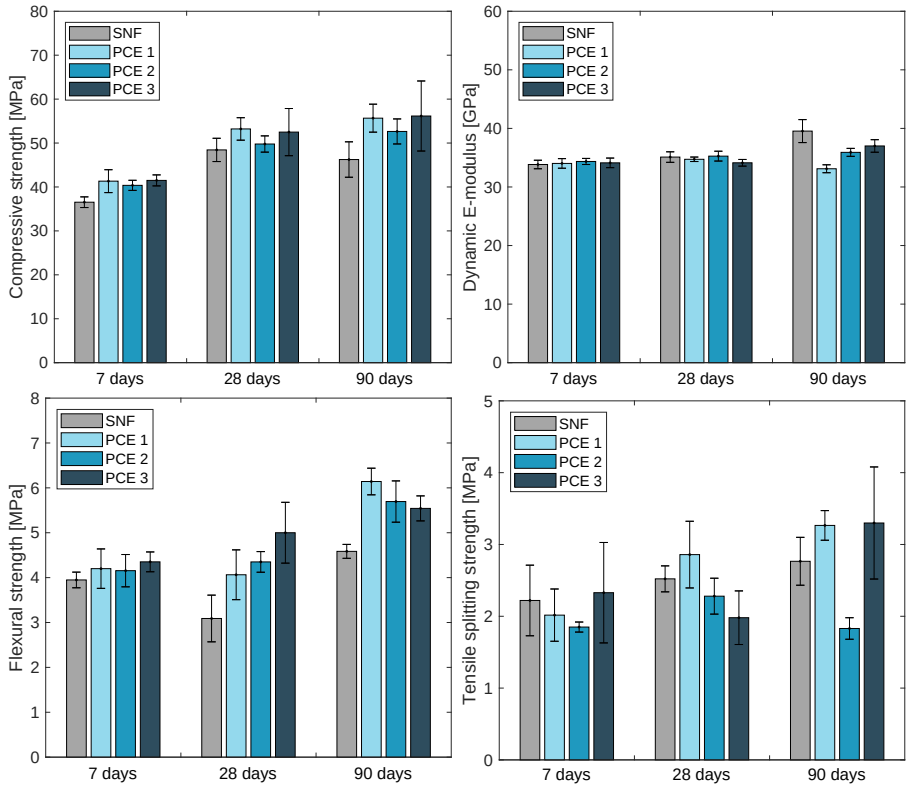

Figure 4.3: Mechanical properties of the CFC 30 mix for different types of superplasticizer (n=3 for f_c and E_d, n=4 for $f_{ct,ft}$ and n=8 for $f_{ct,sp}$).

superplasticizer, which is detrimental for the strength development. For the flexural and tensile splitting strength, overall the same phenomena as with the compressive strength are visible: an almost equal strength for all PCE concrete mixes and a lower strength for the concrete with SNF-based superplasticizer. Some abnormalities in the test results and large standard deviations of the tensile splitting strength results should be remarked.

Conclusion

It is concluded that PCE superplasticizers are most efficient in combination with CFC. The required slump class could be reached for all types of PCE superplasticizers, without exceeding the maximal dosage as prescribed by the producer. By using the traditional superplasticizers (LS and SNF), on the other hand, the required workability could not be reached without exceeding the maximal dosage and overdose of the superplasticizer led to lower strength values. All three PCE superplasticizers showed similar strength development and are therefore all suitable to be used in combination with CFC.

4.3 W/B ratio

The water-to-binder ratio of a concrete mix is an important factor controlling its mechanical and durability properties, and its final scope of application. High W/B ratios lead to, among others, better workability of the fresh concrete mix, lower strength and higher porosity of the hardened concrete; whereas low W/B ratios, on the other hand, lead to higher strengths and lower porosity, but also higher susceptibility to autogenous shrinkage. It is thus important to find the right balance between these properties in function of the envisaged application. Since the used W/B ratio of 0.5 is rather high and in order to broaden the range of applications for CFC concrete, it was investigated if the W/B ratio could be lowered by increasing the superplasticizer content, but keeping the same workability.

Experimental program

The influence of the W/B ratio on fresh and hardened concrete properties was investigated on the CFC 30 concrete mix (see Table 4.1) and PCE superplasticizer 3 (ViscoCrete®) was used for further testing. The results of W/B ratio 0.5 (or $W_{eff}/B = 0.47$) were compared with a lower W/B ratio of 0.45 (or $W_{eff}/B = 0.42$).

Fresh concrete properties

The amount of superplasticizer needed in the concrete mix with W/B ratio 0.45 in order to reach the targeted workability (slump class S2 and flow class F2), was investigated experimentally. After trial and error, the final dosage of superplasticizer was found to be 0.70 wt.% by mass of the binder and the corresponding fresh concrete properties are summarised in Table 4.5. The targeted slump class was reached and the maximal dosage of superplasticizer as prescribed by the producer was not exceeded. The targeted flow class, however, was not reached, but this was also the case for the CFC 30 mix with higher W/B ratio (see Table 4.4). The concrete mix was also found to be more sticky and less easy to handle, due to the higher amount of superplasticizer and lower water content.

Table 4.5: Final dosages of superplasticizer and fresh concrete properties of the CFC 30 mix for different W/B ratios (n=1).

		W/B = 0.5	W/B = 0.45
PCE 3	[wt.%/B]	0.45	0.70
Slump	[mm]	70	90
Flow	[mm]	330	330
Air content	[%]	2.3	2.2

Hardened concrete properties

The results of the hardened concrete properties of the CFC 30 concrete mix with W/B ratio 0.45 are shown in Fig. 4.4, compared to mechanical properties of the concrete mix with W/B ratio 0.5. Strength results after 7 days already show a significant strength increase for decreasing W/B ratio. Compared to the concrete mix with W/B = 0.5, the compressive strength was 10 MPa higher and flexural and tensile splitting strengths were 1.5 MPa higher for the concrete mix with W/B = 0.45, after 7 days. After 28 and 90 days, strength values further increase. The influence of the W/B ratio on the dynamic elastic modulus was marginal. The results were expected, since less water results in lower porosity and accordingly higher strength. Also here, abnormalities in the test results and large standard deviations of the tensile splitting strength results are observed. As explained before, this can be attributed to the heterogeneity of concrete and the indirect character of the flexural and tensile splitting strength testing methods.

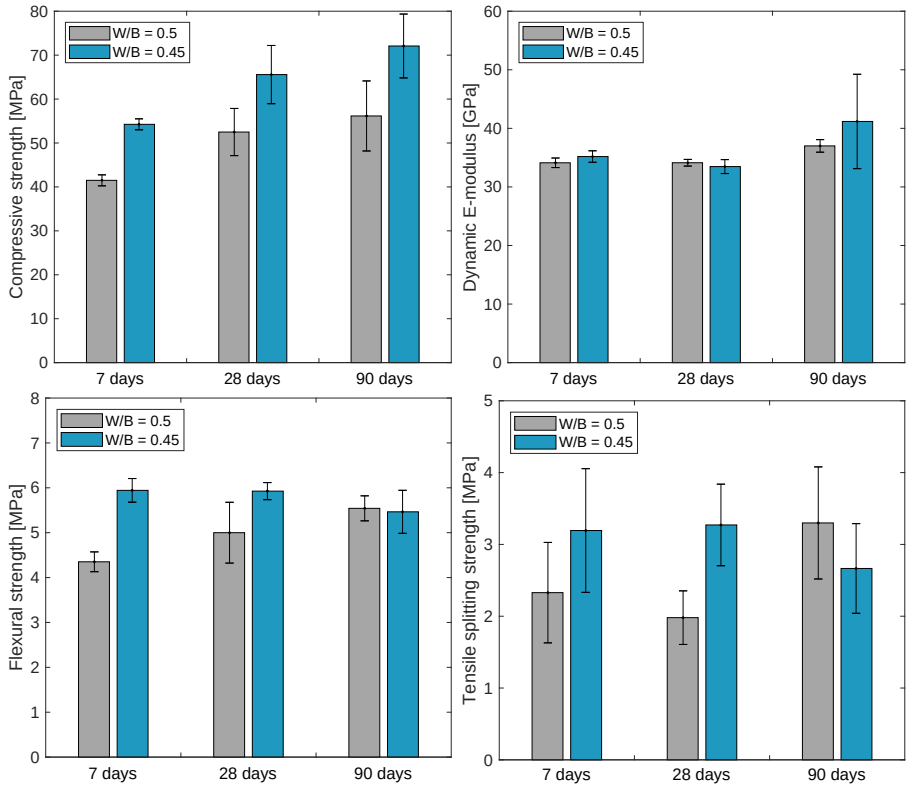

Figure 4.4: Mechanical properties of the CFC 30 mix for different W/B ratios (n=3 for f_c and E_d, n=2 for $f_{ct,ft}$ and n=4 for $f_{ct,sp}$).

Conclusion

The water-to-binder ratio of 0.5 could be reduced to 0.45 for the CFC 30 concrete mix, by increasing the amount of superplasticizer, without compromising on the workability. By lowering the W/B ratio, the strength of the concrete significantly increased. The fresh concrete mix with lower W/B ratio, however, was more sticky and less easy to handle.

4.4 Final concrete mix design

Since an important part of this PhD thesis focusses on shrinkage, especially autogenous shrinkage (which is more prominent/important at lower W/B ratios),

and since the targeted workability could still be reached for a W/B ratio of 0.45 (without exceeding the maximal dosage of superplasticizer), W/B ratio 0.45 ($W_{eff}/B = 0.42$) was used for all further experiments of the thesis.

In Section 4.3, the dosage of superplasticizer was already determined for the CFC 30 concrete mix with W/B = 0.45. The dosages of superplasticizer needed for the other mixes with lower W/B ratio were also determined experimentally, by means of fresh workability tests on concrete batches of 25 litres. After trial and error testing, the results as shown in Table 4.6 are found. Same as for the mixtures with W/B = 0.5, the least amount of superplasticizer was needed for the reference mix with FA and more superplasticizer was needed for increasing amount of CFC. Slump class S2 was reached for all concrete mixes, using the dosages of superplasticizer as shown in Table 4.6. Flow class F2, however, was only reached for the RC II mix, while for the other mixes only flow class F1 was reached. Considering Tables 4.4-4.6, it is thus concluded that flow class F2 could never be reached by using superplasticizer ViscoCrete®, while slump class S2 was always largely reached. On the other hand, by using superplasticizer Tixo®, flow class F2 was always reached, while slump class S2 was barely reached (see Tables 4.2 and 4.4). Both PCE superplasticizers, thus, have an opposite effect on the slump and flow of the fresh concrete mixes. For the results of the mechanical properties testing, reference is made to Chapter 5 (Section 5.3), where the strength and stiffness development of the final mix compositions are discussed thoroughly, with focus on the early-age behaviour.

Table 4.6: Final dosages of superplasticizer and fresh concrete properties for the different concrete compositions with W/B = 0.45 (n=2).

		RC I	RC II	CFC 20	CFC 30	CFC 40
PCE 3	[wt.%/B]	0.35	0.20	0.55	0.70	0.75
Slump	[mm]	70 ± 40	80 ± 0	80 ± 50	90 ± 0	70 ± 10
Flow	[mm]	340 ± 40	360 ± 50	310 ± 60	320 ± 20	270 ± 10
Air content	[%]	2.9 ± 0.5	2.4 ± 0.1	2.2 ± 0.8	2.3 ± 0.1	2.7 ± 0.1

For every concrete batch made for further testing, the workability, by means of a slump test, was measured. The mean values of the slump over all batches are given in Fig. 4.5. The error bars represent the standard deviation and n is the number of batches made for each composition.

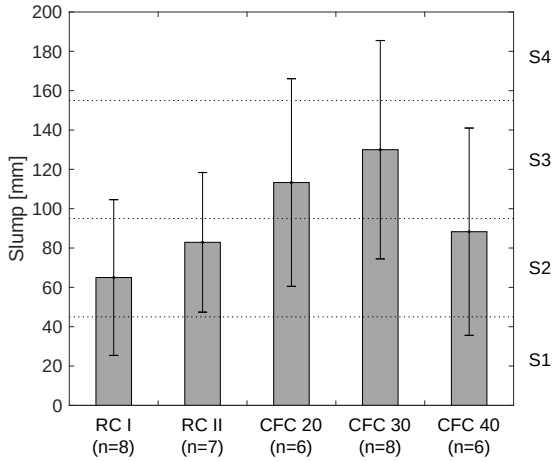

Figure 4.5: Average slump values of the different batches of concrete made (n = number of concrete batches).

Although the initial tests demonstrated that the targeted slump class S2 could be reached by using the dosages of superplasticizer as shown in Table 4.6, only three mixes reached slump class S2 on average over all batches (see Fig. 4.5). Furthermore the standard deviations of the slump values are rather high for all compositions. The reason for this behaviour is not completely clear. The differences in concrete volumes and concrete mixers used, are the most plausible explanation. However, no link can be found between the volume of concrete made and the corresponding slump class, neither between the concrete mixers used and the corresponding slump class. The higher dosages of superplasticizer used for the CFC mixes, resulting in less stable mixes, may explain the higher standard deviations and deviating slump values of the CFC mixes. Furthermore the environmental - and material temperatures were not strictly kept constant and were not measured either. However, several studies proved that the concrete temperature has no influence on the workability of a fresh concrete mix, as long as this temperature remains between 5°C and 30°C [172, 222]. In the authors opinion, these temperatures were never exceeded. Finally, the assumption of a constant water absorption by the aggregates (10 litres of water per m^3 of concrete) may also explain the differences in workability. It is thus concluded that no clear cause can be found for the deviating slump results, however, the differences in concrete mixers and volumes, and the rather high dosages of superplasticizer are the most plausible explanations. Further research regarding the influence of CFC on rheological properties will contribute to a better understanding of concrete workability.

4.5 Conclusion

In this chapter, the mix design optimisation of CFC blended cement concrete was presented, by studying the influence of three different concrete design parameters (cement replacement ratio, type and dosage of superplasticizer and W/B ratio) on fresh and hardened concrete properties.

It is concluded that the addition of a superplasticizer is necessary to contribute to the higher specific surface area of CFC, in order to meet predetermined workability requirements. Higher dosages of superplasticizer were needed for higher replacement ratios of cement by CFC. However, this led to more stickiness of the fresh concrete mixtures. PCE superplasticizers were found to be the most effective in combination with CFC and a slump class S2 could be reached for a W/B ratio of 0.45 without exceeding the maximal dosage of superplasticizer as prescribed by the producer. The addition of CFC led to a slower strength development compared to the OPC reference mix, but a faster strength development compared to the Portland FA reference mix.

The final concrete mix compositions used for further testing are summarised in Table 4.7.

Table 4.7: Final concrete mix compositions.

		RC I	RC II	CFC 20	CFC 30	CFC 40
Sand 0/4	[kg]	640	640	640	640	640
Gravel 4/14	[kg]	1225	1225	1225	1225	1225
CEM I 52.5N	[kg]	360	-	288	252	216
CEM II/B-V 42.5N	[kg]	-	360	-	-	-
CFC	[kg]	-	-	72	108	144
Water	[l]	162	162	162	162	162
ViscoCrete® (PCE 3)	[wt.%/B]	0.35	0.20	0.55	0.70	0.75
W/B	[-]	0.45	0.45	0.45	0.45	0.45
W_{eff}/B	[-]	0.42	0.42	0.42	0.42	0.42

Chapter 5

Early-age development

This chapter presents the influence of CFC on the early-age development of cement paste and concrete. First, the impact of CFC on the hydration process is investigated by a combination of isothermal calorimetry, X-ray diffraction and internal relative humidity measurement, to study the hydration kinetics, hydration products and RH development (Section 5.1). Secondly, the setting behaviour of CFC blended cement pastes and concretes is studied, by performing both traditional Vicat measurements, as well as ultrasonic wave measurements (Section 5.2). The third part of this chapter describes the early-age strength and stiffness development of CFC blended cement concretes (Section 5.3) and the fourth part investigates correlations between calorimetry results, ultrasonic measurements and strength results (Section 5.4). Afterwards, the temperature development is modelled and the existing mechanical properties model according to Eurocode 2 is assessed for CFC blended cement concretes (Section 5.5). Finally, the main conclusions are summarised (Section 5.6). *

5.1 Hydration process

A basic understanding of the hydration process and microstructural changes of cementitious materials is the key to the understanding of its properties and

*Parts of this chapter have been published in Van Bunderen, C. et al. Early-age hydration and autogenous deformation of cement paste containing flash calcined dredging sediments. *Construction and Building Materials* 200 (2019), 104-115 [224] and in Van Bunderen, C. et al. Experimental analysis and modelling of mechanical properties and shrinkage of concrete recycling flash calcined dredging sediments. *Cement and Concrete Composites* (under review).

performance [193]. The early-age (autogenous) deformations - an important focus of this thesis -, are strongly affected by the microstructural changes, since the main hydration processes are the driving mechanisms of these deformations. A schematic overview of the relationship between the hydration mechanisms (heat release, formation of hydration products and filling of capillary porosity) and the early-age deformations, is given in Fig. 5.1, which is a more complete version of the scheme developed by Carette et al. [47].

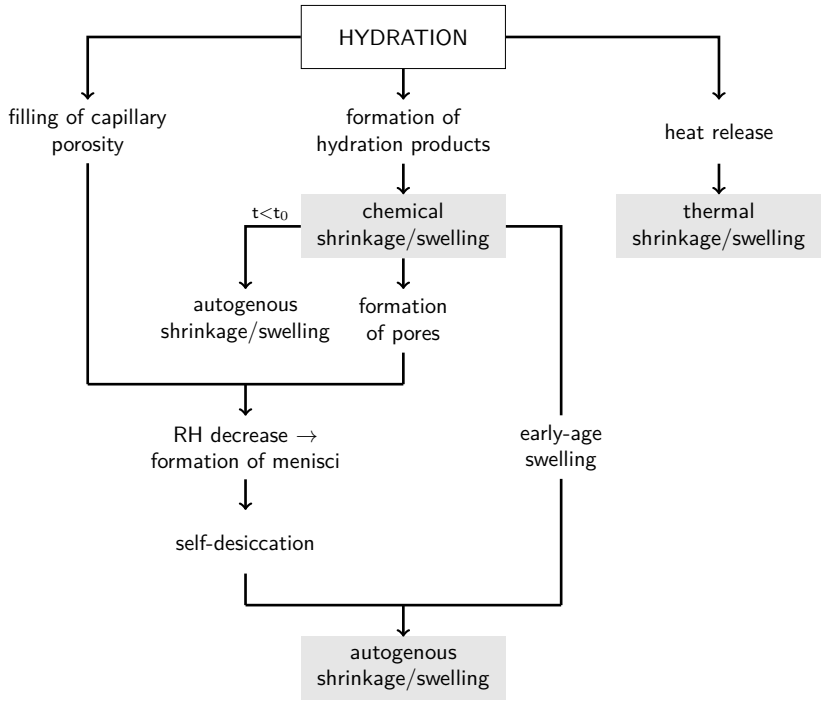

Figure 5.1: From hydration to early-age deformations.

Autogenous deformations are defined as external volume changes occurring without any moisture loss to the surrounding environment. The main driving mechanism behind the autogenous shrinkage is chemical shrinkage, caused by the formation of hydration products. Before setting ($t < t_0$), this chemical shrinkage will be completely converted into an external volume change, i.e. autogenous shrinkage. After setting, the chemical shrinkage will be translated into the formation of internal pores or in an early-age swelling (as a result of e.g. ettringite formation or CH growth). At the start of hydration, the capillary pores are filled with water. As the hydration continues, water is consumed, the internal relative humidity drops and water-air menisci are formed. This results in self-

desiccation. The self-desiccation and an eventual early-age swelling are the main driving mechanisms of autogenous shrinkage after setting [21, 22, 47, 131, 132]. Furthermore, the hydration is accompanied by heat release, which can cause thermal deformations.

In this section, heat release, formation of hydration products and internal RH development (filling of capillary porosity), are analysed, to better understand and evaluate the role of CFC in concrete properties, that are discussed in the next chapters.

5.1.1 Heat of hydration

As the cement hydration reaction is an exothermic reaction, measurement of the heat released during the hydration is typically used to study the reaction kinetics. The hydration kinetics of the CFC blended cements were studied by isothermal calorimetry on cement paste and concrete samples. Both the influence of the partial replacement of cement by CFC and the influence of the addition of superplasticizer are investigated.

Cement paste

Influence of CFC The heat flow and cumulative heat development of the different cement paste samples without superplasticizer are shown in Fig. 5.2 (the asterix* represents cement paste mixes without superplasticizer). The results are normalised to the initial Portland cement content, in order to cancel out the dilution effect and to distinguish OPC and CFC hydration. The exact amount of FA in the RC II mix is not known, since Portland fly ash cement (CEM II/B-V) is used. An average FA content of 28% (according to the datasheet of the CEM II/B-V, see Appendix A) is therefore used to normalise the results of the RC II mix to the OPC content. An increased heat flow over both the induction and main hydration period is observed for higher replacement ratios of cement by CFC. This is mainly attributed to the filler effect, and partly to the early pozzolanic reaction of CFC, as discussed in [207]. A slight shortening of the induction period and elongation of the main hydration period are also observed for the CFC blended cement mixes, compared to the OPC reference mix. Furthermore, the main hydration peak is slightly accelerated by the presence of CFC. The increased heat flow of the CFC blended cement mixes obviously translates in a higher cumulative heat for higher replacement ratios of cement by CFC for equal OPC content. The use of fly ash blended cement also results in an increased and accelerated main hydration peak, even more prominent compared to CFC blended cement. This can also be attributed

to the filler effect of FA, providing additional surfaces, accelerating nucleation and formation of cement hydrates [156].

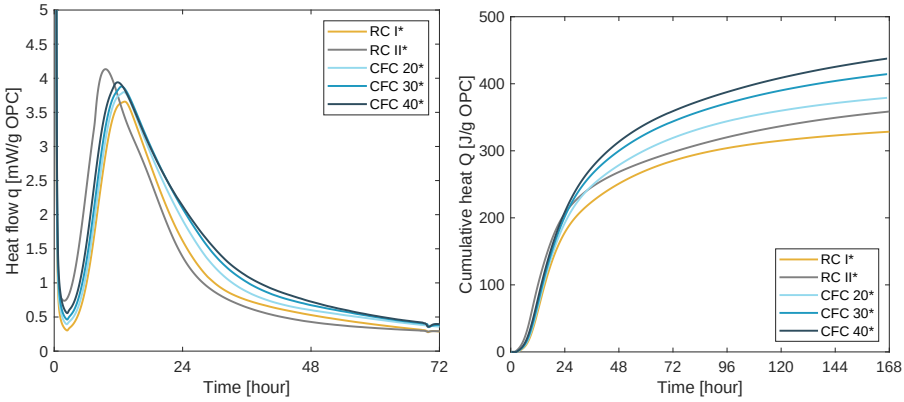

Figure 5.2: Heat flow (left) and cumulative heat (right) of the different cement paste mixes without superplasticizer, normalised to the OPC content (n≥2).

Influence of superplasticizer Since the addition of a superplasticizer is necessary in the CFC mixes (in order to counterbalance the effect of the higher specific surface area of CFC) and since superplasticizers are known to delay the cement hydration process, the influence of the admixture addition was investigated. Fig. 5.3 compares the heat flow and cumulative heat of all cement paste mixes with (full lines) and without (dotted lines) the addition of superplasticizer. The heat flow measurements depicted in Fig. 5.3 clearly show that the addition of superplasticizer produces a retardation of the cement hydration, as observed by a prolonged induction period. The cement hydration retardation effect of PCE superplasticizers is known to be mainly due to the adsorption of superplasticizer molecules on the surface of hydrating cement grains and hydration products, hindering the diffusion of water and ions near the cement-solution interface [193, 239]. Furthermore, a small decrease in the hydration peak and a slight shortening of the main hydration period are also observed as a result of the superplasticizer addition. This translates in a slight decrease in total cumulative heat after 7 days and can be explained by the impact of PCE on depressing the nucleation of hydrates during the hydration period [239]. Overall, these side-effects do not affect the kinetics and mechanisms of hydration in a very negative way. Since the dosages of superplasticizer are rather small, the retardation of the cement hydration is limited. In terms of hydration kinetics, the addition of a superplasticizer is therefore proven to be a viable option to improve CFC concrete properties.

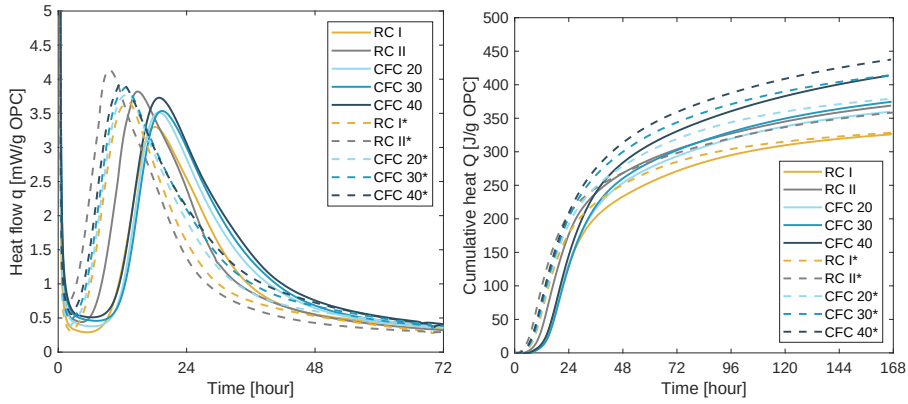

Figure 5.3: Heat flow (left) and cumulative heat (right) of the different cement paste mixes with (full lines) and without (dashed lines) superplasticizer, normalised to the OPC content.

Concrete

The results of the calorimetry measurements of the concrete samples are shown in Fig. 5.4, normalised to their initial OPC content. Generally, the heat flow and cumulative heat of the concrete mixes follow the same trend as the cement paste results. Increased heat flows are observed for the FA and CFC blended cement concretes, due to the filler effect and early pozzolanic reaction, and superplasticizer addition led to cement hydration retardation. However, also some differences are observed between the cement paste and concrete samples. The main hydration peak and final cumulative heat values are sligthly higher for the concrete samples, in comparison with the cement paste samples, and the retardation effect of the superplasticizer is more prominent for the concrete mixes. In order to quantitatively compare these observations, the corresponding key values are summarised in Table 5.1. The differences between the amplitude of the main hydration peaks (q_{max}) are negligible for all mixes, except for the RC II mix. The differences between the time of the main hydration peak and differences between the cumulative heat values after 7 days (Q_{max}), on the other hand, are more prominent, especially for the RC II mix and for mixes containing more CFC and superplasticizer. Both the influence of the aggregates as well as the differences in energy between the cement paste and concrete mixers can explain this behaviour. The presence of aggregates in cement paste results in the formation of an interfacial transition zone (ITZ), a region of perturbed cement paste around the aggregate. The ITZ typically contains small, and thus less, cement grains, resulting in a higher water-to-cement ratio in this zone,

and lower water-to-cement ratio (up to 0.05 less) in the 'bulk' cement paste zone [195]. Lower water-to-binder ratios result in increased early-age hydration kinetics and decreased cumulative heat values [193]. This effect can possibly explain the lower cumulative heat values and earlier occurring hydration peaks of the reference concrete mixes, compared to the cement paste mixes. However, this explanation is not valid for the CFC blended cement mixes. The CFC concrete mixes, on the other hand, show higher cumulative heat values and their main hydration peak is more delayed, compared to the reference cement paste mixes. The higher amounts of superplasticizer are most likely to explain this behaviour, however, the exact mechanisms are not clear.

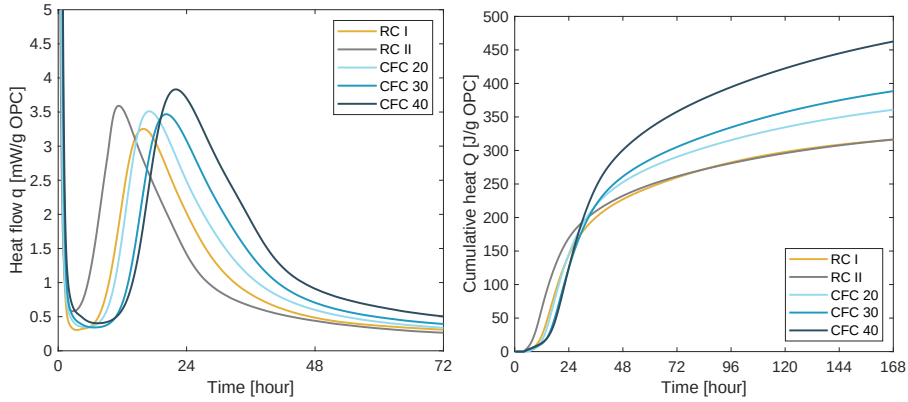

Figure 5.4: Heat flow (left) and cumulative heat (right) of the different concrete mixes with superplasticizer, normalised to the OPC content (n=1).

Table 5.1: Comparison of main calorimetry characteristics between cement paste and concrete samples.

	q_{max} [mW/g OPC]		$t(q_{max})$ [h]		Q_{max} [J/g OPC]	
	paste	concrete	paste	concrete	paste	concrete
RC I	3.31	3.25	17.89	15.93	325.60	316.28
RC II	3.94	3.59	14.04	11.32	368.34	316.37
CFC 20	3.53	3.51	18.78	17.03	359.49	360.75
CFC 30	3.53	3.47	19.43	20.20	374.00	388.51
CFC 40	3.78	3.83	18.54	22.02	413.49	462.59

5.1.2 Hydration products

The hydration product assemblages of the RC I and CFC 30 cement paste mixes were characterised in detail over a hydration period of 3 days up to 182 days in [207]. It was concluded that the pozzolanic reaction of CFC consumed portlandite and produced additional ettringite and AFm phases. Since the focus of this thesis is on the early-age behaviour, additional XRD measurements were carried out on cement paste samples at 10, 20, 30, 40, 50 and 60 hours of hydration. Fig. 5.5-5.7 show the XRD patterns of the RC I, RC II and CFC 30 mixes, respectively. The patterns of all mixes show the disappearance of the clinker minerals and the appearance of the hydration products over time. The main hydration products observed are ettringite and portlandite. The formation of AFm phases is also noticed for the RC II and CFC 30 mixes after about 50-60 hours. These early-age AFm phases are a solid solution of hemicarbonate (AFm-CO_3) and OH^- substituted monosulphate (OH-AFm) [158]. Hydroxy-AFm phases are often formed during the early reaction stage, but generally decompose to hydrogarnet and portlandite at later ages [20, 158]. Furthermore quartz and feldspars components remained present in the CFC 30 sample, as inert components of the filter cakes, and typical FA phases (quartz and mullite) are visible in the RC II mix. Overall, no big differences in hydration product assemblages are observed between the three mixes.

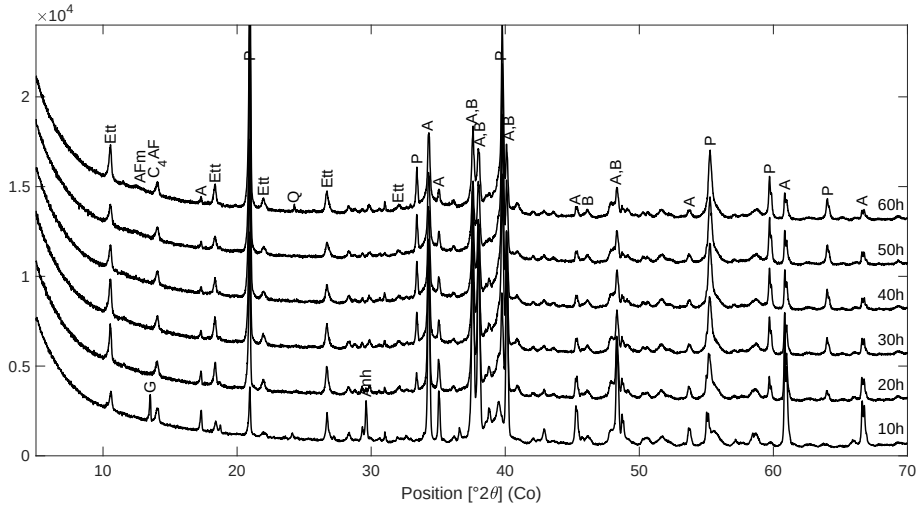

Figure 5.5: XRD patterns of the RC I cement paste mixes at early ages. The main peaks of ettringite (Ett), portlandite (P), alite (A), belite (B), gypsum (G), anhydrite (Anh), quartz (Q), calcium aluminoferrite (C_4AF) and AFm phases (AFm) are indicated.

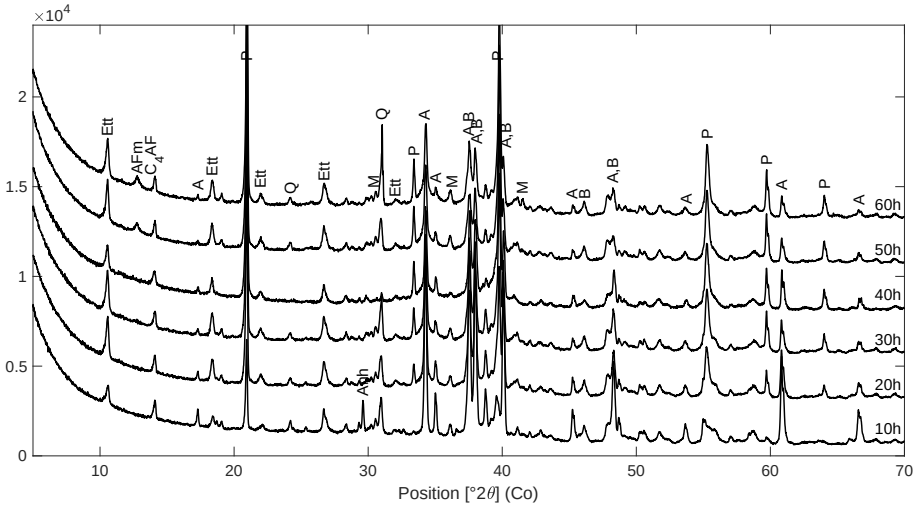

Figure 5.6: XRD patterns of the RC II cement paste mixes at early ages. The main peaks of ettringite (Ett), portlandite (P), alite (A), belite (B), anhydrite (Anh), quartz (Q), mullite (M), calcium aluminoferrite (C_4AF) and AFm phases (AFm) are indicated.

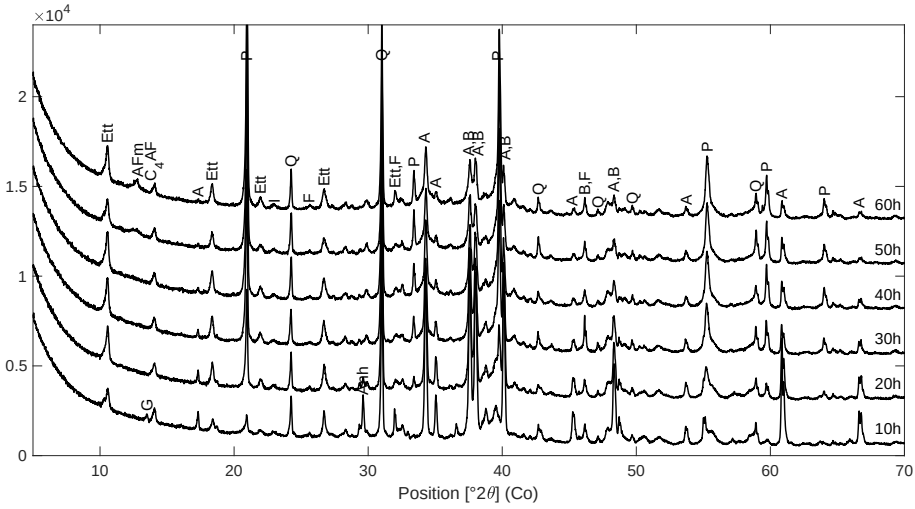

Figure 5.7: XRD patterns of the CFC 30 cement paste mixes at early ages. The main peaks of ettringite (Ett), portlandite (P), alite (A), belite (B), gypsum (G), anhydrite (Anh), quartz (Q), feldspars (F), calcium aluminoferrite (C_4AF) and AFm phases (AFm) are indicated.

In order to quantify the evolution of the individual phases during the early cement hydration, the Rietveld method was used to analyse the XRD measurements [193]. Fig. 5.8 shows the evolution of the consumption of the clinker minerals and formation of hydration products at early ages, for the RC I, RC II and CFC 30 mixes, normalised as per initial OPC content. The consumption of alite (C_3S) and belite (C_2S) and respective formation of portlandite (CH) and amorphous phases (mainly C-S-H) are depicted on the upper figures. The consumption of aluminate (C_3A) and aluminoferrite (C_4AF) and respective formation of ettringite (Ett) and hemicarbonate (Hc) are depicted on the lower figures.

The calcium silicates hydration at early ages is mainly governed by the hydration of alite (the main component of OPC), responsible for the strength development. This is observed by a strong decrease of the C_3S content, while the C_2S content remains stable during the first three days of hydration. The hydration of belite only starts at later ages, from 14 days onwards [207]. The hydration of alite results in a significant increase in the amount of portlandite and C-S-H (amorphous phases) formed. At early ages, FA and CFC contribute to the formation of additional hydrates (portlandite and amorphous phases), compared to the RC I reference mix, mainly due to the additional surface for hydration (filler effect) and the increased effective W/B ratio (dilution effect) [64, 207]. After 60 hours, the portlandite content is still increasing, indicating that the pozzolanic reaction has not yet started and does not compensate for the filler effect at that time.

The hydration of the aluminate phases at early ages is mainly governed by the hydration of C_3A. C_4AF reacts more slowly and contributes to later age strength development of cement based materials. During the early ages, ettringite is formed as main hydration product, and the presence of FA and CFC increases the amount of ettringite per 100 g OPC. Upon sulphate depletion, ettringite is converted into AFm phases. This is observed as a decrease in the ettringite content (starting from 30-40 hours) and the formation of hemicarbonate (starting from 40-50 hours). The increased ettringite content and the formation of hemicarbonate instead of monosulphate in the CFC 30 mix are the result of the increased total sulphate and carbonate level. Some residual calcite remained present in CFC after flash calcination and anhydrite was formed from pyrite oxidation in the presence of free lime [205, 207]. The higher amounts of ettringite and hemicarbonate in the RC II mix with fly ash can be attributed to the presence of anhydrite, formed from the reaction of CaO, SO_2 and O_2 in the furnace or flue, and the presence of alkali sulphates ($(N,K)_2SO_4$) in fly ash [200, 209]. Furthermore, since hemicarbonate is formed, the decomposition of ettringite to monosulphate upon sulphate depletion is prevented, as hemicarbonate is more stable than monosulphate. Stabilisation

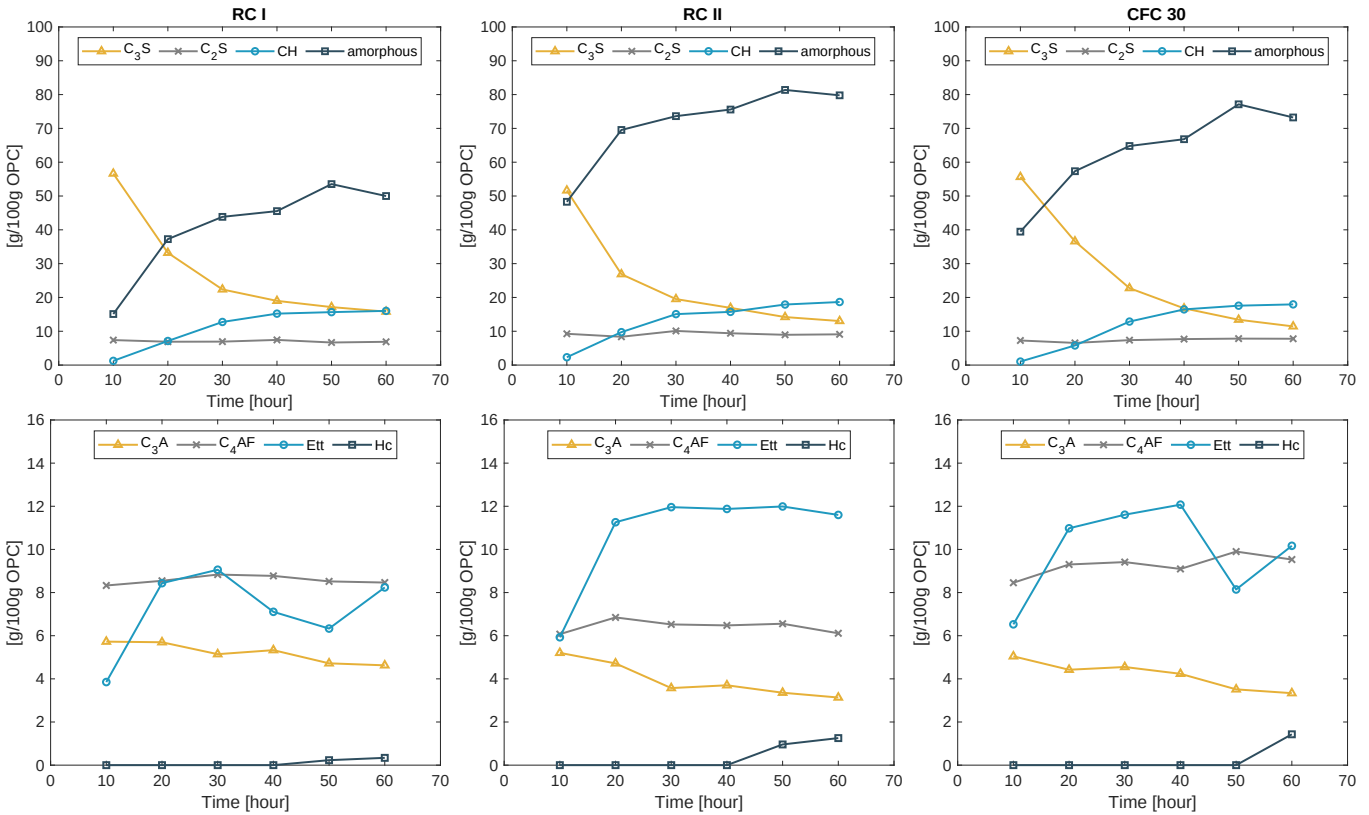

Figure 5.8: Evolution of the consumption of the clinker minerals (C_3S, C_2S, C_3A, C_4AF) and formation of hydration products (portlandite (CH), amorphous phases, ettringite (Ett) and hemicarbonate (Hc)), for RC I, RC II and CFC 30 cement paste mixes at early ages, normalised to the initial OPC content.

of the voluminous ettringite instead, leads to an increase of the total solids volume of hydration products [64, 151, 207].

It is thus concluded that the hydration products of the CFC cement paste mix, formed at early ages, are similar to the hydration products of the reference mixes. Incorporation of CFC results in additional formation of portlandite and amorphous phases per g OPC. Furthermore, the presence of CFC increases the amount of ettringite per g OPC, due to the increased total sulphate and carbonate level, and the formation of hemicarbonate in the CFC mix leads to stabilisation of the voluminous ettringite.

5.1.3 Internal relative humidity development

The development of the internal relative humidity (RH) in the cement paste samples was measured as from final setting and the results are shown in Fig. 5.9. The measured RH drop is the combination of the RH drop attributed to the dissolution of salts in the pore solution (RH_S) and the RH drop due to menisci formation or self-desiccation (RH_K) [54, 153]:

$$RH = RH_S \cdot RH_K \tag{5.1}$$

The initial RH drop (RH_S) is the result of the water activity depression caused by the dissolved ions in the pore solution. Mainly the alkali hydroxides present in the pore fluid, rather than the calcium ions, whose solubility is depressed by the presence of the former, are responsible for this RH drop. RH_S can be estimated by Raoult's law [54, 153]:

$$RH_S = \frac{n_{H_2O}}{n_{solution}} \tag{5.2}$$

with n_{H_2O} the number of moles of water in the pore solution and $n_{solution}$ the total number of moles in the solution. It should be remarked that this initial RH drop due to dissolution of salts does not lead to any deformations, since no capillary pressures are built up [54]. The measured RH drop is depicted in Fig. 5.9 (left) and the absolute values of the RH drop due to salt dissolution are summarised in Table 5.2. It can be seen that the RH drop due to dissolved salts is the highest for the RC II mix with fly ash and increases for increasing amount of CFC. The higher sodium - and potassium oxide content of FA and CFC, as shown in Tables 3.1 and 3.4, can explain the higher dissolution rate of Na^+ and K^+ ions in the pore solution and the larger initial RH drop.

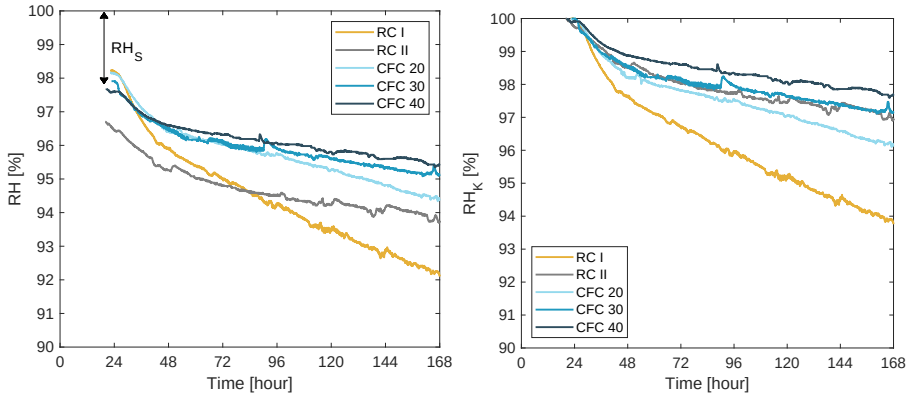

Figure 5.9: Internal RH development of the different cement paste samples, as from final setting: measured RH (left) and RH due to menisci formation (RH_K) (right) (n=2).

Table 5.2: RH drop due to the dissolution of salts (RH_S).

	RH_S
RC I	1.77 %
RC II	3.30 %
CFC 20	1.83 %
CFC 30	2.09 %
CFC 40	2.31 %

Fig. 5.9 (right) shows the RH drop due to the formation of menisci and thus due to self-desiccation (RH_K). After final setting, chemical shrinkage is translated into the formation of pores, which empty as the hydration continues, resulting in a decrease in RH and the formation of water-air menisci. This RH drop is consequently attributed to self-desiccation of the cement paste and can be described using the Kelvin's law [54, 153]:

$$RH_K = \exp\left(-\frac{2 \cdot \gamma_w \cdot M_w \cdot \cos\theta}{\rho_w \cdot r \cdot RT}\right) \tag{5.3}$$

where γ_w is the surface tension of water, M_w is the molecular weight of water, θ the angle between the water surface and the pore wall, ρ_w is the density of water, r is the Kelvin radius or radius of the capillary pores, R is the ideal gas constant and T is the temperature. It is observed from Fig. 5.9 (right) that the OPC reference mix shows the highest drop in internal relative humidity up to 7 days (93.8%). The blended cement mixes show a much lower decrease in RH, with decreasing RH drop for increasing amount of CFC. The dilution effect and

higher effective water-to-cement ratio can explain this behaviour. The results suggest the blended cement mixes to encounter less autogenous shrinkage due to self-desiccation, compared to the OPC reference mix.

5.2 Setting behaviour

5.2.1 Vicat setting time

The results of the Vicat setting time measurements are shown in Fig. 5.10, both for cement paste mixes with and without addition of superplasticizer. It is observed that the presence of FA or CFC has almost no influence on the initial and final setting time (see Fig. 5.10 (left)). The addition of superplasticizer, on the other hand, delays both the initial and final setting time, due to the retardation effect on the cement hydration. Higher dosages of superplasticizer also result in more delay. For the RC II mix with superplasticizer (0.2 wt.% SP/B), the initial and final setting times were respectively extended by 2.7 hours and 4.4 hours, while for the CFC 20 mix with superplasticizer (0.55 wt.% SP/B), the initial and final setting time were extended by 5.5 hours and 7.0 hours, respectively.

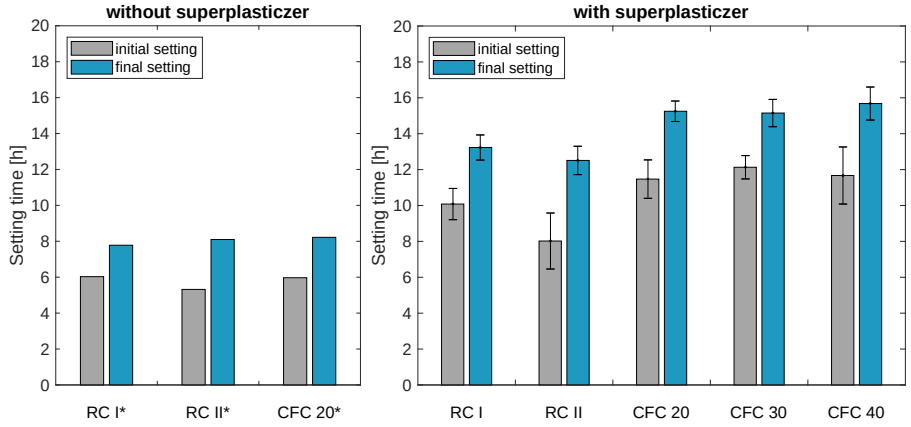

Figure 5.10: Vicat setting times of the different cement paste mixes without (left) (n=1) and with (right) (n≥2) superplasticizer.

5.2.2 Ultrasonic measurements

Ultrasonic measurements were performed both on cement paste and concrete samples. P-waves were used to study the early-age ultrasonic behaviour of the cement paste samples, while both P- and S-wave were used to study the early-age ultrasonic behaviour of the concrete samples.

Cement paste

Development of UPV curves The general development of the P-wave velocity in cement paste mixes, determined with the UltraTest device, is explained using the results of the RC I reference mix without superplasticizer. The P-wave velocity (V_P) and corresponding derivative of the P-wave velocity are shown in Fig. 5.11 (left). The P-wave velocity curve is composed of two S-shaped functions, resulting in two peaks in the derivative of the velocity curve. This is in contrast with the general description of the P-wave velocity in literature (see subsection 2.3.2), which only shows one S-shaped curve. The deviating development of the P-wave velocity is discussed in detail below. Correlations are also made with the temperature development inside the cement paste sample and the results of the temperature evolution are shown in Fig. 5.11 (right).

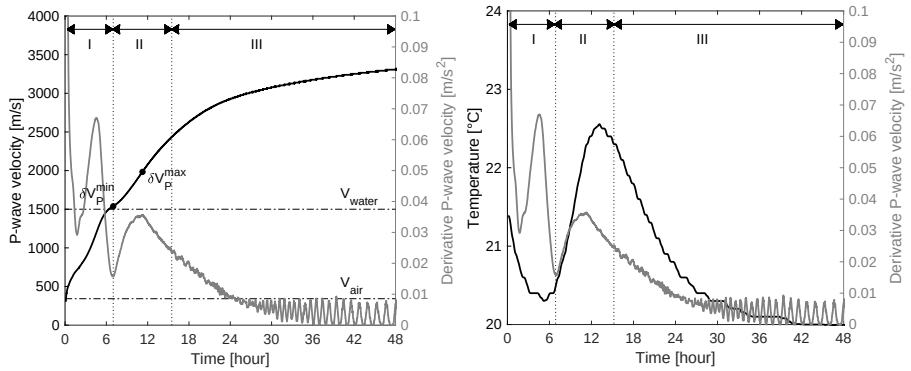

Figure 5.11: General development of the P-wave velocity and derivative of the P-wave velocity (left) and development of the temperature and derivative of the P-wave velocity (right) in cement paste, with corresponding stages (I: dormant period, II: acceleration period, III: deceleration period), P-wave velocity inflection points (δV_P^{min} and δV_P^{max}) and P-wave velocity values in water and air (V_{water} and V_{air}).

The initial value of the P-wave velocity equals approximately 300 m/s. This value is close to the values found in the literature [54, 219, 238]. However, for completely de-aerated fresh cement paste, values around 1500 m/s (i.e. P-wave velocity in water) are reported [144, 236, 242]. This suggests that the observed low initial value of the P-wave velocity is caused by air entrapped in the fresh cement paste, due to incomplete removal of air bubbles [54]. However, the value of the initial P-wave velocity is even lower than the P-wave velocity in air ($\pm$ 342 m/s). Two different causes for this lower velocity have been reported in literature: (1) an elongation of the length of the wave-path due to the suspended cement particles in the fresh cement paste [218] and (2) air entrapped in the fresh cement paste due to a lot of tiny air bubbles entrapped during mixing or due to a certain amount of air bubbles in the mixing water [140, 187, 218].

During the dormant period (I), there is a steep increase in the P-wave velocity (from $\pm$ 300 m/s to $\pm$ 1500 m/s), while there is not yet an increase in temperature. This initial velocity increase is caused by the formation of hydration products with no or little influence on the penetration resistance (e.g. ettringite) and by internal settling due to gravity forces [49, 54, 218]. Compared to the literature [49, 236, 238], the initial P-wave velocity increase observed in Fig. 5.11 is much steeper. However, this behaviour was also observed by Trtnik et al. [218, 217] and Chen et al. [54]. The steep increase (and the resulting initial peak in the derivative of the P-wave velocity) can be attributed to the high amount of entrained air in the specimen due to incomplete compaction. During the dormant period, this entrained air is removed by internal settling and formation of hydration products, resulting in higher P-wave velocities. At the end of the dormant period, the P-wave velocity in water (1500 m/s) is reached and this moment corresponds very well with the first inflection point of the curve (δV_P^{min}). The influence of the entrapped air in the fresh cement paste mix is, thus, only limited to the dormant period.

During the acceleration period (II), both the P-wave velocity and temperature increase significantly, and the temperature increase corresponds very well with the second peak of the derivative of the P-wave velocity. This stage corresponds to a period of intense hydration and is characterised by the rapid formation of C-S-H, CH and ettringite. The connected solid phase starts to develop and setting of the material takes place. The second inflection point of the P-wave velocity curve (δV_P^{max}) corresponds to the percolation threshold or the start of the development of penetration resistance [54, 218, 236]. During the deceleration period (III), the fast increase in P-wave velocity slows down and the temperature starts to decrease. In this period, hydration products with different physical properties are formed and the threshold status of the solid structure is achieved [54, 218, 236].

Influence of CFC The effect of CFC on the P-wave velocity is shown in Fig. 5.12 (left). It is observed that all curves develop in the same way and two S-shaped functions are observed for all mixes. During the early ages (dormant and acceleration period) the difference in P-wave velocity between the different compositions is marginal. However, from the start of the deceleration period, the OPC reference mix reaches higher P-wave velocity values, while the blended cement mixes show lower values. After 7 days, the mixes with CFC also show slightly lower P-wave velocities, with decreasing velocity for increasing replacement level of CFC.

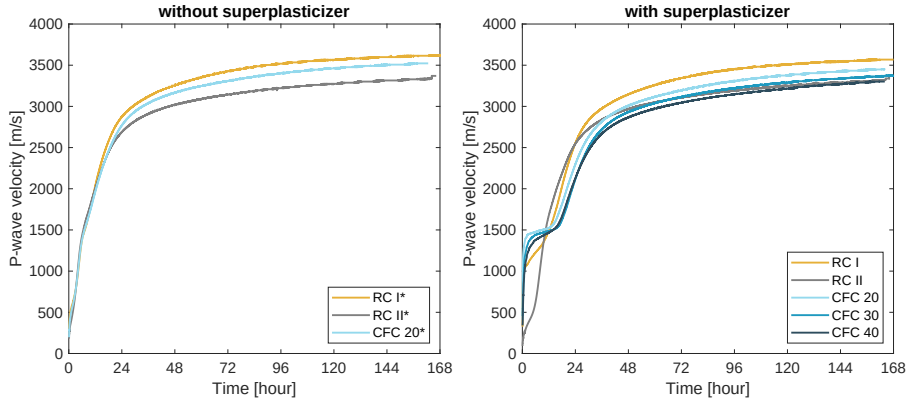

Figure 5.12: Influence of CFC (left) and combined influence of CFC and superplasticizer (right) on the P-wave velocity (n≥2).

However, when considering the cement paste mixes with superplasticizer, as shown in Fig. 5.12 (right), the early-age P-wave velocity development is strongly affected. The values of the P-wave velocities of the mixes with superplasticizer after 7 days, on the other hand, are comparable with those of the mixes without superplasticizer. The influence of superplasticizer on the P-wave velocity is thus limited to the early ages and will be discussed in the next paragraph.

Influence of superplasticizer The addition of a PCE superplasticizer strongly affects the development of the P-wave velocity at early ages. Fig. 5.13 shows the P-wave velocity and the derivative of the P-wave velocity for three OPC reference mixes with different amounts of superplasticizer: 0 wt.%, 0.35 wt.% and 0.7 wt.% per mass of the binder content. During the very early ages, the P-wave velocity of the mixes with superplasticizer immediately increases to a value of about 1000 m/s. As a result, the first peak of the derivative of the P-wave velocity, attributed to the removal of entrapped air in the specimen, disappears. The initial increase in P-wave velocity for the mixes with superplasticizer is

possibly the result of less air entrainment in the cement paste mixture, because of the more workable mixture, resulting in higher initial P-wave velocities. After this steep velocity increase, a long plateau is observed for the mix with the highest amount of superplasticizer. An elongation of both the dormant and acceleration period is visible as a result of the cement hydration retardation effect of the PCE superplasticizer [217]. From 48 hours on, the influence of the superplasticizer is less visible, and almost the same P-wave velocity values are attained for the three mixes with different amounts of superplasticizer. The influence of the superplasticizer, thus, disappears during the deceleration stage.

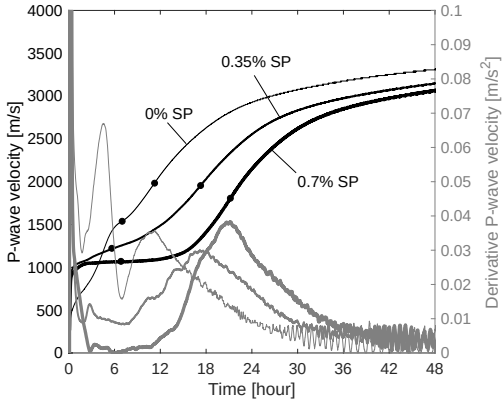

Figure 5.13: Effect of superplasticizer (0 wt.%, 0.35 wt.% and 0.7 wt.% per mass of binder content) on the P-wave velocity and derivative of the P-wave velocity for an OPC reference mix (n≥2).

Elastic properties derivation The dynamic elastic modulus (E_d), dynamic bulk modulus (K_d) and dynamic shear modulus (G_d) of the different cement paste mixes can be calculated using Eq. 2.8-2.11 and the results are shown in Fig. 5.14. Since only P-waves are used, a constant Poisson's ratio (ν_d) of 0.22 is assumed for all cement paste mixes. The relationship between the moduli of the different mixes corresponds very well to the relationship of the P-wave velocities of the cement paste mixes. After 7 days, the highest E_d, K_d and G_d values are observed for the RC I reference mix and their values gradually decrease for higher replacement levels of cement by CFC. The influence of the superplasticizer at early ages is also strongly visible in the results of the dynamic moduli and their development at early ages is thus distorted. Furthermore, the assumption of a constant Poisson's ratio also overestimates the dynamic elastic modulus at early ages.

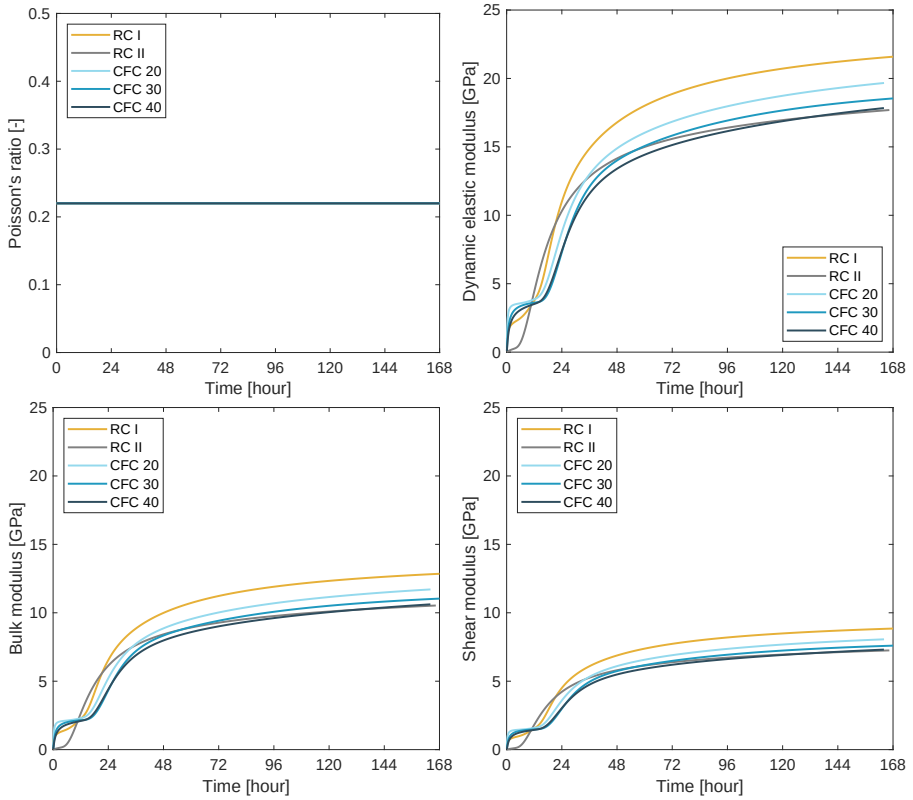

Figure 5.14: Elastic properties (ν_d, E_d, K_d and G_d) of the different cement paste mixes with superplasticizer, calculated from the P-wave velocities.

Setting time determination The different setting time criteria existing in literature were already discussed in subsection 2.3.2. In order to accurately determine the different inflection points on the velocity curves, smoothing of the curves by mathematical modelling is recommended. Different mathematical functions to model S-shaped curves exist in literature. Appendix D explains these different mathematical functions and compares them with each other. The tri-exponential function (see Eq. 5.4) was concluded to be the best fitting function (based on the criteria of the lowest RMSE) for the P-wave velocity at early ages, provided that fitting of the experimental results was done only up to 48 days for the cement paste mixes without superplasticizer.

$$V_P(t) = \sum_{i=1}^{3} a_i \cdot \exp\left(-\left(\frac{b_i}{t}\right)^{c_i}\right) + d \tag{5.4}$$

The modelling of the velocity curves allows accurate determination of the different inflection points and the results of the derivatives of the modelled P-wave velocities are shown in Fig. 5.15. The results of the initial and final setting times, determined according to the methods described in subsection 2.3.2, are shown in Table 5.3, both for the mixes with and without superplasticizer.

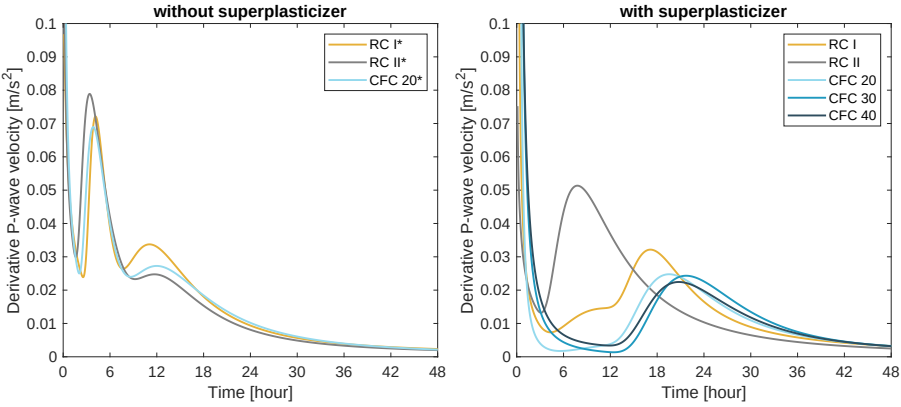

Figure 5.15: Smooth derivative of the P-wave velocity curves for the cement paste mixes without (left) and with (right) superplasticizer.

Table 5.3: Initial and final setting times of the different cement paste mixes with and without superplasticizer, determined from UPV measurements.

	initial setting [h]		final setting [h]		
	$t(\delta V_P^{min})$	$t(V_P$=1500 m/s)	$t(\delta V_P^{max})$	$t(V_P$=1650 m/s)	$t(\delta E_d^{max})$
RC I*	7.68	7.20	11.07	8.73	12.32
RC II*	9.22	6.57	11.70	7.97	12.88
CFC 20*	8.63	7.08	11.98	8.72	13.50
RC I	4.33	12.08	17.13	14.38	18.13
RC II	3.12	10.87	7.78	11.92	10.72
CFC 20	5.58	9.32	19.53	15.82	20.85
CFC 30	12.42	14.00	21.72	18.38	23.20
CFC 40	11.87	14.12	20.77	17.72	22.23

Although, the same main trends as with the results of the Vicat measurements are observed, some values deviate. For the mixes without superplasticizer, two clear peaks are observed in the derivative of the P-wave velocity (see Fig. 5.15 (left)). The first one corresponding to the removal of entrained air in the cement paste during the dormant period and the second one corresponding to the actual solid percolation. The setting times of the mixes without superplasticizer (as summarised in Table 5.3) are quite similar for all three compositions, as

also observed for the Vicat results. On the other hand, for the mixes with superplasticizer, the first peak of the derivative of the P-wave velocity partly or completely disappears, because of the more workable mixture. However, for some mixes, a small first peak is still visible, negatively influencing the determination of the minimum of the derivative of the P-wave velocity (δV_P^{min}) and explaining the very low values of the initial setting times determined with the δV_P^{min} method for the RC I and CFC 20 mixes. It is thus concluded that the addition of superplasticizer disturbs the development of the P-wave velocity at early ages, and makes it difficult to accurately determine the initial setting times. Since the second peak of the P-wave velocity derivative is still clearly visible, final setting time determination is easier and less dependent on the influence of the superplasticizer at early ages. The RC II mix with superplasticizer shows an inexplicable different P-wave velocity derivative behaviour, which makes the determination of both initial and final setting time difficult/impossible.

Fig. 5.16 and 5.17 compare the Vicat setting times with the setting times derived from the UPV results for all cement paste mixes with and without superplasticizer. Regarding the initial setting time (Fig. 5.16), the method based on the absolute P-wave velocity value of water (V_P=1500 m/s) corresponds best with the Vicat measurements, both for the mixes with and without superplasticizer. Compared to the Vicat results, the δV_P^{min} method slightly overestimates the initial setting times for the mixes without superplasticizer. Regarding the mixes with superplasticizer, on the other hand, this method strongly underestimates the initial setting time of the RC I, RC II and CFC 20 mixes (as already discussed before), but shows good agreement with the Vicat setting times of the CFC 30 and CFC 40 mixes.

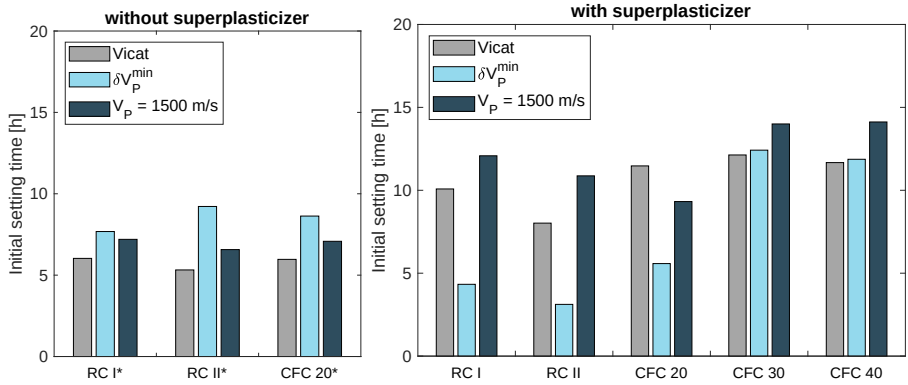

Figure 5.16: Overview of the initial setting times according to the standardised Vicat method and the UPV method for the cement paste mixes without (left) and with (right) superplasticizer.

The final setting times are depicted in Fig. 5.17. As for the initial setting times, the absolute value method (V_P = 1650 m/s) shows the best agreement with the Vicat final setting times for all mixes, especially for the mixes without superplasticizer. The two other methods (δV_P^{max} and δE_d^{max}) show higher final setting times, compared to the Vicat results, for all mixes, both with and without superplasticizer, except for the RC II mix with superplasticizer.

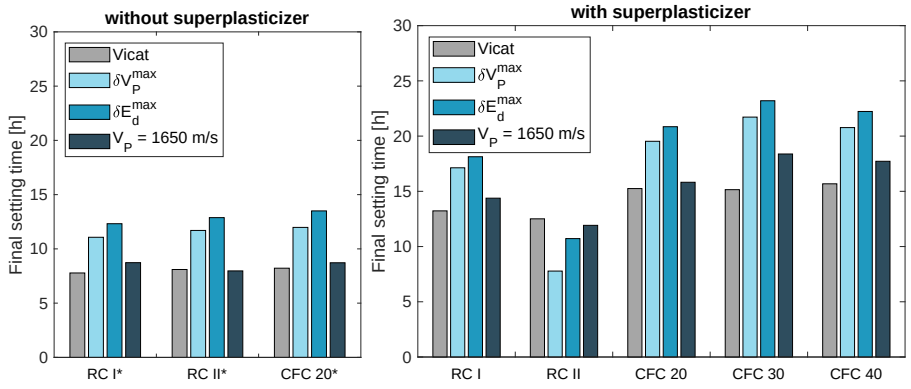

Figure 5.17: Overview of the final setting times according to different methods for the cement paste mixes without (left) and with (right) superplasticizer.

The influence of superplasticizer on the initial P-wave velocity development cannot be denied, and determination of the initial setting time based on velocity gradient values (inflection points) is therefore difficult and not recommended. For final setting time determination, the inflection point based methods give unambiguous and consistent results, both for the reference mixes and the blended cement mixes, with and without superplasticizer. Higher values of the final setting time are obtained with these methods, compared to the Vicat final setting times. However, the standard Vicat method should be assessed critically as a reference comparison. The standard Vicat test is a destructive, non-continuous method, from which only data at specific times can be obtained. The ultrasonic pulse velocity method, on the other hand, is a non-destructive, continuous method, which provides a complete description of the early-age evolution and solid phase transition of cement-based materials. Although the UPV method is not standardised, this method has already been widely used for determination of setting times in the last decade and has proven to be successfully [46]. The final setting time results of the UPV method are therefore considered to be more accurate and the δV_P^{max} method is retained as final setting time criteria.

Concrete

Development of P- and S-waves The results of the P- and S-wave velocities of the concrete mixes with superplasticizer are shown in Fig. 5.18. All depicted results are directly the result of the tri-exponential model fitting and the parameters of the model can be found in Appendix D. In contrast to the development of the P-waves in the cement paste mixes, the P- and S-wave velocities in concrete show similar development as described in the literature (see subsection 2.3.2), i.e. one S-shaped curve. The influence of air entrainment is, after all, more pronounced in cement paste mixes, since concrete mixes contain, besides cement paste, also aggregates, which are insensitive to changes in the air content.

After a dormant period, where initial ettringite formation, internal settling and initial densification of the microstructure take place, there is a rapid increase of the P-wave velocity. The hydration products fill up the pore space, creating a denser structure and resulting in a higher bulk modulus. During the deceleration period, progressive stiffening of the material takes place [49]. The S-wave velocity, which is related to the development of the penetration resistance and actual connection of the particles, develops more slowly. The increase in S-wave velocity corresponds to a period of intense hydration and is characterised by the rapid formation of CH, C-S-H and ettringite. Complete pathways of interconnected particles start to form and the shear modulus starts to develop [49, 50].

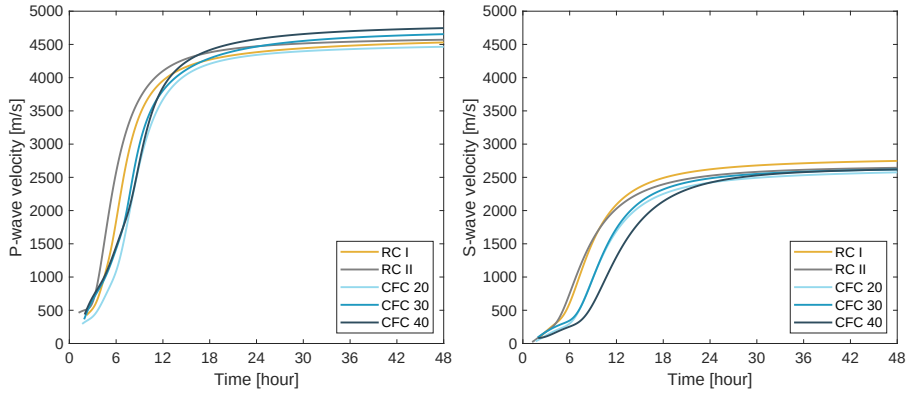

Figure 5.18: P-wave velocities (left) and S-wave velocities (right) of the different concrete mixes with superplasticizer (n=1).

Influence of CFC It is observed from Fig. 5.18 that for all compositions, the velocities develop in the same way. The influence of the superplasticizer is observed with a small delay in the velocities of the CFC mixes compared to the velocities of the reference mixes. The P-wave velocity of the CFC 30 and CFC 40 mixes reaches the highest values after two days, while for the cement paste samples, the P-wave velocity was the highest for the RC I mix. The differences, however, are relatively small. The S-wave velocity (V_S) of the RC I mix reaches the highest value after two days, while all blended cement mixes reach quite similar S-wave velocity values after two days.

Derivation of elastic properties Fig. 5.19 shows the development of the dynamic Poisson's ratio, the dynamic elastic modulus, the dynamic bulk modulus

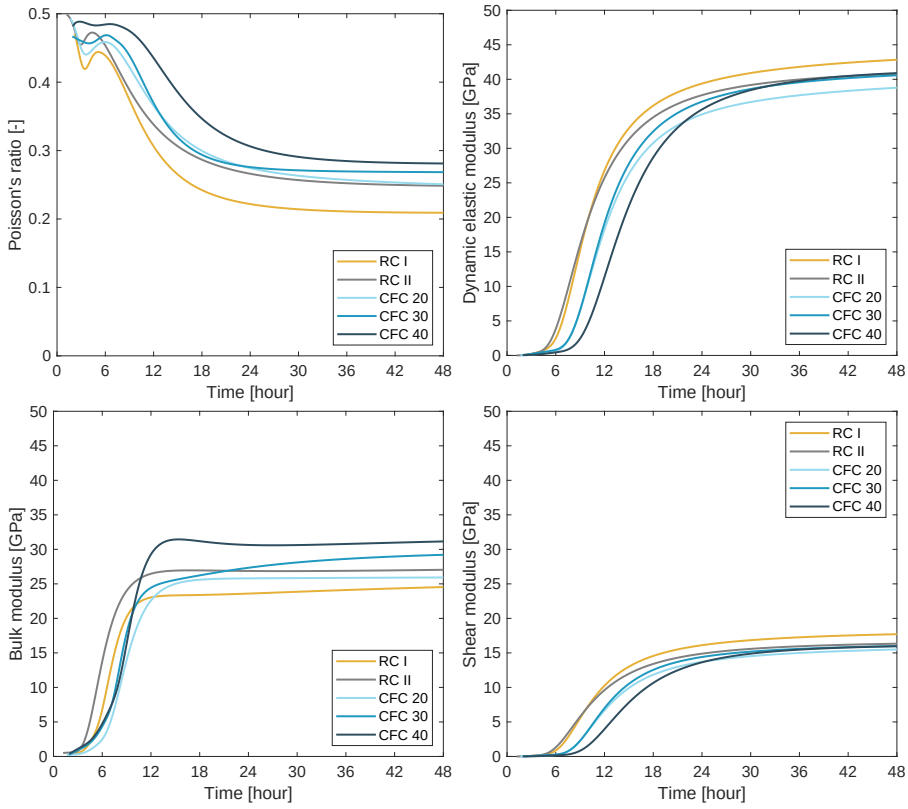

Figure 5.19: Elastic properties (ν_d, E_d, K_d and G_d) of the different concrete mixes with superplasticizer, calculated from the P- and S-wave velocities.

and the dynamic shear modulus for all different concrete mixes. During the early hydration until initial setting, the values of E_d, K_d and G_d stay close to 0, due to the low initial value of V_S, corresponding to the dormant stage. On the other hand, the elastic properties of the cement paste mixes only determined by means of P-wave velocities, were strongly influenced by the sensitivity of the P-waves to the air content at early ages. The exact determination of the Poisson's ratio also results in more accurate determination of the elastic properties. Initially, the Poisson's ratio of the fresh concrete mixes equals around 0.5, considering the fact that a deformation of the fresh concrete does not results in a volume change. During hydration, ν_d decreases to reach a minimum right after the start of the strength development. Afterwards, the Poisson's ratio slightly increases again to reach a final value of about 0.25 [24]. The RC I mix shows the lowest Poisson's ratio (0.21 after 48 hours), while an increasing ν_d is observed for increasing amount of CFC. The presence of CFC, thus, results in a slightly higher sensitivity of the concrete mix to lateral deformations upon axial deformations. The dynamic elastic modulus and dynamic shear modulus show similar development. At early ages the development of E_d and G_d of the CFC mixes is slowed down due to the influence of the superplasticizer. Up to two days, the RC I mix reaches the highest E_d and G_d values, while all blended cement mixes show slightly lower values. The development of the dynamic bulk modulus shows similar behaviour at early ages. However, after two days, the blended cement concretes show slightly higher K_d values.

Setting time determination Also for concrete, different methods exist in the literature to determine the initial and final setting time, as discussed in subsection 2.3.2. In Table 5.4, the initial and final setting times derived from the UPV measurements are shown. As regards the presence of the aggregates, both initial and final setting occur sooner in the concrete mixes, compared to the setting times of the cement paste mixes. This is the result of the increased percolation probability in the presence of aggregates [50]. The same main

Table 5.4: Initial and final setting times of the different concrete mixes with addition of superplasticizer, determined from UPV measurements.

	initial setting [h]			final setting [h]	
	$t(\delta V_P^{max})$	$t(\delta V_S^{max})$	$1.45 \cdot t(\delta V_P^{max})$	$t(\delta E_d^{max})$	$t(0.2 \cdot \delta V_P^{max})$
RC I	6.25	7.12	9.06	8.37	10.98
RC II	4.53	6.25	6.57	7.80	10.08
CFC 20	7.65	8.60	11.09	10.12	13.52
CFC 30	7.83	8.87	11.36	10.22	12.43
CFC 40	8.73	10.38	12.66	12.22	13.82

trend as with the cement paste mixes is observed, i.e. a delayed setting time with increasing superplasticizer content. Furthermore, the values of the initial and final setting times of the different methods show some deviations. The $1.45 \cdot t(\delta V_P^{max})$ method gives initial setting times greater than the final setting times of the $t(\delta E_d^{max})$ method. Since S-waves are better indicators of the setting process [49] and since the results of the P-wave velocity based setting time determination methods deviate quite a lot from the other methods, the δV_S^{max} and δE_d^{max} methods are retained for initial and final setting time determination of concrete, respectively. Carette and Staquet [49, 50] have already shown the applicability of these methods to mortar and concrete mixes containing different types of SCMs (such as GBFS, LS and FA). These criteria are now proven to be also applicable to CFC blended cement concretes.

5.3 Strength and stiffness development

5.3.1 Compressive strength

The compressive strength of the different concrete mixes was determined from early ages up to 90 days. The average compressive strength results are shown in Fig. 5.20, with the error bars indicating the standard deviation. After 12 hours (0.5 day), the CFC blended cement mixes show the lowest compressive strength. This can be explained by the higher amount of superplasticizer, delaying the setting to approximately 12 hours after casting. From 1 day up to 7 days,

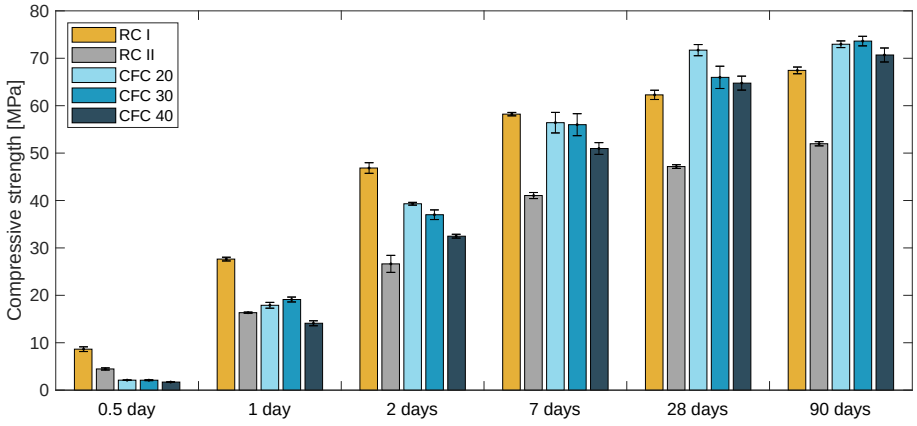

Figure 5.20: Compressive strength values of the different concrete mixes, from early ages up to 90 days (n=3).

the compressive strength of the CFC blended cement mixes strongly increases, surpassing the compressive strength of the fly ash cement concrete (RC II) and from 28 days on, overtaking even the compressive strength of the OPC reference mix (RC I). The filler effect and pozzolanic reaction of CFC explain this behaviour. A slightly lower compressive strength for higher replacement levels of CFC is observed, but, this difference is negligible at later ages.

The characteristic compressive strength of concrete (f_{ck}) is defined as the value of the compressive strength having a probability of 5% of not being attained in a hypothetical unlimited test series, and can be calculated according to the European standard EN 1990 [75] (considering 3 experimental test results available) as:

$$f_{ck} = f_{cm} - 3.37 \cdot \sigma \tag{5.5}$$

with f_{cm} the mean concrete compressive strength and σ the standard deviation. With regards to characteristic compressive strength at 28 days, concrete is subdivided into different strength classes, according to the European standard EN 206-1 [74]. Table 5.5 summarises the characteristic cubic compressive strength for the different concrete mixes, and their corresponding strength class. The CFC blended cement concretes all reach a strength class equal to or higher than the one of the OPC reference cement concrete, while the FA blended concrete reaches a much lower strength class. Considering the density of the concrete, the CFC 20 mix can even be considered as high-strength concrete, according to EN 1992-1-1 [77].

Table 5.5: Characteristic cubic compressive strength after 28 days and strength classes of the different concrete mixes.

	$f_{ck,cube}$ [MPa]	Strength class
RC I	59.00	C45/55
RC II	45.84	C35/45
CFC 20	67.75	C55/67
CFC 30	58.06	C45/55
CFC 40	59.80	C45/55

5.3.2 Tensile strength

The tensile strength can be derived from the experimentally determined tensile splitting strength by using Eq. 3.2 [77]. The results of the tensile splitting strength and tensile strength of the different concrete mixes are shown in Fig. 5.21. The tensile strength values of all CFC mixes are lower than the tensile strength values of the RC I reference mix for all ages, however, they

are higher than the tensile strength values of the reference mix with fly ash (RC II). No trend is observed for the tensile strength values in relation with the CFC cement replacement ratio and the marginal differences are therefore considered as negligible. The same relationship between the tensile strength values of the different concrete compositions is observed as for the relationship of the compressive strength values of the different concrete mixes up to 7 days.

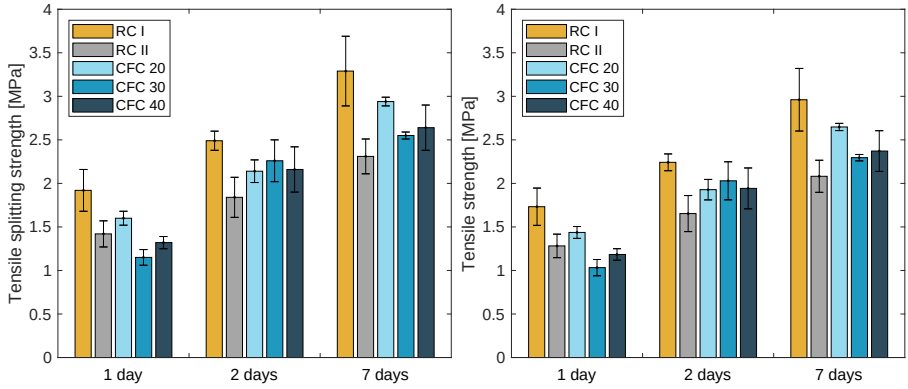

Figure 5.21: Tensile splitting strength (left) and tensile strength (right) of the different concrete mixes, after 1, 2 and 7 days (n=3).

According to Eurocode 2 [77] and Model Code 2010 [129], there exists a relationship between the compressive strength and tensile strength (depending on the strength class achieved), given as:

$$\begin{cases} f_{ctm} = 0.3 \cdot f_{ck}^{2/3} & \leq \text{C50/60} \\ f_{ctm} = 2.12 \cdot \ln\left(1 + \frac{f_{cm}}{10}\right) & > \text{C50/60} \end{cases} \tag{5.6}$$

with f_{ctm} the average tensile strength, f_{ck} the characteristic cylindric compressive strength and f_{cm} the mean cylindric compressive strength. Table 5.6 shows the comparison between the experimentally determined tensile strength and the tensile strength calculated from the compressive strength after 7 days. It is observed that the experimentally determined values are much lower than the calculated ones. This can possibly be explained by the underestimation of the real tensile strength when calculating the tensile strength from the tensile splitting strength according to EC 2 (see Eq. 3.2). However, MC 2010 proposes a higher multiplication factor (1 compared to 0.9) for calculating the tensile strength from the tensile splitting strength. Furthermore, the indirect character of the tensile splitting strength test may also lead to the underestimation of the experimentally determined tensile strength values.

Table 5.6: Difference between the experimentally determined tensile strength and the tensile strength calculated from the compressive strength results at 7 days.

	$f_{ctm,experiment}$ [MPa]	$f_{ctm} = 0.3 \cdot f_{ck}^{2/3}$ [MPa]
RC I	2.96	3.95
RC II	2.08	3.15
CFC 20	2.65	3.54
CFC 30	2.30	3.57
CFC 40	2.37	3.64

5.3.3 Static elastic modulus

The results of the static elastic modulus at early ages are shown in Fig. 5.22. The values of E_s of the CFC 20 mix correspond very well with the E_s values of the RC I mix, while the CFC 30 and CFC 40 mixes show lower static elastic moduli. A clear decreasing stiffness for increasing replacement ratio of CFC is observed and the RC II mix shows the lowest E_S for all ages.

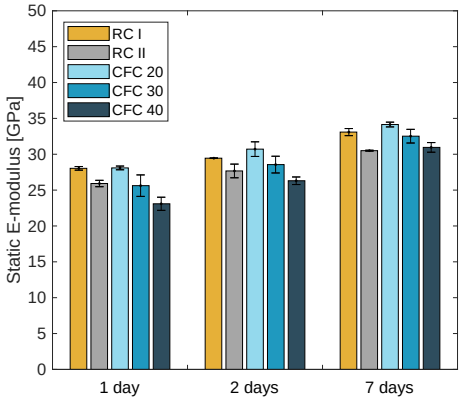

Figure 5.22: Static elastic modulus of the different concrete mixes, after 1, 2 and 7 days (n=3).

According to Eurocode 2 [77] and Model Code 2010 [129], there also exists a relationship between the compressive strength and static elastic modulus, given as:

$$E_{cm} = 22 \cdot \left(\frac{f_{cm}}{10}\right)^{0.3} \tag{5.7}$$

Table 5.7 shows the comparison between the experimentally determined static elastic modulus and the static elastic modulus calculated from the compressive strength after 7 days. It is observed that the experimentally determined values are slightly lower than the calculated ones.

Table 5.7: Difference between the experimentally determined static elastic modulus and the static elastic modulus calculated from the compressive strength results at 7 days.

	$E_{s,experiment}$ [GPa]	$E_s = 22 \cdot \left(\frac{f_{cm}}{10}\right)^{0.3}$ [GPa]
RC I	33.09	37.32
RC II	30.50	33.61
CFC 20	34.14	36.97
CFC 30	32.52	36.89
CFC 40	30.96	35.86

5.4 Correlations

Since the UPV method is a not standardised method, correlations between the ultrasonic measurements, calorimetry measurements and strength measurements are made, in order to critically evaluate the UPV method and provide general correlations/relationships with early-age properties.

5.4.1 Ultrasonic measurements versus isothermal calorimetry

Ultrasonic measurements and isothermal calorimetry measurements are two very different methods used to characterise the hydration process. The ultrasonic measurements describe the mechanical aspects associated with the hydration, which are the changes in elastic properties of the mixture, related to the microstructural changes. The heat release, on the other hand, characterises the chemical changes that occur during hydration, which are the formation of hydration products through exothermic hydration reactions [68]. Although several authors state that there is no relationship between the heat release and the solid percolation, or so between the hydration process and the setting process, setting generally occurs during the cement hydration acceleration period (for usual water-to-binder ratios) and initial and final setting both occur at a specific point on the accelerating phase [46, 193]. For most conventional concrete mixtures, the initial set occurs soon after the main reaction has started, i.e. the onset of the acceleration period: $t(q^{min})$ or $t(q^{min}+ 0.25$ W/g) for mixtures

containing PCE superplasticizers [243]. Ge et al. [105], however, described the initial set as the maximum of the first derivative curve of the heat flow $t(\delta q^{max})$. The final set, on the other hand, occurs close to the maximum heat release: $t(q^{max})$ [193]. Both methods can thus be characterised using key concrete ages, related to the start and end of the setting process. For the ultrasonic measurements, these ages were already described in subsection 5.2.2 and summarized in Table 5.4. The key concrete ages related to the heat development are summarised in Table 5.8.

Table 5.8: Key concrete ages derived from calorimetry results.

	initial setting [h]			final setting [h]
time [h]	$t(q^{min})$	$t(q^{min}+0.25\ W/g)$	$t(\delta q^{max})$	$t(q^{max})$
RC I	3.45	6.33	11.67	15.93
RC II	2.78	4.22	9.60	11.32
CFC 20	5.18	7.87	12.65	17.03
CFC 30	6.87	10.20	15.62	20.20
CFC 40	7.40	11.15	16.53	22.02

Fig. 5.23 and 5.24 show correlations between the setting times and key concrete ages derived from calorimetry results and ultrasonic measurements, respectively for the start and end of the setting process. Only linear correlations are assumed: correlation lines that go through the origin (assuming a constant ratio between the two concrete ages), or correlation lines parallel to x=y (assuming a constant delay between the two concrete ages). The equations and coefficients of determination (R^2) of the correlation lines are also given in the figures. The coefficient of determination is calculated as:

$$R^2 = 1 - \frac{\sum (y_i - \hat{y}_i)^2}{\sum (y_i - \bar{y}_i)^2} \tag{5.8}$$

with y_i the key concrete ages derived from calorimetry results, $\hat{y}_i$ the fitted key concrete ages derived from ultrasonic results (corresponding to the correlation lines) and $\bar{y}_i$ the average value of the key concrete ages derived from calorimetry results.

With regard to the initial setting time, overall, quite good correlations are observed. With regard to the final setting time, on the other hand, the correlations found are worse. This indicates that the ultrasonic velocity and isothermal heat release are not completely affected in the same way by changes in hydration kinetics. The solid percolation and heat release can therefore not be correlated. This demonstrates the importance of complementing calorimetry measurements with ultrasonic measurements, in order to get a complete picture

of the early-age hydration behaviour. By using both methods, both the mechanical aspects, as well as the chemical changes occurring during hydration, are covered.

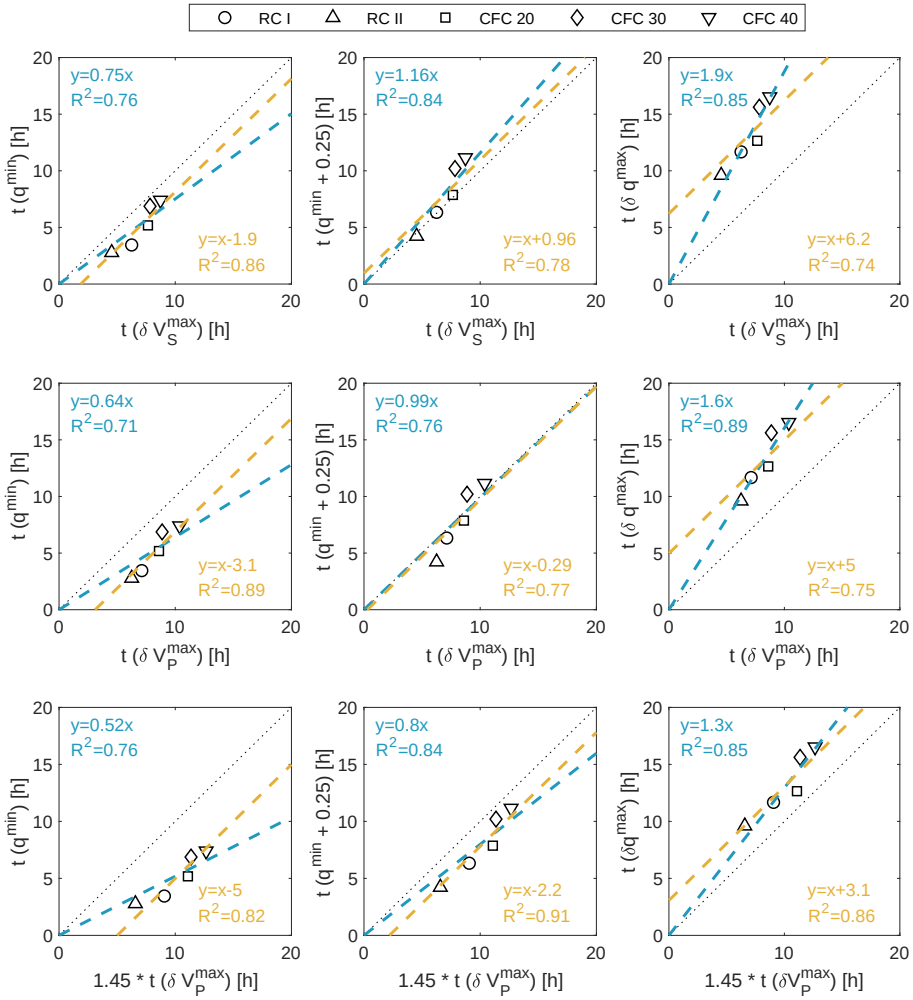

Figure 5.23: Correlation between initial setting times derived from ultrasonic measurements and key concrete ages from calorimetry measurements. Trend lines (dashed lines) with equations and errors (R^2) and x=y (black dotted line).

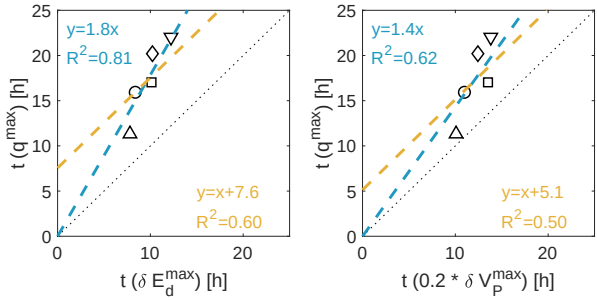

Figure 5.24: Correlation between the final setting times derived from ultrasonic measurements and key concrete ages from calorimetry measurements. Trend lines (dashed lines) with equations and errors (R^2) and x=y (black dotted line).

5.4.2 Ultrasonic measurements versus strength measurements

The ultrasonic velocity measurements and elastic properties derived from UPV measurements can be correlated with concrete strength. The results of the correlations of the compressive strength at early ages (12, 24 and 48 hours) with the P-wave velocity, S-wave velocity and dynamic elastic modulus (calculated based on the P- and S-wave velocities) are shown in Fig. 5.25. Correlations were made considering all concrete compositions (orange trendlines) and considering only the CFC concrete compositions (blue trendlines), in order to check if CFC has a different correlation behaviour. An exponential function was fitted to the results:

$$f_c = a \cdot \exp(b \cdot X) \tag{5.9}$$

where X represents the P-wave velocity (V_P), S-wave velocity (V_S) or dynamic elastic modulus (E_d), and a and b are fitting parameters. Both the equations as well as the coefficients of determination (R^2) are shown in the graphs of Fig. 5.25. The best correlations are observed between the compressive strength and the S-wave velocity, and between the compressive strength and the dynamic elastic modulus, while the P-wave velocities show the worst correlation with the compressive strength. The development of the S-wave velocity best represents the development of the compressive strength, and the relationship is given by:

$$f_c = 0.0082 \cdot \exp(0.0032 \cdot V_S) \tag{5.10}$$

The dynamic elastic modulus can subsequently be correlated with the compressive strength. This allows accurate prediction of the compressive strength development at early ages, by only knowing E_d values, according to the following relationship:

$$f_c = 0.18 \cdot \exp(0.13 \cdot E_d) \tag{5.11}$$

Correlation of the CFC mixes only shows slightly higher coefficients of determination compared to correlation of all mixes, however, the differences are rather small, especially for correlation of V_S and E_d. It can, thus, be concluded that CFC shows similar correlation behaviour as the reference mixes, as only slight differences in the trendline equations are noticed.

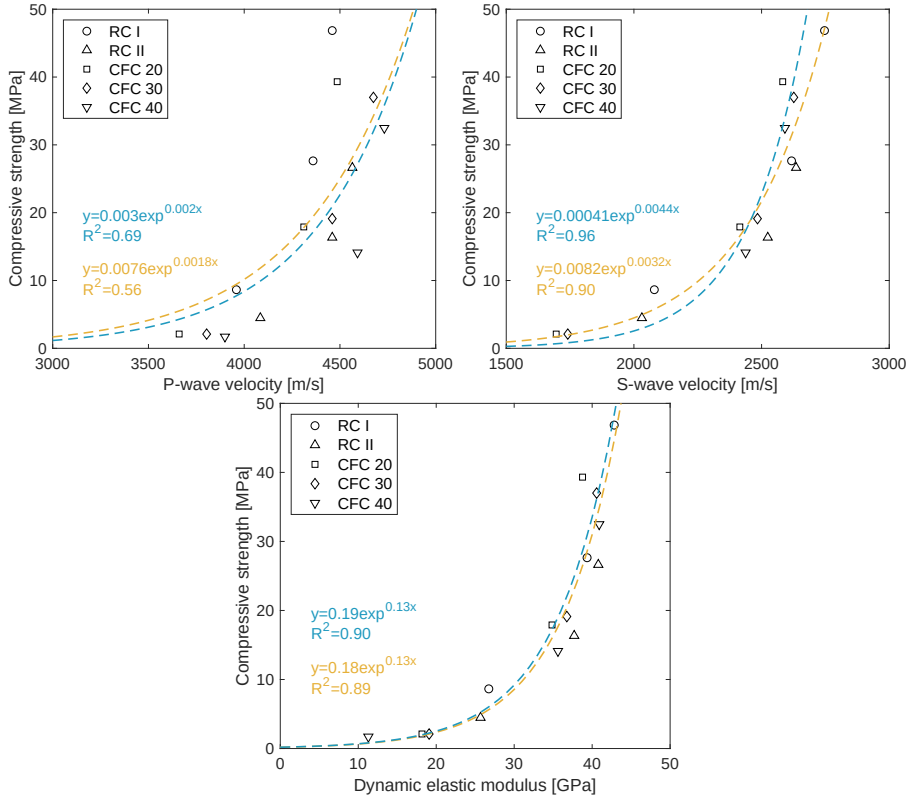

Figure 5.25: Correlations of the compressive strength with the P-wave velocity, S-wave velocity and dynamic elastic modulus at 12, 24 and 48 hours, both for all compositions (orange trendlines) as for only the CFC concrete mixes (blue trendlines).

5.4.3 Static elastic modulus versus elastic dynamic modulus

The elastic moduli of the concrete samples were determined both by measurement according to EN 12390-13 [85] (static elastic modulus), as well as by calculation from ultrasonic measurements (dynamic elastic modulus). Since the ratio

between the static modulus of elasticity and the dynamic modulus of elasticity increases for increasing strength, there is no simple conversion of the value of E_d into an estimate of the value of E_s [166]. Nevertheless, different empirical relationships have been developed over years.

- Lydon and Balendran [166]: $E_s = 0.83 \cdot E_d$
- British design code (BS CP 110:1972) [166]: $E_s = 1.25 \cdot E_d - 19$
- Eurocode 2 [77]: $E_s = 0.95 \cdot E_d$

Fig. 5.26 shows the relationship between the static elastic modulus and dynamic elastic modulus for the five studied concrete mixes, at early ages (1, 2 and 7 days). The relationship between the static and dynamic elastic modulus for all mixes can be described by the following formula:

$$E_s = 0.72 \cdot E_d \tag{5.12}$$

The factor 0.72 is lower than the values found in the literature. This means that lower static elastic moduli are found for the corresponding dynamic elastic moduli. The lower value of the correlation factor (see Eq. 5.12) can be explained with the fact that the correlation in Fig. 5.26 is done only up to 7 days, while the above described formulas from literature assume an age of 28 days.

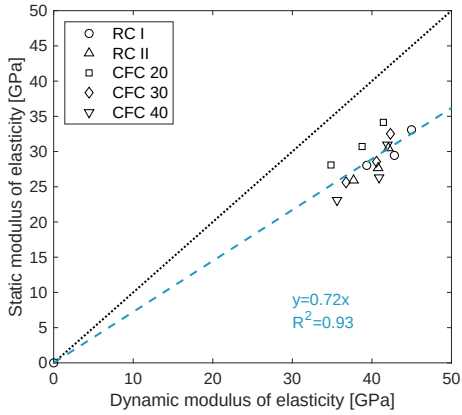

Figure 5.26: Correlation of the static and dynamic elastic modulus.

5.5 Modelling

Modelling of early-age concrete properties allows prediction of concrete performance and durability at later ages. The temperature development of concrete is modelled numerically in time and space by solving the heat equation, using a finite difference scheme and calorimetry results are used for parameter identification. The development of the mechanical properties is modelled using the model according to Eurocode 2 and this model is parametrised for CFC blended cement concretes.

5.5.1 Temperature development

Chemo-thermal model

In order to determine the evolution of temperature (T) inside a concrete element, the energy balance equation, which includes the heat release due to the hydration reaction, is solved [10, 27, 40]:

$$C \cdot \dot{T} = \nabla \cdot (k \cdot \nabla T) + \dot{Q} \tag{5.13}$$

where C is the volumetric heat capacity [J/m^3/K], k is the thermal conductivity [W/m/K] and Q is the cumulative heat release [J/m^3]. Since the volumetric heat capacity and thermal conductivity can be considered as constant in space and time, the heat equation can be expressed as:

$$C \cdot \dot{T} = k \cdot \Delta T + \dot{Q} \tag{5.14}$$

The heat source term ($\dot{Q}$) comes from the exothermic hydration reaction and can be expressed as:

$$\dot{Q} = L \cdot \dot{\xi} \tag{5.15}$$

where L is the latent heat of hydration [J/m^3] and $\dot{\xi}$ is the rate of degree of hydration [-]. Since the hydration of cement paste is a thermo-activated process, the evolution of the degree of hydration can be obtained by using an Arrhenius type law [220]:

$$\dot{\xi} = \tilde{A}(\xi) \cdot \exp\left(\frac{E_a}{R} \cdot \left(\frac{1}{293} - \frac{1}{T}\right)\right) \tag{5.16}$$

where E_a is the activation energy [J/mol], R is the ideal gas constant [8.314 J/mol/K] and $\tilde{A}(\xi)$ is the chemical affinity [1/h].

The boundary conditions for early-age concrete are assumed to be of the convective type. Convection refers to the heat transfer occurring between the

concrete surface and the surrounding air [10, 244]. The imposed heat flux (ϕ) equals:

$$\phi = h_p \cdot (T_S - T_{ext}) \cdot \mathbf{n} \tag{5.17}$$

where h_p is the coefficient of heat exchange by convection [W/m^2/K], T_S is the surface temperature [K], T_{ext} is the ambient temperature [K] and $\mathbf{n}$ is the normal unit vector to the surface.

The latent heat of hydration L and the chemical affinity $\tilde{A}(\xi)$ can be obtained experimentally from isothermal calorimetry results. The determination of these parameters mainly consists of extrapolating the laboratory test results, by fitting mathematical models to the experimental observations. The development of the cumulative heat Q (and the hydration in general) in time can be best represented by an exponential/S-shaped mathematical model:

$$Q(t) = Q_\infty \cdot \exp\left(-\frac{\tau}{t}\right)^\beta \tag{5.18}$$

where Q_∞ is the ultimate cumulative heat (equal to the latent heat of hydration L), τ is the hydration time parameter and β is the hydration shape parameter (all fitting parameters).

The normalised affinity $\tilde{A}(\xi)$ characterises the macroscopic hydration kinetics of a concrete mixture and is associated with the micro-diffusion process of water reacting with unhydrated cement [27, 52]. The chemical affinity $\tilde{A}(\xi)$ can be calculated from the experimental data using the following equation:

$$\tilde{A}(\xi) = \frac{\dot{Q}}{L} \cdot \exp^{-1}\left(\frac{E_a}{R} \cdot \left(\frac{1}{293} - \frac{1}{T}\right)\right) \tag{5.19}$$

and several models could be used to describe this process. Cervera et al. [52] developed the following analytical form:

$$\tilde{A}(\xi) = \frac{k_\xi}{\eta_{\xi 0}} \cdot \left(\frac{A_{\xi 0}}{k_\xi \cdot \xi_\infty} + \xi\right) \cdot (\xi_\infty - \xi) \cdot \exp\left(-\bar{\eta} \cdot \frac{\xi}{\xi_\infty}\right) \tag{5.20}$$

where ξ_∞ is the final degree of hydration and k_ξ, $A_{\xi 0}$, $\eta_{\xi 0}$ and $\bar{\eta}$ are material constants. In order to reduce the amount of parameters, the following equation will be used to describe the chemical affinity:

$$\tilde{A}(\xi) = \beta \cdot \left(1 + \frac{\xi}{\xi_1}\right) \cdot \left(1 - \frac{\xi}{\xi_\infty}\right) \cdot \exp\left(-\bar{\eta} \cdot \frac{\xi}{\xi_\infty}\right) \tag{5.21}$$

where β, ξ_1, $\bar{\eta}$ (and ξ_∞) are then considered as the fitting parameters.

In order to numerically solve the 1D heat equation (Eq. 5.22), the Euler implicit method is used.

$$C \cdot \frac{\delta T}{\delta t} = k \cdot \frac{\delta^2 T}{\delta x^2} + \dot{Q} \tag{5.22}$$

This results into the following formulas for the first and second derivative of the temperature over time and space, respectively:

$$\forall n \in [1,N], \forall j \in [1,N_x-1] = \begin{cases} \frac{\delta T}{\delta t}(t_n,x_j) = \frac{T_j^n - T_j^{n-1}}{dt} \\ \frac{\delta^2 T}{\delta x^2}(t_n,x_j) = \frac{T_{j\text{-}1}^n + T_{j+1}^n - 2\cdot T_j^n}{dx^2} \end{cases} \tag{5.23}$$

with N the number of time steps and N_x the number of discrete elements in the structure. Implementing the Euler implicit method and imposing the boundary conditions, leads to the following set of linear equations ($\forall n \in [1,N]$):

$$\Leftrightarrow T_j^n - T_j^{n-1} = \alpha\left(T_{j\text{-}1}^n - T_{j+1}^n - 2\cdot T_j^n\right) + \delta\cdot\dot{\xi} \tag{5.24}$$

$$\Leftrightarrow -\alpha\cdot T_{j\text{-}1}^n + (1+2\alpha)\cdot T_j^n - \alpha\cdot T_{j+1}^n = T_j^{n-1} + \delta\cdot\dot{\xi} \tag{5.25}$$

$$\Leftrightarrow \begin{bmatrix} 1 & -1 & 0 & \dots & \dots & 0 \\ -\alpha & 1+2\alpha & -\alpha & 0 & \dots & 0 \\ 0 & \ddots & \ddots & \ddots & \ddots & \vdots \\ \vdots & \ddots & \ddots & \ddots & \ddots & 0 \\ 0 & \dots & 0 & -\alpha & 1+2\alpha & -\alpha \\ 0 & \dots & \dots & 0 & 1+\gamma & -\gamma \end{bmatrix} \cdot \begin{bmatrix} T_0^n \\ \vdots \\ T_j^n \\ \vdots \\ T_{N_{x-1}}^n \\ T_{N_x}^n \end{bmatrix} = \begin{bmatrix} 0 \\ \vdots \\ T_j^{n-1} + \delta\dot{\xi} \\ \vdots \\ T_{N_{x-1}}^{n-1} + \delta\dot{\xi} \\ T_{ext} \end{bmatrix} \tag{5.26}$$

with $\alpha = \frac{k\cdot dt}{C\cdot dx^2}$, $\delta = \frac{dt\cdot L}{C}$ and $\gamma = \frac{k}{h\cdot dx}$.

Parameter identification

The parameter results of the cumulative heat and chemical affinity model fitting are respectively given in Table 5.9, assuming a constant activation energy for all mixes ($E_a/R = 4400$ K) and constant final degree of hydration ($\xi_\infty = 1$) for all mixes. The obtained values of the ultimate cumulative heat (Q_∞) can be compared to values found in the literature. Values in the range of 129-173 MJ/m^3 for OPC and in the range of 108-145 MJ/m^3 for pozzolanic cements are reported

Table 5.9: Fitting parameters of the cumulative heat model (left) and fitting parameters of the chemical affinity model (right).

	Q_∞ [MJ/m^3]	τ [-]	β [-]
RC I	128.13	1030.64	82.45
RC II	88.36	921.00	73.68
CFC 20	118.25	1081.57	86.53
CFC 30	113.05	1174.32	93.95
CFC 40	116.80	1229.33	98.35

	β [-]	ξ_1 [-]	ξ_∞ [-]	$\bar{\eta}$ [-]
RC I	0.008	0.028	1	4.085
RC II	0.009	0.025	1	4.105
CFC 20	0.009	0.036	1	3.944
CFC 30	0.008	0.041	1	3.865
CFC 40	0.007	0.041	1	3.859

by the 254-CMS RILEM Technical Committee [95] †. Benboudjema and Torrenti [27] reported a value of 154.7 MJ/m^3 for OPC concrete and Briffaut [41] reported a value of 117.84 MJ/m^3. It it thus concluded that the obtained values of the ultimate cumulative heat of the RC I reference mix and the CFC blended cement mixes correspond well to the values found in the literature for OPC and pozzolanic cements, respectively. The FA blended cement mix (RC II), on the other hand, shows quite a low value for Q_∞, compared to the literature. This can be explained by the fact that FA can still react significantly at later ages, due to the pozzolanic reaction becoming dominant after 28 days of hydration [67, 227] and calorimetry measurements were limited to only 7 days of hydration. Additional heat generated in the RC II mix due to the pozzolanic reaction of FA at later ages is thus not considered, probably resulting in an underestimation the value of Q_∞.

The results of the modelled cumulative heat and the experimental results are shown in Fig. 5.27 (left). The development of the modelled cumulative heat corresponds well to the development of the experimental data. The results of the modelled chemical affinity as a function of the degree of hydration are also shown in Fig. 5.27 (right).

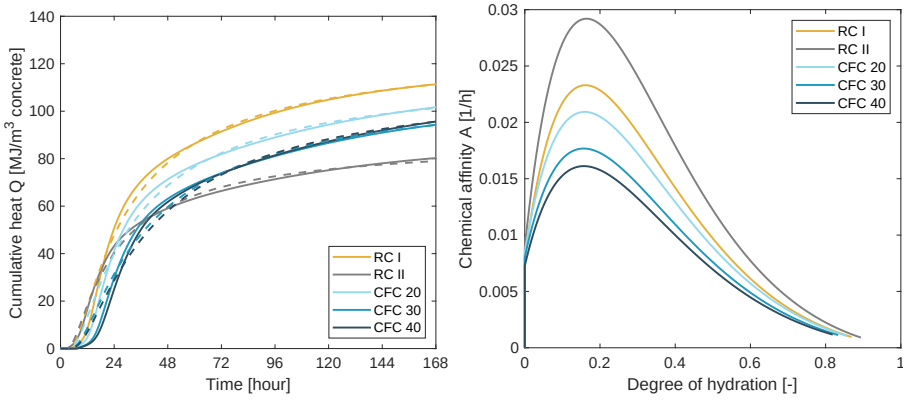

Figure 5.27: Modelled cumulative heat (dashed lines) versus experiments (full lines) (left) and modelled chemical affinity as a function of the degree of hydration (right).

†The values are recalculated from the reported values in J/g cement, assuming a cement density of 2300 kg/m^3 and an average of 15 wt.% cement in concrete.

Results

Temperature development of the different concrete compositions as a function of time and distance from the center of the considered structure is shown in Fig. 5.29, assuming the boundary conditions as summarised in Table 5.10 and a specimen thickness of the structure of 1.2 m, representing a massive concrete structure (see Fig. 5.28). Because of symmetry, only half of the considered structure is modelled. Higher temperatures are observed in the center of the specimen, compared to the surfaces. The maximal temperature developed in the concrete structures is also shown on the graphs in Fig. 5.29. The model indicates that the RC I mix reaches the highest maximal temperature, while the blended cement mixes show lower maximal temperatures. This can be explained by the lower cumulative heat of the blended cements. The temperature difference between the three CFC blended cement mixes is negligible. The lower temperature developed in the CFC mixes, compared to the RC I reference mix, is promising for its application in massive concrete structures. Higher temperatures lead to higher thermal stresses, causing more thermal swelling and eventually cracking, which is a major concern in massive concrete structures.

Table 5.10: Parameters and boundary conditions of the temperature model.

c_p	1000 J/kg/K
k	1.2 W/m/K
E_a/R	4400 K
h_p	17.5 W/m^2/K
T_S	293 K
T_{ext}	293 K

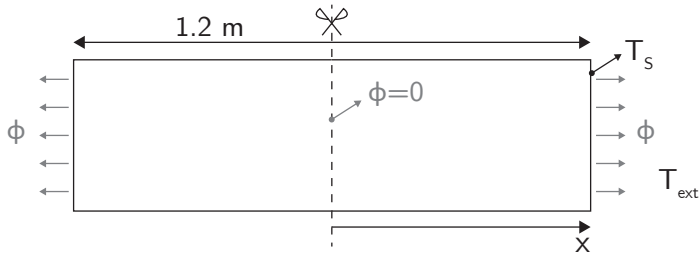

Figure 5.28: Geometry of the considered concrete structure in 1D (ϕ: heat flux, T_S: surface temperature, T_{ext}: ambient temperature).

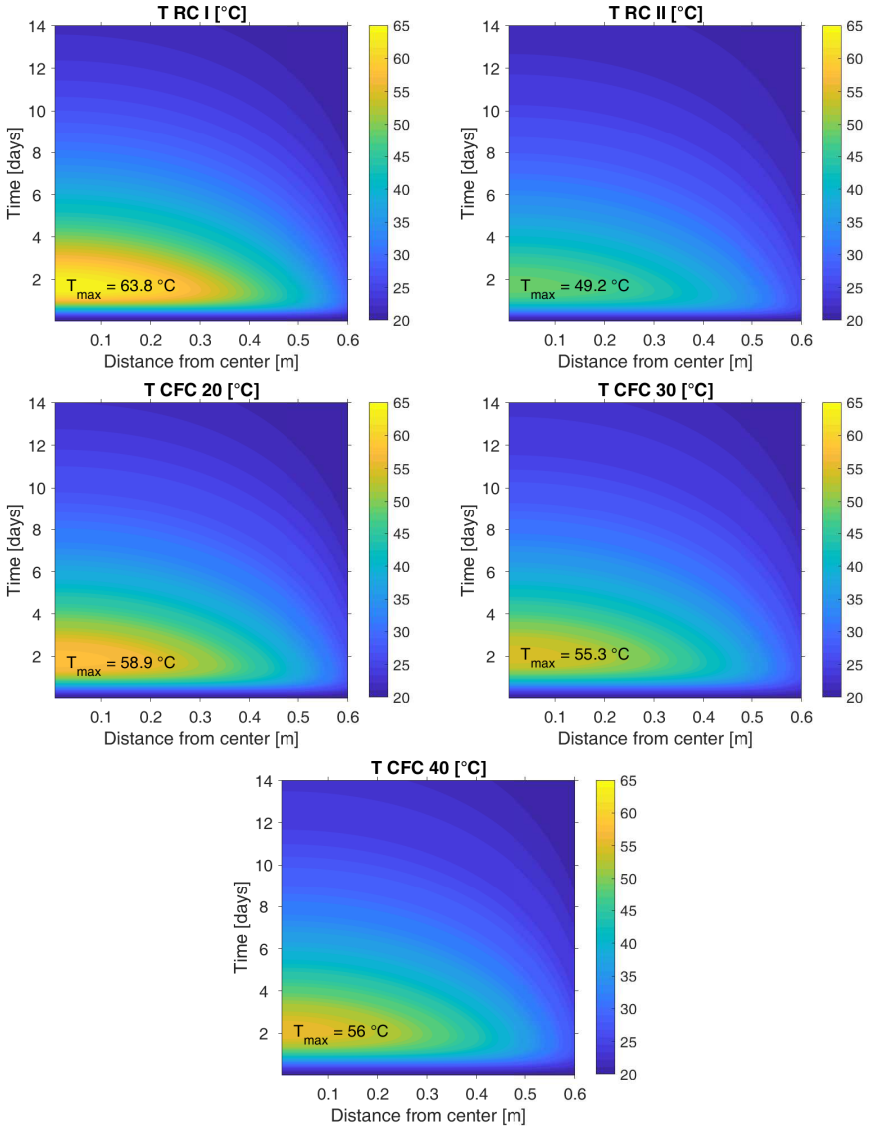

Figure 5.29: Temperature development of the different concrete mixes as a function of time and distance from the center of the specimen (for a concrete structure with thickness of 1.2 m).

The average temperature development (over the section of the element) of the different concrete mixes as a function of time and thickness of the specimen, is shown in Fig. 5.30. As expected, the bigger the element, the higher the temperatures developed.

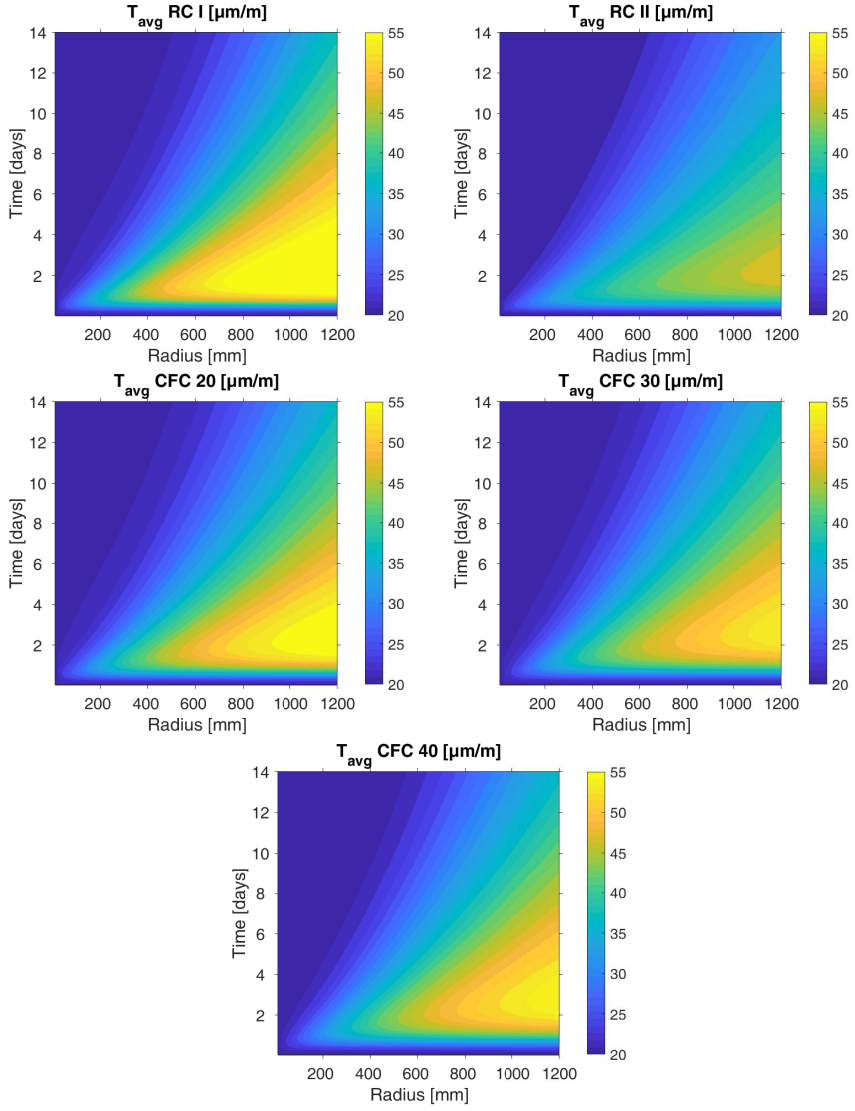

Figure 5.30: Average temperature development of the different concrete mixes as a function of time and thickness of the specimen.

5.5.2 Mechanical properties development

Model

According to Eurocode 2 [77] and Model Code 2010 [129], development of the studied mechanical properties in time can be described by the following equations:

$$X(t_{eq}) = X_{28} \cdot \beta_X(t_{eq})^{n_X} \tag{5.27}$$

$$\beta_X = \exp\left[s \cdot \left(1 - \sqrt{\frac{28 - t_0}{t_{eq} - t_0}}\right)\right] \tag{5.28}$$

where X is the studied mechanical material property, X_{28} is the value of the material property after 28 days, β_X is a function describing the development of the material property in time, n_X is an aging parameter, s is a coefficient depending on the type of cement, t_0 is the final setting time and t_{eq} is the equivalent time, which can be derived from the temperature development as:

$$t_{eq} = \sum_{0}^{t} \exp\left(\frac{E_a}{R} \cdot \left(\frac{1}{293} - \frac{1}{T}\right)\right) \cdot \Delta t \tag{5.29}$$

with t the age of the concrete [s] and R the universal gas constant.

For the compressive strength (f_c), tensile strength (f_{ct}), and static Young's modulus (E_c), the equations become:

$$f_c(t_{eq}) = f_{c28} \cdot \exp\left[s \cdot \left(1 - \sqrt{\frac{28 - t_0}{t_{eq} - t_0}}\right)\right]^{n_{f_c}} \tag{5.30}$$

$$f_{ct}(t_{eq}) = f_{ct28} \cdot \exp\left[s \cdot \left(1 - \sqrt{\frac{28 - t_0}{t_{eq} - t_0}}\right)\right]^{n_{f_{ct}}} \tag{5.31}$$

$$E_c(t_{eq}) = E_{c28} \cdot \exp\left[s \cdot \left(1 - \sqrt{\frac{28 - t_0}{t_{eq} - t_0}}\right)\right]^{n_{E_c}} \tag{5.32}$$

Parameter identification

Since the coefficient s is a cement type dependent parameter, it is constant for all three material properties. According to Eurocode 2 [77] and Model Code 2010 [129], s is equal to 0.20 for CEM 42.5 R, CEM 52.5 N and CEM 52.5 R, s is equal to 0.25 for CEM 32.5 R and CEM 42.5 N, and s is equal to 0.38

for CEM 32.5 N. However, Kanstad et al. [139] found values of 0.12-0.22 for blended cements, Darquennes and Benboudjema [60] found values of 0.09-0.23 for alkali activated blended cements and Klemczak et al. [142] found values of 0.20-0.38 for cements with mineral additives. This demonstrates the importance of experimental data to accurately determine the coefficient s, especially for (new) blended cement systems. The experimental results of the compressive strength were used here to determine this coefficient s, for multiple reasons: compressive strength tests were performed at six different points of time (while tensile strength and static Young's modulus test were only performed at three different points of time), the compressive strength test is a direct test and is easy to perform, and the experimental error and statistical scatter of the compressive strength results were smallest.

In literature, only one value for n_{f_c} is found: 1 [77, 129, 139]. In order to validate this value for blended cement concretes, model fitting was done both with taking n_{f_c} equal to 1 and with taking n_{f_c} as a fitting parameter. Since experimental data of the compressive strength after 28 days is available, parameter f_{c28} can be taken, or as the experimentally determined value, or as a fitting parameter. Both options were considered. The above described methodology leads to four different 'fitting' methods in order to validate the Eurocode 2 model (Eq. 5.27-5.28) for new blended cement systems, summarized in Table 5.11. The resulting parameters of the model fitting can be found in Table 5.12. It was chosen to only consider one parameter s and one parameter n_{f_c} for the three CFC blended cement systems, since these parameters are cement/binder type dependent parameters and in this way, one general/uniform value is valid for all CFC mixes.

Table 5.11: Different methods for model fitting of the compressive strength results according to Eq. 5.30.

	s	n_{f_c}	f_{c28}
Method A	fitting parameter	1	f_{cm28}
Method B	fitting parameter	1	fitting parameter
Method C	fitting parameter	fitting parameter	f_{cm28}
Method D	fitting parameter	fitting parameter	fitting parameter

It can be seen from Table 5.12 that the values of s are lower than the values predicted by Eurocode 2 [77] for cement with normal strength development. However, they are in the range of the values found by Kanstad [139] for blended cements. Compared to the OPC reference mix (RC I), the values of s are higher for the blended cement mixes, demonstrating a slower mechanical properties development of the blended cement mixes. In order to compare the four different fitting methods, an average root mean square error (RMSE) is calculated per

Table 5.12: Parameters of the compressive strength development according to Eq. 5.30, using four different fitting methodologies (see Table 5.11). The values in *italic* are fitting parameters. f_{c28} in MPa.

	Method A			Method B			Method C			Method D		
	s	n_{f_c}	f_{c28}	s	n_{f_c}	f_{c28}	s	n_{f_c}	f_{c28}	s	n_{f_c}	f_{c28}
RC I	*0.14*	1	62.28	*0.15*	1	*64.30*	*0.15*	*0.97*	62.28	*0.17*	*0.90*	*64.30*
RC II	*0.20*	1	47.16	*0.21*	1	*47.88*	*0.21*	*0.97*	47.16	*0.22*	*0.95*	*47.88*
CFC 20	*0.23*	1	71.72	*0.22*	1	*69.18*	*0.24*	*0.96*	71.72	*0.24*	*0.94*	*69.18*
CFC 30	*0.23*	1	65.97	*0.22*	1	*67.43*	*0.24*	*0.96*	65.97	*0.24*	*0.94*	*67.43*
CFC 40	*0.23*	1	64.76	*0.22*	1	*63.74*	*0.24*	*0.96*	64.76	*0.24*	*0.94*	*63.68*
RMSE	2.28 MPa			1.97 MPa			2.28 MPa			2.28 MPa		

method. The RMSE of the different methods is also shown in Table 5.12 and is calculated as:

$$\mathrm{RMSE} = \sqrt{\frac{\sum_i \left(\hat{y}_i - y_i\right)^2}{n}} \tag{5.33}$$

with $\hat{y}_i$ the modelled values of the compressive strength, y_i the experimental values of the compressive strength and n the amount of data points. It is remarkable that the RMSE's of methods A and C, and, B and D are exactly the same. This proves that the results of fitting methods C and D are not unique and both methods do not contribute to a better fitting. Comparing the errors of method A and B, method B shows a slightly lower RMSE, resulting in a slightly better fit. However, since the difference in RMSE is rather small and in order to keep the amount of fitting parameters as low as possible, it is chosen to retain the values of method A. The Eurocode 2 model for describing the compressive strength development is, thus, proven to be also valid for new blended cement mixtures, provided that parameter s is adjusted according to the new blended cement system.

Since the values of the aging parameters $n_{f_{ct}}$ and n_{E_c} are varying considerably in literature (from 0.5-1 for $n_{f_{ct}}$ and from 0.3-0.5 for n_{E_c} [77, 129, 139]), these values are taken as fitting parameters. Since the tensile strength and static E-modulus were not determined experimentally after 28 days, the parameters f_{ct28} and E_{c28} were also considered as fitting parameters. The results of the model fitting can be found in Table 5.13. The values of $n_{f_{ct}}$ are in the range of the values found in literature, while the values of n_{E_c} were lower than the ones predicted by literature, meaning that the development of the static E-modulus is faster than in literature.

Table 5.13: Parameters of the tensile strength and static E-modulus development according to Eq. 5.31-5.32.

	s	$n_{f_{ct}}$	f_{ct28}	n_{E_c}	E_{c28}
RC I	0.14	0.97	3.38	0.29	34.00
RC II	0.20	0.61	2.35	0.20	31.51
CFC 20	0.23	0.65	3.04	0.23	36.22
CFC 30	0.23	0.65	2.75	0.23	33.96
CFC 40	0.23	0.65	2.83	0.23	31.80

Results

Fig. 5.31 and 5.32 show the development of the considered mechanical properties according to Eurocode 2. For the compressive strength, the RC I mix reaches the highest values during early ages. From the age of 4.5 days approximately, the compressive strength of the CFC 20 mix surpasses the compressive strength of the RC I mix and later on, also the compressive strength of CFC 30 and CFC 40 overtake the compressive strength values of RC I. After approximately 14 days, the values of the compressive strength of all CFC blended cement mixes thus surpass the RC I compressive strength values. The values of the compressive strength of the RC II mix with fly ash are remarkably lower. Regarding the tensile strength, on the other hand, the RC I mix always reaches the highest values, followed by the CFC mixes and the RC II mix. The static elastic modulus of the CFC 20 mix reaches the highest values, while there is a gradual decrease in the final static elastic modulus for increasing CFC replacement ratios.

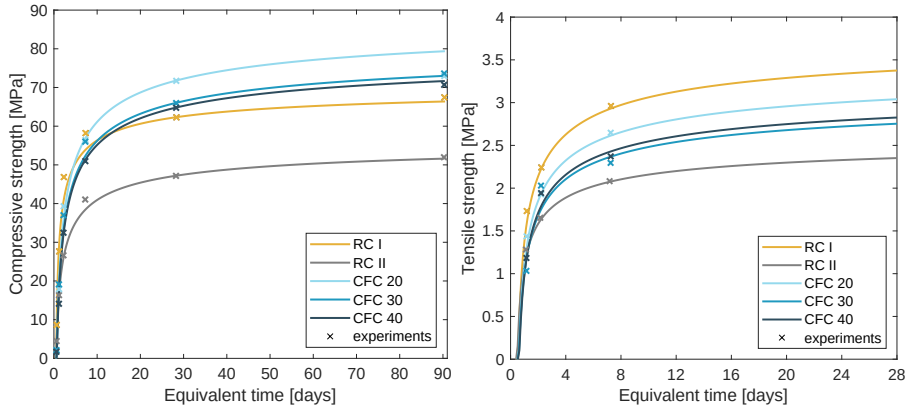

Figure 5.31: Compressive strength (left) and tensile strength (right) models of the different concrete compositions, compared to the experimental data.

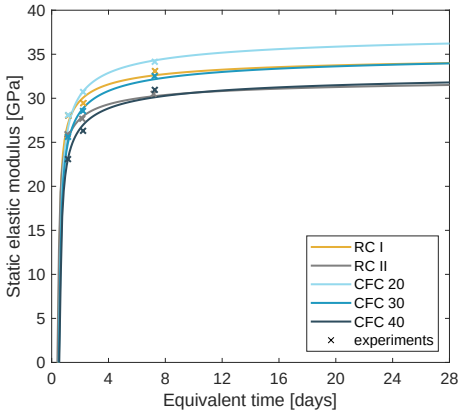

Figure 5.32: Static E-modulus model of the different concrete compositions, compared to the experimental data.

In Fig. 5.33 and 5.34, the relative values of the mechanical properties are plotted (relative to their value after 1000 days). The curves of all CFC mixes overlap, since the same cement type dependent parameter s and the same aging parameters n are used. In contrast to the absolute values of the compressive strength, the RC I mix reaches the highest relative values, so the strength development is the fastest, while the development of the blended cement mixes is relatively slower. It is also observed that the compressive strength development of the CFC mixes is slightly slower than the development of the RC II mix with fly ash. Although the CFC mixes reach the highest absolute compressive strength values (see Fig. 5.31), the development of their strength is slower compared to the two reference mixes. This was already visible in the higher value of s for the CFC blended cement mixes (see Table 5.13), compared to the two reference mixes. For both the tensile strength and static elastic modulus, the same behaviour is observed. The RC I and RC II mixes show the fastest development of the mechanical properties, while the CFC blended cement concretes show a slower development. This behaviour is known for blended cement concretes and is explained by the pozzolanic reaction, taking place later than the hydration reactions, thereby leading to gradual strength development.

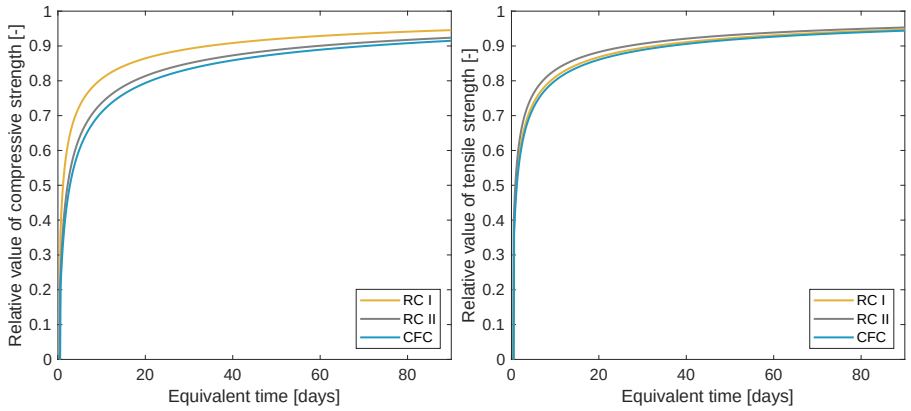

Figure 5.33: Relative compressive strength (left) and tensile strength (right) development of the different concrete mixes.

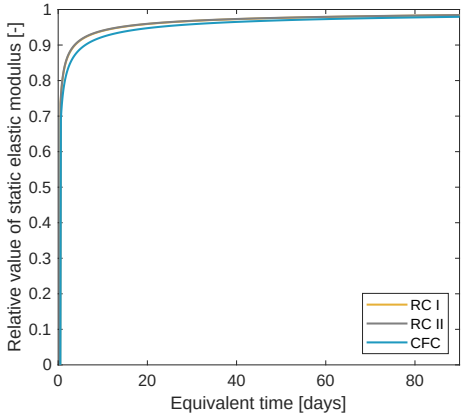

Figure 5.34: Relative static E-modulus development of the different concrete mixes.

5.6 Conclusion

In this chapter, the influence of CFC on the hydration process and early-age mechanical development was studied. CFC enhances the OPC hydration process at early ages by the filler effect and at later ages by the formation of additional hydration products by the pozzolanic reaction, contributing to the strength development. The use of a superplasticizer, on the other hand, delays the cement hydration, but is necessary to counterbalance the higher water demand

derived from the high specific surface area of CFC. Initial and final setting times are subsequently delayed by the superplasticizer effect. The pozzolanic activity of CFC strongly increases concrete compressive strength at late ages, while early-age compressive strengths were reduced, compared to OPC concrete.

The non-standardised UPV method was used to determine setting time in both cement paste and concrete, and was compared to the standard Vicat method for cement paste. Initial setting time determination using the UPV method was found to be difficult, due to the strong influence of superplasticizer on the initial P-wave velocity development of cement paste mixes. Final setting time determination using the UPV method, on the other hand, gave unambiguous and consistent results, and the $t(\delta V_P^{max})$ method was retained as final setting time criteria for cement paste. Compared to the Vicat method, slightly higher final setting times were observed using this method. However, as the Vicat method is a non-continuous method, the accuracy of this method should be questioned and the UPV method is therefore considered to be a better method for setting time determination. For the concrete mixes, both P- and S-waves were used to evaluate the early-age behaviour, and the $t(\delta V_S^{max})$ and $t(\delta E_d^{max})$ methods were found to be the best predictors of the initial and final setting times, respectively.

Correlations between calorimetry results, UPV results and strength results were also investigated. It was concluded that calorimetry results (i.e. heat release) and UPV results (i.e. solid percolation) cannot be correlated, since changes in hydration kinetics affect both methods in different ways. On the other hand, good correlations were observed between concrete compressive strength and S-wave velocity results. Both for the reference mixes and the CFC blended cement mixes, the same correlation factors could be used.

The temperature development in concrete can be modelled based on calorimetry results. Lower temperatures develop in the CFC concrete mixes, due to their lower cumulative heat values, favourable for their application in massive concrete structures. The model of EC 2 describes well the development of the compressive strength, tensile strength and static elastic modulus of CFC blended cement concretes, provided that the cement type dependent parameters are adjusted according to the new blended cement system, using CFC.

Chapter 6

Shrinkage behaviour

This chapter describes the shrinkage behaviour of CFC blended cement paste and concrete. First, the chemical shrinkage of cement paste mixes is described (Section 6.1). Secondly, the autogenous shrinkage and, in particular, the autogenous swelling of cement paste and concrete samples are discussed thoroughly (Section 6.2). Thirdly, the drying shrinkage development of concrete samples is determined, in relation with the drying shrinkage weight loss (Section 6.3). Finally, the autogenous and drying shrinkage of cement paste and concrete are modelled. Parametrisation of existing empirical shrinkage models is done for prediction of the autogenous and drying shrinkage of CFC concrete, while the Biot-Bischop method (a mechanistic shrinkage model) is evaluated for prediction of the autogenous shrinkage of CFC cement paste (Section 6.4). The chapter ends with a summary of the main conclusions (Section 6.5). *

6.1 Chemical shrinkage

The chemical shrinkage, caused by the formation of hydration products, results in an autogenous deformation before setting and in the formation of pores after setting. Fig. 6.1 shows the chemical shrinkage of the reference and CFC blended cement paste mixes, relative to its OPC content. The chemical shrinkage is

*Parts of this chapter have been published in Van Bunderen, C. et al. Early-age hydration and autogenous deformation of cement paste containing flash calcined dredging sediments. *Construction and Building Materials* 200 (2019), 104-115 [224] and in Van Bunderen, C. et al. Experimental analysis and modelling of mechanical properties and shrinkage of concrete recycling flash calcined dredging sediments. *Cement and Concrete Composites* (under review).

only plotted as from final setting, since only the chemical shrinkage resulting in the formation of pores (and possible self-desiccation) is of interest. The RC I mix shows the lowest chemical shrinkage per g of OPC, while the CFC mixes show higher chemical shrinkage, with a slightly increasing shrinkage for higher replacement levels of OPC by CFC. The addition of fly ash has the same influence on the chemical shrinkage as the addition of CFC. Higher chemical shrinkage values for fly ash cements were also reported by other researchers [64, 67], as a result of the filler effect and partly as a result of the early pozzolanic reaction of fly ash. The results of the evolution of the portlandite and amorphous phases content at early ages (see Fig. 5.8), confirm the formation of additional hydration products in the RC II and CFC 30 mix, resulting in more chemical shrinkage. The higher cumulative hydration rate per OPC content also explains the higher early-age chemical shrinkage of the blended cement compositions.

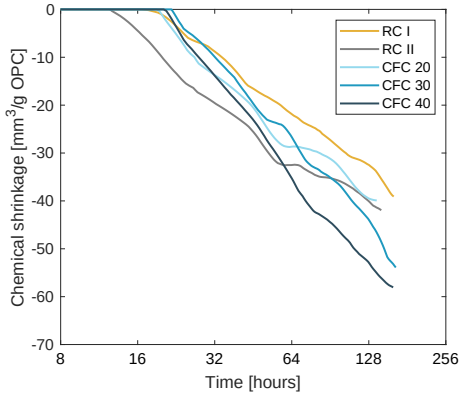

Figure 6.1: Chemical shrinkage of the different cement paste samples up to 7 days, plotted as from final setting (negative values = shrinkage).

6.2 Autogenous shrinkage

Cement paste

The results of the autogenous deformations of the cement paste samples, measured with the corrugated tube method, are shown in Fig. 6.2. Very large autogenous deformations are observed for all mixes and no trend can be noticed between the different cement paste compositions. The initial sharp decrease of the autogenous deformations is attributed to chemical shrinkage and internal settling of the cement paste in the tube. Before setting, the autogenous

shrinkage is completely attributed to chemical shrinkage. Furthermore, after filling of the corrugated tube and placing the tube in the metallic frame, some movement/settling of the cement paste in the tube can still occur (due to improper filling/closure of the tubes), resulting in relatively large deformations measured. Since the autogenous tube method does not allow accurate determination of the deformations occurring when the cement paste is still in its fluid state, the results of the autogenous deformation measurements should only be interpreted as from time-zero. As already described in subsection 2.5.1., time-zero is defined as the moment when the cement paste transforms from fluid to solid, or the moment when autogenous shrinkage starts to diverge from chemical shrinkage and becomes the result of self-desiccation.

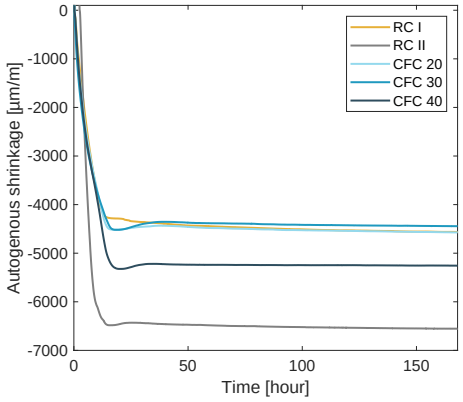

Figure 6.2: Measured autogenous deformations of the different cement paste samples up to 7 days (negative values = shrinkage).

Time-zero (t_0) Different approaches exist to determine time-zero and the three main definitions, found in the literature, are: the final setting time, the change of slope of the autogenous deformation curve (the start of the swelling peak) or the onset of the RH drop. The autogenous shrinkage results of the cement paste samples, plotted from the three defined time-zero's, are shown in Fig. 6.3. Both the final setting time according to the Vicat method and the final setting time according to the ultrasonic method ($t(\delta V_P^{max})$) are considered. The δV_P^{max} criteria was chosen since this inflection point corresponds to the solid percolation threshold, i.e. the moment when solid phases are connected. What stands out immediately are the remarkable swelling peaks observed for the blended cement mixtures. This swelling behaviour is discussed in the next paragraph. Regarding the four considered definitions of time-zero, it is observed that all approaches approximately result in the same autogenous

shrinkage/swelling behaviour, except for the Vicat final setting time approach. The shrinkage behaviour of the RC II mix also deviates for $t_0 = t(\delta V_P^{max})$, as was already remarked in subsection 5.2.2. Both the onset of the internal relative humidity drop and the solid percolation threshold, thus, correspond very well with the start of the observed swelling peak and, thus, the start of the self-desiccation shrinkage. This also confirms the accuracy of the UPV method (δV_P^{max} criteria) for final setting time determination, compared to the Vicat method.

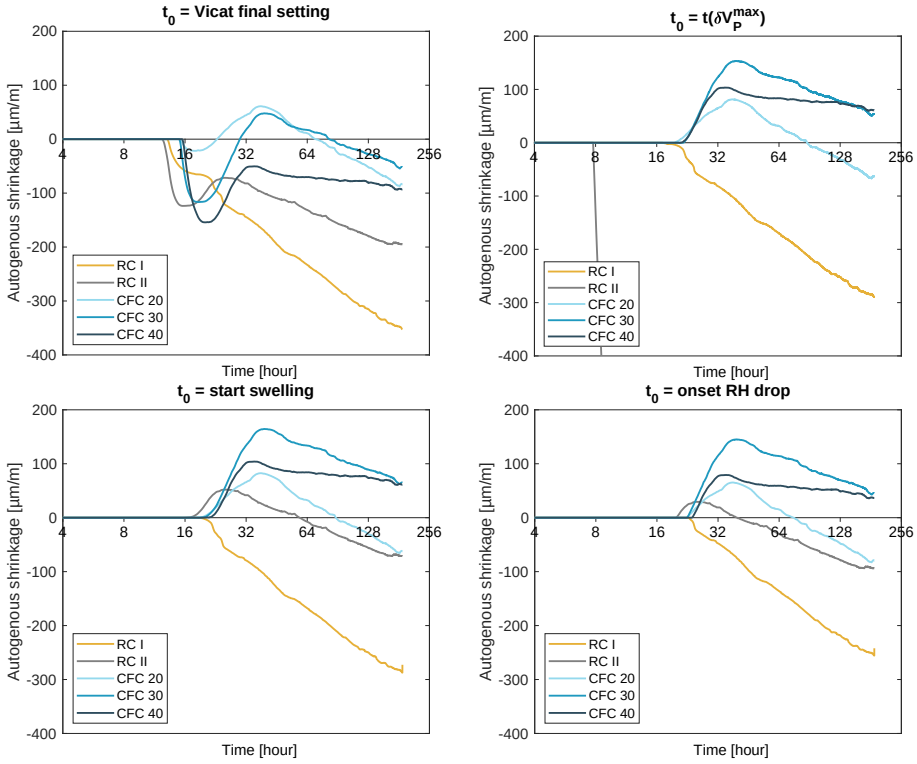

Figure 6.3: Autogenous deformation of the different cement paste samples up to 7 days for W/B = 0.42, plotted as from Vicat final setting (upper left), from δV_P^{max} (upper right), from the start of the swelling (bottom left) and from the onset of the RH drop (bottom right) (negative values = shrinkage).

An overview of the main characteristics of the autogenous deformation curves, i.e. start and amplitude of the swelling, and start and slope of the shrinkage, is given in Table 6.1 (corresponding to t_0 = start swelling).

Table 6.1: Characteristics of the swelling and shrinkage of the autogenous deformation curves for the different cement paste mixes.

	RC I	RC II	CFC 20	CFC 30	CFC 40
Start swelling [h]	16.86	15.61	17.95	18.70	20.17
Amplitude swelling [µm/m]	0.06	52.07	82.50	164.50	104.06
Start shrinkage [h]	17.83	25.07	37.78	39.42	35.08
Slope shrinkage [µm/m]	-2.04	-0.92	-1.06	-0.69	-0.28

Swelling The biggest swelling peaks are observed for the RC II and CFC blended cement mixes. Swelling starts few hours after final setting and lasts for 15 to 20 hours. Early-age expansion has been reported by other researchers [22, 58, 154] for medium to high W/B ratios and can be the result of several phenomena. First of all, the swelling peak can be partially attributed to the *reabsorption of bleeding water* [46, 154]. In order to investigate this possible cause, autogenous shrinkage measurements at a higher water-to-binder ratio (W/B = 0.5) were performed and the results are shown in Fig. 6.4. Since for the same water-to-binder ratio, the swelling is clearly higher for higher CFC replacement ratios (30% and 40%), and since the swelling peaks do not decrease for the lower W/B ratio (0.42), compared to the higher W/B ratio (0.5), there must be another reason for the observed expansion.

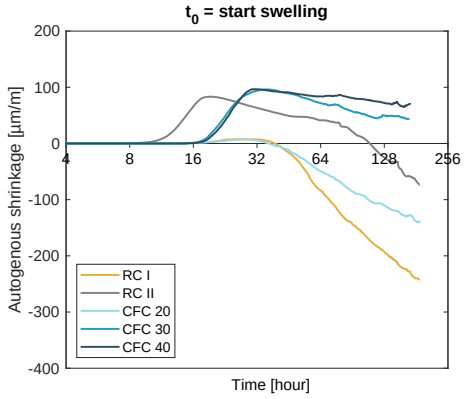

Figure 6.4: Autogenous deformation of the different cement paste mixes up to 7 days for W/B = 0.5, plotted from the start of swelling (negative values = shrinkage).

From calorimetry results, is it also clear that the swelling is not a result of *thermal swelling* caused by a temperature increase due to the heat of hydration.

The developed cumulative heat per g binder of the reference mix is higher than that of the CFC mixes, while the swelling peaks are higher for the CFC mixes. Furthermore, the small size of the test specimens ensures the thermal variations to disappear quickly, while the swelling lasted for more than 15 hours [22]. Fig. 6.5 shows the autogenous deformations (plotted from the start of the swelling) and the heat flow curves as a function of time. These graphs confirm the exclusion of thermal swelling as a cause of the autogenous swelling, since the observed swelling started after the main hydration peak.

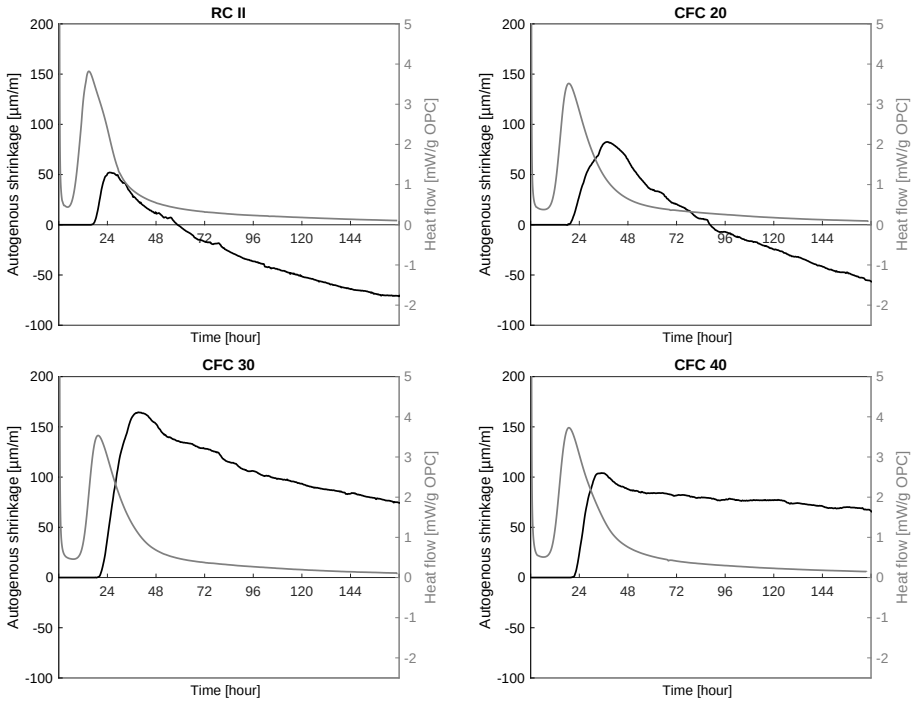

Figure 6.5: Comparison between the autogenous deformations (t_0 = start swelling) and heat flow for the different blended cement paste mixes.

Other possible explanations for the observed swelling peak are the *formation/ growth of hydration products*, such as ettringite, portlandite, AFt needles, AFm crystals, etc. (= structural swelling), or *water absorption by the filler* [22, 58, 61]. From chemical point of view, the formation of hydration products leads to a decrease in volume, known as the chemical shrinkage. However, crystal growth can generate a crystallisation pressure on the pore walls, inducing expansion of the microstructure [58]. In case of the FA and CFC compositions, growth of portlandite crystals is not plausible, since the pozzolanic reaction is known to

consume portlandite [207], and the mixes with the highest CFC levels show the highest swelling peak. During the very early ages, the pozzolanic reaction has not yet started. However, per g binder, the portlandite content is still higher for the RC I mix (7.12 g/100 g binder after 20 hours, compared to 7.01 g/100 g binder for the RC II mix and 4.06 g/100 g binder for the CFC 30 mix after 20 hours). The formation of ettringite, on the other hand, is more likely, since the presence of FA and CFC increases the amount of ettringite per g OPC. Expansion of the cement matrix associated to the formation or crystallisation of ettringite is known for calcium aluminate cements and calcium sulfoaluminate cements. The most plausible mechanism of expansion of these cements is the theory of crystallisation pressure, where the driving force for the development of the crystallisation pressure is the supersaturation of the pore solution with respect to ettringite. The main factors determining the expansion are the sulphate to aluminate ratio, the hydration kinetics and the pore structure. The higher the sulphate to aluminate ratio, the greater the expansion, since higher degrees of supersaturation towards ettringite are reached (after solidification of the cement matrix), hereby increasing the associated crystallisation pressures. A fast depletion of calcium sulphate and fast formation of ettringite, on the other hand, will decrease the expansion [34, 35, 99, 232].

Fig. 6.6 shows the autogenous swelling together with the evolution of the ettringite content of the RC II and CFC 30 mixes as a function of time. For both blended cement mixes, swelling starts during the increase in ettringite content, and shrinkage starts as the ettringite content stabilises/drops. The swelling, thus, does not immediately start from the moment ettringite starts

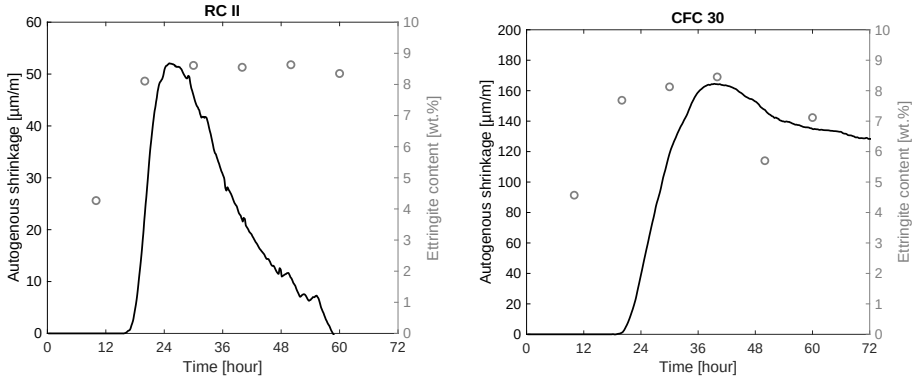

Figure 6.6: Comparison between the autogenous deformations (black lines) and evolution of the ettringite content (gray dots) for the RC II mix (left) and CFC 30 mix (right) (positive values = swelling).

to form. This can be explained by the fact that first a certain degree of solidification of the matrix needs to be reached (setting needs to be completed), before certain degrees of supersaturation of the pore solution with respect to ettringite can be obtained. The swelling therefore starts after final setting, when a dense solid cement paste matrix is formed, and after the sulphate content in the pore solution reaches supersaturation, causing a crystallisation pressure. Furthermore, the sulphate to aluminate ratio will also be higher for the RC II and CFC 30 blended cement mixes, due to the higher total sulphate levels [200, 207] and the smaller amounts of available alumina. This results in a high continuous supply of sulphates to the pore solution, causing high degrees of supersaturation towards ettringite.

The above findings leave the theory of crystallisation pressure, as a result of the supersaturation of the pore solution with respect to ettringite, as the most plausible mechanism of the expansion/swelling of the FA and CFC blended cement paste mixes. In order to confirm this explanation, an extra autogenous shrinkage test was performed on the CFC 30 cement paste mix with additional amount of gypsum (5 wt.%). An extra amount of gypsum available in the cement paste increases the amount of sulphates in the pore solution, enhancing the formation of ettringite. An increased autogenous swelling peak would thus be expected for the CFC 30 cement paste mix with gypsum, if crystallisation pressure due to ettringite formation, is the cause of the observed swelling. The results of the autogenous deformations of the CFC 30 cement paste mix with and without extra addition of gypsum are shown in Fig. 6.7. A larger swelling peak is clearly observed for the CFC 30 mix with additional amount of gypsum.

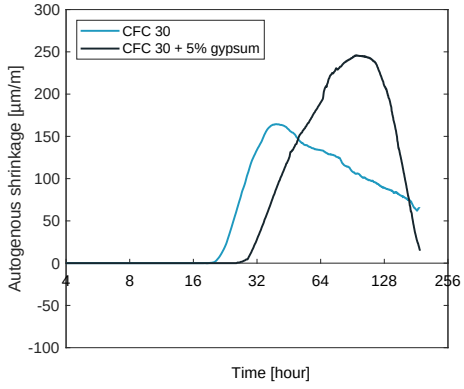

Figure 6.7: Autogenous deformations of the CFC 30 cement paste mix with addition of 5% gypsum, compared to the original CFC 30 cement paste mix (positive values = swelling).

This proves the crystallisation pressure due to ettringite formation to be the main cause of the autogenous swelling peak. The swelling peak of the CFC 30 mix with gypsum addition starts to occur later than the swelling peak of the original CFC 30 mix. This can be explained by the lower workability of the CFC 30 mix with gypsum addition, and less amount of water available for hydration, delaying the hydration process and setting.

Shrinkage After the swelling period, and as long as the hydration proceeds, shrinkage occurs at a decreasing rate. The slopes of the autogenous shrinkage curves of the different mixes are summarised in Table 6.1. It is observed that the slope decreases for increasing replacement ratios of OPC by CFC. The shrinkage rate thus decreases when more CFC is added, positively influencing the total autogenous shrinkage after 7 days. This is also clearly visible in Fig. 6.3, where a strong decline of the RC I curve is observed, while the CFC 40 curve tends to stabilise. The same behaviour is also observed for the RC II mix with fly ash and was already noted by other researchers [5, 211, 215]. Different explanations for the low autogenous shrinkage of fly ash cements, found in literature, are: less hydration due to the dilution effect and lower early activity of fly ash [124, 211] and larger amount of free water due to the spherical shape of fly ash particles [211]. The lower autogenous shrinkage of the CFC mixes at early ages can, in the first place, be explained by the dilution effect (i.e. less hydration due to less cement, resulting in less shrinkage). Furthermore, the formation of different AFm phases also positively affects the total solids volume, as the decomposition of ettringite to monosulphate is prevented due to the presence of hemicarbonate, and voluminous ettringite is stabilised [207].

Finally, the influence of the PCE superplasticizer on the autogenous deformations was neglected, since it was reported by other researchers that the influence of type and dosage of superplasticizer on the autogenous shrinkage was marginal [100, 108, 213].

Autogenous shrinkage versus RH Since self-desiccation shrinkage is mainly related to the decrease of RH in the capillary pores, autogenous shrinkage can be plotted against the development of the internal relative humidity (see Fig. 6.8), expecting a certain (linear) relationship. It is observed that for the same RH, significantly different autogenous shrinkage values are observed for the different cement paste compositions. The early-age observed swelling peak for the blended cement mixes ensures the autogenous shrinkage to start only from a certain degree of emptying of the capillary pores (RH $< 100\%$). Furthermore, from the moment of start of shrinkage, a linear relationship is observed between the autogenous shrinkage and the decrease in RH due to self-

desiccation (RH_K). The slopes of this relationship are summarised in Table 6.2. Ignoring the slope of the CFC 40 mix, it is observed that the slopes of the blended cement mixes are higher than the slope of the OPC reference mix, with increasing slope for increasing replacement level of cement by CFC. This means that with decreasing RH, the blended cement mixes encounter more autogenous shrinkage, compared to the OPC cement paste, for the same decrease in RH. This suggests the porosity of the CFC blended cement mixes to be finer than that of the OPC reference mix. The RH decrease of the CFC blended cement paste mixes, however, develops slower in time, resulting in lower autogenous shrinkage values. The deviating slope value for the CFC 40 mix, is probably due to its lower RH range achieved/reached after 7 days. It is thus concluded that CFC behaves as a typical SCM, reducing the RH drop and accordingly developing lower autogenous shrinkage.

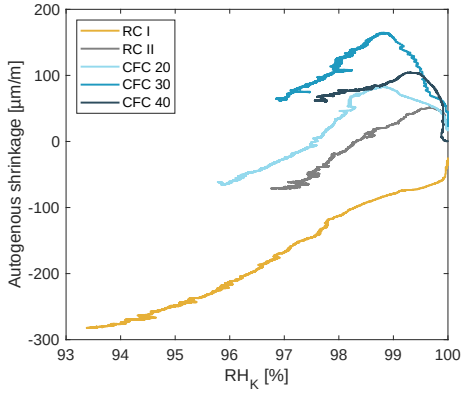

Figure 6.8: Autogenous deformations as a function of the internal relative humidity development up to 7 days, for the different cement paste mixes.

Table 6.2: Slopes of the relationship between the autogenous shrinkage and RH development for the different cement paste mixes.

	Slope [µm/m]
RC I	38.6
RC II	51.1
CFC 20	50.4
CFC 30	54.3
CFC 40	20.3

Concrete

The average autogenous deformations of the concrete samples, measured with the BTJADE device, are shown in Fig. 6.9, plotted from final setting. Compared to the OPC reference mix (RC I), the addition of CFC clearly results in a decrease in the autogenous shrinkage by self-desiccation. Compared to the reference mix with fly ash (RC II), the shrinkage behaviour of CFC is similar. At high replacement ratios (40%), the CFC blended concrete reaches the same autogenous shrinkage values as the RC II mix with fly ash, after 14 days. The mixes with lower replacement ratios (20% and 30% CFC) and the OPC reference mix, on the other hand, develop more autogenous shrinkage. The lower shrinkage of the blended cement concretes can be explained by the dilution effect and the occurrence of a small swelling peak after about 1 day. This swelling peak was already observed for cement paste mixes and was attributed to the formation of ettringite [224]. A lower autogenous shrinkage for concrete mixtures with fly ash was already reported by other researchers [5, 124, 211, 215, 227] and was attributed to the low reactivity of FA, the inhibited hydration reaction at early age and the dilution effect [124, 227]. Bouhamou et al. [38] also reported lower autogenous deformations for concrete mixes with calcined mud.

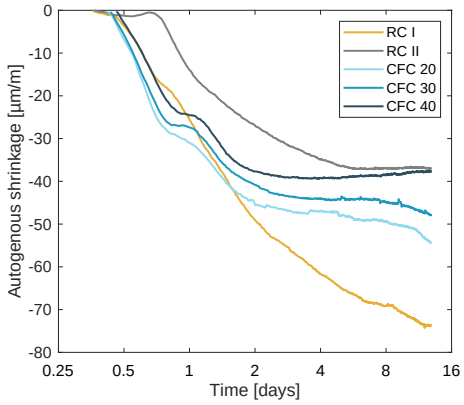

Figure 6.9: Autogenous shrinkage development of the different concrete mixes up to 14 days (negative values = shrinkage).

6.3 Drying shrinkage

Drying shrinkage strains

The drying shrinkage of the studied concrete mixes was determined in two ways: by means of continuous measurements up to 90 days (at KU Leuven) and by means of manual measurements (at ENS Cachan), allowing corresponding mass loss measurements and creep determination (see Chapter 7). The measured deformations are the total shrinkage deformations (combination of drying and autogenous shrinkage), but are in this section further called 'drying shrinkage'.

The average results of the drying shrinkage deformations are shown in Fig. 6.10, both for the continuous measurements (left), as for the manual measurements (right). The drying shrinkage was only measured for the two CFC mixes with the highest replacement ratio (CFC 30 and CFC 40), in which the highest impact of CFC was expected. The drying shrinkage at KU Leuven was measured on cylindrical test specimens (ϕ 120 mm x 300 mm) and drying started after 1 day, while the drying shrinkage at ENS Cachan was measured on prismatic test specimens (80 x 80 x 270 mm) and drying only started after 2 days. The environmental drying conditions were almost the same: at KU Leuven, drying occurred at 20°C and 60% RH, while at ENS Cachan, drying occurred at an average temperature of 22.4°C and average RH of 55.5%. Furthermore, error bars, representing the standard deviations of the results, are shown in Fig. 6.10, as the drying shrinkage was measured on three different specimens. Much

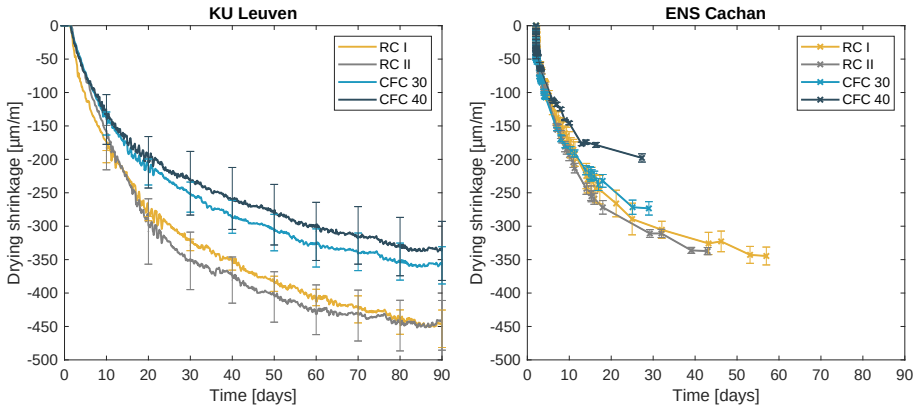

Figure 6.10: Drying shrinkage of the different concrete mixes up to 90 days, determined by continuous measurements at KU Leuven (left) and by manual measurements at ENS Cachan (right) (negative values = shrinkage).

higher standard deviations are observed for the continuous measurements at KU Leuven, with an average standard deviation of 6.75%, while the average standard deviation of the manual measurements at ENS Cachan was only 1.9%.

In general, lower drying shrinkage values are observed for the CFC blended cement mixes, compared to the OPC and FA reference mixes. The RC II mix follows the same trend as the CFC blended cement mixes at early ages. However, from about 7 days the drying shrinkage of the RC II mix starts to increase more, and reaches about the same values as the RC I mix. The relationship between the drying shrinkage of the different concrete compositions agrees well for both methods (CFC 40 < CFC 30 < RC I < RC II), only the drying shrinkage of the CFC 30 mix deviates. The drying shrinkage results of ENS Cachan overall shows slightly lower values, compared to the drying shrinkage results of KU Leuven. Furthermore, the initial slope of the manual drying shrinkage results is much steeper, compared to the initial slope of the continuous measurements. The differences in specimen size, start of drying and drying conditions can explain this behaviour. The decreased drying shrinkage due to addition of CFC can most probably be explained by the dilution effect and the altered porosity and pore size distribution of the CFC blended cement concretes. A decrease in drying shrinkage was also observed for concrete with addition of calcined mud [38]. For concrete mixes with fly ash, a decrease in drying shrinkage was reported by most researchers, ascribed to the reduced hydration rate and the pore refinement of FA [1, 124, 183, 227]. Akkaya et al. [5], however, also reported increased drying shrinkage.

Drying shrinkage weight loss

Along with the manual drying shrinkage measurements at ENS Cachan, the corresponding mass loss was also measured. The results of the drying shrinkage weight loss as a function of both time and drying shrinkage strains are shown in Fig. 6.11, respectively. It is immediately observed from Fig. 6.11 that the mass loss of the blended cement mixes is significantly higher than the mass loss of the OPC reference mix, with increasing weight loss for increasing replacement of cement by CFC. The higher mass loss of the blended cement concretes at early ages can be explained by their slower hydration and slower development of a porous network, allowing free water to evaporate more easily [167]. It is also observed from Fig. 6.11 that initially, the weight loss increases with low increase in drying shrinkage strains (especially for the blended cement mixes), while at later ages, the drying shrinkage strains significantly increase with increasing drying shrinkage weight loss. During the early ages, the biggest capillary pores empty first, according to Laplace's law ($\Delta p = 2 \cdot \gamma / r$), resulting in a lot of mass loss and little shrinkage (due to the lower capillary pressures developed in the

bigger pores). When the hydration continues, pores with smaller pore sizes empty, resulting in higher capillary tension and consequently higher drying shrinkage, but less weight loss.

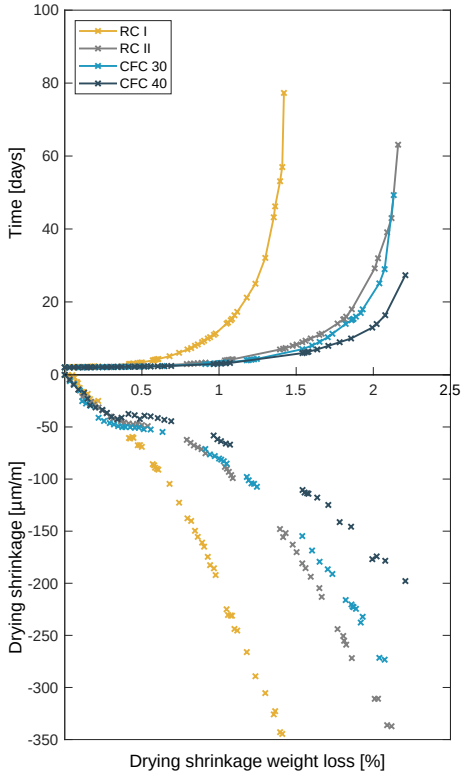

Figure 6.11: Drying shrinkage weight loss as a function of time (above) and as a function of the drying shrinkage strains (ENS Cachan) (below) for the different concrete mixes.

The drying shrinkage weight loss versus drying shrinkage strain curve can thus be divided into two parts with different slopes (see Fig. 6.12). These results are similar to those obtained by Granger [111] and Olivier [167]. In order to quantify this behaviour, the double slopes of the curves are calculated and summarised in Table 6.3. The initial slopes (slope 1) are all lower than the slopes of the second part of the curve (slope 2), confirming the previously described behaviour. This behaviour is also more pronounced for the blended cement concretes, as observed by much lower initial slopes. Initially, the drying shrinkage weight loss is thus much higher for the blended cement mixes, compared to the OPC reference mix, for the same increase in drying shrinkage strains. The smaller mass loss

of the OPC reference mix during the first day can be explained by a faster development of the porous network and therefore larger stresses in the solid skeleton. In the blended cement concretes, on the other hand, higher initial weight losses occur because the porous network is not yet completely developed and free water can evaporate easily [167]. Table 6.3 also summarises the slopes of the two curves as found in the literature [167]. It is observed that the slopes of the RC I mix correspond well with the slope found for a CEM I reference mix. A lower slope was also found for slag blended cement concretes, as observed for the CFC and FA blended cement concretes.

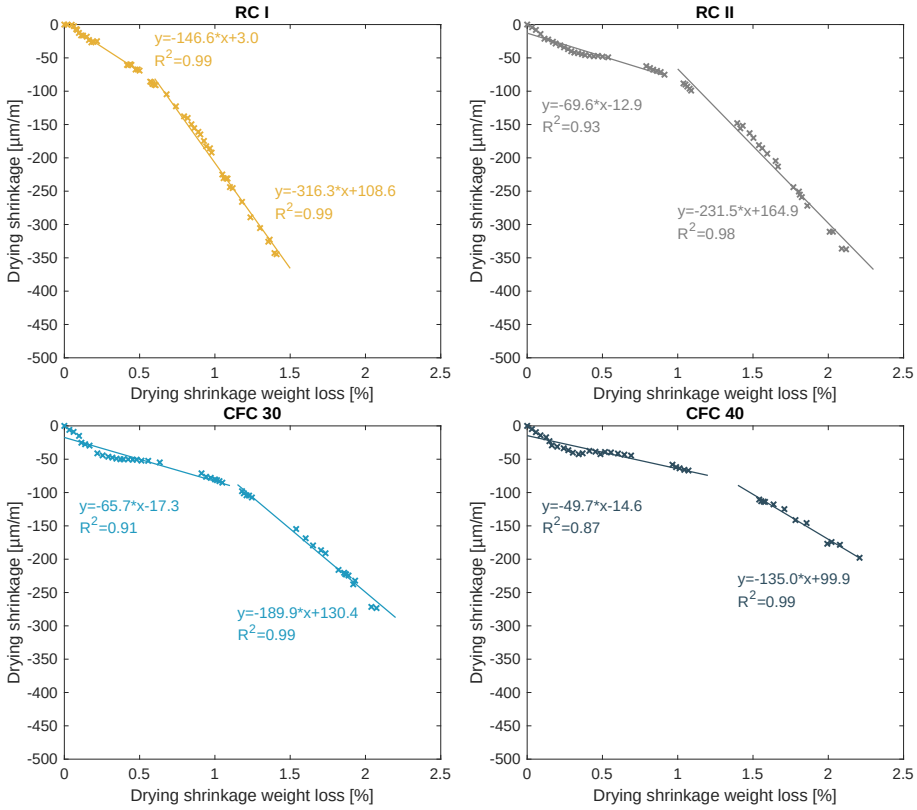

Figure 6.12: Drying shrinkage strains as a function of the drying shrinkage weight loss, with corresponding trendlines, of the different concrete mixes.

Table 6.3: Slopes of the relationship between the drying shrinkage strains and weight loss, for the different concrete mixes and compared to the literature.

[μm/m]	Slope 1	Slope 2
RC I	-146.6	-316.3
RC II	-69.6	-231.5
CFC 30	-65.7	-189.9
CFC 40	-49.7	-135.0
CEM I [167]	-108.1	-281.3
CEM III/A [167]	-56.4	-258.5
CEM I + GBFS [167]	-0.55	-174.0

6.4 Modelling

Modelling of concrete shrinkage, calibrated by early-age experimental data, allows prediction of the concrete shrinkage at later ages. Autogenous and drying concrete shrinkage is modelled using empirical shrinkage models. These models are parametrised for the CFC blended cement concretes, by considering the cement type dependent parameters as fitting parameters. Mechanistic shrinkage models, based on poroelasticity, on the other hand, are used for autogenous shrinkage modelling of the cement paste samples. The Biot-Bischop approach is evaluated for the CFC blended cement pastes, by using experimentally determined input parameters.

6.4.1 Empirical shrinkage models

Empirical shrinkage models generally describe shrinkage as the product of two terms: the final/ultimate shrinkage ϵ_∞ (a magnitude function) and the shrinkage rate β or S (a time function). For autogenous shrinkage, the general equation is:

$$\epsilon_{as}(t) = \epsilon_{as\infty} \cdot \beta(t) \tag{6.1}$$

where $\epsilon_{as\infty}$ is the ultimate autogenous shrinkage, depending on the concrete mix design and mechanical properties, and $\beta(t)$ is the autogenous rate function. For drying shrinkage, the general equation is:

$$\epsilon_{ds}(t) = \epsilon_{ds\infty}(RH,T) \cdot S(t, t_s, h_0) \tag{6.2}$$

where $\epsilon_{ds\infty}$(RH,T), the ultimate drying shrinkage, depends both on the concrete mix design and mechanical properties, as well as on the initial and external conditions: ambient temperature (T) and relative humidity (RH). The rate

function $S(t, t_s, h_0)$ depends on the age of the concrete (t), the age of the concrete at the start of drying (t_s) and the notional size of the specimen (h_0), defined as:

$$h_0 = \frac{2 \cdot V}{S} \tag{6.3}$$

where V is the volume and S the drying surface of the specimen. In this case the notional size is taken as D/2 (with D the diameter of the specimen), neglecting drying at the top and bottom of the specimen. This assumption is acceptable, since the ratio of the height of the specimen to the diameter of the specimen, is relatively high (i.e. 2.5).

Autogenous shrinkage

For autogenous shrinkage, five different existing models are considered: the Bazant B4 model [18], the Eurocode 2 model [77], the Model code 2010 model [129], the β-n model (see Eq. 5.27-5.28) and a model described by Rifai [176]. The expressions of the different autogenous shrinkage models, as a function of the equivalent time (t_{eq}), are summarised below. The autogenous shrinkage only starts to develop from the moment of final setting (t_0).

- Bazant B4 model:

$$\epsilon_{as}(t_{eq}) = \epsilon_{as\infty} \cdot \left[1 + \left(\frac{\tau_{as}}{t_{eq} - t_0}\right)^{\alpha}\right]^{r_t} \tag{6.4}$$

  where $\epsilon_{as\infty}$ (the final autogenous shrinkage), τ_{as} (the autogenous shrinkage halftime), α and r_t are cement type dependent parameters, determined by fitting the experimental results to the model [18].

- Eurocode 2 (EC 2) model:

$$\epsilon_{as}(t_{eq}) = \epsilon_{as}(\infty) \cdot \beta_{as}(t_{eq}) \tag{6.5}$$

  with $\epsilon_{as}(\infty)$ the final autogenous shrinkage and $\beta_{as}(t_{eq})$ the time function, described as:

$$\epsilon_{as}(\infty) = 2.5 \cdot (f_{ck} - 10) \cdot 10^{-6} \tag{6.6}$$

$$\beta_{as}(t_{eq}) = 1 - \exp\left(-0.2 \cdot \sqrt{t_{eq} - t_0}\right) \tag{6.7}$$

  with f_{ck} the characteristic compressive strength of the concrete [77].

- Model code 2010 (MC 2010) model:

$$\epsilon_{as}(t_{eq}) = \epsilon_{as,0}(f_{cm}) \cdot \beta_{as}(t_{eq}) \tag{6.8}$$

with $\epsilon_{as,0}(f_{cm})$ the notional autogenous shrinkage coefficient and $\beta_{as}(t_{eq})$ the time function, described as:

$$\epsilon_{as,0}(f_{cm}) = -\alpha_{as} \cdot \left(\frac{f_{cm}}{60 + f_{cm}}\right)^{2.5} \cdot 10^{-6} \tag{6.9}$$

$$\beta_{as}(t_{eq}) = 1 - \exp\left(-0.2 \cdot \sqrt{t_{eq} - t_0}\right) \tag{6.10}$$

with α_{as} a cement type dependent parameter, considered here as a fitting parameter, and f_{cm} the mean concrete compressive strength [129].

- β-n model:

$$\epsilon_{as}(t_{eq}) = \epsilon_{as,28} \cdot \beta_{\epsilon_{as}}(t_{eq})^{n_{\epsilon_{as}}} \tag{6.11}$$

with $\epsilon_{as,28}$ the autogenous shrinkage value after 28 days and $n_{\epsilon_{as}}$ an aging parameter, both considered as fitting parameters. $\beta_{\epsilon_{as}}(t_{eq})$ is the time function, described as:

$$\beta_{\epsilon_{as}}(t_{eq}) = \exp\left[s \cdot \left(1 - \sqrt{\frac{28 - t_0}{t_{eq} - t_0}}\right)\right] \tag{6.12}$$

with s a cement type dependent parameter, already determined for every concrete composition in Chapter 5, subsection 5.5.2.

- Rifai model:

$$\epsilon_{as}(t_{eq}) = y_0 + A_1 \cdot \exp\left(-\frac{t_{eq} - t_0}{t_1}\right) + A_2 \cdot \exp\left(-\frac{t_{eq} - t_0}{t_2}\right) \tag{6.13}$$

with y_0, A_1, A_2, t_1 and t_2 all fitting parameters [176].

It should be noted that for the Bazant B4 model, a simplified model from [18] is used. Parameters $\epsilon_{as\infty}$, τ_{as}, α and r_t are directly considered as cement type dependent fitting parameters, rather than calculating them from an even larger set of cement type dependent parameters. It should also be remarked that all models, except for the Eurocode 2 model, depend on one or more cement type depending parameters, which are all considered as fitting parameters. The amount of fitting parameters strongly determines the goodness of fit. The Eurocode 2 model does not depend on the cement type, only on the compressive strength of the concrete mix. Furthermore, the Rifai model does not follow the general mathematical formula for autogenous shrinkage development (see Eq. 6.1), but uses a different formulation. Finally, all cement type dependent fitting parameters of the CFC mixes are (as also with the cement type dependent mechanical properties parameters) taken as constant, in order to get general/uniform cement type dependent parameters for all CFC mixes.

The results of the model fitting are presented in Fig. 6.13 and the corresponding model parameters can be found in Appendix E.

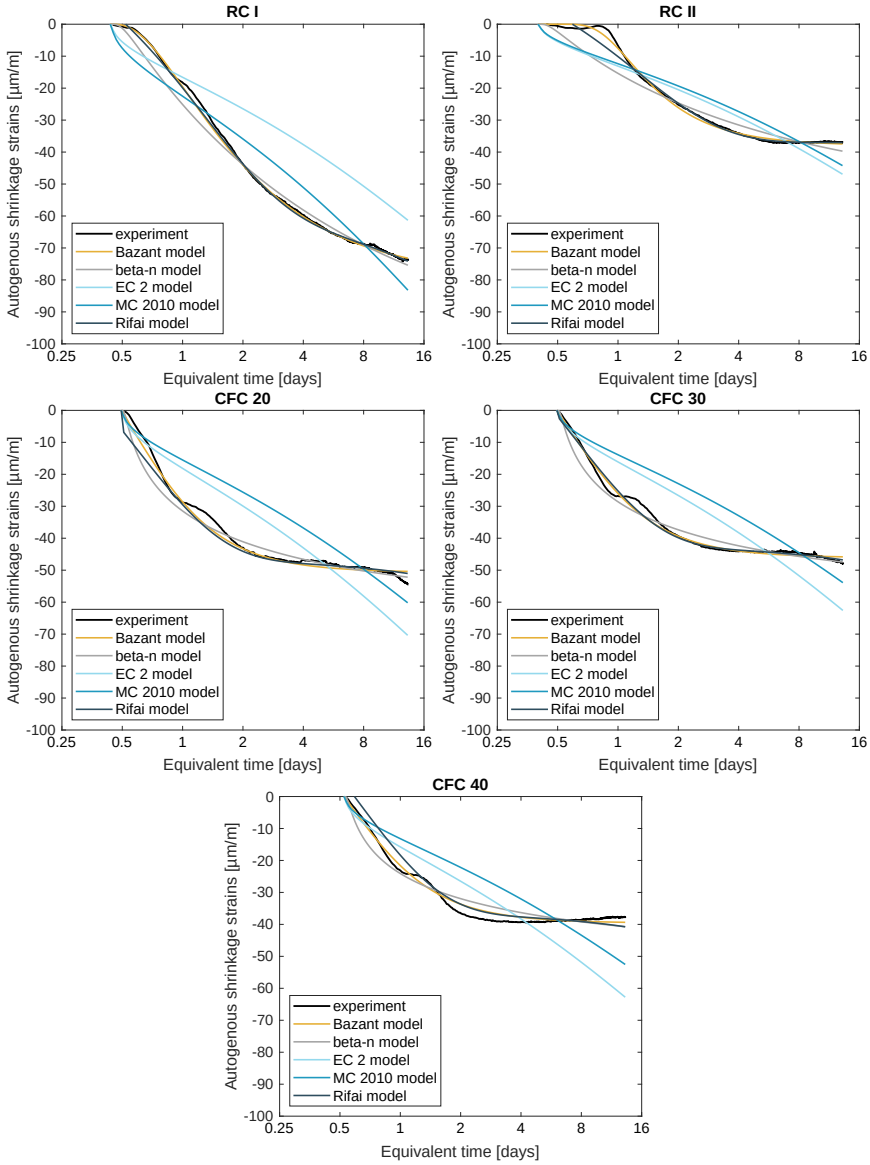

Figure 6.13: Different autogenous shrinkage models for the different concrete mixes, compared with the experimental results.

At first sight, it is remarkable that the Eurocode 2 model and Model code 2010 model deviate significantly from the experimental results, both at very early ages, as well as at later ages. Since the same time functions β were used for both models, the models follow the same shrinkage development, slightly differing due to a different final autogenous shrinkage value. The other three models (Bazant model, β-n model and Rifai model) all predict the autogenous shrinkage quite well. However, the small autogenous swelling, which is observed for the CFC mixes, cannot be taken into account in the different models. At early ages all models therefore over- or underestimate the real autogenous shrinkage.

In order to compare the different models and determine the best predictor, a root mean square error (RMSE) is determined. The RMSE of the different autogenous shrinkage models for the different concrete compositions is shown in Fig. 6.14. As already noticed in Fig. 6.13, the EC 2 and MC 2010 models show the biggest error. The difference in error between the other three models is quite small. The small errors of the Bazant model and the Rifai model are quite obvious, since for these models, respectively 4 and 5 fitting parameters were considered. Overall, the Bazant B4 model can be considered as the best predictor for autogenous shrinkage, both for the traditional concrete mix as for the blended cement mixtures.

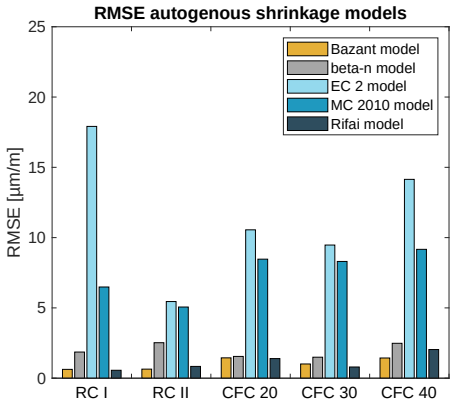

Figure 6.14: RMSE of the different autogenous shrinkage models for the different concrete compositions.

Drying and total shrinkage

Four different existing drying shrinkage models are considered: the Bazant B4 model [18], the EC 2 model [77], the MC 2010 model [129] and the β-n model. The expressions of the different drying models are summarised below.

- Bazant B4 model:

$$\epsilon_{ds}(\tilde{t}, \tilde{t_s}) = \epsilon_{ds\infty}\left(\tilde{t_s}\right) \cdot k_h \cdot S\left(\tilde{t}\right) \tag{6.14}$$

where $\tilde{t_s}$ is the temperature corrected age at start of drying ($t_{s,eq}$) and $\tilde{t}$ is the temperature corrected duration of drying ($t_{eq} - t_{s,eq}$). The humidity dependent correction factor k_h and the time curve $S(\tilde{t})$ are respectively given by:

$$k_h = \begin{cases} 1 - h^3 & h \leq 0.98 \\ 12.94 \cdot (1-h) - 0.2 & 0.98 \leq h \leq 1 \end{cases} \tag{6.15}$$

$$S\left(\tilde{t}\right) = \tanh\sqrt{\frac{\tilde{t}}{\tau_{ds}}} \tag{6.16}$$

with h the ambient relative humidity and τ_{ds} the drying shrinkage halftime, which is:

$$\tau_{ds} = \tau_0 \cdot k_{\tau a} \cdot (k_s \cdot h_0)^2 \tag{6.17}$$

with τ_0 a cement type dependent parameter, $k_{\tau a}$ an aggregate dependent parameter, k_s a parameter depending on the geometry of the specimen and h_0 the notional size or effective thickness of the specimen. The final drying shrinkage ($\epsilon_{ds\infty}$) and the parameter τ_0 are cement type dependent parameters, determined by fitting the experimental results to the model.

- Eurocode 2 model:

$$\epsilon_{ds}\left(t_{eq}\right) = k_h \cdot \epsilon_{ds,0} \cdot \beta_{ds}\left(t_{eq}, t_s\right) \tag{6.18}$$

with k_h a coefficient depending on the effective thickness (h_0), $\epsilon_{ds,0}$ the nominal unrestrained drying shrinkage value and $\beta_{ds}(t_{eq}, t_s)$ the time function, respectively described as:

$$\epsilon_{ds,0} = 0.85 \cdot \left[(220 + 110 \cdot \alpha_{ds1}) \cdot \exp\left(-\alpha_{ds2} \cdot \frac{f_{cm}}{f_{cm0}}\right)\right] \cdot 10^{-6} \cdot \beta_{RH} \tag{6.19}$$

$$\beta_{ds}\left(t_{eq}, t_s\right) = \frac{(t_{eq} - t_s)}{(t_{eq} - t_s) + 0.04 \cdot \sqrt{h_0^3}} \tag{6.20}$$

with α_{ds1} and α_{ds2} coefficients depending on the type of cement, here considered as fitting parameters, f_{cm} the mean concrete compressive strength, f_{cm0} equal to 10 MPa and β_{RH} an ambient relative humidity dependent coefficient, described as:

$$\beta_{RH} = 1.55 \cdot \left[1 - \left(\frac{RH}{RH_0}\right)^3\right] \tag{6.21}$$

with RH the ambient relative humidity and RH_0 equal to 100%.

- Model code 2010 model:

$$\epsilon_{ds}\left(t_{eq}\right) = \epsilon_{ds,0}\left(f_{cm}\right) \cdot \beta_{RH}\left(RH\right) \cdot \beta_{ds}\left(t_{eq}, t_s\right) \tag{6.22}$$

with $\epsilon_{ds,0}\left(f_{cm}\right)$ the notional drying shrinkage coefficient, $\beta_{RH}\left(RH\right)$ a coefficient taking into account the effect of the ambient relative humidity and $\beta_{ds}\left(t_{eq}, t_s\right)$ a time function, respectively described as:

$$\epsilon_{ds,0}\left(f_{cm}\right) = \left[\left(220 + 110 \cdot \alpha_{ds1}\right) \cdot \exp\left(-\alpha_{ds2} \cdot f_{cm}\right)\right] \cdot 10^{-6} \tag{6.23}$$

$$\beta_{RH}\left(RH\right) = \begin{cases} -1.55 \cdot \left[1 - \left(\frac{RH}{100}\right)^3\right] & 40 \leq RH < 99 \cdot \beta_{s1} \\ 0.25 & RH \geq 99 \cdot \beta_{s1} \end{cases} \tag{6.24}$$

$$\beta_{ds}\left(t_{eq}, t_s\right) = \sqrt{\frac{\left(t_{eq} - t_s\right)}{\left(t_{eq} - t_s\right) + 0.035 \cdot h_0^2}} \tag{6.25}$$

with α_{ds1} and α_{ds2} coefficients depending on the type of cement, here considered as fitting parameters, f_{cm} the mean concrete compressive strength, RH the ambient relative humidity and β_{s1} equal to $\left(35/f_{cm}\right)^{0.1}$.

- β-n model:

$$\epsilon_{ds}\left(t_{eq}\right) = \epsilon_{ds,28} \cdot \beta_{\epsilon_{ds}}(t_{eq})^{n_{\epsilon_{ds}}} \tag{6.26}$$

with $\epsilon_{ds,28}$ the drying shrinkage value after 28 days and $n_{\epsilon_{ds}}$ an aging parameter, both considered as fitting parameters. $\beta_{\epsilon_{au}}$ is the time function, described as:

$$\beta_{\epsilon_{ds}} = \exp\left[s \cdot \left(1 - \sqrt{\frac{28 - t_s}{t_{eq} - t_s}}\right)\right] \tag{6.27}$$

with s a cement type dependent parameter, already determined in Chapter 5, subsection 5.5.2.

All drying shrinkage models, except for the β-n model, are depending both on the effective/notional size (h_0) and on the ambient relative humidity (RH). It should also be remarked that only the Eurocode 2 and Model code 2010 models depend on the compressive strength of the concrete mix. Furthermore, all models have the same amount of cement type dependent parameters and thus the same amount of fitting parameters. Also here, these parameters are taken constant for all CFC mixes.

The measured total shrinkage strains are the sum of the drying shrinkage and autogenous deformations. The above described models for drying shrinkage thus only apply for a part of the measured deformations. In order to also take the autogenous deformations into account, the total shrinkage results are modelled

as the sum of the autogenous shrinkage strains and the drying shrinkage strains, using the previously found parameters for the autogenous shrinkage models. The results of the combined model fitting are presented in Fig. 6.15 (using the continuous total shrinkage results of the tests performed at KU Leuven) and the RMSE of the different models is shown in Fig. 6.16. The corresponding model parameters can be found in Appendix E. What stands out immediately is the fact that the total shrinkage model curves do not all start at the same point. This is due to the fact that the previous autogenous shrinkage models are taken into account, and at the moment of start of drying, already some autogenous shrinkage has developed. In general, all four models show a quite good fit, especially at later ages. During the very early ages, the EC 2 and β-n model show a better fit, compared to the Bazant B4 and the MC 2010 model. This is mainly the result of the different descriptions of the time functions for

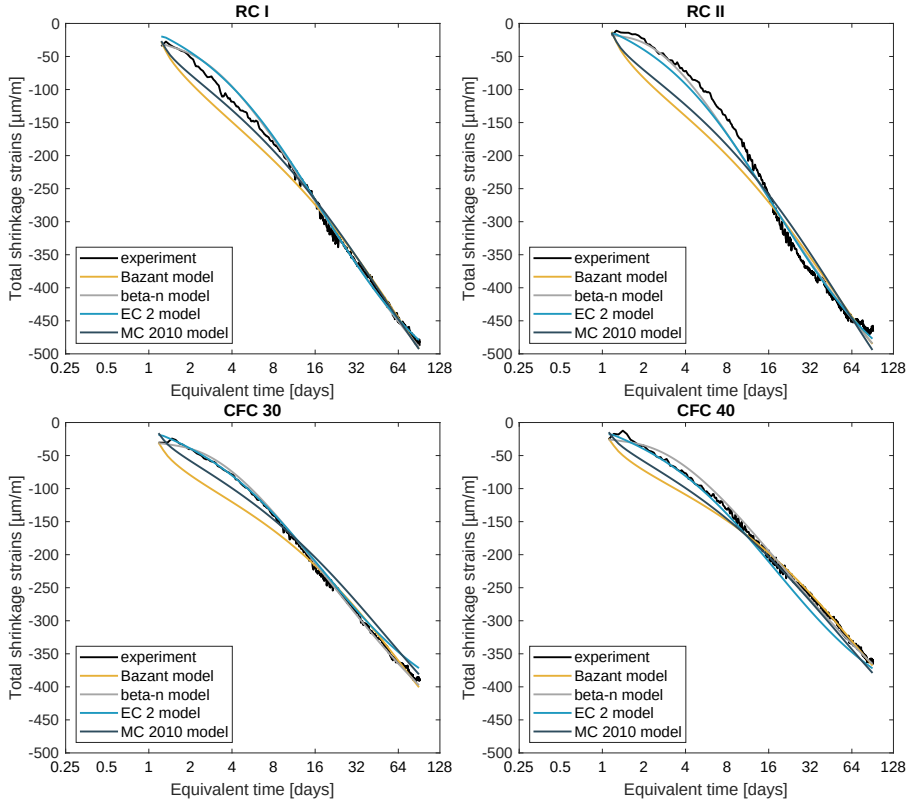

Figure 6.15: Different total shrinkage models for the different concrete mixes, compared with the experimental results.

the different models. At later ages, all models show a quite perfect fit for the RC I mix, while for the blended cement concretes, the Bazant B4 and β-n model show a better fit. Looking at the errors in Fig. 6.16, it can be seen that there is no clear trend between the errors of the different models for the different concrete mixes. For the RC I and RC II mixes, the Bazant B4 and the MC 2010 models show the worst fit, while for the CFC blended cement mixes, the EC 2 and MC 2010 models show the worst fit. Overall, the β-n model appears to be the best predictor for all compositions, followed by the EC 2 model for the two reference mixes and the Bazant B4 model for the two CFC mixes.

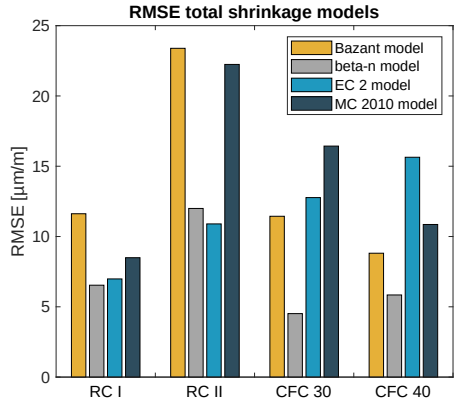

Figure 6.16: RMSE of the different total shrinkage models for the different concrete compositions.

The previously used methodology, however, is not completely correct, since the autogenous deformations occurring in completely sealed (autogenous) conditions, are not equal to the autogenous deformations occurring in a drying environment. In drying conditions, less water is available, so the hydration will be slowed down and will be less complete, resulting in less autogenous shrinkage. The autogenous shrinkage even might be negligible compared to the drying shrinkage strains, in drying conditions. Therefore, also fitting of the drying shrinkage models to the total shrinkage results, neglecting autogenous shrinkage, is performed. The results of the model fitting are presented in Fig. 6.17 and the RMSE of the different models is summarised in Fig. 6.18. The corresponding model parameters can be found in Appendix E.

It is observed from Fig. 6.17 that the same general behaviour as with the total shrinkage model fitting is noticed. The fitting of the Bazant B4 and Model code 2010 model is worse at early ages, while at later ages the fitting of all models is quite good and almost perfect for the RC I mix. Comparing the errors of the total - and drying shrinkage model fitting (Fig. 6.16 and Fig. 6.18), it

can be concluded that for the Bazant B4 and Eurocode 2 model, the error is lower for the drying shrinkage model fitting, while for the β-n model the error is lower for the total shrinkage model fitting. The error of the Model code 2010 model of the reference mixes (RC I and RC II) is higher for the drying shrinkage model fitting, while for the CFC mixes the error was the highest for the total model fitting. However, the differences are marginal. Based on the RMSEs of the different drying shrinkage models (Fig. 6.18), it can thus be concluded that, similar to the total shrinkage model fitting, the β-n model appears to be the best predictor of the drying shrinkage, followed by the EC 2 model for the two reference mixes and followed by the Bazant B4 model for the two CFC mixes. The main drawback of the β-n model is the independence of the ambient relative humidity and notional size, limiting its use in practice.

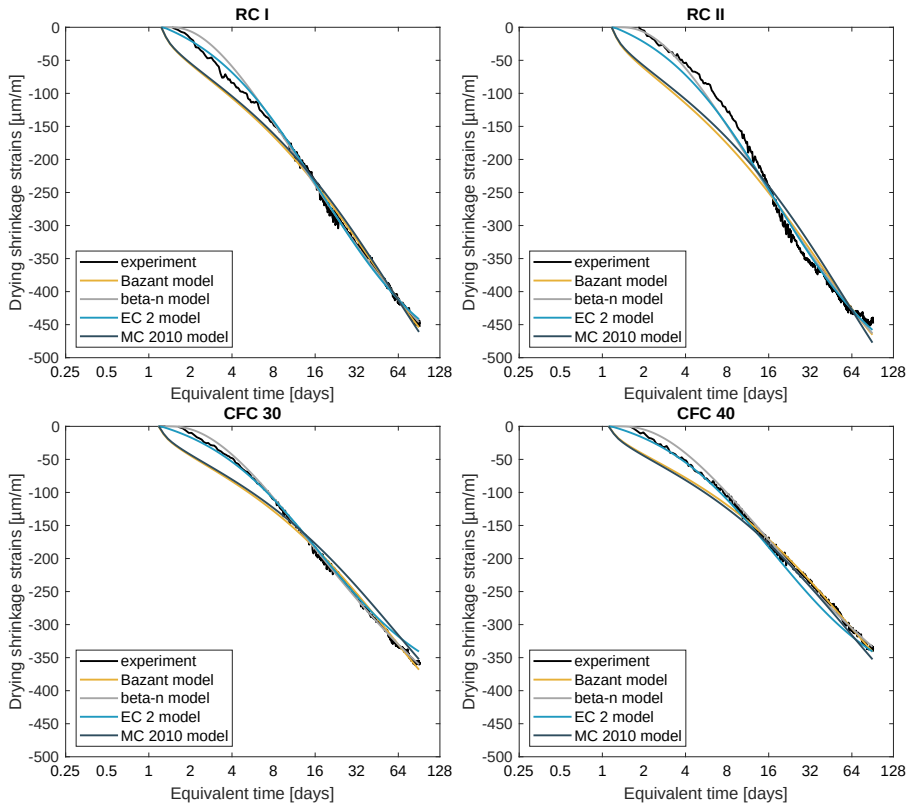

Figure 6.17: Different drying shrinkage models for the different concrete mixes, compared with the experimental results.

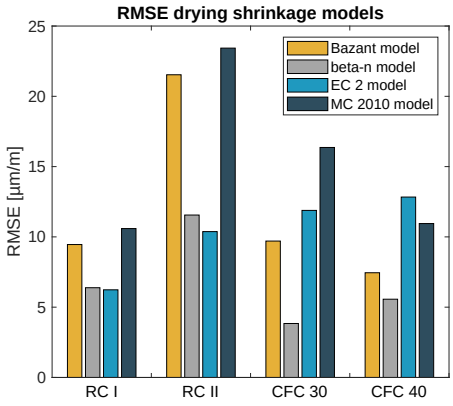

Figure 6.18: RMSE of the different drying shrinkage models for the different concrete compositions.

6.4.2 Mechanistic shrinkage models

In order to predict the autogenous shrinkage strains of the cement paste mixes, the Biot-Bischop approach, being the basis of most poromechanics models, is used:

$$\epsilon = -\mathrm{S_w} \cdot \mathrm{p_c} \cdot \left(\frac{1}{\mathrm{K_b}} - \frac{1}{\mathrm{K_s}} \right) \tag{6.28}$$

with $\mathrm{S_w}$ the water saturation degree, $\mathrm{p_c}$ the capillary pressure in the pores, $\mathrm{K_b}$ the bulk modulus of the porous body and $\mathrm{K_s}$ the bulk modulus of the solid skeleton. The water saturation degree is depending on the degree of hydration and the capillary pressure is depending on the internal relative humidity. Since at early ages the degree of hydration and internal relative humidity are both changing significantly, Eq. 6.28 is converted to Eq. 6.29:

$$\Delta\epsilon = -\Delta\left(\mathrm{S_w} \cdot \mathrm{p_c}\right) \left(\frac{1}{\mathrm{K_b}} - \frac{1}{\mathrm{K_s}} \right) \tag{6.29}$$

This equation takes into account the early-age changes, and should especially be used for early-age autogenous shrinkage prediction. The resulting predicted deformations are the volumetric deformations of the cement paste. Since both autogenous and drying shrinkage are usually measured as linear deformations, the resulting values should be divided by 3, assuming isotropy [230].

Parameter identification

The results of the early-age properties of the different cement paste compositions, measured in Chapter 5, are used as input data for the autogenous shrinkage modelling. Determination/calculation of the different input parameters is described below.

Capillary pressure The capillary pressure (p_c) can be determined from the internal relative humidity measurements according to the Kelvin-Laplace equation:

$$p_c = -\frac{RT \cdot \rho_w}{M_w} \cdot \ln(RH) \tag{6.30}$$

with ρ_w the density of water (1000 kg/m^3), M_w the molecular weight of water (18.02 g/mol), R the ideal gas constant (8.314 J/K/mol), T the temperature (293 K) and RH the development of the internal relative humidity due to self-desiccation (RH_K) inside the cement paste sample. RH_K was already determined in Chapter 5, subsection 5.1.3, and from these results, the capillary pressure development can be calculated (as shown in Fig. 6.19). This capillary pressure thus corresponds to the capillary tension developed in the capillary pores, as a result of the decrease in RH and corresponding self-desiccation. It is observed from Fig. 6.19 that the capillary tension is the highest for the OPC reference mix, due to the highest RH drop, and that the blended cement mixes develop lower capillary tension.

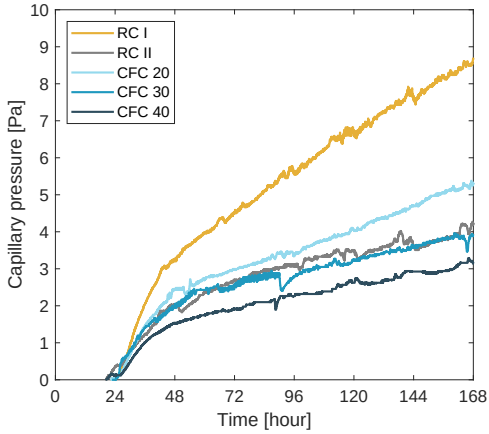

Figure 6.19: Capillary tension development of the different cement paste mixes, calculated from internal RH measurements according to the Kelvin-Laplace law.

Bulk modulus of porous body The bulk modulus of the porous body (K_b) can be calculated using the following formula:

$$K_b = \frac{E}{3 \cdot (1 - 2 \cdot \nu)} \tag{6.31}$$

with E the static elastic modulus, which can be calculated from the ultrasonic measurements (and correlation with the experimentally determined static elastic modulus). The dynamic Poisson's ratio ν, on the other hand, was not determined experimentally and a constant value of 0.22 was assumed. The results of the calculated bulk modulus are shown in Fig. 6.20. The OPC reference mix shows the highest bulk modulus, while lower bulk moduli are observed for the blended cement mixes, due to the dilution effect.

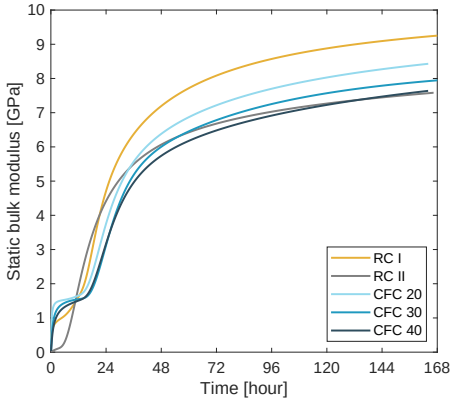

Figure 6.20: Bulk modulus development of the different cement paste mixes, calculated from the ultrasonic measurements.

Bulk modulus of solid skeleton The bulk modulus of the solid skeleton (K_s) depends on the bulk moduli of all solid phases (hydration products) forming in the cement paste and its determination is not trivial. Grasley et al. [113] experimentally quantified the bulk modulus of the solid skeleton for cement paste and concrete, and the results of K_s of the cement paste samples ranged between 40 and 55 GPa. Di Bella et al. [69], however, used a value of 38 GPa for K_s. In this study, the bulk modulus of the solid skeleton was therefore assumed to be 40 GPa.

Water saturation degree The water saturation degree (S_w) is defined as the ratio of the volume of evaporable water (V_{ew}) to the volume of pores (V_p), as a function of the advancement of the degree of hydration (α):

$$S_w = \frac{V_{ew}(\alpha)}{V_p(\alpha)} \tag{6.32}$$

The advancement of the degree of hydration α is defined as the amount of hydrated cement divided by the amount of cement to react at a given term [46] and can be calculated from calorimetry measurements as:

$$\alpha = \frac{Q}{Q_\infty} \tag{6.33}$$

with Q the cumulative heat of the cement paste mixes and Q_∞ the ultimate cumulative heat value, calculated by fitting the cumulative heat results to Eq. 5.18. The results are summarised in Appendix E.

The definition of the water saturation degree is based on Powers' model of the phase distribution of hardening cement paste and the derivation, resulting in Eq. 6.34, can be found in Appendix E.

$$S_w = \frac{p - w_{cbw} \cdot \rho_c/\rho_w \cdot (1-p) \cdot \alpha}{p - [w_{cbw} \cdot \rho_c/\rho_w - \Delta V_{cs} \cdot 10^{-5} \cdot \rho_c] \cdot (1-p) \cdot \alpha} \tag{6.34}$$

The water saturation degree is thus dependent on the density of water (ρ_w) and cement (ρ_c), the advancement of the degree of hydration (α), the amount of chemically bound water (w_{cbw}), the volume of chemical shrinkage (ΔV_{cs}) and the initial porosity (p), depending on the water-to-cement (W/C) ratio:

$$p = \frac{W/C}{W/C + \rho_w/\rho_c} \tag{6.35}$$

The volume of the chemical shrinkage ΔV_{cs} (in mL per 100 g of cement reacted) can be calculated from the chemical shrinkage measurements (Section 6.1). In order to determine the chemical shrinkage in function of the amount of cement reacted, the chemical shrinkage results are plotted against the advancement of the degree of hydration (see Fig. 6.21 (left)). The slope of the ϵ_{ch}-α curve then corresponds to the volume of chemical shrinkage per g of binder reacted. Table 6.4 summarises the obtained volumes of chemical shrinkage in g per 100 g of binder reacted.

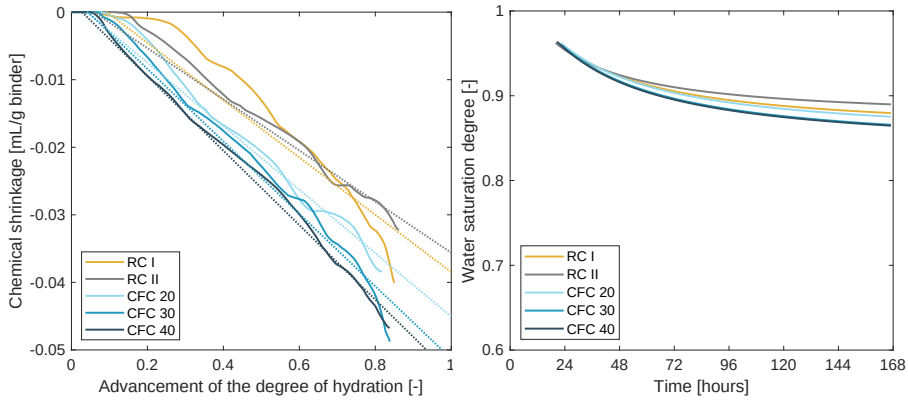

Figure 6.21: Chemical shrinkage ϵ_{ch} as a function of the advancement of the degree of hydration α (left) and water saturation degree S_w (right) for the different cement paste mixes.

Table 6.4: Volume of chemical shrinkage (ΔV_{cs}) and amount of chemically bound water (w_{cbw}) of the different cement paste mixes.

	RC I	RC II	CFC 20	CFC 30	CFC 40
ΔV_{cs} [mL/100 g binder reacted]	4.94	4.30	5.21	5.72	5.75
w_{cbw} [g/g binder reacted]	0.148	-	-	0.126	-

The bound water content was not measured for RC II, CFC 20 and CFC 40.

According to Powers' model, the evaporable water (free capillary water and physically bound water) is the water lost after drying at 105°C [125]. The amount of chemically bound (non-evaporable) water w_{cbw} was therefore calculated as the total weight loss over the 105-550°C temperature range, determined from TGA measurements at early ages (10, 20, 30, 40, 50 and 60 hours of hydration). The amount of chemically bound water per gram of reacted cement can accordingly be determined by plotting w_{cbw} as a function of the advancement of the degree of hydration and calculating the slope. The results of w_{cbw} are also summarised in Table 6.4. The obtained values of w_{cbw} are rather small compared to literature, where generally 0.23 g water is bound per g of cement reacted during OPC hydration (based on Powers' measurements) [133]. The fact that the values in Table 6.4 are derived from early-age measurements (up to 60 hours) can explain the lower values. TGA measurements were only performed for the RC I and CFC 30 mix. Due to the small differences in the results and their marginal impact on the final autogenous shrinkage values, the bound water content of the CFC 30 mix is also used for the other blended cements. Fig. 6.21 (right) shows the resulting water saturation degrees for the different cement paste mixes.

Decoupling autogenous swelling from self-desiccation

The Biot-Bischop approach describes the development of the (autogenous) self-desiccation shrinkage. The measured autogenous deformations, on the other hand, are a combination of the self-desiccation shrinkage (ϵ_{sd}) plus an eventual early-age swelling (ϵ_{sw}):

$$\epsilon_{as,meas} = \epsilon_{sd} + \epsilon_{sw} \tag{6.36}$$

The decoupling approach according to Carrete et al. [47, 48] is therefore used to separate the self-desiccation shrinkage from the swelling. The self-desiccation shrinkage is considered to be linearly dependent on the advancement of the degree of hydration (α), characterised by a parameter A_{sd}:

$$\epsilon_{sd} = A_{sd} \cdot \frac{\alpha - \alpha_0}{1 - \alpha_0} \tag{6.37}$$

with α_0 the advancement of the degree of hydration at time-zero (t_0). Parameter A_{sd} can thus be determined by a linear fit of the autogenous shrinkage results after the swelling peak, plotted against the degree of hydration (see Fig. 6.22 (left)). A clearly linear relationship is observed between the autogenous shrinkage results after swelling and the degree of hydration, and the corresponding slopes of the trendlines are also shown on the graph. Determination of the slopes then allows calculation of the self-desiccation shrinkage (according to Eq. 6.37) and respective derivation of the early-age autogenous swelling (according to Eq. 6.36). The results of the decoupling approach are shown in Fig. 6.22 (right).

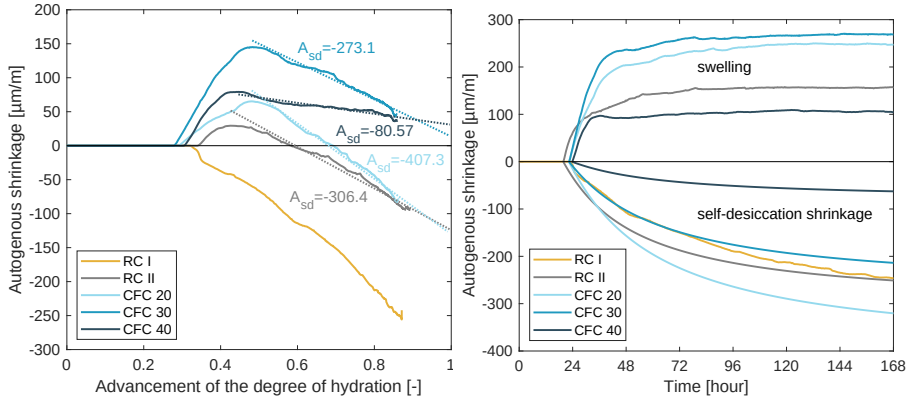

Figure 6.22: Determination of self-desiccation shrinkage (left) and decoupled self-desiccation shrinkage and swelling as a function of time (right).

Results

The results of the Biot-Bischop modelling are shown in Fig. 6.23, compared to the measured autogenous deformations, as well as to the decoupled self-desiccation shrinkage and early-age autogenous swelling (for the blended cement paste mixes). The RMSEs are summarised in Table 6.5. Overall, no good correlations are observed between the model and the self-desiccation shrinkage results, and high RMSEs are noticed. The model slightly overestimates the actual self-desiccation shrinkage for the RC I and CFC 40 cement paste mixes and for the CFC 30 mix at early ages (up to 3 days), while the model underestimates the actual self-desiccation shrinkage for the RC II and CFC 20 mix and for the CFC 30 mix at later ages (from 3 days on). At early ages (up to two days), however, quite good correlations are found for both the RC II, CFC 20 and CFC 30 cement paste mixes. The underestimation of the model can possibly be explained by the fact that the viscoelastic behaviour of the material (i.e. creep) is not taken into account in the model and was also reported by Hu et al. [125] for OPC and FA blended cements. The autogenous shrinkage is, after all, influenced by creep at later ages. The overestimation can possibly be explained by an underestimation of the static elastic modulus. To calculate the static elastic modulus from the dynamic elastic modulus, the conversion factor obtained for concrete was used ($E_s = 0.74 \cdot E_d$) (see Chapter 5, subsection 5.4.3). This conversion factor, however, was not calibrated/validated for cement paste. Furthermore, determination/calculation of the different input parameters is difficult, since understanding of the fundamental shrinkage mechanisms and knowledge of the development of various physical and chemical material properties at early ages (which determination is not straight-forward) is required.

Table 6.5: RMSE of the Biot-Bischop model for the different cement paste mixes.

	RMSE [μm/m]
RC I	26.79
RC II	61.60
CFC 20	91.89
CFC 30	24.63
CFC 40	56.65

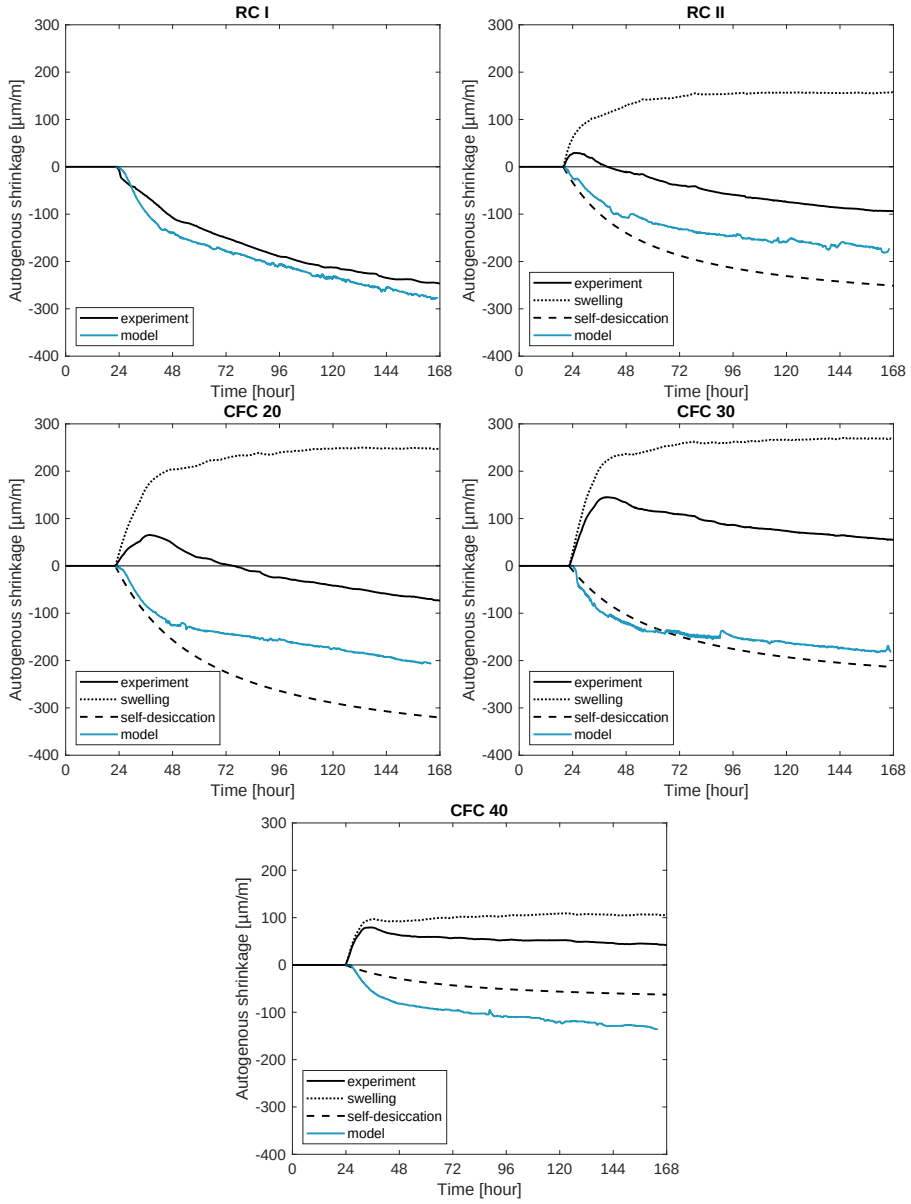

Figure 6.23: Autogenous shrinkage of the cement paste mixes: experimental values (decoupled self-desiccation and swelling) versus Biot-Bischop model.

6.5 Conclusion

This chapter examined the shrinkage behaviour of CFC blended cement pastes and concretes. Chemical shrinkage, autogenous shrinkage and drying shrinkage were studied. Empirical autogenous and drying shrinkage models were parametrised for CFC concrete and a mechanistic shrinkage model (the Biot-Bischop model) was evaluated for CFC cement paste.

Up to 7 days, higher chemical shrinkage values are observed for the CFC blended cement pastes, normalised to their OPC content, compared to the reference mixes. This can be explained by the filler effect and the early pozzolanic reaction of CFC. The autogenous shrinkage of the cement paste mixes is decreased by the effect of CFC as an SCM. This can primarily be explained by an increased early-age swelling, delaying the shrinkage. Furthermore, the dilution effect and the formation of different hydration products are responsible for a lower autogenous shrinkage rate of the CFC blended cement pastes. The observed swelling peak can be attributed to the development of a crystallisation pressure as a result of supersaturation of the pore solution towards ettringite, since additional ettringite was formed in the CFC mixes and a higher sulphate to aluminate ratio was found for the CFC blended cement mixes. Compared to fly ash, CFC has a similar early-age hydration and autogenous deformation behaviour. The drying shrinkage was also reduced by addition of CFC. This can be explained by the dilution effect and altered porosity and pore size distribution of the CFC blended cement concretes.

The autogenous and drying concrete shrinkage were both modelled by parametrisation of existing empirical shrinkage models. The Bazant B4 model appeared to be the best prediction model for the autogenous shrinkage. The β-n model was the best predictor for the drying shrinkage, followed by the EC 2 model for the reference mixes and the Bazant model for the CFC blended cement mixes. Only very small differences were found in the shrinkage strains of the drying shrinkage and total shrinkage model approaches. The Biot-Bischop model was evaluated for prediction of the autogenous shrinkage of cement paste. The predicted autogenous shrinkage values did not well correspond to the measured self-desiccation shrinkage values, both over- and underestimation were observed. The main shortcoming of the Biot-Bischop model is the neglect of the viscoelastic behaviour, i.e. creep. This will be studied in the next chapter.

Chapter 7

Creep behaviour

This chapter presents a first attempt on characterisation of the creep behaviour of CFC blended concrete. First, a general description of the total strains of a loaded concrete specimen is given (Section 7.1). Secondly, the creep experiments are described in detail and the influence of CFC on the instantaneous elastic strains, basic creep strains and drying creep strains is discussed (Section 7.2). Finally, basic creep and drying creep are modelled, respectively by using a rheological model based on a Kelvin-Voigt and Maxwell chain, and by using the relationship between drying creep and drying shrinkage (Section 7.3). The chapter ends with the main conclusions and some critical reflections (Section 7.4).

7.1 Concrete strains

The total concrete strain (ϵ) of a loaded specimen includes instantaneous elastic strains (ϵ_e), thermal strains (ϵ_{th}), autogenous and drying shrinkage strains (ϵ_{as} and ϵ_{ds}), basic and drying creep strains (ϵ_{bc} and ϵ_{dc}) and possible inelastic strains (ϵ_{in}), such as cracking [95, 107].

$$\epsilon = \epsilon_e + \epsilon_{th} + \epsilon_{as} + \epsilon_{ds} + \epsilon_{bc} + \epsilon_{dc} + \epsilon_{in} \tag{7.1}$$

At constant temperature, the strain components of a concrete specimen uniaxially loaded at time t_{load} and unloaded at time t_{unload} are illustrated in Fig. 7.1. Shrinkage strains start to develop from final setting (t_0) and continue to increase at decreasing rate. A sudden jump in the strain diagram is noticed on application of stress (i.e. the instantaneous strain), followed by

an additional increase in strain (i.e. creep strains). Upon unloading, there is a sudden decrease in total strain due to the elimination of the instantaneous strain. The instantaneous strain upon unloading is lower than the instantaneous strain upon loading, due to an increased elastic modulus in time. A gradual reduction of the creep strains occurs with time. A large portion of the creep strains is irrecoverable or permanent, while usually a smaller portion is recoverable [107].

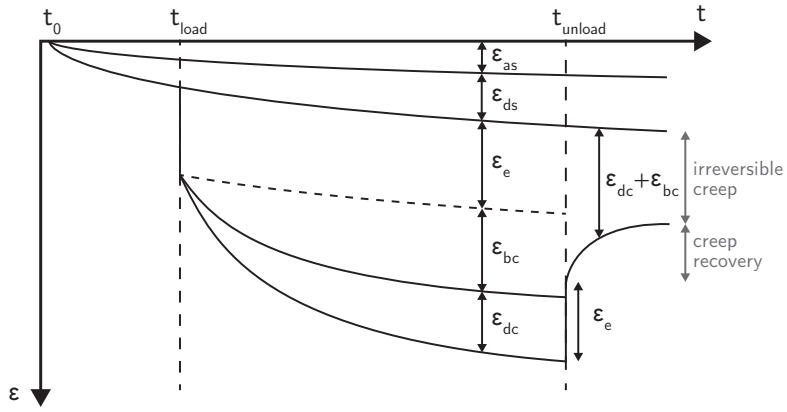

Figure 7.1: Strain-time curve of concrete loaded at t_{load} and unloaded at t_{unload} (neglecting thermal and inelastic strains).

7.2 Creep experiments

Creep in compression was measured both in autogenous conditions (i.e. basic creep) and in drying conditions (i.e. drying creep). The measured deformations in autogenous conditions are the combination of the instantaneous elastic strain, the basic creep strain and the autogenous shrinkage strain:

$$\epsilon_{meas,au} = \epsilon_e + \epsilon_{bc} + \epsilon_{as} \tag{7.2}$$

while in drying conditions, the measured deformations are the combination of the instantaneous elastic strain, the drying and basic creep strains, and the drying and autogenous shrinkage strains:

$$\epsilon_{meas,dr} = \epsilon_e + \epsilon_{dc} + \epsilon_{bc} + \epsilon_{ds} + \epsilon_{as} \tag{7.3}$$

In order to compute the actual basic and drying creep strains (ϵ_{bc} and ϵ_{dc}), simple mathematical operations are necessary. Fig. 7.2 shows the total strains of the concrete specimens, measured in autogenous (left) and drying (right)

conditions. Drying conditions were ± 23 °C and ± 50% relative humidity. Loading (and drying) started two days after casting and unloading took place 14 days after the start of loading (except for the CFC 40 mix, which was not unloaded). The applied load levels were different for the different concrete compositions (as equal to 30% of their compressive strength after two days) and are summarised in Table 7.1. The error bars in Fig. 7.2 represent the standard deviations of the results, as creep measurements were performed on two different concrete specimens. The error bars are relatively small for all compositions, except for the autogenous creep measurement of the CFC 40 mix, which shows higher standard deviations (8.9% on average). For the drying creep measurement of the CFC 40 mix, the result of only one specimen was retained and the standard deviation therefore equals zero. The higher standard deviation of the measured creep strains in autogenous conditions of the CFC 40 mix, however, is most likely due to an experimental error, rather than due to the mix composition itself. The measured strains in drying conditions are much higher than the measured strains in autogenous conditions. This, however, does not mean that the drying creep strains are also higher than the basic creep strains, since a large part of the strains measured in drying conditions, includes drying shrinkage strains.

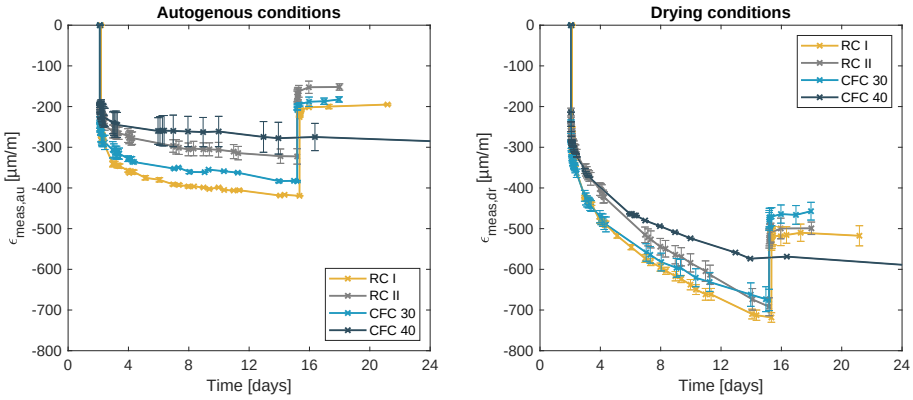

Figure 7.2: Total concrete strains measured in autogenous (left) and drying (right) conditions of the different concrete mixes.

Table 7.1: Load levels of the different concrete mixes.

	RC I	RC II	CFC 30	CFC 40
σ [MPa]	8.12	6.36	7.62	6.73

As the reported results are the average values of the deformations of the four sides of the creep specimens, verification of the eccentricity of the creep specimens can be done in order to check the influence of the development of parasitic bending moments on the load application. Appendix G summarises the calculation of the bending moments and eccentricities. It is concluded that the impact of the eccentricity of the creep specimens on the stress level is negligible.

7.2.1 Instantaneous strain

From the results of the creep measurements, as shown in Fig. 7.2, the elastic strains can be derived. Accurate differentiation between the instantaneous elastic strains and early creep strains, however, is difficult [166], due to the limitations of the execution of the test. Table 7.2 summarises the instantaneous elastic strains, both in autogenous and drying conditions, as well as at the time of loading and unloading. Since different stress levels were applied to the different concrete mixes, it is difficult to compare the elastic strains of the different mix compositions. However, it is concluded from Table 7.2 that the instantaneous strains decrease in time (as lower instantaneous strains are observed after unloading, compared to after loading, due to an increased stiffness of the material) and that the instantaneous strains in drying conditions are slightly higher than the instantaneous strains in autogenous conditions. The latter can be explained by drying shrinkage to be very prominent soon after the start of drying. Since drying started shortly before application of the load, the early development of some drying shrinkage strains can probably explain these small differences.

Table 7.2: Instantaneous elastic strains in autogenous and drying conditions, at loading and unloading, for the different concrete mixes.

	RC I	RC II	CFC 30	CFC 40
$\epsilon_{e,au,load}$ [μm/m]	221.88 ± 2.65	198.75 ± 3.37	232.50 ± 7.53	199.79 ± 2.21
$\epsilon_{e,au,unload}$ [μm/m]	193.75 ± 1.77	147.50 ± 0.00	175.63 ± 2.65	
$\epsilon_{e,dr,load}$ [μm/m]	255.83 ± 5.89	213.33 ± 9.43	249.50 ± 16.62	213.75
$\epsilon_{e,dr,unload}$ [μm/m]	187.50 ± 10.61	166.29 ± 0.06	193.13 ± 4.42	

The instantaneous strain at any time may be expressed as:

$$\epsilon_e(t) = \frac{\sigma(t)}{E(t)} \tag{7.4}$$

with σ the applied stress and E the elastic modulus of concrete. The instantaneous elastic modulus, however, is different compared to the static elastic modulus determined by cyclic testing according to EN 12390-13 [85].

This is clarified in Table 7.3, summarising the instantaneous elastic moduli determined according to Eq. 7.4 (both in autogenous and drying conditions, as well as at loading and unloading), and the static elastic modulus, determined according to EN 12390-13, of the different concrete compositions.

Table 7.3: Instantaneous elastic moduli derived from creep experiments (in autogenous and drying conditions, at loading and unloading) and measured static elastic modulus after 2 days (i.e. t_{load}) of the different concrete mixes.

	RC I	RC II	CFC 30	CFC 40
$E_{au,load}$ [GPa]	36.60 ± 0.44	32.00 ± 0.57	32.77 ± 0.00	33.69 ± 1.54
$E_{au,unload}$ [GPa]	41.91 ± 0.38	43.12 ± 0.00	43.39 ± 0.66	
$E_{dr,load}$ [GPa]	31.74 ± 0.73	29.81 ± 1.32	30.54 ± 2.04	31.49
$E_{dr,unload}$ [GPa]	43.31 ± 2.45	38.25 ± 0.01	39.46 ± 0.90	
$E_{s,2d}$ [GPa]	28.97 ± 0.87	29.19 ± 1.3	29.23 ± 1.09	27.83 ± 1.23

It is clearly observed from Table 7.3 that the instantaneous elastic modulus is much higher than the static elastic modulus determined by cyclic testing. Especially the instantaneous moduli from the unloading phase are quite high. The differences in load application can explain this behaviour. During cyclic testing, three different loading cycles are applied (with an average loading rate of 8.7 kN/s), from which the two last cycles are used to calculate E_s, while during the creep measurements, the load is applied instantaneously. Furthermore, the instantaneous elastic modulus also increases in time (E_{unload} compared to E_{load}), as also observed by decreased elastic strains (see Table 7.2), due to higher stiffness of the concrete with time.

7.2.2 Basic creep strain

The results of the basic creep strains are shown in Fig. 7.3, calculated as:

$$\epsilon_{bc} = \epsilon_{meas,au} - \epsilon_e - \epsilon_{as} \tag{7.5}$$

The autogenous shrinkage of concrete samples of the same size as the creep specimens was also determined. However, since the measured autogenous shrinkage values were marginal compared to the measured creep strains, autogenous shrinkage was neglected. In order to cancel out the different applied stress levels for the different concrete compositions, the results are plotted per MPa. It is concluded from Fig. 7.3 that the basic creep of the RC I concrete mix is the highest, while the basic creep of the blended cement concretes is lower, with decreasing basic creep for increasing amount of CFC. Since the exact creep mechanisms are not yet fully understood, it is difficult to explain the lower basic

creep of the CFC blended cement concretes. However, the altered porosity and pore size distribution of CFC concrete and the formation of different hydration products, especially the amount and composition of C-S-H, are most likely to explain the reduced basic creep. Furthermore, the remaining unreacted CFC particles could also influence the basic creep behaviour. Lower basic creep values were also observed in literature for FA [42, 106] or SF [106, 148, 159] blended cement concrete. For GBFS, on the other hand, both reduced [106, 148, 141] and increased [199] basic creep were reported.

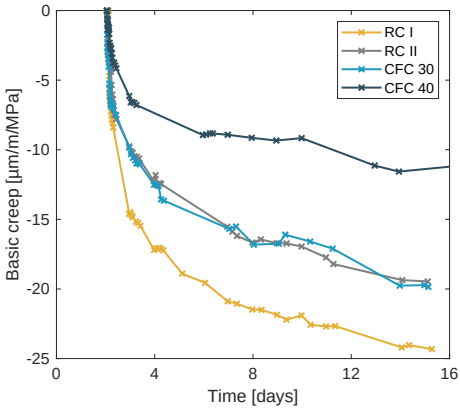

Figure 7.3: Basic creep strains per MPa of the different concrete mixes.

7.2.3 Drying creep strain

The results of the drying creep strains are shown in Fig. 7.4, calculated as:

$$\epsilon_{dc} = \epsilon_{meas,dr} - \epsilon_{e} - \epsilon_{bc} - \epsilon_{ds} - \epsilon_{as} \tag{7.6}$$

Also here, autogenous shrinkage is neglected and drying shrinkage was measured on specimens of the same size as the creep specimens, exposed to exactly the same environmental (drying) conditions. Initially, negative values are observed for the drying creep strains and the early-age development of the drying creep curves does not evolve smoothly. Different explanations for this behaviour can be found:

- The difference between the basic creep in autogenous conditions and the basic creep in drying conditions. In drying conditions, less water is available and the hydration will be subsequently less complete, resulting in less autogenous shrinkage and less basic creep. The basic creep strains

used in Eq. 7.6, however, are the basic creep strains measured in completely autogenous conditions, and are therefore (possibly) an overestimation of the real basic creep strains, occurring in drying conditions.

- The high error of the drying creep strains. The standard deviations of the measured total drying strains (see Fig. 7.2) were relatively small (1.6% on average). The error of the calculated drying creep strains, on the other hand, will be much higher, since the error of the drying creep strains is the result of the sum of the errors of three separate measurements (total drying strain, total autogenous strain and drying shrinkage measurements):

$$\Delta\epsilon_{\mathrm{dc}} = \Delta\epsilon_{\mathrm{meas,dr}} + \Delta\epsilon_{\mathrm{meas,au}} + \Delta\epsilon_{\mathrm{ds}} \tag{7.7}$$

- Microcracking due to drying shrinkage. If microcracking would occur in drying conditions (due to high drying shrinkage strains), these microcracks would be obstructed by the drying creep strains (under sustained loading), resulting in a distorted picture of the actual drying creep strains. As observed by microscope investigations, small microcracks appeared on the surface of the drying shrinkage concrete samples (see Appendix F).

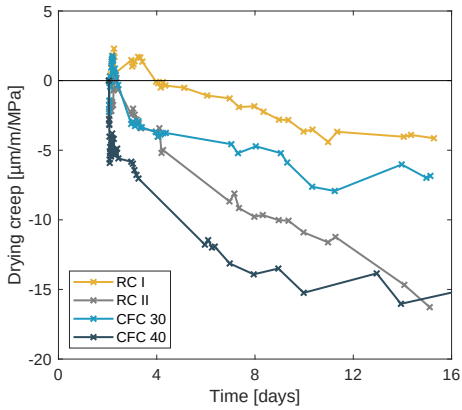

Figure 7.4: Drying creep strains per MPa of the different concrete mixes.

Furthermore, it is observed from Fig. 7.4 that the drying creep strains are the highest for the blended cement concretes (with increasing drying creep for increasing amount of CFC) and the lowest for the OPC reference mix. The absolute drying creep strains, however, are relatively small, while the error of the drying creep strains (calculated according to Eq. 7.7) is relatively high for all compositions (see Table 7.4). Therefore, the drying creep strain results must be treated with caution and no conclusions about the effect of CFC on the

drying creep strains can be made. What can be concluded is that the drying creep strains are rather small for all compositions.

Table 7.4: Average errors of the drying creep strain for all compositions (according to Eq. 7.7).

		RC I	RC II	CFC 30	CFC 40
$\Delta\epsilon_{\mathrm{meas,au}}$	[µm/m]	3.41	12.84	7.94	25.83
$\Delta\epsilon_{\mathrm{meas,dr}}$	[µm/m]	8.97	15.42	15.10	0.00
$\Delta\epsilon_{\mathrm{ds}}$	[µm/m]	10.59	5.07	3.77	2.20
$\Delta\epsilon_{\mathrm{dc}}$	[µm/m]	22.97	33.33	26.81	28.03
$\Delta\epsilon_{\mathrm{dc}}$	[%]	64.14	32.20	44.38	25.97

7.3 Modelling

7.3.1 Basic creep model

A rheological model, based on an aging Burger chain, consisting of a Kelvin-Voigt chain in series with a Maxwell chain (see Fig. 7.5), is used for predicting basic creep strains. The Kelvin-Voigt chain represents the reversible part of the basic creep and describes the initial fast development of the short-term basic creep. The Maxwell chain, on the other hand, represents the irreversible basic creep and determines the long-term basic creep. The elastic (instantaneous) part is also included and is represented by a spring with stiffness E.

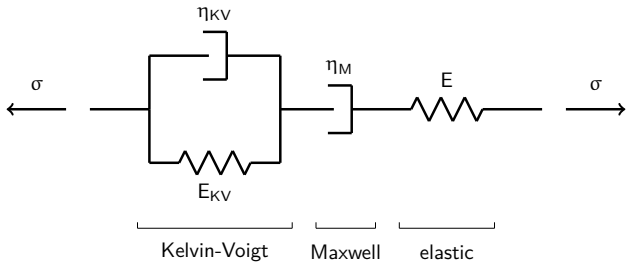

Figure 7.5: Aging Burger model for basic creep.

Since the Kelvin-Voigt, Maxwell and elastic chain are combined in series, the total basic creep strains (including instantaneous elastic strains) are:

$$\epsilon_{\mathrm{bc}} = \epsilon_{\mathrm{KV}} + \epsilon_{\mathrm{M}} + \epsilon_{\mathrm{e}} \tag{7.8}$$

with ϵ_{KV} the basic creep strains associated to the Kelvin-Voigt chain and ϵ_{M} the basic creep strains associated to the Maxwell chain.

Constitutive equations

Considering the Kelvin-Voigt chain, the stresses σ are equal to the sum of the stresses developed in the dashpot ($\sigma_{\eta_{KV}}$) and in the spring ($\sigma_{E_{KV}}$):

$$\sigma = \sigma_{E_{KV}} + \sigma_{\eta_{KV}} \tag{7.9}$$

The constitutive laws of the spring and dashpot are respectively:

$$\dot{\sigma}_{E_{KV}} = E_{KV} \cdot \dot{\epsilon}_{KV} \tag{7.10}$$

$$\sigma_{\eta_{KV}} = \eta_{KV} \cdot \dot{\epsilon}_{KV} \tag{7.11}$$

with E_{KV} the apparent stiffness and η_{KV} the apparent viscosity of the Kelvin-Voigt chain. The apparent stiffness and viscosity are assumed to follow the same aging law as the mechanical properties (see Eq. 5.27 and 5.28):

$$E_{KV}(t) = E_{KV28} \cdot \exp\left[s \cdot \left(1 - \sqrt{\frac{28 - t_0}{t - t_0}}\right)\right]^{n_{E_{KV}}} \tag{7.12}$$

$$\eta_{KV}(t) = \eta_{KV28} \cdot \exp\left[s \cdot \left(1 - \sqrt{\frac{28 - t_0}{t - t_0}}\right)\right]^{n_{n_{KV}}} \tag{7.13}$$

with η_{KV28} and E_{KV28} respectively the values of the apparent viscosity and stiffness after 28 days, s a coefficient depending on the type of cement, $n_{\eta_{KV}}$ and $n_{E_{KV}}$ functions describing the development of respectively the apparent viscosity and stiffness in time and t_0 the final setting time.

In order to compute the creep strains, the stresses are linearised between t_n and t_{n+1}:

$$t = t_n + \frac{\Delta t}{2} = \frac{t_n + t_{n+1}}{2} \tag{7.14}$$

$$\sigma = \sigma_n + \frac{\Delta \sigma}{2} = \frac{\sigma_n + \sigma_{n+1}}{2} \tag{7.15}$$

with $\Delta t = t_{n+1} - t_n$ and $\Delta \sigma = \sigma_{n+1} - \sigma_n$.

Considering Eq. 7.10-7.11 and Eq. 7.15, the constitutive equation of the Kelvin-Voigt chain (Eq. 7.9) can then be written as:

$$\sigma_n + \frac{\Delta \sigma}{2} = \sigma_{E_{KV}}(t) + \tau \cdot \dot{\sigma}_{E_{KV}}(t) \tag{7.16}$$

with $\tau = \frac{\eta_{KV}(t)}{E_{KV}(t)}$, the characteristic/retardation time, assumed to be constant.

The general solution of the linear differential equation of the Kelvin-Voigt chain (Eq. 7.16) reads:

$$\sigma_{E_{KV}}(t) = \sigma_n + \frac{\Delta\sigma}{2} + \lambda \cdot \exp\left(-\frac{t}{\tau}\right) \tag{7.17}$$

In order to determine the constant λ, it suffices to only know one particular solution of the differential equation. For $t = t_n$:

$$\sigma_{E_{KV}}(t_n) = \sigma_n + \frac{\Delta\sigma}{2} + \lambda \cdot \exp\left(-\frac{t_n}{\tau}\right) \tag{7.18}$$

$$\Rightarrow \lambda = \left(\sigma_{E_{KV}}(t_n) - \sigma_n - \frac{\Delta\sigma}{2}\right) \cdot \exp\left(\frac{t_n}{\tau}\right) \tag{7.19}$$

The basic creep strains associated to the Kelvin-Voigt chain ϵ_{KV} can then be expressed as:

$$\Delta\epsilon_{KV} = \frac{\Delta\sigma_{E_{KV}}}{E_{KV}} \sim \frac{\dot{\sigma}_{E_{KV}}}{E_{KV}} \cdot \Delta t = -\frac{\lambda \cdot \Delta t}{\eta_{KV}} \cdot \exp\left(-\frac{t}{\tau}\right) \tag{7.20}$$

$$\boxed{\Rightarrow \Delta\epsilon_{KV} = -\frac{\Delta t}{\eta_{KV}} \cdot \left[\sigma_{E_{KV}}(t_n) - \sigma_n - \frac{\Delta\sigma}{2}\right] \cdot \exp\left(-\frac{\Delta t}{2 \cdot \tau}\right)} \tag{7.21}$$

The constitutive equation of the Maxwell chain is written as:

$$\sigma = \eta_M \cdot \dot{\epsilon}_M \tag{7.22}$$

with η_M the apparent viscosity of the Maxwell chain. For the Maxwell chain, it is assumed that the apparent viscosity is evolving linear with time:

$$\frac{\eta_M(t)}{t} = \frac{\eta_{M28}}{t_{28}} \Rightarrow \eta_M(t) = \frac{\eta_{M28}}{t_{28}} \cdot t \tag{7.23}$$

Using this expression and solving the constitutive equation (Eq. 7.22), gives:

$$\epsilon_M = \int_{t_{load}}^{t} \frac{\sigma}{\eta_M(t)} \cdot dt \tag{7.24}$$

$$\boxed{\Rightarrow \epsilon_M = \frac{\sigma \cdot t_{28}}{\eta_{M28}} \cdot \log\frac{t}{t_{load}}} \tag{7.25}$$

The constitutive equation of the elastic part, finally, is written as:

$$\epsilon_e = \frac{\sigma}{E} \tag{7.26}$$

with E the elastic modulus.

Parameter identification

The material parameters E_{KV28}, η_{KV28} and η_{M28}, and the aging parameters $n_{E_{KV}}$ and $n_{\eta_{KV}}$ are considered as fitting parameters and are determined by fitting the experimental results to the basic creep model. This is done by using the least squares method (with the `lsqnonlin` function in Matlab©). Since the characteristic time τ_{KV} is assumed to be constant, the aging parameters $n_{E_{KV}}$ and $n_{\eta_{KV}}$ must be the same. Therefore, one aging parameter n_{KV} is henceforth considered. The instantaneous elastic modulus (E) is derived from the experimental creep results that were already summarised in Table 7.3.

It should, however, be noted that the optimisation is an ill-posed problem. Several sets of parameters can be found strongly depending on the initial parameters and the imposed constraints (upper and lower limits of the fitting parameters). Different options of initial parameters, and upper and lower limits were considered and the finally chosen fitting parameters (resulting in the best fit for both the loading and unloading part) are summarised in Table 7.5. The initial values for E_{KV28}, η_{KV28}, n_{KV} and η_M, were respectively, 25 GPa, 100 GPa·days, n_E and 1000 GPa·days, and their upper and lower limits were respectively equal to 0.1 and 10 times their initial parameters. It is observed from Table 7.5 that the upper and lower limit of E_{KV28} and η_{KV28}, respectively, are reached for all compositions. This means that E_{KV28} and η_{KV28} (or τ_{KV}) can actually be seen as constant parameters of the basic creep model. The values of the fitting parameters are all in the same order of magnitude as the values reported in the literature [27, 40].

Table 7.5: Fitting parameters of the basic creep model.

		RC I	RC II	CFC 30
E_{KV28}	[GPa]	250	250	250
η_{KV28}	[GPa·days]	10	10	10
τ_{KV}	[days]	0.04	0.04	0.04
n_{KV}	[-]	3.19	1.39	1.11
η_M	[GPa·days]	4977.46	4495.87	3925.99

Results

The results of the basic creep model fitting are shown in Fig. 7.6. Overall, quite good fitting is observed for all compositions, both for the loading and unloading part. Only at the end of the loading phase of the CFC 30 mix, the basic creep is slightly overestimated. A different origin of the basic creep mechanisms in

the CFC blended concrete could explain this behaviour. The characteristic time (τ_{KV}) is quite low for all compositions (0.04 days) and this is translated into a high initial development of the basic creep strains (related to the Kelvin-Voigt chain) and a fast recovery of the reversible basic creep strains after unloading. The Maxwell chain, on the other hand determines the long-term creep behaviour. Lower values of η_M are observed for the blended cement concretes, which means that for the same stress level, higher strains associated to the Maxwell chain (irreversible strains) are observed for the FA and CFC blended cement mixes. Furthermore, the aging parameter n_{KV} is the highest for the RC I mix and decreases for the blended cement mixes. The apparent viscosity and stiffness of the Kelvin-Voigt chain thus develops much faster in the RC I mix, resulting in higher initial basic creep strains, associated to the Kelvin-Voigt chain.

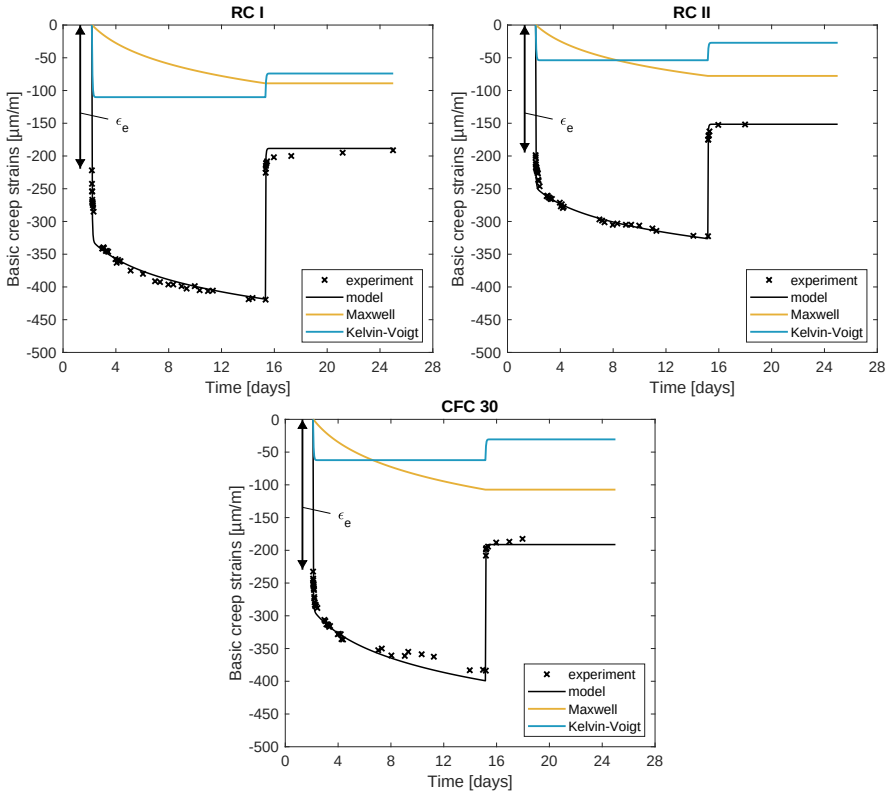

Figure 7.6: Basic creep model, with subdivision into the elastic strains (ϵ_e), Kelvin-Voigt strains and Maxwell strains, for the RC I, RC II and CFC 30 concrete compositions.

7.3.2 Drying creep model

Despite the doubts about the reliability of the drying creep results, an attempt was made to model the drying creep strains. The linear relationship between the drying creep (ϵ_{dc}) and drying shrinkage (ϵ_{ds}) strains was used to predict the drying creep [101, 122]:

$$\dot{\epsilon}_{dc} = \beta_{dc} \cdot \sigma \cdot \dot{\epsilon}_{ds} \tag{7.27}$$

with β_{dc} the proportionality factor between drying shrinkage and drying creep strains and σ the applied stress. Eq. 7.27 only accounts for the irreversible drying creep, since the drying creep strain is proportional to the stress level. The assumption of considering only irreversible drying creep strains, however, is debatable, since drying creep also originates from structural behaviour (microcracking effect). The factor β_{dc} can be determined by calculating the slopes of the ϵ_{dc}-ϵ_{ds} curves (see Fig. 7.7) and the results are summarised in Table 7.6. Compared to the literature, the slopes are relatively low [122]. This confirms the hypothesis of underestimation of the measured drying creep strains.

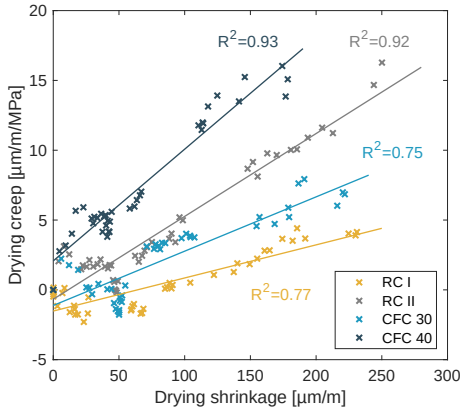

Figure 7.7: Evolution of the drying creep strains as a function of the drying shrinkage strains of the different concrete mixes.

Table 7.6: Slopes (β_{dc}) of the drying creep versus drying shrinkage curves for the different concrete mixes.

	RC I	RC II	CFC 30	CFC 40
β_{dc}	0.0237	0.0593	0.0389	0.0800

The results of the drying creep model are shown in Fig. 7.8, compared to the experimental results. It is observed from Fig. 7.8 that the model slightly

overestimates the experimentally determined drying creep strains for the RC I, RC II and CFC 30 mixes, while for the CFC 40 mix, the model underestimates the drying creep strains. The high errors of the experimentally determined drying creep strains, however, explain the poor fitting of the drying creep model.

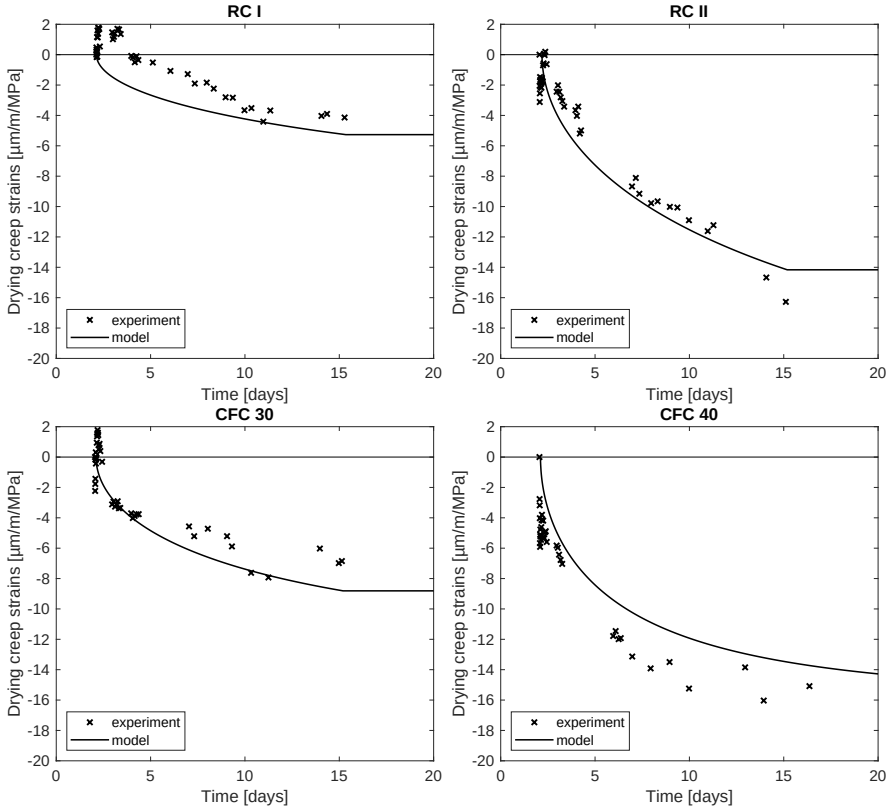

Figure 7.8: Drying creep model of the different concrete compositions.

7.3.3 Total strains

The total measured strains in drying conditions (see Fig. 7.2 (right)) can now be predicted using the basic creep model (including instantaneous elastic strains), the drying shrinkage model and the drying creep model. The results of the total strain prediction are shown in Fig. 7.9. It is observed that for the RC II and CFC 30 mix, the total strains are quite well predicted. Only a slight underestimation of the total strains is noticed at the end of the loading phase

for the RC II mix and a slight overestimation of the total strains is observed for the CFC 30 mix during the unloading phase. For the RC I mix, on the other hand, the model slightly underestimates the total strains, both during the loading phase and unloading phase. The less good correspondence between the total strain model and the total strain experiments for the RC I mix, is most probably due to an underestimation of the measured drying creep strains.

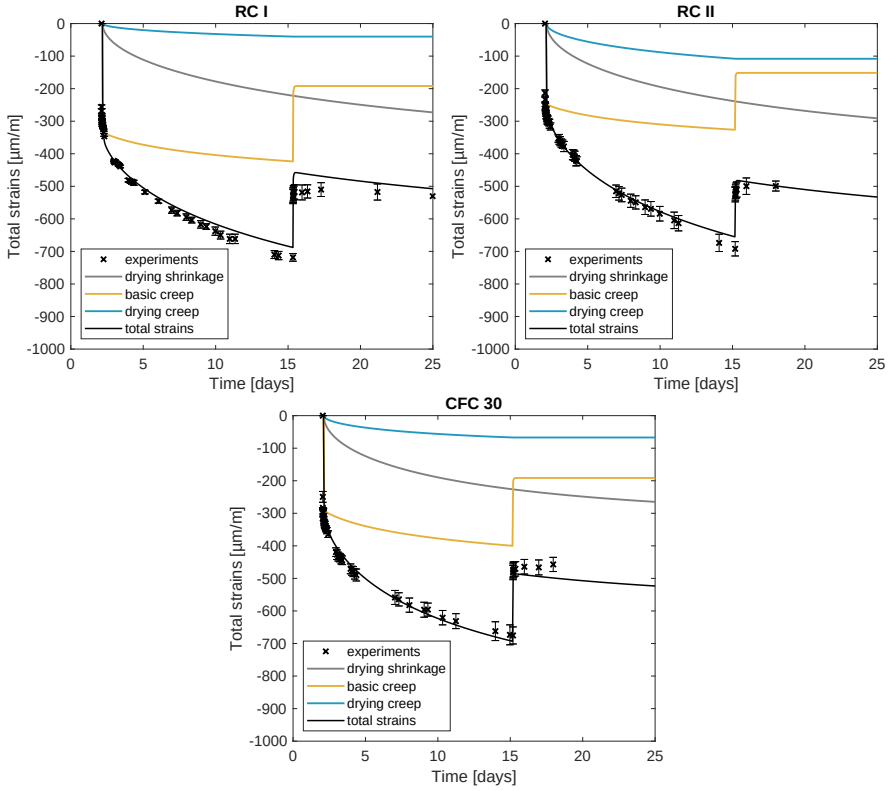

Figure 7.9: Total strain model, including elastic strains, drying shrinkage strains, basic and drying creep strains.

In order to better predict the total strains, the slopes of the drying creep model were determined in a different way: by fitting the total strain model to the total strain results and taking β_{dc} as a fitting parameter. This was done since the calculated drying creep strains were most probably underestimated, resulting in a bad parametrisation of the drying creep model. The newly obtained slopes are summarised in Table 7.7 and the results are depicted in Fig. 7.10.

Table 7.7: Slopes (β_{dc}) of the drying creep versus drying shrinkage curves for the different concrete mixes, obtained by fitting the total strain model to the total strain results.

	RC I	RC II	CFC 30
β_{dc}	0.0438	0.0655	0.0376

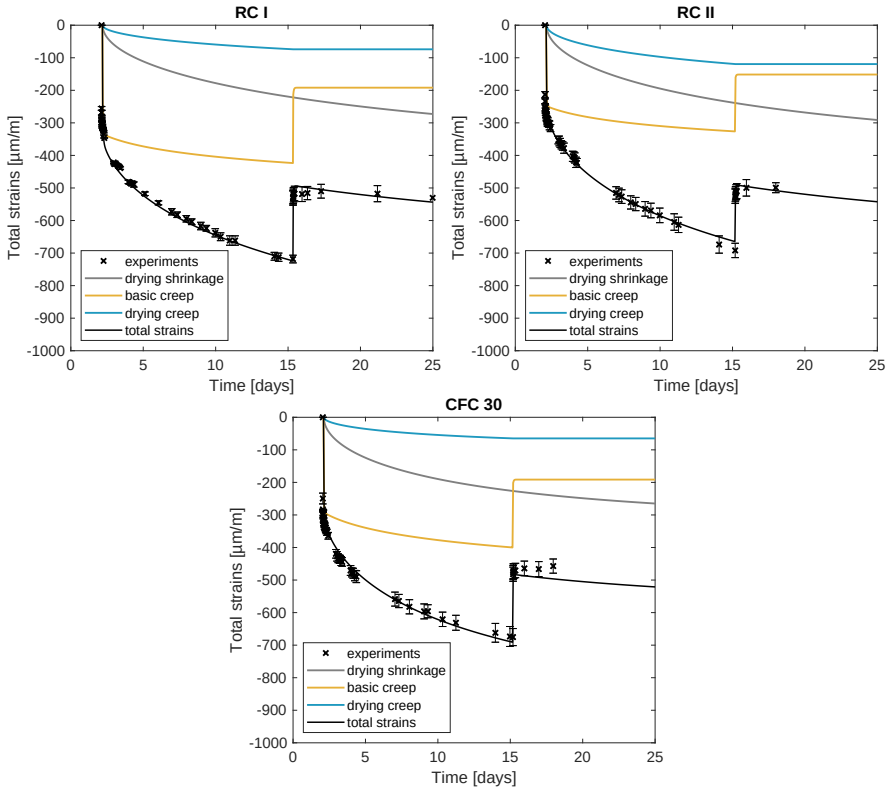

Figure 7.10: Total strain model, including elastic strains, drying shrinkage strains, basic and drying creep strains.

A higher slope is observed for the RC I mix and a slightly higher slope for RC II mix, while the slope of the CFC 30 was almost unchanged. Especially for the RC I mix a much better fit is observed, while for the blended cement mixes, there is not a lot of difference, compared to the previous method for determining β_{dc}.

7.4 Conclusion

In this chapter, the creep behaviour of CFC concrete was studied. CFC reduces concrete basic creep, compared to an OPC reference mix. The influence of CFC on the porosity and properties of C-S-H, are most likely to explain the reduced basic creep of CFC concrete. No conclusions could be made regarding the influence of CFC on the drying creep, due to high errors of the experimental results of the drying creep. It should be noted, however, that measurement of creep is not an easy task. Creep strains are sensitive to many factors, such as preservation of the specimens, ambient relative humidity and temperature, age at loading, application of load, mix composition, etc. [95], and cannot be purely measured. Measured creep strains always include pure elastic strains, shrinkage strains, creep strains and possible cracking, and are thus dependent on many different phenomena. This explains the high errors of the calculated drying creep strains.

A rheological model, consisting of a Kelvin-Voigt and Maxwell chain, was used for prediction of the basic creep strains. For all compositions, good agreement between the model and experimental results was observed, although a slight overestimation was observed for the CFC blended cement mix. A different origin of the basic creep of the CFC concrete mix could explain this overestimation. Despite the low reliability of the drying creep results, an attempt was made to model the drying creep strains, using the relationship between drying shrinkage and drying creep. Both over- and underestimation of the actual drying creep strains were observed. The total strains, on the other hand, were quite well predicted using a combination of the basic creep model, drying creep model and drying shrinkage model, especially for the blended cement mixes. Slight modifications of the drying creep model even result in good prediction of the total strains for all concrete mixes.

Overall, CFC seems to positively influence the creep behaviour of concrete and the proposed models predict well the total creep strains. However, it should be remarked that research into the creep behaviour of SCM blended concrete is limited, especially with regards to the influence of SCMs on the creep mechanisms and the inclusion of SCMs in rheological creep models. These two aspects therefore strongly require further investigation.

Chapter 8

Cracking risk

Early-age thermal and shrinkage effects could cause severe cracking in concrete structures during the first days after casting. Autogenous, drying and thermal deformations may either be restrained by the geometry of the concrete structure, or by self-restraint occurring due to temperature and/or relative humidity gradients inside the concrete element, leading to internal stress development and eventual cracking. Cracking of concrete is a major concern, since it affects the durability, serviceability and appearance of the concrete structure [143]. It is therefore important to be able to predict this cracking sensitivity, especially in new blended cement systems. This chapter presents the development of a 'simple' predictive tool to assess the thermal-shrinkage-creep induced (early-age) cracking risk of concrete. First, the methodology is discussed (Section 8.1). A stress approach, based on the definition of a cracking index, is used. Secondly, the thermal-shrinkage-creep induced cracking risk is presented (Section 8.2). Initially, the autogenous shrinkage induced, drying shrinkage induced and thermal shrinkage induced cracking risk are described separately. Afterwards the combined cracking risk, considering only elastic stresses as well as viscoelastic stresses, is discussed. Finally, the cracking risk prediction tool using the rate form of the strains and stresses, is compared to the non-rate form. The chapter ends with the main conclusions (Section 8.3).

8.1 Methodology

To evaluate the moment of cracking of a hardening concrete element in time, either restrained deformation experiments, such as the ringtest or TSTM

(temperature stress testing machine), are performed, or theoretical prediction methods, based on cracking criteria, are used. Two basic cracking risk prediction approaches exist: strain-based approaches (e.g. Eurocode 2 method, CIRIA C660 method, etc.) and stress-based approaches (e.g. JCI method, ACI method, etc.) [28, 95, 143]. The strain approach compares the strain capacity (ϵ_{ctu}), which relates the tensile strength and the elastic modulus with the restrained strain (ϵ). Cracking occurs when $\epsilon > \epsilon_{ctu}$. The stress-based approach postulates that cracking occurs when the tensile stress in a given point of the structure (σ) exceeds the tensile strength of the concrete (f_{ct}), i.e. when $\sigma > f_{ct}$ [95]. The cracking prediction tool, proposed in this chapter, is based on the stress approach. The following subsections discuss the definition of the cracking index, the determination/calculation of the restrained stresses and the input parameters.

Cracking index

Considering a stress based cracking sensitivity approach, failure or cracking of a concrete structure occurs when the restraining stress exceeds the tensile strength of the concrete [28]. In order to quantitatively predict this cracking risk at any age, a cracking index I_{cr} is defined as the ratio of the theoretical calculated stress (σ) over the tensile strength (f_{ct}), at time t_{eq} (the equivalent time) [28, 60]:

$$I_{cr} = \frac{\sigma\,(t_{eq})}{f_{ct}\,(t_{eq})} \tag{8.1}$$

The higher the value of the cracking index, the more important the cracking risk of the studied concrete structure. When the value of I_{cr} exceeds 1, i.e. when the developed stresses exceed the tensile strength, there is a risk of cracking. It should be noted that Eq. 8.1 is only valid if the developed stresses in the concrete are tensile stresses (e.g. when there is shrinkage). When compressive stresses develop (e.g. when there is swelling), the tensile strength (f_{ct}) in Eq. 8.1 should be replaced by the compressive strength (f_c).

Restrained stresses

The restrained stresses inside a concrete element are calculated assuming fully restraint conditions/boundaries, i.e. the total strains equal zero ($\epsilon = 0$):

$$\Delta\epsilon = \Delta\epsilon_e + \Delta\epsilon_{as} + \Delta\epsilon_{ds} + \Delta\epsilon_{th} + \Delta\epsilon_{bc} + \Delta\epsilon_{dc} = 0 \tag{8.2}$$

with ϵ_e elastic strains, ϵ_{as} autogenous shrinkage strains,ϵ_{ds} drying shrinkage strains, ϵ_{th} thermal strains, ϵ_{bc} basic creep strains and ϵ_{dc} drying creep strains.

Before derivation of the restrained stresses, the different strains will first be discussed in detail.

- Elastic strains Elastic strains are instantaneous, reversible strains, dependent on the stress level:

$$\Delta\epsilon_e = \frac{\Delta\sigma}{E_c\,(t_{eq})} \tag{8.3}$$

  with E_c the elastic modulus of concrete. Since the modulus of elasticity changes with time, the instantaneous strains depend on the age of the concrete [107]. The elastic modulus is also dependent on the concrete temperature, since the hydration, and consequently the mechanical properties, will develop faster at higher temperatures. The equivalent time (t_{eq}) is therefore used.

- Shrinkage strains Shrinkage strains, both autogenous (ϵ_{as}) and drying (ϵ_{ds}), generally induce tensile stresses inside a concrete element and are independent on the stress level. Autogenous shrinkage strains are the result of hydration reactions, consuming water, and therefore result in constant stresses throughout the structure. Drying shrinkage strains, on the other hand, start to occur at the surface of the concrete due to differences in relative humidity between the concrete and the environment, hereby creating a drying shrinkage gradient through the concrete element. The concrete surface encounters more drying shrinkage and will therefore be more likely to experience (micro)cracking, compared to the core of the element. Drying shrinkage is only considered as from final setting, neglecting early-age plastic shrinkage. The development of the autogenous and drying shrinkage strains is also considered to be dependent on the temperature development, taken into account by using t_{eq}.

- Thermal strains Thermal strains arise due to the exothermic hydration reactions, resulting in a temperature increase inside the concrete element, inducing thermal swelling and corresponding compressive stresses. After the main hydration peak, the temperature decreases, inducing thermal shrinkage and corresponding tensile stresses. Thermal stresses vary over the section of the element, with higher temperatures reached in the core of the specimen and lower temperatures reached at the concrete surfaces. The thermal strains are independent on the stress level and can be calculated knowing the coefficient of thermal expansion (CTE) and the temperature (T) development inside the concrete element in time:

$$\Delta\epsilon_{th} = \mathrm{CTE} \cdot \Delta\mathrm{T} \tag{8.4}$$

In order to avoid time consuming finite element calculations, and to provide a simple tool for cracking risk prediction, only cracking or failure of the global/total element is considered (neglecting local surface cracking). The thermal and drying shrinkage strains are therefore averaged over the section of the concrete structure.

- Creep strains Creep strains are dependent on the stress level and reduce elastic tensile or compressive stresses under constant strain due to relaxation, either positively or negatively influencing the total cracking risk. Considering only shrinkage (i.e. development of tensile stresses), creep will positively influence the cracking risk, since tensile stresses are reduced, delaying or avoiding cracking (see Fig. 8.1 (left)). Considering both shrinkage and swelling (e.g. thermal or autogenous swelling), both compressive and tensile stresses will develop, possibly expediting cracking (see Fig. 8.1 (right)). Since creep strains are affected by temperature in several ways [95], creep is also considered as a function of the equivalent time.

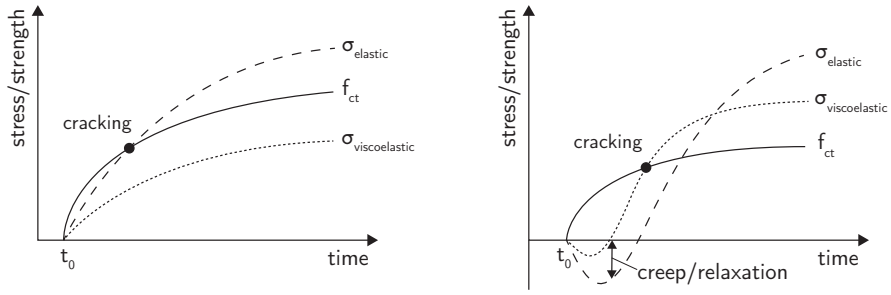

Figure 8.1: Effect of creep on concrete cracking, considering only shrinkage (left) and considering both shrinkage and swelling (right) (f_{ct}: tensile strength, $\sigma_{elastic}$: elastic stresses (neglecting creep), $\sigma_{viscoelastic}$: viscoelastic stresses (incorporating creep/relaxation)) (positive stresses = tensile stresses), adapted from [65].

Considering the respective strains, the restrained stresses can be derived from Eq. 8.2, by rewriting the stress-dependent strains (elastic and creep strains) as a function of their stress level, according to Eq. 8.3 and Eq. 7.21, 7.25 and 7.27 (basic and drying creep model):

$$\Leftrightarrow \Delta\epsilon = \underbrace{\frac{\Delta\sigma}{E_c\,(t_{eq})}}_{\Delta\epsilon_e} + \Delta\epsilon_{as} + \Delta\epsilon_{ds} + \Delta\epsilon_{th} + \underbrace{\alpha' + \alpha \cdot \frac{\Delta\sigma}{2}}_{\Delta\epsilon_{bc,Kelvin\text{-}Voigt}} + \ldots$$

$$\cdots + \underbrace{\frac{1}{\eta_M\,(t_{eq})} \cdot \left(\sigma_n + \frac{\Delta\sigma}{2}\right) \cdot \Delta t_{eq}}_{\Delta\epsilon_{bc,Maxwell}} + \underbrace{\beta_{dc} \cdot \left(\sigma_n + \frac{\Delta\sigma}{2}\right) \cdot \Delta\epsilon_{ds}}_{\Delta\epsilon_{dc}} = 0 \quad (8.5)$$

with:

$$\alpha = \frac{\Delta t_{eq}}{E_{KV}\,(t_{eq}) \cdot \tau_{KV}} \cdot \exp\left(-\frac{\Delta t_{eq}}{2 \cdot \tau_{KV}}\right) \quad (8.6)$$

$$\alpha' = \alpha \cdot (\sigma_n - \sigma_{E_{KV}}\,(t_{eq,n})) \quad (8.7)$$

Eq. 8.5 rewrites as:

$$\Leftrightarrow \Delta\sigma = -\frac{\sigma_n \cdot \left(\beta_{dc} \cdot \Delta\epsilon_{ds} + \frac{\Delta t_{eq}}{\eta_M(t_{eq})}\right) + \alpha' + \Delta\epsilon_{th} + \Delta\epsilon_{ds} + \Delta\epsilon_{as}}{\frac{1}{E_c(t_{eq})} + \frac{\beta_{dc}}{2} \cdot \Delta\epsilon_{ds} + \frac{\Delta t_{eq}}{2 \cdot \eta_M(t_{eq})} + \frac{\alpha}{2}} \quad (8.8)$$

The total restrained stresses can then be calculated as:

$$\sigma\,(t_{eq,n}) = \sigma\,(t_{eq,n\text{-}1}) + \Delta\sigma \quad (8.9)$$

Input parameters

The cracking index I_{cr} is dependent on the hydration process (t_0, $T \rightarrow t_{eq}$), the coefficient of thermal expansion (CTE), the elastic properties (E_c), the strength development (f_c, f_{ct}), the shrinkage behaviour (ϵ_{as}, ϵ_{ds}) and the creep behaviour (ϵ_{bc}, ϵ_{dc}). The temperature and drying shrinkage development are, on their turn, influenced by the boundary conditions: the thickness of the concrete element and, respectively, the ambient temperature and relative humidity. The concrete properties, needed as input parameters to calculate/predict the cracking index, are all highly dependent on the concrete mix, and have been thoroughly studied and modelled in the previous chapters. The Bazant B4 model was used for prediction of both the autogenous and drying shrinkage. Although the β-n model was found to be the best predictor for the drying shrinkage, the Bazant B4 model was chosen, since the β-n model is independent on the ambient relative humidity and geometry of the concrete specimen. The coefficient of thermal expansion (CTE) is assumed to be constant for all concrete mixes and constant as a function of time (10 μm/m/K).

8.2 Cracking risk

8.2.1 Autogenous shrinkage induced cracking risk

Considering only autogenous shrinkage strains, Eq. 8.8 simplifies to:

$$\Delta\sigma = -\mathrm{E_c}\left(\mathrm{t_{eq}}\right) \cdot \Delta\epsilon_{\mathrm{as}} \tag{8.10}$$

The autogenous shrinkage induced cracking index is shown in Fig. 8.2, respectively as a function of the equivalent time (left) and as a function of the autogenous shrinkage (right), using both the experimental autogenous shrinkage results (full lines) as well as the modelled autogenous shrinkage results (dashed lines) to calculate the developed stresses. The autogenous shrinkage is independent of the specimen size and the ambient relative humidity.

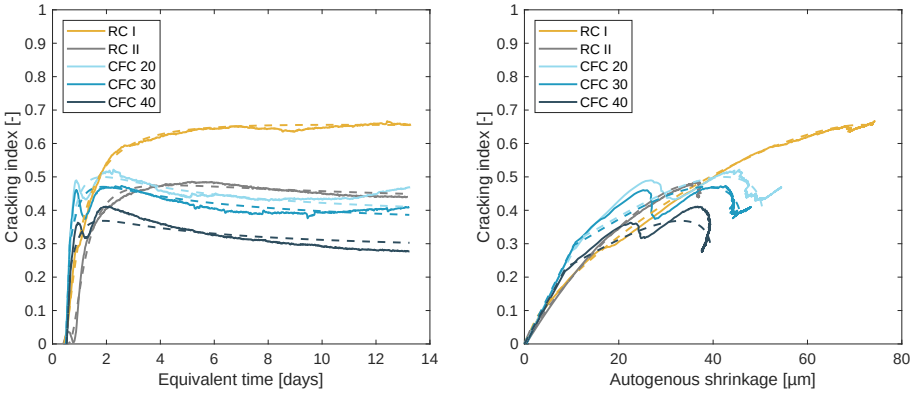

Figure 8.2: Autogenous shrinkage induced cracking index versus equivalent time (left) and versus autogenous shrinkage (right) for the different concrete mixes: experiments (full line) versus model (dashed line).

It is observed from Fig. 8.2 (left) that the cracking index using the experimental autogenous shrinkage results slightly deviates from the cracking index using the modelled autogenous shrinkage results, especially in the beginning and for the blended cement mixes. This is the result of the autogenous swelling peak at early ages, which is not taken into account in the model. From about two days up to 14 days, the cracking indexes using the experimental data and model correspond well. Fig. 8.2 (left) also shows that, after 14 days, the cracking risk is the highest for the reference mix with OPC, and the lowest for the CFC mix with 40% of CFC. This is the result of the lower autogenous shrinkage, but still considerable tensile strength and elastic modulus of the blended cement concretes. The cracking risk of the CFC blended cement concretes is also

lower than the cracking risk of the FA blended cement mix. For all mixes, the cracking index stays below 1, meaning that there is no risk of cracking induced by autogenous shrinkage strains.

Fig. 8.2 (right) shows the correlation between the autogenous shrinkage induced cracking risk and the autogenous shrinkage strains. It is observed that no perfect correlations exist between the cracking index and the autogenous shrinkage strains. The cracking index does not increase linearly with increasing autogenous shrinkage. This is the result of the combined influence of the tensile strength, elastic modulus and autogenous shrinkage on the cracking risk.

8.2.2 Drying shrinkage induced cracking risk

Considering only drying shrinkage strains, Eq. 8.8 simplifies to:

$$\Delta\sigma = -\mathrm{E_c}\left(\mathrm{t_{eq}}\right) \cdot \Delta\epsilon_{\mathrm{ds}} \tag{8.11}$$

The calculated cracking index, when considering only drying shrinkage strains, is shown in Fig. 8.3, as a function of the equivalent time (left) and as a function of the drying shrinkage (right), using both the experimental (full lines) as well as the modelled (dashed lines) shrinkage results.

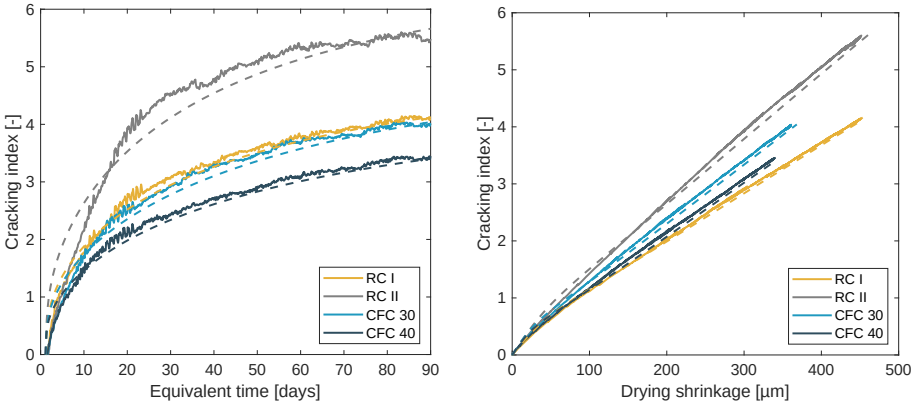

Figure 8.3: Drying shrinkage induced cracking index versus equivalent time (left) and versus drying shrinkage (right) for the different concrete mixes: experiments (full line) versus model (dashed line) (r = 60 mm).

The above cracking indexes correspond to a structure with the size of the specimen of the experiment (a cylinder with a radius of 60 mm), exposed to a relative humidity of 60%. The drying shrinkage induced cracking index is the highest for the reference mix with fly ash and the lowest for the CFC blended

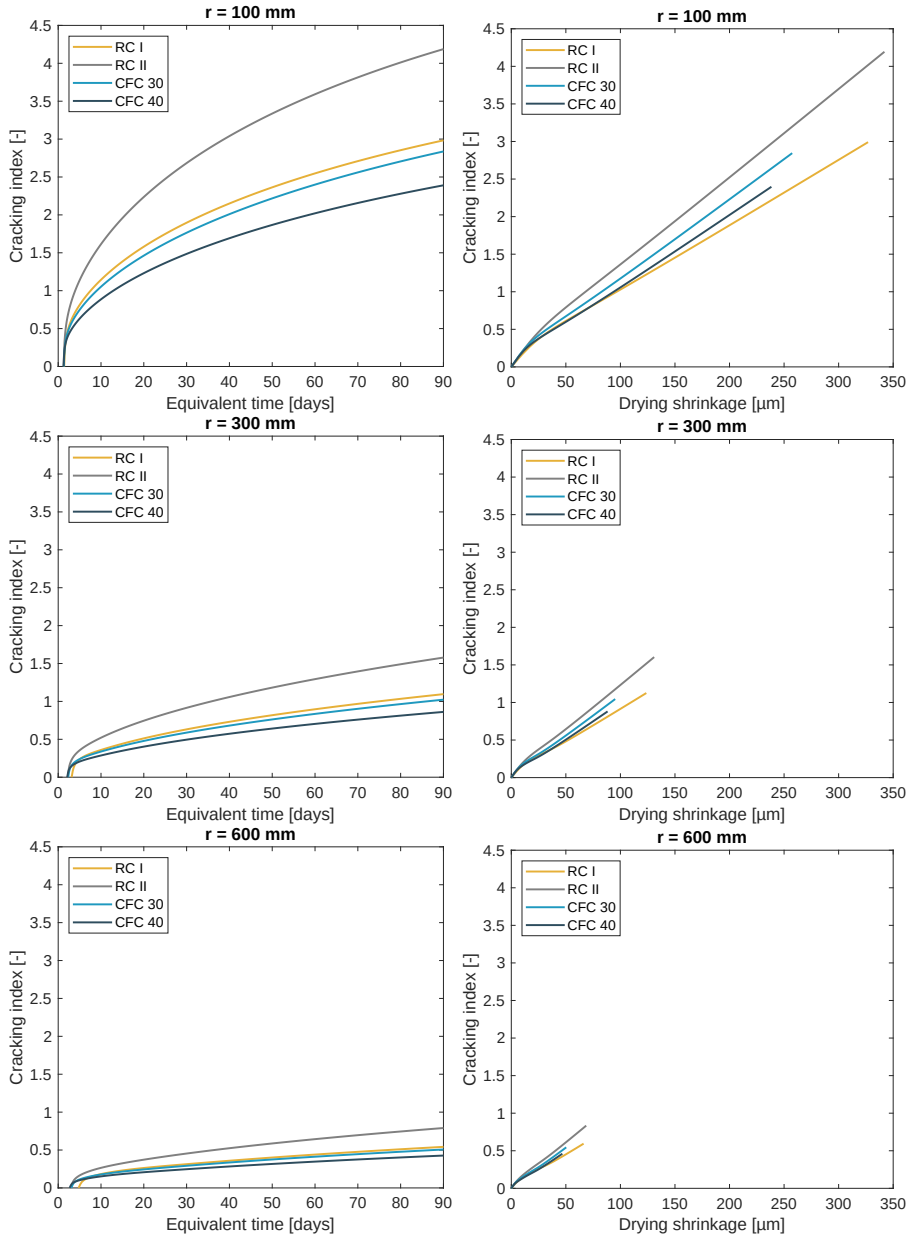

Figure 8.4: Drying shrinkage induced cracking index versus equivalent time (left) and versus drying shrinkage (right) for three different structure sizes (r = 100 mm, r = 300 mm and r = 600 mm).

cement concretes. The high drying shrinkage induced cracking risk of the RC II mix is the result of its considerable drying shrinkage (compared to the CFC mixes) and its low tensile strength (compared to the RC I mix). From around two days on, the cracking indexes of all mixes surpass the value 1, causing a cracking risk for the concrete structure. In contrast to the autogenous shrinkage induced cracking index, the relationship between the total shrinkage and the cracking index is linear. The drying shrinkage induced cracking index thus increases for increasing drying shrinkage.

For real applications, however, the size of the structures will be bigger. Therefore, three different structure sizes are considered, all representing a different building element: (1) a small structure of around 20 cm thickness (e.g. walls, classical slabs, etc.), (2) a semi-massive structure of around 60 cm thickness (e.g. bridges, tunnels, waste-water stations, etc.) and (3) a massive structure of 1.2 m thickness (e.g. dams, nuclear power plants, etc.). Fig. 8.4 shows the cracking index as a function of the time (left) and as a function of the drying shrinkage (right) for the three different structure sizes respectively.

It is observed that the cracking index decreases for increasing specimen size, due to the lower average drying shrinkage. In massive structures, drying shrinkage can a priori be neglected [95]. Also, the bigger the concrete element, the smaller the difference in cracking index between the different mixes. For massive concrete structures (r = 600 mm), the cracking indexes of the RC I and CFC mixes are almost the same, while for smaller elements, the CFC blended cement mixes clearly show a lower cracking index. The relationship between the cracking index of the different mixes stays the same. For the largest structure size, all mixes even show cracking indexes lower than 1. However, it should be remarked that, although there is no risk of cracking of the global element, microcracking at the surface of the concrete element is most likely to occur, due to development of a drying shrinkage gradient.

8.2.3 Thermal strain induced cracking risk

Considering only thermal strains, Eq. 8.8 simplifies to:

$$\Delta\sigma = -\mathrm{E_c}\,(\mathrm{t_{eq}}) \cdot \Delta\epsilon_{\mathrm{th}} \tag{8.12}$$

The cracking index as a result of thermal strains is shown in Fig. 8.5, as a function of the equivalent time (left) and as a function of the temperature development (right), for the three considered structures sizes. The results in Fig. 8.5 (left) all first show a small increase in cracking index, which later on goes back to zero and finally increases again to a much larger value. This first

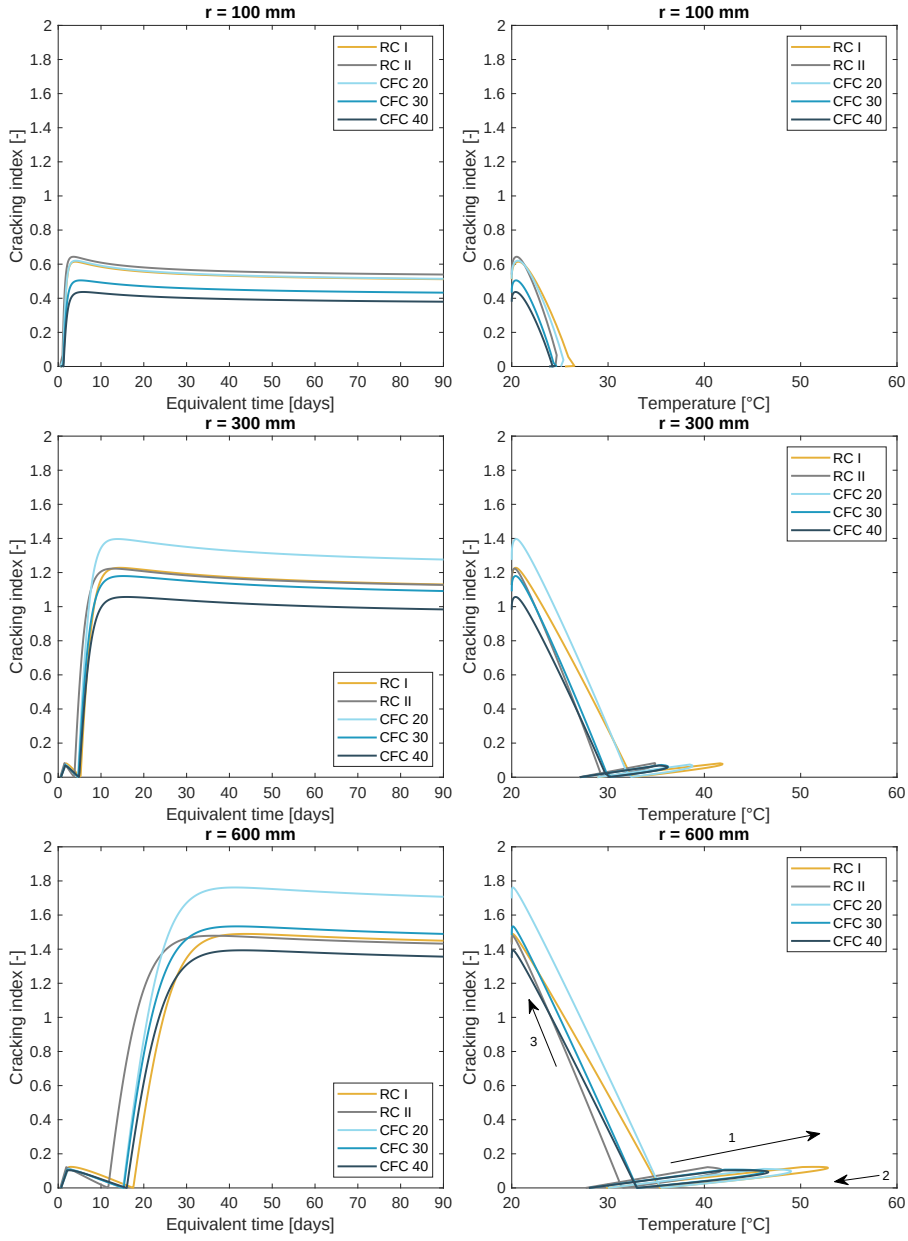

Figure 8.5: Temperature induced cracking index versus equivalent time (left) and versus temperature (right) for three different structure sizes (r = 100 mm, r = 300 mm and r = 600 mm).

'peak' corresponds to the development of compressive stresses, due to the temperature increase (as a result of the exothermic hydration reactions) and corresponding thermal swelling. After the main hydration peak, the temperature decreases, and thermal shrinkage strains starts to develop during this cooling period. This corresponds to the second increase of the cracking index and the development of tensile stresses. In the results in Fig. 8.5 (right), the same development is visible. First an increase in temperature and cracking index due to thermal swelling and corresponding compressive stresses is observed (arrow 1), second a decrease in temperature and cracking index, as the main hydration peak has passed (arrow 2) and third back an increase in cracking index due to the development of tensile stresses, while the temperature still keeps decreasing back to the ambient temperature (arrow 3).

It can be concluded that the bigger the concrete structure, the higher the cracking risk due to thermal stresses and the longer the period of compressive stresses in the concrete structure. For the smallest structure size, the initial compressive stresses are even negligible, due to the very small temperature rise. The relationship between the different concrete mixes varies depending on the size of the element, due to the combined influence of thermal stresses and mechanical properties on the cracking index. For a radius of the element of 100 mm for example, the RC II mix shows the highest cracking index, while the CFC 40 mix shows the lowest cracking index. For the biggest element size (r = 600 mm), however, the CFC 20 and CFC 30 mixes show the highest cracking risk, followed by the two reference mixes and the CFC 40 mix still shows the lowest cracking risk. It is thus concluded that, although lower temperatures develop in the CFC mixes, the cracking risk of these mixes is higher in bigger structures, due to the lower tensile strength and equal (or higher) elastic modulus of the CFC 20 and CFC 30 mix.

8.2.4 Total cracking risk

The total cracking index, as a result of autogenous shrinkage, drying shrinkage and temperature strains, is shown in Fig. 8.6 (right), both considering only elastic stresses (full lines) and considering viscoelastic stresses (dashed lines), taking into account creep/relaxation. Considering only elastic stresses, Eq. 8.5 simplifies to:

$$\Delta\sigma = -\mathrm{E_c}\left(\mathrm{t_{eq}}\right) \cdot \left(\Delta\epsilon_{\mathrm{as}} + \Delta\epsilon_{\mathrm{ds}} + \Delta\epsilon_{\mathrm{th}}\right) \tag{8.13}$$

Considering viscoelastic stresses, Eq. 8.5 is used. The corresponding total stresses are also depicted in Fig. 8.6 (left). It should be remarked that for the prediction of the autogenous shrinkage stains, the values from 14 up to 90 days are extrapolated from the Bazant B4 model, whose parameters were calibrated

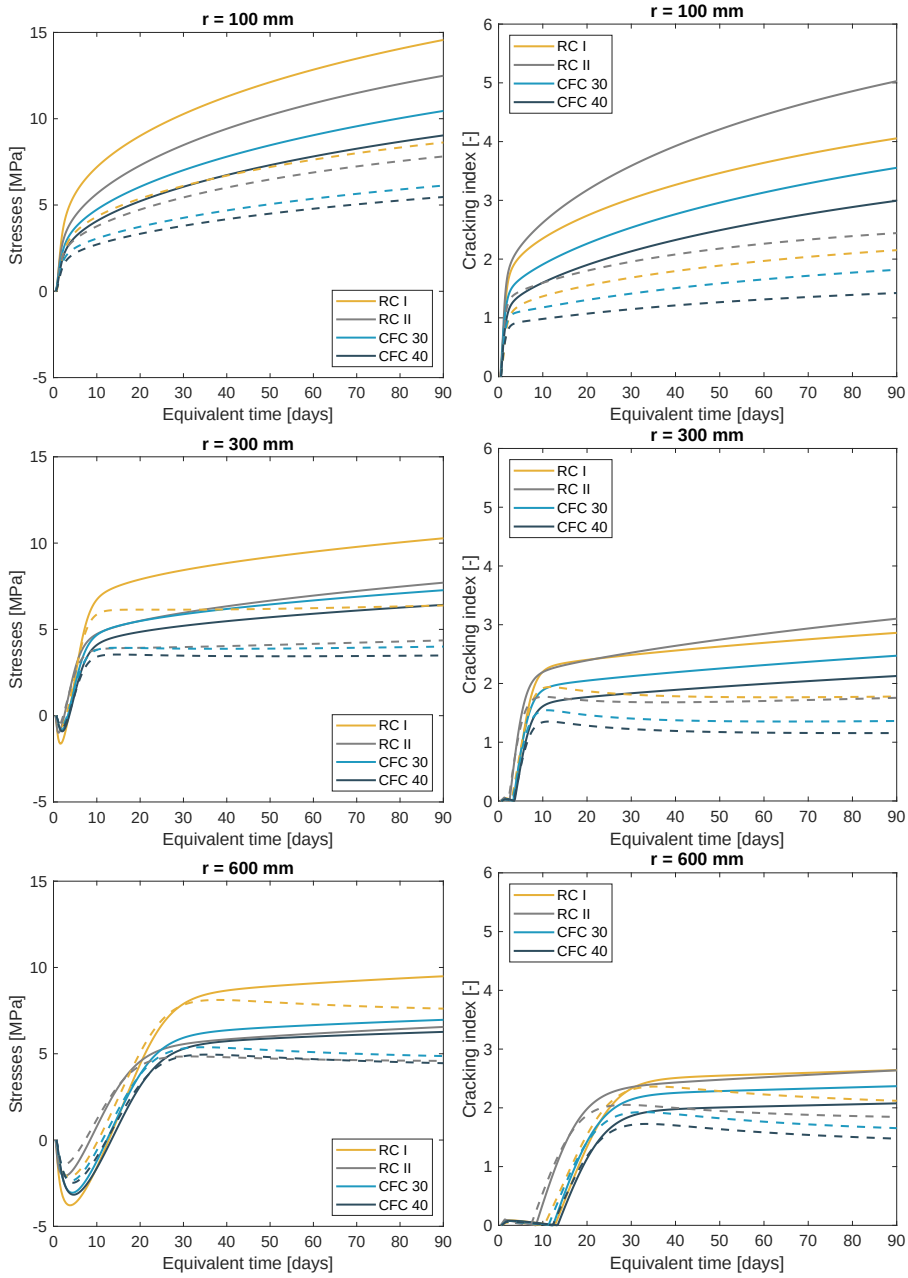

Figure 8.6: Total cracking index versus equivalent time for three different structure sizes (r = 100 mm, r = 300 mm and r = 600 mm), considering only elastic stresses (full lines) and considering viscoelastic stresses (dashed lines).

using experimental autogenous shrinkage results up to 14 days. It is immediately observed from Fig. 8.6 (left) that incorporation of creep strongly reduces the total tensile stresses, especially for smaller concrete elements. As the total stresses are the result of the autogenous, drying and thermal stresses, compressive stresses develop in the beginning due to thermal swelling. Regarding massive concrete structures (r = 600 mm), it is observed that tensile stresses occur slightly earlier considering viscoelastic stresses, compared to considering only elastic stresses, as the compressive stresses are also reduced.

From the drying shrinkage and thermal shrinkage induced cracking risk, it was concluded that bigger structures encounter more risk of cracking due to thermal variations, while smaller structures, on the other hand, encounter more risk of cracking due to drying shrinkage strains. Both effects thus compensate each other while considering total stresses. The differences between the cracking indexes of the concrete structures with different size, are therefore rather small (compared to the differences between the cracking indexes considering only thermal or drying shrinkage strains), especially for r = 300 mm and r = 600 mm. However, bigger concrete structures still result in lower total cracking risk, concluding that the drying shrinkage strains dominate the thermal strains. Overall, it is concluded that the two reference mixes (RC I and RC II) encounter the highest cracking indexes, while the CFC blended cement mixes have the lowest cracking risk, for all structure sizes. The development of compressive stresses in the beginning, delays the development of tensile stresses and associated cracking risk, especially for bigger concrete structures. However, the cracking index exceeds the value 1 for all mixes, for all structure sizes. The results of Fig. 8.6 also confirm that incorporation of creep is highly important, especially for smaller concrete elements, in order not to overestimate the developing restrained stresses.

8.2.5 Rate form versus non-rate form

The cracking indexes, calculated using Eq. 8.8 for prediction of the restrained stresses, assume a rate form of both the stresses and strains ($\Delta\sigma = E_c \cdot \Delta\epsilon$). It would, however, be easier to use the non-rate form ($\sigma = E_c \cdot \epsilon$), as this would simplify the calculations. Fig. 8.7 shows the cracking indexes, calculated with both the rate form (full lines) and the non-rate form (dashed lines), for the autogenous shrinkage induced cracking risk, drying shrinkage induced cracking risk, thermal strain induced cracking risk and total cracking risk (only assuming elastic strains), for r = 300 mm. It is observed that the cracking risk due to autogenous and drying shrinkage is overestimated using the non-rate form, while the thermal strain induced cracking risk is highly underestimated. The latter is the result of the rapid change in thermal stresses in the beginning, which is not

properly taken into account in the non-rate calculation of the cracking index. As a result, the compressive stresses are highly overestimated and tensile stresses do not even occur anymore. The total cracking risk, therefore, is also highly underestimated by using the non-rate form. This proves the importance of the rate form, correctly describing the early-age cracking behaviour of concrete.

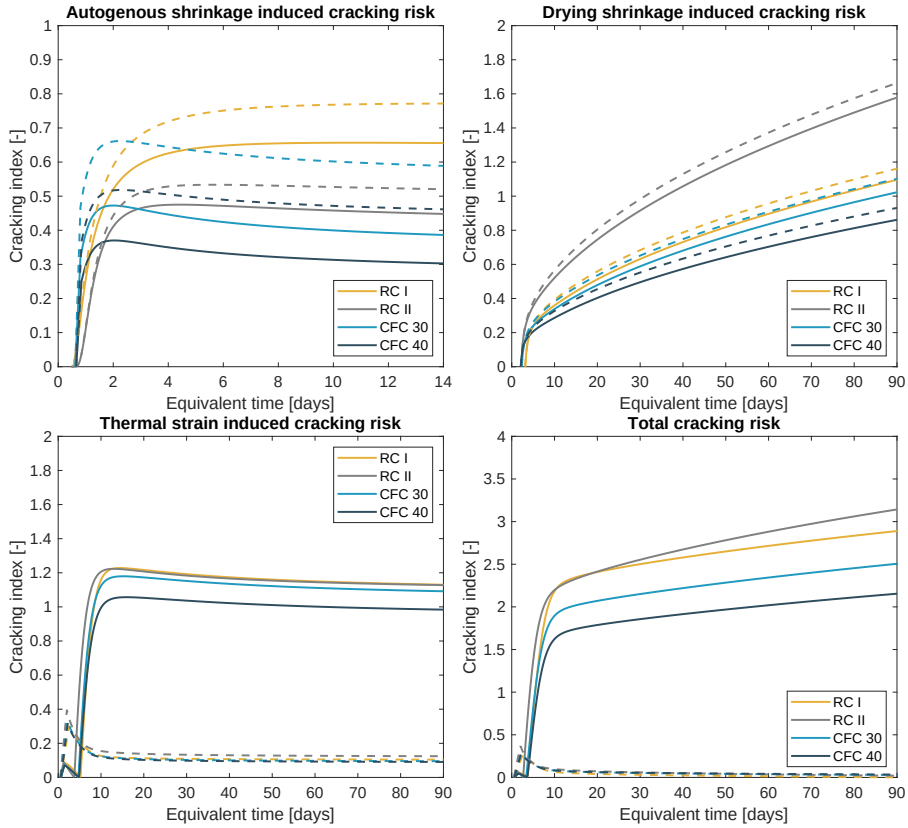

Figure 8.7: Cracking index versus equivalent time: rate form (full lines) versus non-rate form (dashed lines), for autogenous shrinkage induced (upper left), drying shrinkage induced (upper right), thermal strain induced (bottom left) and total (bottom right) cracking risk (r = 300 mm).

8.3 Conclusion

This chapter presented the development of a 'simple' tool to predict early-age and long-term thermal-shrinkage-creep induced cracking risk of concrete, using the definition of a cracking index. This cracking index is dependent on the hydration process, coefficient of thermal expansion, elastic properties, strength development, shrinkage behaviour and creep behaviour of concrete. All these parameters are therefore needed as input parameters. The experimentally assessed models for temperature, mechanical properties, shrinkage and creep, presented in the previous chapters, were used to predict these concrete properties.

It is concluded that CFC blended cement reduces both the autogenous shrinkage and drying shrinkage induced cracking risk of concrete, due to the lower autogenous and drying shrinkage strains. Although the temperature developed in concrete structures is reduced by the use of CFC blended cement, the thermal strain induced cracking risk of CFC concrete is higher at low replacement ratios (CFC 20 and CFC 30), due to the slightly lower tensile strength, but still considerable elastic modulus. Regarding the total cracking index (taking into account thermal, autogenous shrinkage and drying shrinkage strains), it is concluded that CFC blended cement reduces the cracking risk of concrete, compared to the two reference mixes. This is the result of the combined influence of the tensile strength, elastic modulus and total strains on the cracking risk.

The bigger the concrete structure, the higher the risk of cracking of the global element due to thermal variations, while the lower the risk of cracking due to drying shrinkage strains, independent of the cement type. Regarding the total cracking risk, bigger concrete structures result in lower cracking index, concluding the total cracking risk is more dominated by drying shrinkage strains, rather than thermal strains. However, the differences become smaller for bigger concrete structures. It should be remarked that, although the drying shrinkage cracking risk of the global element is less important for massive structures, bigger concrete structures will experience a higher drying shrinkage gradient, strongly increasing the cracking risk at the surface of the concrete element.

The influence of creep/relaxation was also taken into account by considering viscoelastic stresses. It is concluded that incorporation of creep results in the same relationship between the cracking indexes of the different concrete mixes (the CFC mixes still show the lowest cracking risk). However, the total cracking risk is strongly reduced by taking into account creep, especially considering smaller concrete structures. In order to accurately predict the cracking risk of a concrete structure, it is therefore of major importance to also take the creep/relaxation behaviour into account, in order not to underestimate the material and over-dimension the concrete structure.

Chapter 9

Conclusion

9.1 General conclusions

The use of supplementary cementitious materials (SCMs) as partial cement replacement in concrete is the most promising and well-established option to reduce the environmental impact of the cement industry. However, due to the limiting regional availability and production of suitable, high-quality SCMs, there is a strong need for new sources of SCMs, in order to further reduce the global clinker factor. Yet, understanding of early-age and long-term performance and durability of concrete blended with alternative SCMs currently lacks scientific knowledge.

The use of dewatered and calcined dredging sediments (CFC) from the port of Antwerp as a potential new SCM for the production of sustainable cement and concrete, was investigated in this thesis. Replacement of ordinary Portland cement (OPC) by SCMs alters the hydration process, early-age properties, mechanical behaviour, as well as the shrinkage and creep behaviour. The main objective of this research is to assess the effect of CFC on the early-age properties of concrete, in order to understand its early-age deformation potential and to predict its time-dependent deformations at long term.

Fresh and mechanical properties of CFC concrete

Fresh and mechanical properties of CFC concrete were studied while optimising the concrete mix design. Three different concrete design parameters were

investigated: cement replacement ratio, type and dosage of superplasticizer and water-to-binder ratio. The main conclusions are summarised as follows:

- The use of a superplasticizer is necessary in CFC concrete to counterbalance the higher water demand, resulting from the high specific surface area of CFC. Increasing replacement ratios of OPC by CFC require higher levels of superplasticizers and PCE superplasticizers were found to be the most effective to work in combination with CFC.
- For a water-to-binder ratio of 0.45, slump class S2 - often used for production of ready-mix concrete - is reached without exceeding the maximal dosage of superplasticizer as prescribed by the producer.
- CFC blended cement reduces the early-age concrete strength, but strongly increases the concrete strength at later ages due to the pozzolanic activity of CFC. The strength development of CFC concrete is similar to the strength development of fly ash (FA) concrete. However, CFC concrete reaches higher absolute strength values than FA concrete.

Hydration process and early-age properties of CFC blended cement

The effect of CFC on the hydration process and early-age properties was studied by isothermal calorimetry, XRD, internal relative humidity and ultrasonic pulse velocity (UPV) measurements. The main conclusions are summarised as follows:

- CFC enhances OPC hydration by the filler effect at early ages and by the formation of additional hydration products, contributing to the strength development, at later ages. The use of a superplasticizer, on the other hand, delays the cement hydration.
- The hydration products of CFC blended cements are similar to the hydration products formed in OPC and FA reference mixes. The use of CFC blended cement results in additional formation of portlandite and amorphous phases. In addition, the presence of CFC increases the amount of ettringite due to the increased total sulphate and carbonate level. Nevertheless, formation of hemicarbonate in the CFC blend stabilises voluminous ettringite formation.
- Due to the dilution effect and higher effective water-to-cement ratio, CFC blended cement mixes show a lower drop in internal relative humidity, compared to an OPC reference mix. This positively influences the development of autogenous shrinkage due to self-desiccation.

- The UPV method was used as an alternative method for setting detection in cement paste and concrete, and monitors changes in elastic properties of cement paste and concrete mixes (i.e. the mechanical aspects associated with the hydration). UPV setting times are more accurate than standard Vicat setting times due to the destructive and non-continuous character of the Vicat method. However, the use of a superplasticizer strongly influences initial P-wave velocity development, complicating/impeding initial setting time detection in cement paste. The $t(\delta V_P^{max})$ criteria was used for final setting time determination in cement paste, while for concrete the $t(\delta V_S^{max})$ and $t(\delta E_d^{max})$ methods were found to be the best predictors of the initial and final setting times, respectively. As superplasticizer delays the cement hydration, the initial and final setting times of CFC blended cement and concrete were subsequently delayed.

Shrinkage and creep of CFC concrete

The chemical shrinkage, autogenous shrinkage and drying shrinkage behaviour, and basic and drying creep behaviour of CFC blended cement concrete were studied experimentally. The main conclusions regarding the influence of CFC on the time-dependent volumetric changes are summarised as follows:

- CFC blended cement increases chemical shrinkage per g of OPC as a result of the filler effect and early pozzolanic reaction of CFC.
- CFC blended cement reduces autogenous shrinkage due to the development of an autogenous swelling peak, delaying the shrinkage, and due to the dilution effect and formation of different hydration products, reducing the rate of autogenous shrinkage of CFC cement paste and concrete. The observed swelling peak is attributed to the development of a crystallisation pressure as a result of supersaturation of the pore solution with respect to ettringite. The additional amount of ettringite formed in the CFC mixes and the higher sulphate to aluminate ratio of the CFC blended cements confirm this hypothesis. The autogenous shrinkage development of CFC concrete is similar to the autogenous shrinkage behaviour of FA concrete in delaying the shrinkage by developing a swelling peak and reducing the autogenous shrinkage rate.
- CFC blended cement reduces drying shrinkage, as a result of the dilution effect and altered porosity and pore size distribution of CFC concrete. Drying shrinkage weight loss, on the other hand, is significantly increased for the CFC blended concretes, due to their slower hydration and slower development of a porous network, allowing free water to evaporate more easily at early ages.

- CFC blended cement reduces basic creep of concrete. Since the exact mechanisms at the origin of creep are not yet fully understood for OPC concrete, it is difficult to find out the reason for the reduced basic creep of CFC concrete. However, the formation of different hydration products, in which the amount and composition of C-S-H play a significant role, and the altered porosity and pore size distribution of CFC concrete are most likely to explain the reduced basic creep.
- Due to the high errors of the experimental drying creep results, no conclusions could be made regarding the influence of CFC on the drying creep. The high uncertainty of these measurements resulted from: (1) the fact that drying creep is calculated using a combination of drying creep measurements, basic creep measurements and shrinkage measurements, increasing the total experimental errors, (2) the difference between basic creep in autogenous conditions and basic creep in drying conditions and (3) the occurrence of microcracking due to drying shrinkage.

Modelling of concrete properties

Modelling of early-age concrete properties allows prediction of concrete performance and durability at later ages. The temperature development of CFC concrete was modelled by numerically solving the heat equation, using concrete calorimetry results for parameter identification. The model of EC 2 describes well the development of the compressive strength, tensile strength and static elastic modulus of CFC blended cement concrete, provided that the cement type dependent parameters are adjusted according to the CFC blended cement system. Autogenous and drying shrinkage of CFC concrete were modelled by parametrising existing empirical shrinkage models, using the experimental shrinkage data for calibration. The Bazant B4 model appears to be the best prediction model for the autogenous shrinkage. The β-n model is the best predictor for the drying shrinkage, followed by the EC 2 model for the reference mixes and the Bazant model for the CFC blended cement mixes. Basic creep was modelled using a rheological model consisting of a Kelvin-Voigt and Maxwell chain, and drying creep was modelled using the relationship between drying shrinkage and drying creep.

Development of a cracking prediction tool

In order to assess the thermal-shrinkage induced cracking risk of CFC concrete structures, a 'simple' cracking prediction tool was developed, based on the definition of a cracking index (I_{cr}). The cracking index is defined as the ratio of

the restrained tensile stresses (σ) to the tensile strength (f_{ct}) of the concrete structure, and cracking occurs when $I_{cr} > 1$. The restrained stresses are calculated assuming fully restrained conditions (i.e. $\Delta\epsilon = 0$) and using the models described above for prediction of the concrete properties. The viscoelastic behaviour of concrete is taken into account by considering creep/relaxation.

Fig. 9.1 summarises the methodology to calculate the cracking index and the model equations used for concrete properties prediction. The input data needed for calibration of the models is indicated in blue and includes calorimetry data, strength and stiffness data, shrinkage data and creep data. The variable boundary conditions are indicated in orange. The temperature development is influenced by the initial concrete temperature (T_0), the ambient temperature (T_{ext}), the coefficient of heat exchange by convection (h_p) and the concrete element size, while the drying shrinkage development is influenced by the ambient relative humidity (RH) and geometry of the concrete structure. The thermal properties (thermal conductivity (k), specific heat capacity (c_p), coefficient of heat exchange by convection (h_p) and coefficient of thermal expansion (CTE)) and the activation energy (E_a) are assumed to be constant for all compositions and constant in time. The mechanical properties, shrinkage and creep of concrete are assumed to develop as from final setting (t_0) and the influence of temperature on the mechanical properties, shrinkage and creep behaviour is taken into account by using the equivalent time (t_{eq}).

It is concluded that the thermal-shrinkage induced cracking risk of concrete is reduced by using CFC blended cement. This is the result of the combined influence of the tensile strength, elastic modulus and total strains of CFC concrete on the cracking risk. Bigger concrete structures experience a lower risk of cracking of the global element, due to their lower average drying shrinkage induced cracking risk. However, it should be noted that in practice, bigger concrete structures will experience a higher superficial cracking risk, due to the development of a higher drying shrinkage gradient. Incorporation of creep, finally, is of major importance to accurately predict the cracking risk of concrete structures, so that the material is not underestimated and the concrete structure is not over-dimensioned.

CFC as alternative SCM

The main objective of this thesis is to assess the influence of CFC on main concrete properties, in order to validate CFC as a suitable alternative SCM for the production of sustainable cement and concrete. The potential of CFC as alternative SCM in concrete is clearly proven, as the use of CFC blended cement reduces concrete autogenous and drying shrinkage, develops concrete

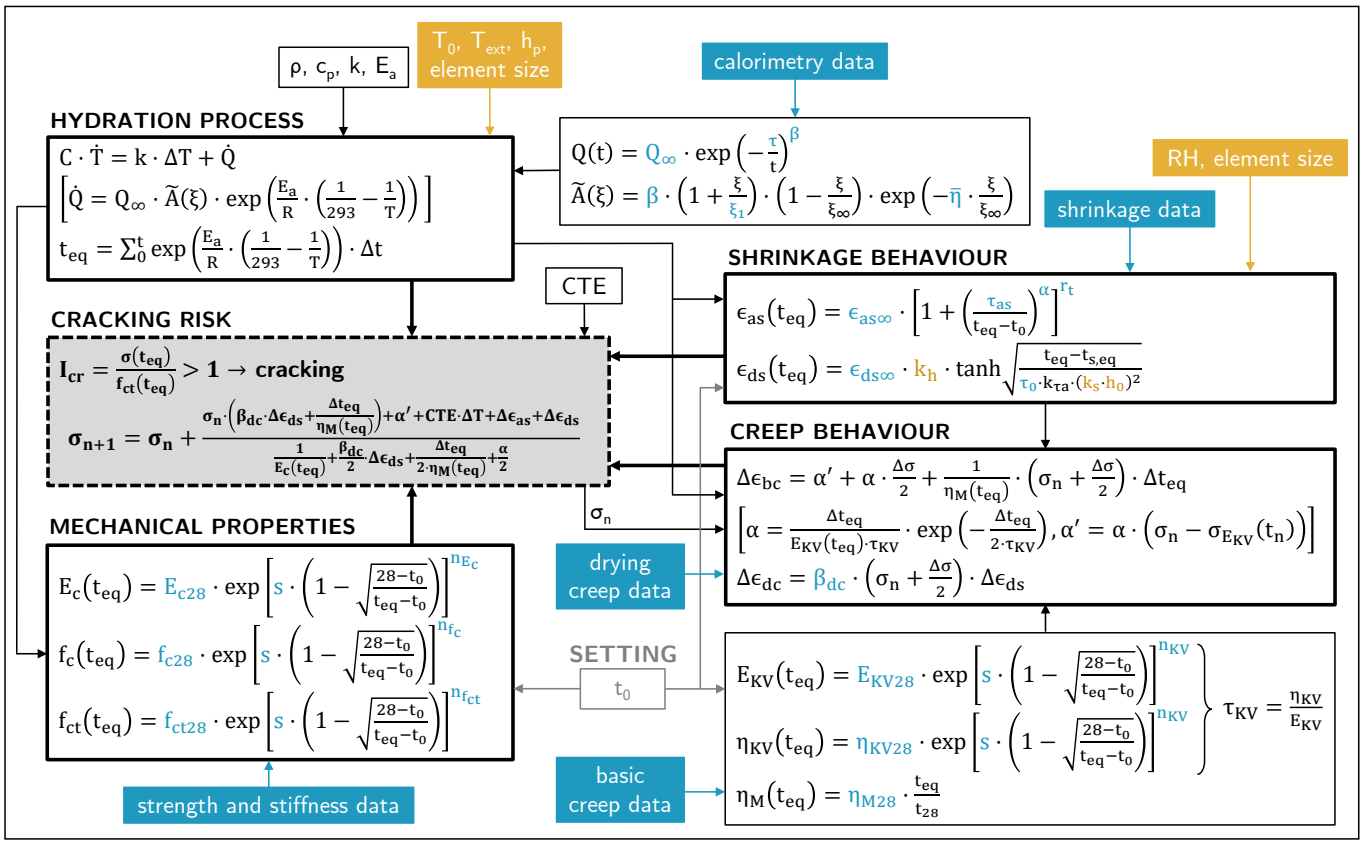

Figure 9.1: Schematic overview of the methodology for prediction of the cracking risk of concrete structures, using experimentally assessed temperature, mechanical properties, shrinkage and creep models.

strengths similar to those of OPC reference concretes and reduces the cracking risk of concrete structures. The pozzolanic behaviour of CFC is clearly shown by strength results. Lower early-age strengths are observed for CFC concrete, while at later ages, the strength significantly increases due to the pozzolanic reaction induced by CFC, reaching strength class C45/55. Large similarities between CFC blended cement and FA blended cement are observed regarding hydration, strength and shrinkage behaviour, proving CFC to behave as a typical SCM in concrete. Furthermore, parametrised models are provided to predict the CFC concrete temperature, mechanical performance, dimensional changes and cracking risk. The only 'drawback' of CFC is the high specific surface area, increasing the water demand of concrete and requiring the use of a superplasticizer, slightly delaying the setting. However, a delayed setting should not always be a drawback, since it also delays the development of internal stresses, positively influencing the shrinkage and durability of a concrete structure.

The results of this thesis clearly support the use of CFC as SCM in concrete. Provided that rheology properties, durability properties, structural behaviour and bond behaviour are further investigated (see Section 9.3) and relevant requirements are fulfilled, application of CFC blended cement for ready-mix concrete can be envisaged. Although a slump class S3 or S4 is demanded for these kind of applications, and the concrete mixes used in this thesis have a slump class S2, the results in Fig. 4.2 clearly show the potential of the material to reach higher slump classes.

Research findings cannot be generalised to all dredging sediments, since they vary from place to place in terms of composition, mineralogy, pretreatment, etc. However, the results may well be applied to important Western European ports with a similar geological and geographical situation such as Rotterdam and Hamburg [207].

9.2 Original contributions

In this thesis, the influence of the use of calcined dredging sediments as partial cement replacement in concrete has been investigated thoroughly, in order to provide a novel alternative SCM to meet the local needs of cement and concrete demands in Belgium, and to contribute to achieving the United Nations sustainable development goals [221].

Various essential aspects of early-age properties of CFC blended cement have been studied experimentally at two different material levels: cement paste and concrete. A number of standardised methods were used to study concrete properties, however, also some new (non-standardised) techniques were

assessed in order to be able to continuously capture the early-age behaviour of CFC blended cement and concrete. Furthermore, concrete properties have been modelled, allowing prediction of concrete performance at later ages. This doctoral thesis thus combines both experimental analysis and numerical modelling, and thereby provides a broad perspective on understanding of the influence of CFC as SCM in concrete.

Insights have been gained on the inclusion of CFC in mechanical properties, empirical shrinkage and rheological creep models, which is innovative and can be extended to other types of SCMs. Furthermore, a predictive tool to assess the cracking risk of CFC concrete was developed. Current research mainly considers only shrinkage as criteria for cracking. However, it is of major importance to also include the mechanical properties development (especially tensile strength and elastic modulus), temperature development and creep behaviour, as these properties also strongly influence the cracking risk of concrete and are highly affected by inclusion of SCMs. This thesis thus proposes a simple tool to accurately predict the global cracking risk of concrete structures, by considering a combination of all parameters influencing the cracking risk. The methodology can also be applied to other (SCM blended) concrete mixes.

9.3 Recommendations for future research

Based on the obtained results, a number of recommendations for further research can be formulated.

- Rheology properties should be studied in order to accurately determine the influence of CFC on the workability as well as the interaction between CFC and superplasticizer.
- In order to better understand the shrinkage and creep mechanisms in CFC concrete, the pore structure should be investigated: porosity, pore size distribution and analysis of the pore solution. To analyse the origin of creep in CFC concrete, further investigation regarding the amount of C-S-H, composition of C-S-H and elastic properties of C-S-H, is required. Creep in tension should also be studied.
- Durability properties, such as carbonation resistance, sulphate resistance, freeze-thaw resistance, chloride ingress, acid resistance, etc., should be investigated to get a complete picture of the performance of CFC concrete. Some durability properties of CFC blended cement concrete were already investigated in the BIND-AMOR project. It was concluded that CFC blended cement increases resistance against chloride ingress, carbonation,

sulphuric acid and alkali-silica reaction at long term, but decreases freeze-thaw resistance of concrete. Further in-depth analysis of the durability performance, however, is required.

- Regarding structural concrete applications, structural aspects of CFC concrete, fracture/cracking mechanisms, bond behaviour, etc. should be investigated. Finite element modelling (FEM) can be used to accurately analyse the structural behaviour.
- Validation of the cracking prediction tool could be done by experimental evaluation of the cracking risk by performing a ringtest.
- To improve the cracking prediction tool developed in this thesis, various experimental and numerical modifications/adjustments are proposed.
  - First of all, the models predicting the concrete properties could be improved in different ways, advancing the prediction of the cracking risk. The calibrated fitting parameters of all models could be determined more accurately if more data, especially at longer term, is available. Thus, additional long-term experiments to validate the models are recommended.
  - The temperature model could be improved by experimental determination of thermal conductivity (k), specific heat capacity (c_p), coefficient of heat exchange by convection (h) and the activation energy (E_a), increasing the accuracy of the predicted temperature development. Validation of the temperature model with temperature measurements is also recommended.
  - The basic creep model could be improved by more accurate estimation of the initial parameters and their boundaries. This could, for example, be done by calibrating the Kelvin-Voigt parameters by only using the reversible creep part of the unloading phase, as this part only represents reversible creep, while the loading phase always contains both reversible and irreversible creep, which cannot be distinguished. Additional basic creep measurements at different loading ages and for extended loading durations, could also give more confidence to the creep model and calibrated parameters. Furthermore, other rheological models could be investigated.
  - The drying creep model could be improved by adding potential differences in drying creep due to cracking differences in drying shrinkage and creep tests (microcracking). As for the basic creep, additional drying creep experiments at different loading ages and loading durations, could also improve parameter identification/determination of the drying creep model.

– Finally the coupling between creep and damage at early ages should also be studied.

Appendix A

Technical datasheets

This appendix contains the technical datasheets of the following cements, aggregates and superplasticizers:

- Ordinary Portland cement CEM I 52.5 N (ENCI/CBR);
- Portland fly ash cement CEM II/B-V 42.5 N (ENCI/CBR);
- River sand 0/4 (Coeck);
- River sand 0/2 (Volbrockshof);
- River sand 0/4 (Zandhandel);
- River gravel 4/16 (Coeck);
- River gravel 4/14 (Eurogri n.v.);
- River gravel 4/16 (Hülskens);
- MasterPozzolith 390N con 40% (BASF);
- MasterRheobuild 1100 con 40% (BASF);
- MasterGlenium 51 (BASF);
- Tixo® (Sika);
- ViscoCrete®-4035 M (Sika).

Portlandcement

CEM I 52,5 N

CEM I 52,5 N

1. Normen en certificaten

Benaming	Label	Norm	Certificaat N°
CEM I 52,5 N CE	CE	NBN EN 197-1	0965-CPR-C0019
CEM I 52,5 N CE BENOR	BENOR	NBN B12	18/02/019
CEM I 52,5 N CE	KOMO	BRL 2601	1118-16-1020

2. Opgegeven samenstelling

	Eenheden	Proefmethode	Gemiddelde waarden	Normeisen	
				Min	Max
Bestanddelen in % van de som van de hoofd- en nevenbestanddelen					
Klinker (K)	%	-	97	95	100
Slak (S)	%	-	-	-	-
Vliegas (V)	%	-	-	-	-
Kalksteen (LL)	%	-	-	-	-
Filler	%	-	3	0	5
Toevoegingen in % van het cement					
Bindtijdregelaar	%	-	5	-	-
Maalhulpstof	%	-	0.063	-	-
Reductiemiddel *	%	-	0.5	-	-

* Overeenkomstig de verordening EG 1907/2006 (Reach) wordt aan sommige cementen een reductiemiddel toegevoegd om het gehalte aan oplosbaar chroom (VI) te beperken tot maximaal 0,0002%.

3. Chemische en mineralogische kenmerken

	Eenheden	Proefmethode	Gemiddelde waarden	Normeisen	
				Min	Max
CaO	%	EN 196-2	63.3	-	-
SiO_2	%	EN 196-2	20.5		-
Al_2O_3	%	EN 196-2	5.0	-	-
Fe_2O_3	%	EN 196-2	3.3		-
C_3A	%	EN 196-2	7.6	-	-
SO_3	%	EN 196-2	3.1	-	≤ 4.0
Onoplosbare rest	%	EN 196-2	0.7		≤ 5.0
Gloeiverlies	%	EN 196-2	1.6	-	≤ 5.0
Chloride	%	EN 196-2	0.06	-	≤ 0.10
Chroom (VI) *	%	EN 196-10	< 0.0002	-	≤ 0.0002
Na_2Oeq**	%	EN 196-2	0.74	-	-
Sulfiden	%	EN 196-2	-	-	-

* Overeenkomstig de verordening EG 1907/2006 (Reach) moet het gehalte aan oplosbaar chroom (VI) beperkt zijn tot maximaal 0,0002%.

** Waarde van het gemiddelde + 1,96 x standaardafwijking.

CBR Cementbedrijven
Technische Voorlichting
Parc de l'Alliance - Boulevard de France 3 – 5
1420 Braine-l'Alleud - België
Tel : + 32 2 678 35 10
Fax : + 32 2 675 23 91
communication@cbr.be
www.cbr.be

ENCI
Technische Voorlichting
Postbus 3233
5203 DE 's-Hertogenbosch
Tel : + 31 73 640 12 20
Fax : + 31 73 640 12 18
tv@enci.nl
www.enci.nl

4. Fysische kenmerken

	Eenheden	Proefmethode	Gemiddelde waarden	Normeisen	
				Min	Max
Witheid	%	CIE 1931	0.0	-	-
Helderheid L	%	CIE Lab	59.7	-	-
Waterbehoefte	%	EN 196-3	29.7	-	-
Begin van de binding	min	EN 196-3	200	≥ 45	-
Einde van de binding	min	EN 196-3	250	-	≤ 720
Vormhoudendheid	mm	EN 196-3	<1	-	≤ 10
Specifiek oppervlak (Blaine)	cm^2/g	EN 196-6	3850	-	-
Zeefrest op 200 µm	%	EN 196-6	0.02	-	≤ 3.0
Hydratatiewarmte op 7d	J/g	EN 196-8	-	-	-
Volumieke massa - Absoluut	kg/m^3	-	3100	-	-
Volumieke massa - Stortgewicht	kg/m^3	-	1100	-	-

5. Mechanische kenmerken

Druksterkte	Eenheden	Proefmethode	Gemiddelde waarden	Normeisen	
				Min	Max
Na 1 dag	MPa	EN 196-1	21.1	-	-
Na 2 dagen	MPa	EN 196-1	37.1	≥ 20	-
Na 7 dagen	MPa	EN 196-1	54.5	-	-
Na 28 dagen	MPa	EN 196-1	66.7	≥ 52.5	-
2d/28d	-	-	0.56	-	-

6. Productie en levering

Dit cement kanop de volgende wijze worden afgeleverd :

Scheepsbulk	Vrachtbulk	Verpakt
X	X	X

7. Gecertificeerd managementsysteem van de fabriek.

8. Prestatieverklaring

Prestatieverklaring conform CPR(EU) Nr.305/2011

Identificatie : 0965-CPR-C0019

Website : www.cbr.be

De resultaten weergegeven in de tabellen zijn gebaseerd op gemiddelde waarden en zijn louter indicatief.

Enkel de normeisen worden gewaarborgd.

Portlandvliegascement

CEM II/B-V 42,5 N

MAASTRICHT

1. Normen en certificaten

Type cement	Certificaat	Norm	Certificaat N°
CEM II/B-V 42,5 N	CE	EN 197-1	0956-CPR-1101.1046
CEM II/B-V 42,5 N	KOMO	BRL 2601	1101-16-1085
CEM II/B-V 42,5 N	Benor	NBN B12	18/10/011

2. Opgegeven samenstelling

	Eenheden	Gemiddelde waarde	Normgrenzen	
			Min	Max
	Bestanddelen in % van de som van de hoofd- en nevenbestanddelen			
Klinker (K)	%	73	65	79
Hoogovenslak (S)	%		-	-
Poederkoolvliegas (V)	%	27	21	35
Filler	%		-	5
	Toevoegingen in % van het cement			
Bindtijdregelaar	%	4,5	–	–
Maalhulpstof	%	0,022	–	–
Reductiemiddel*	%	0,2	–	–

3. Chemische kenmerken

De chemische kenmerken van het cement worden bepaald volgens EN 196-2

	Eenheden	Gemiddelde waarde	Normgrenzen	
			Min.	Max.
CaO	%	47	-	-
SiO_2	%	29	-	-
Al_2O_3	%	9,97	-	-
Fe_2O_3	%	5	-	-
Sulfaat SO_3	%	2,48	-	3,5
Onoplosbare rest	%		-	5,0
Gloeiverlies	%	2	-	5,0
Chloride	%	0,06	-	0,10
Chroom (VI)*	%	< 0,0002	-	0,0002
Na_2O equivalent	%	0,81		

* Overeenkomstig de verordening EG 1907/2006 (Reach) moet het gehalte aan oplosbaar chroom (VI) beperkt zijn tot maximaal 0,0002%. Dit gehalte wordt bepaald volgens EN 196-10.

ENCI
Technische Voorlichting
Postbus 3233
5203 DE 's-Hertogenbosch
Tel: +31(0)73 640 12 20
tv@enci.nl
www.enci.nl

CBR Cementbedrijven
Technische Voorlichting
Parc de l'Alliance
Boulevard de France 3-5
1420 BRAINE-L'ALLEUD
Tel: +32(0)2 678 35 10
Fax: +32(0)2 675 23 91
communications@cbr.be
www.cbr.be

4. Fysische kenmerken

De fysische kenmerken worden bepaald volgens de genormaliseerde proefmethoden vermeld in de 2e kolom.

	Proefmethode	Eenheden	Gemiddelde waarde	Normgrenzen	
				min	max
Waterbehoefte	EN 196-3	%	29	-	-
Begin van de binding	EN 196-3	min.	185	60	-
Einde van de binding	EN 196-3	min.	250	-	-
Vormhoudendheid	EN 196-3	mm	0	-	10
Specifiek oppervlak (Blaine)	EN 196-6	cm²/gr	4465	-	-
Zeefrest 200 µm	EN 196-6	%		-	-
Hydratatiewarmte op 7d	-	J/g	>270	-	-
Volumieke massa				-	-
Absoluut	-	kg/m³	2960	-	-
Stortgewicht	-	kg/m³	1080	-	-
C-Waarde	-		1,20	-	-

5. Mechanische kenmerken

De druksterkte van het cement, gemeten op proefstukken gemaakt van een genormaliseerde mortel, wordt bepaald volgens EN 196-1.

Druksterkte	Eenheden	Gemiddelde waarde	Normgrenzen	
			min.	max.
Na 1 dag	MPa		-	-
Na 2 dagen	MPa	24	10,0	-
Na 7 dagen	MPa	38	-	-
Na 28 dagen	MPa	50	42,5	62,5

6. Productie en levering

Dit cement kan op de volgende wijzen worden afgeleverd:

Scheepsbulk	Vrachtbulk	Verpakt
x	x	-

7. Het management van de fabriek is gecertificeerd

kiwa gecertificeerd ISO 9001 kiwa gecertificeerd ISO 14001 kiwa gecertificeerd OHSAS 18001

8. Prestatieverklaring conform CPR(EU) Nr.305/2011

Identificatie : 0956-CPR-1101.1046

Website www.enci.nl

De resultaten weergegeven in de tabellen zijn gebaseerd op gemiddelde waarden en zijn louter indicatief. Enkel de normeisen worden gewaarborgd.

PRESTATIEVERKLARING

BFCV-A2-002

Producent - distributeur:
Coeck NV - De Laetstraat 6 - 2845 Niel - België
Tel. +32 3/880.75.00 - Fax. +32 3/880.75.10

Jaar van de markering: 13
Systeem 2+

Product **Rivierzand 0/4**

Toepassing: Zand voor bereiding van beton en mortel voor bouwwerken, wegen en andere civieltechnische werken.

Essentiële kenmerken	**Prestaties**		**Geharmoniseerde technische specificaties**
Korrelgroep	0-8		NEN-EN 12620:2002 + A1:2008 NEN-EN 13139:2002 + C1:2006
Categorie korrelverdeling	$G_{NG}90$		
	ISO 565:1990 R20	Grenzen [%]	
	11,2 8 5,6 4 2 1 0,250 0,125	100 - 100 97 - 100 88 - 100 82 - 99 73 - 93 58 - 78 0 - 20 0 - 3	
Korrelvorm	Ecs<30		
Waterabsorptie	≤ 0,5%		
Deeltjesdichtheid	2,60 ± 0,07 (Mg/m³)		
Schelpgehalte	SC_{10}		
Hoeveelheid fijne deeltjes < 63 µm	F3		
Weerstand tegen verbrijzeling	LA_{NR}		NEN-EN 12620:2002 + A1:2008
Weerstand tegen afslijten	$M_{DE}NR$		
Weerstand tegen polijsten	PSV_{NR}		
Weerstand tegen afslijten van het korreloppervlak	AAV_{NR}		
Weerstand tegen afslijten door spijkerbanden	AN_{NR}		
Bestanddelen in grove gerecyclede toeslagmaterialen	NR		
Chloridegehalte	≤ 0,005%		NEN-EN 12620:2002 + A1:2008 NEN-EN 13139:2002 + C1:2006
In zuur oplosbaar sulfaat	AS0,2		
Totaal zwavelgehalte	Voldoet (<1%)		
Gehalte aan in water oplosbaar sulfaat van gerecyclede toeslagmaterialen	SS_{NR}		NEN-EN 12620:2002 + A1:2008
Bindings– en verhardingsvertraging	Voldoet		NEN-EN 12620:2002 + A1:2008 NEN-EN 13139:2002 + C1:2006
Invloed op bindtijd van cement (gerecyclede toeslagmaterialen)	A_{NR}		NEN-EN 12620:2002 + A1:2008
Gehalte aan carbonaten	≤ 0,2% m/m		
Volume stabiliteit	NPD		NEN-EN 12620:2002 + A1:2008 NEN-EN 13139:2002 + C1:2006
Bestanddelen die de vormvastheid van luchtgekoelde hoogovenslak beïnvloeden	NR		NEN-EN 12620:2002 + A1:2008
Vrijkomende gevaarlijke bestanddelen	NPD		NEN-EN 12620:2002 + A1:2008 NEN-EN 13139:2002 + C1:2006
Vorst/dooi bestandheid	F_{NR}		
ASR gevoeligheid	Niet gevoelig		

De aangemelde certificatie-instantie IKOB-BKB (nr 0957) heeft onder systeem 2+ de initiële inspectie van de productie-installatie en van de productiecontrole in de fabriek uitgevoerd en zal tevens de permanente bewaking, beoordeling en evaluatie van de productiecontrole op zich nemen. Op basis daarvan is het conformiteitscertificaat voor de productiecontrole in de fabriek verstrekt.
De prestaties van het omschreven product zijn conform de aangegeven prestaties. Deze prestatieverklaring wordt verstrekt onder de exclusieve verantwoordelijkheid van de fabrikant. Ondertekend voor en namens de distributeur.

Ludo Coeck
Gedelegeerd Bestuurder

Robert Coeck
Gedelegeerd Bestuurder

Productspecificatieblad BU 15-12.02 d.d. 01 december 2015

Natuurlijk kwarts zand 0/2
Conform NEN-EN 12620 voor toepassing in beton
Conform NEN-EN 13139 voor toepassing in Mortel

Kieswerk Volbrockshof
Postfach 1154
D-47648 Weeze
Duitsland

CE **0778-CPR-8.622-1/1**

KOMO® **835**

12620	**13139**	
4.3	5.3	Korrelgradering

Zeef volgens ISO 565 : 1990 R20	**Grenswaarden voor doorval volgens NEN-EN 12620**			**90% van de bepalingen voldoen aan onderstaande grenswaarden voor doorval**
	Algemeen CE	**Gemiddelde CE/Komo**	**Grens tov gem. CE/Komo**	**Komo**
4 mm	100	100	100	100
2,8 mm	95-100	98	95-100	95-100
2 mm	89-99	94	89-99	89-99
1 mm		79	59-99	59-99
0,25 mm		20	0-45	0-45
0,063 mm		0	0-3	0-3

12620	**13139**		**12620**	**13139**	
4.3		Categorie	G_T85		
4.6	5.5	Hoeveelheid fijne deeltjes < 63 µm	f_3	Categorie 1	
	5.5.2	Kwaliteit fijne delen		voldoet	
5.5	6.2.1	Dichtheid ρ_{rd}	2,64 Mg/m^3	2,64 Mg/m^3	
5.5	6.2.2	Waterabsorptie	0,1%	0,1%	
5.7.2	7.5.1	Volumen stabiliteit	NPD	NPD	
5.7.3		ASR gevoeligheid	E1	E1	(DIN-EN 932-3)
		Natriumequivalent	0,009%		
		K_2O	0,007%		
6.2	7.2	Chloridengehalte	<0.001%	<0.001%	
6.3.1	7.3.1	In zuur oplosbare sulfaten	$AS_{0,2}$	$AS_{0,2}$	
6.3.2	7.3.2	Totaal zwavelgehalte	<0.05%	<0.05%	
6.4.1	7.4	Binding en verhardingsvertraging	Voldoet	voldoet	
6.5		Carbonaatgehalte	NR		

EG Conformiteitverklaring

Ondergetekende, verklaart op grond van de Europese regelgeving bouwproducten (No 305/2011) namens **Kieswerk Volbrockhof te Uedem** dat het in dit product specificatieblad genoemde product, afkomstig van de productie-eenheid "Volbrockshof"te Uedem voldoet aan de eisen in de EN 12620 en EN 13139 voor de eigenschappen genoemd in tabel ZA.1a van bijlage ZA van deze normen

Het FPC systeem is door de certificatie instelling BÜV NW beoordeeld en het FPC certificaat met nummer:

0778-CPR-8.622-1/1 GKBM

Werd per 01 januari 2014 toegekend

Uedem, 1 december 2015

Getekend:

L. Hekkenberg
Kwaliteitsverantwoordelijke

Zandhandel Lummen Tel: 011 45368 Fax: 011 262396 Industriestraat 16 B-3560 Lummen

Technische fiche nr.: **L 08-06-01** Datum :01-07-2019 Vervangt:01-04-2019	CE 19 0965-CPR-GT0535		DoP: L08-06-01

Aanduiding	Kwartszand	**Rondzand 0/4 CF A f3 a NG**	**Weselzand 0/7**

Norm van toepassing
EN 12620 : Toeslagmaterialen voor beton EN 13139 : Toeslagmaterialen voor mortel EN 13242: Toeslagmaterialen voor asfalt

Zeef EN 933-1	**(mm)**	**8**	**5.6**	**4**	**2**	**1**	**0.500**	**0.250**	**0.125**	**0.063**
Gem doorval	%	100	100	96	79	64	32	6	0	0,1
Min.	%	100	98	91	69	54	22	0	0	0
Max.	%	100	100	99	89	74	42	16	10	3
FM	3.32									

Kenmerken	**Norm**	**Gemiddelde**	**CE**			**BENOR**
			12620	13139	13242	-
Categorie			0/4 G_F85	-	0/4G_F 85 GT_F10	-
Reële dichtheid ρ_{rd}	EN 1097-6	2.64 Mg/m^3	2.64 Mg/m^3			±0.1Mg/m^3
Absorptie	EN 1097-6	0.4%	0.4%			± 0,3 %
Gehalte fijne deeltjes		0.2%	Cat.f_3	Cat.1	Cat.f_3	Cat.f_3
Chloorionen	EN 1744-1	<0,001%	<0,001%	-	-	-
In zuur opl. sulfaten	EN 1744-1	-	Cat. $AS_{0,2}$			-
Bindtijd vertragend stoffen	EN 1744-1	-	geen			-
Carbonaat/Schelpgehalte	NBN 289-209	-	-	-	-	-
Zware metalen+pak's		-	NPD			-
Alkali silica gevoeligheid		-	Niet reactief		-	-
NA2O-eq.	0.005% (bepaald op ontzilt materiaal)					-

EC- Conformiteitsverklaring

De BENOR-certificatie van het product geeft aan dat op basis van een periodieke externe controle een voldoende mate van vertrouwen bestaat dat de leverancier in staat is om doorlopend de overeenstemming van het product, zoals vastgelegd in technische referentiespecificaties, te waarborgen. Voorliggende BENOR-fiche bevat de prestaties die door de producent verklaard worden en wordt door de certificatie-instelling geverifieerd.
Het FPC-systeem werd geëvalueerd door de certificatie-instelling BE-CERT, gevestigd Edmond van Nieuwenhuyselaan 6, 1160 Oudergem en het FPC-certificaat nummer 0965-CPR-GT0535 werd toegekend op 19/01/2006.

Antwerpen, 01-07-2019 getekend: H. De Backker

Datum	Vertegenwoordiger	Titel	Handtekening

PRESTATIEVERKLARING BFCV-A2-022

Producent - distributeur:
Coeck NV - De Laetstraat 6 - 2845 Niel - België
Tel. +32 3/880.75.00 - Fax. +32 3/880.75.10

Jaar van de markering: 13
Systeem 2+

Product **Parelgrind 4/16**

Toepassing: Grind voor toepassing in beton.

Essentiële kenmerken	**Prestaties**	**Europees beoordelingsdocument**
Categorie korrelverdeling	GC 90/15 GT 17,5	NEN-EN 12620:2008
Korrelvorm	FI15	
Waterabsorptie	≤ 1,2%	
Deeltjesdichtheid	2,61 Mg/m³	
Schelpgehalte	SC_{10}	
Hoeveelheid fijne deeltjes < 63 µm	F1,5	
Los Angeles	LA_{25}	
Micro-Deval	$M_{DE}15$	
PSV	NPD	
AAV	NPD	
Nordic abrasion value	NPD	
Chloridegehalte	< 0,005%	
In zuur oplosbaar sulfaat	AS0,2	
Totaal zwavelgehalte	Voldoet	
Bindings– en verhardginsvertraging	Voldoet	
Vorst/dooi bestandheid	F1	
Volume stabiliteit	Voldoet	
ASR gevoeligheid	< 2,0%	
Vrijkomende gevaarlijke bestanddelen	NL-BSB	

De aangemelde certificatie-instantie Kiwa BMC BV (nr 0956) heeft onder systeem 2+ de initiële inspectie van de productie-installatie en van de productiecontrole in de fabriek uitgevoerd en zal tevens de permanente bewaking, beoordeling en evaluatie van de productiecontrole op zich nemen. Op basis daarvan is het conformiteitscertificaat voor de productiecontrole in de fabriek verstrekt.
De prestaties van het omschreven product zijn conform de aangegeven prestaties. Deze prestatieverklaring wordt verstrekt onder de exclusieve verantwoordelijkheid van de fabrikant. Ondertekend voor en namens de distributeur.

Ludo Coeck
Gedelegeerd Bestuurder

Robert Coeck
Gedelegeerd Bestuurder

nr. technische fiche / nr. fiche technique: TF-SBS-133-HRG-4/14	**datum / date:** 1/01/2017	**versie / version:** 2017-1

commercieële zetel / siège commercial:	**productie-eenheid / unité de production:**
EUROGRI NV. Geistingen 102 B-3640 Kinrooi T: +32 89 564 638 F: +32 89 566 305	**GRINDBEDRIJF SBS NV.** Steenweg naar As z/n B-3630 Maasmechelen T: +32 89 657 819 T: +32 89 659 566

specificaties / spécifications

aanduiding volgens PTV 411 / indication selon PTV 411

half-gerold grind / gravier semi-roulé 4/14 Cb4 f1 C-/70 NG

korrelverdeling / granulométrie

zeef / tamis (mm) EN 933-1	**28**	**20**	**14**	**10**	**4**	**2**	**0,063**
maximum (%) :	100	100	99	70	15	5	1
gemiddelde / moyenne (*) :	100	100	95	58	1	0	0
minimum (%) :	100	98	90	40	0	0	0

(*) informatief gemiddelde van laatste 6 maanden / informative moyenne des 6 derniers mois

kenmerken / caractéristiques:	**norm / norme**	**waarde / valeur**	**PTV 411**
gehalte aan fijne deeltjes / fines (*):	EN 933-1	≤ 1	f1
afplattingscoëfficient / coefficient d'aplatissement (*):	EN 933-3	≤ 20	code I
LA coëfficient / Los Angeles (*):	EN 1097-2	≤ 25	Cb4 (NG)
M_{DE} coëfficient - Micro Deval (*):	EN 1097-1	≤ 20	
LA + M_{DE}:	PTV 411	≤ 45	
polijstingscoëfficient / le coefficient de polissage PSV (*):	EN 1097-8	-	
graad van breken / degré de concassage (*):	EN 933-5	half-gerold / semi-roulé	$C_{-/70}$
vorst-dooi weerstand / resistance au gel-dégel (*):	EN 1367-1/2	-	-
cloorionen / teneur en chlorures (%) (*):	EN 1744-1	-	-
schelpdelen / teneur en elements coquilliers (%) (*):	NBN 589-209	-	-
reële volumieke massa fractie 10/14 / massa volumique réelle fraction 10/14 - ρ_{rd} (Mg/m³):	EN 1097-6	2,53 Mg/m³	tol. ± 0.07 Mg/m³
waterabsorptie fractie 10/14 / absorption d'eau fraction 10/14 - WA (%):	EN 1097-6	1,60%	tol. ± 0.7 %
organische stoffen / matierères organiques:	EN 1744-1	negatief / négatif	-

(*) verklaring van de fabrikant ontleend van zijn DoP / déclaration du producteur reprise sur sa DoP

naam / nom	**functie / fonction**	**handtekening / signature**
Dhr. Teunissen J.	Directeur	

De BENOR-certificatie van het product geeft aan dat op basis van een periodieke externe controle een voldoende mate van vertrouwen bestaat dat de leverancier in staat is om doorlopend de overeenstemming van het product, zoals vastgelegd in technische referentiespecificaties, te waarborgen. Voorliggende BENOR-fiche bevat de prestaties van kenmerken die door de fabrikant verklaard worden en wordt door de certificatie-instelling geverifieerd.

La certification BENOR du produit indique que, sur base d'un controle externe périodique, il existe une confiance suffisante dans la capacité du producteur à garantir la conformité du produit de façon permanente, comme définie dans les specifications de référence technique. La présente fiche BENOR contient les performances des caractéristiques déclarées par le producteur et est vérifieé par l'organisme de certification.

HÜLSKENS GMBH & CO.KG

Hülskensstraße 4-6
D - 46483 Wesel

411 | BENOR | 239

946

0778-CPR-8.312-1/18

Toeslagmaterialen voor beton volgens EN 12620: Grind 4/16	**Datum:** 2017	**Rev. Nr.: 9**
	Petrografische beschrijving : kwartsgrind **Type** : gerold grind / riviergrind	
Werk: Milchplatz	**Identificatie volgens PTV 411:**	
Winplaats: Rhein-km 800,6	Gerold grind 4/16 (5) III $f_{1,5}$ NG Gewassen	

4.3 korrelgrootteverdeling

zeef volgens ISO 565:1990 R 20	grenswaarden volgens EN 12620	alle bepalingen voldoen aan onderstaande grenswaarden		Aanwijzende gemiddelde waarde	90% van de bepalingen voldoen aan onderstaande grenswaarden	
		minimum* (jaar)	maximum * (jaar)	(09.08.16 tot 31.12.16)	minimum	maximum
31	100	100	100	100	100	100
22,5	98-100	100	100	100	100	100
16	90-99	93	99	96,2	94	99
8	25-70	25	60	41,1	28	58
4	0-15	0	10	4,0	0	7
2	0-5	0	2	0,6	0	2
0,063		0	1,5	0,2	0	1,5

4.3	categorie	$G_C90/15$ $G_T17,5$ (45,0% DG)
4.4	vorm van grof toeslagmateriaal	FI_{20}
4.5	schelpgehalte	SC_{10}
4.6*	gehalte aan fijne bestanddelen < 63 µm	$f_{1,5}$
4.7*	kwaliteit van fijne bestanddelen	NPD
5.2	weerstand tegen verbrijzeling	LA_{30}
5.3	weerstand tegen afslijting	NPD
5.4.1	weerstand tegen polijsten	NPD
5.5*	Reele volume massa [Mg/m^3]	2,63 [± 0,07]
5.5*	waterabsorptie [m/m %]	0,7 [± 0,3]
5.6	dichtheid los gestort [Mg/m^3]	NPD
5.7.1	vorst/dooi bestandheid	F_1
5.7.2	volumestabiliteit	NPD
5.7.3	ASR gevoeligheidsklasse volgens „Alkali-Richtlinie 2007-2“	E I
6.2	chloridegehalte [m/m %]	< 0,01
6.3.1	in zuur oplosbaar sulfaat	$AS_{0,2}$
6.3.2	totaal zwavelgehalte [m/m %]	voldoet
6.4.1*	bestanddelen die de bindtijd en de verharding van beton beïnvloeden (Aanwezigheid van organische stoffen)	voldoet
	lichte bestanddelen [m/m %]	< 0,05
	vrijkomende gevaarlijke bestanddelen	schone grond

De BENOR-certificatie van het product geeft aan dat op basis van een periodieke externe controle een voldoende mate van vertrouwen bestaat dat de leverancier in staat is om doorlopend de overeenstemming van het product, zoals vastgelegd in technische referentiespecificaties, te waarborgen. Voorliggende BENOR-fiche bevat de prestaties van kenmerken die door de fabrikant verklaard worden en wordt door de certificatie-instelling geverifieerd.

Het FPC systeem is door de certificatie-instelling BÜV NW beoordeeld en het FPC certificaat met nummer 0778-CPR-8.312-1/18 werd per 01.01.2014 toegekend.

* Kenmerken gedekt door het BENOR-merk en niet opgenomen in de "identificatie"

Wesel, 17.2.17

Dr. R. Koß
Geschäftsführer

MasterPozzolith 390N con 40%

Plastificeerder/Waterreduceerder

PL EN 934-2 : T2

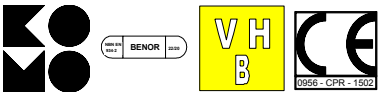

BESCHRIJVING

MasterPozzolith 390N con 40% is een plastificeerder/waterreduceerder voor betonspecie op basis van lignine sulfonaat

TOEPASSING

MasterPozzolith 390N con 40% kan gebruikt worden voor de productie van :

- Transportbeton
- Ongewapend beton
- Gewapend beton
- Voorgespannen beton

MasterPozzolith 390N con 40% kan toegepast worden in betonspecie in de consistentie gebieden (EN 206) :

- S1 tot S3
- F1 tot F3

MasterPozzolith 390N con 40% wordt geadviseerd voor toepassing in betonspecie met een temperatuur bereik van :

- +5 'C tot +30 'C

DOSERING

MasterPozzolith 390N con 40% heeft een doseringsbereik in g per 100 kg cement / bindmiddel van :

- 200 tot 600

MasterPozzolith 390N con 40% heeft het meeste effect indien het gedoseerd wordt nadat het water geheel of gedeeltelijk is toegevoegd aan de overige componenten van de betonspecie.

MasterPozzolith 390N con 40% is een gebruiksklare hulpstof. Voor een goede werking en om een homogene verdeling te bereiken dient voldoende mengtijd aan gehouden te worden.

Voor specifieke toepassingen kunnen andere doseringen worden gehanteerd. Een vooronderzoek is daarbij noodzakelijk.

VERENIGBAARHEID

MasterPozzolith 390N con 40% kan met diverse hulpstoffen van BASF Construction Chemicals gecombineerd worden. Echter vooraf is een onderzoek nodig om de specifieke interactie te bepalen.

MasterPozzolith 390N con 40% is verenigbaar met alle cement types zoals, portland cement en composiet cement

GESCHIKTHEIDSONDERZOEK

MasterPozzolith 390N con 40% dient voorafgaand aan de toepassing door middel van een geschiktheidsonderzoek onderzocht te worden of het het gewenste effect heeft.

Bij dit onderzoek moeten de grondstoffen van de betoncentrale gebruikt worden in de betonsamenstelling waarin de hulpstof toegepast zal worden.

MasterPozzolith 390N con 40% kan een ander effect geven op bijvoorbeeld het behoud van verwerkbaarheid en sterkte ontwikkeling. Enkele aspecten die daarbij van invloed kunnen zijn, zijn :

temperatuur van de omgeving en de specie, cementsoort, -klasse, mengverhouding, andere hulpstoffen, soort toeslagmateriaal, transportmethode en dergelijke.

BIJWERKINGEN

MasterPozzolith 390N con 40% kan bij overschrijding van de geadviseerde dosering een ongewenste bijwerking geven. Hierbij kan gedacht worden aan :

- Lange vertragingstijd
- Langzame sterkteontwikkeling
- Ontmenging, Bleeding
- Verhoging van het luchtgehalte

BASF
We create chemistry

MasterPozzolith 390N con 40%

Plastificeerder/Waterreduceerder

PL EN 934-2 : T2

OPSLAG

MasterPozzolith 390N con 40% moet vorstvrij, uit de zon en in gesloten tanks of verpakking opgeslagen worden.

Geadviseerde opslag temperatuur is tussen +5' C en +30'C.

MasterPozzolith 390N con 40% kan indien het toch bevroren is, langzaam ontdooid worden waarna het mechanisch omgeroerd moet worden tot een homogeen geheel.

Indien het product niet gemengd is gedurende een periode, is het zinvol om dit voor gebruik mechanisch goed te mengen.

Gebruik geen perslucht om het product te mengen.

Bij bulkopslag dient rekening gehouden te worden met lokaal geldende regels ten aanzien van de opslag van chemicaliën.

Aanbevolen wordt om bulkopslag tanks periodiek te reinigen om groei van micro-organismen in met name de spatzone te voorkomen.

Bij wisseling van hulpstof dienen opslagtank, toe- en afvoerleidingen volledig gereinigd te worden om verontreiniging van het product te voorkomen.

HOUDBAARHEID

MasterPozzolith 390N con 40% heeft, indien opgeslagen volgens het opslag advies, een houdbaarheidstermijn van minimaal 12 maanden na productie datum.

VOORZORGSMAATREGELEN

MasterPozzolith 390N con 40% is niet schadelijk voor gezondheid en milieu en heeft ook geen speciale kenmerken nodig volgens de EC richtlijnen.

Voorafgaand aan het gebruik en voor verdere inlichtingen wordt dringend aangeraden het veiligheidsinformatieblad (MSDS) te raadplegen.

BASF Nederland B.V.,
Construction Chemicals

Karolusstraat 2
Postbus 132, NL-4900 AC Oosterhout N.B.
Tel. +31 162 47 66 60. Fax +31 162 42 96 94
e-mail : basf-cc-nl@basf.com
www.master-builders-solutions.basf.nl
B.T.W. NL 001829117B01
HR Arnhem 09022883

EXTRA INFORMATIE

Voor extra informatie en aspecten die niet in dit product informatie blad beschreven zijn verwijzen wij naar ondersteuning bij uw technisch adviseur.

Technische gegevens	
Categorie volgens EN934-2	: PL EN 934-2 : T2
Chloride gehalte in %m	: max. 0,1%
Natriumoxide-eq. in %m	: max. 8,5
Hoofdwerking	: plastificerend
Volumieke massa kg/l	: 1,22
pH	: 6 - 9
Droge stofgehalte Brekingsindex	: 36,1 - 39,9
Aggregatie toestand	: vloeibaar
Toepassingstemperatuur	: vanaf 5'C
Kleur	: bruin
VHB kleurcode	: geel
Effectief bestanddeel	: lignine sulfonaat
Opmerking	: zie voetnoot d van tabel 1 EN934-1 en TRA 500 over droge stofgehalte.

De data die in dit technische informatieblad worden vermeld alsmede adviezen en andere ondersteunende activiteiten zijn gebaseerd op onze huidige technische kennis en ervaring. In verband met de vele factoren bij de verwerking en toepassing van onze producten, wordt de koper van onze producten niet ontslagen van zijn verplichting om deze producten zelf te keuren en te testen, specifiek met betrekking tot de geschiktheid van de geleverde goederen voor de geïmplementeerde processen of daaruit voortvloeiende producten. De data garanderen niet bepaalde eigenschappen of de geschiktheid voor een concrete toepassing van het product. Alle bijbehorende beschrijvingen, tekeningen, foto´s, data, verhoudingen, gewichten etc. kunnen zonder voorafgaande kennisgeving worden gewijzigd en vertegenwoordigen niet de overeengekomen contractuele kwaliteit van het product. Het is de verantwoordelijkheid van de ontvanger van onze producten om eventuele Intellectuele eigendomsrechten, bestaande wet- en regelgeving in acht te nemen. Bij herdruk komen voorgaande uitgaven te vervallen.

MasterRheobuild 1100 con 40%

Superplastificeerder voor betonspecie.

SPL EN 934-2 : T3.1/T3.2

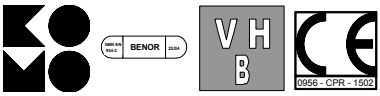

BESCHRIJVING

MasterRheobuild 1100 con 40% is een superplastificeerder voor betonspecie op basis van gesulfoneerd naftaleen formaldehyde condensaat.

TOEPASSING

MasterRheobuild 1100 con 40% kan gebruikt worden voor de productie van :

- Transportbeton
- Prefab beton
- Ongewapend beton
- Gewapend beton
- Voorgespannen beton

MasterRheobuild 1100 con 40% kan toegepast worden in betonspecie in de consistentie gebieden (EN 206) :

- S2 tot S5
- F2 tot F5

MasterRheobuild 1100 con 40% wordt geadviseerd voor toepassing in betonspecie met een temperatuur bereik van :

- +5 'C tot +25 'C

DOSERING

MasterRheobuild 1100 con 40% heeft een doseringsbereik in g per 100 kg cement / bindmiddel van :

- 500 tot 1200

MasterRheobuild 1100 con 40% heeft het meeste effect indien het gedoseerd wordt nadat het water geheel of gedeeltelijk is toegevoegd aan de overige componenten van de betonspecie.

MasterRheobuild 1100 con 40% is een gebruiksklare hulpstof. Voor een goede werking en om een homogene verdeling te bereiken dient voldoende mengtijd aan gehouden te worden.

Voor specifieke toepassingen kunnen andere doseringen worden gehanteerd. Een vooronderzoek is daarbij noodzakelijk.

VERENIGBAARHEID

MasterRheobuild 1100 con 40% is niet verenigbaar en mag niet gecombineerd worden met hulpstoffen zoals o.a. MasterGlenium op basis van PCE

GESCHIKTHEIDSONDERZOEK

MasterRheobuild 1100 con 40% dient voorafgaand aan de toepassing door middel van een geschiktheidsonderzoek onderzocht te worden of het het gewenste effect heeft.

Bij dit onderzoek moeten de grondstoffen van de betoncentrale gebruikt worden in de betonsamenstelling waarin de hulpstof toegepast zal worden.

MasterRheobuild 1100 con 40% kan een ander effect geven op bijvoorbeeld het behoud van verwerkbaarheid en sterkte ontwikkeling. Enkele aspecten die daarbij van invloed kunnen zijn, zijn :

temperatuur van de omgeving en de specie, cementsoort, -klasse, mengverhouding, andere hulpstoffen, soort toeslagmateriaal, transportmethode en dergelijke.

BIJWERKINGEN

MasterRheobuild 1100 con 40% kan bij overschrijding van de geadviseerde dosering een ongewenste bijwerking geven. Hierbij kan gedacht worden aan :

- Lange vertragingstijd
- Langzame sterkteontwikkeling
- Ontmenging, Bleeding

BASF
We create chemistry

MasterRheobuild 1100 con 40%

Superplastificeerder voor betonspecie.

SPL EN 934-2 : T3.1/T3.2

OPSLAG

MasterRheobuild 1100 con 40% moet vorstvrij, uit de zon en in gesloten tanks of verpakking opgeslagen worden.

Geadviseerde opslag temperatuur is tussen +5' C en +30'C.

MasterRheobuild 1100 con 40% kan indien het toch bevroren is, langzaam ontdooid worden waarna het mechanisch omgeroerd moet worden tot een homogeen geheel.

Indien het product niet gemengd is gedurende een periode, is het zinvol om dit voor gebruik mechanisch goed te mengen.

Gebruik geen perslucht om het product te mengen.

Bij bulkopslag dient rekening gehouden te worden met lokaal geldende regels ten aanzien van de opslag van chemicaliën.

Aanbevolen wordt om bulkopslag tanks periodiek te reinigen om groei van micro-organismen in met name de spatzone te voorkomen.

Bij wisseling van hulpstof dienen opslagtank, toe- en afvoerleidingen volledig gereinigd te worden om verontreiniging van het product te voorkomen.

HOUDBAARHEID

MasterRheobuild 1100 con 40% heeft, indien opgeslagen volgens het opslag advies, een houdbaarheidstermijn van minimaal 12 maanden na productie datum.

VOORZORGSMAATREGELEN

MasterRheobuild 1100 con 40% is niet schadelijk voor gezondheid en milieu en heeft ook geen speciale kenmerken nodig volgens de EC richtlijnen.

Voorafgaand aan het gebruik en voor verdere inlichtingen wordt dringend aangeraden het veiligheidsinformatieblad (MSDS) te raadplegen.

BASF Nederland B.V.,
Construction Chemicals

Karolusstraat 2
Postbus 132, NL-4900 AC Oosterhout N.B.
Tel. +31 162 47 66 60. Fax +31 162 42 96 94
e-mail : basf-cc-nl@basf.com
www.master-builders-solutions.basf.nl
B.T.W. NL 001829117B01
HR Arnhem 09022883

EXTRA INFORMATIE

Voor extra informatie en aspecten die niet in dit product informatie blad beschreven zijn verwijzen wij naar ondersteuning bij uw technisch adviseur.

Technische gegevens	
Categorie volgens EN934-2	: SPL EN 934-2 : T3.1/T3.2
Chloride gehalte in %m	: max. 0,1
Natriumoxide-eq. in %m	: max. 8,5
Hoofdwerking	: superplastificerend
Volumieke massa kg/l	: 1,200
Droge stofgehalte EN480-8	: 40%
pH	: 6 - 9
Aggregatie toestand	: Vloeibaar
	: vloeibaar
Toepassingstemperatuur	: vanaf 5'C
oplosbaarheid in water (g/l)	: goed oplosbaar
Kleur	: bruin
VHB kleurcode	: grijs
Effectief bestanddeel	: gesulfoneerd naftaleen formaldehyde condensaat

De data die in dit technische informatieblad worden vermeld alsmede adviezen en andere ondersteunende activiteiten zijn gebaseerd op onze huidige technische kennis en ervaring. In verband met de vele factoren bij de verwerking en toepassing van onze producten, wordt de koper van onze producten niet ontslagen van zijn verplichting om deze producten zelf te keuren en te testen, specifiek met betrekking tot de geschiktheid van de geleverde goederen voor de geïmplementeerde processen of daaruit voortvloeiende producten. De data garanderen niet bepaalde eigenschappen of de geschiktheid voor een concrete toepassing van het product. Alle bijbehorende beschrijvingen, tekeningen, foto´s, data, verhoudingen, gewichten etc. kunnen zonder voorafgaande kennisgeving worden gewijzigd en vertegenwoordigen niet de overeengekomen contractuele kwaliteit van het product. Het is de verantwoordelijkheid van de ontvanger van onze producten om eventuele Intellectuele eigendomsrechten, bestaande wet- en regelgeving in acht te nemen. Bij herdruk komen voorgaande uitgaven te vervallen.

BASF
We create chemistry

MasterGlenium 51

Superplastificeerder/ Waterdichtingsmiddel in de massa

SPL EN 934-2 : T3.1/T3.2 **WRS EN 934-2 : T9**

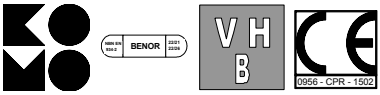

BESCHRIJVING

MasterGlenium 51 is een hulpstof voor betonspecie op basis van polycarboxylaatether die toepasbaar is als superplastificeerder en waterdichtingsmiddel in de massa.

TOEPASSING

MasterGlenium 51 kan gebruikt worden voor de productie van :

- Transportbeton
- Prefab beton
- Ongewapend beton
- Gewapend beton
- Voorgespannen beton

MasterGlenium 51 kan toegepast worden in betonspecie in de consistentie gebieden (EN 206) :

- S2 tot S5
- F2 tot F5
- Zelfverdichtend beton

MasterGlenium 51 wordt geadviseerd voor toepassing in betonspecie met een temperatuur bereik van :

- +5 'C tot +30 'C

DOSERING

MasterGlenium 51 heeft een doseringsbereik in g per 100 kg cement / bindmiddel van :

- 400 tot 1250

MasterGlenium 51 heeft het meeste effect indien het gedoseerd wordt nadat het water geheel of gedeeltelijk is toegevoegd aan de overige componenten van de betonspecie.

Polycarboxylaat ether gebaseerde hulpstoffen hebben vooral bij een concentratie hoger dan 25% vaak een langere mengtijd nodig om hun superieure plastificerende werking volledig tot uiting te laten komen.

Voor specifieke toepassingen kunnen andere doseringen worden gehanteerd. Een vooronderzoek is daarbij noodzakelijk.

VERENIGBAARHEID

MasterGlenium 51 is niet verenigbaar en mag niet gecombineerd worden met hulpstoffen zoals o.a. MasterRheobuild op basis van gesulfoneerd-naftaleen of -melamine.

GESCHIKTHEIDSONDERZOEK

MasterGlenium 51 dient voorafgaand aan de toepassing door middel van een geschiktheidsonderzoek onderzocht te worden of het het gewenste effect heeft.

In dit onderzoek moeten de grondstoffen van de centrale gebruikt worden om de vereiste dosering van de hulpstof te bepalen.

MasterGlenium 51 kan een ander effect geven op bijvoorbeeld het behoud van verwerkbaarheid en sterkte ontwikkeling. Enkele aspecten die daarbij van invloed kunnen zijn, zijn :

temperatuur van de omgeving en de specie, cementsoort, -klasse, mengverhouding, andere hulpstoffen, soort toeslagmateriaal, transportmethode en dergelijke.

BIJWERKINGEN

MasterGlenium 51 kan bij overschrijding van de geadviseerde dosering een ongewenste bijwerking geven. Hierbij kan gedacht worden aan :

- Lange vertragingstijd
- Langzame sterkteontwikkeling
- Ontmenging, Bleeding

MASTER® BUILDERS SOLUTIONS

BASF
We create chemistry

MasterGlenium 51

Superplastificeerder/ Waterdichtingsmiddel in de massa

SPL EN 934-2 : T3.1/T3.2 **WRS EN 934-2 : T9**

OPSLAG

MasterGlenium 51 moet vorstvrij, uit de zon en in gesloten tanks of verpakking opgeslagen worden.

Geadviseerde opslag temperatuur is tussen +5' C en +30'C.

MasterGlenium 51 kan indien het toch bevroren is, langzaam ontdooid worden waarna het mechanisch omgeroerd moet worden tot een homogeen geheel.

Indien het product niet gemengd is gedurende een periode, is het zinvol om dit voor gebruik mechanisch goed te mengen.

Gebruik geen perslucht om het product te mengen.

Bij bulkopslag dient rekening gehouden te worden met lokaal geldende regels ten aanzien van de opslag van chemicaliën.

Aanbevolen wordt om bulkopslag tanks periodiek te reinigen om groei van micro-organismen in met name de spatzone te voorkomen.

Bij wisseling van hulpstof dienen opslagtank, toe- en afvoerleidingen volledig gereinigd te worden om verontreiniging van het product te voorkomen.

HOUDBAARHEID

MasterGlenium 51 heeft, indien opgeslagen volgens het opslag advies, een houdbaarheidstermijn van minimaal 12 maanden na productie datum.

VOORZORGSMAATREGELEN

MasterGlenium 51 is niet schadelijk voor gezondheid en milieu en heeft ook geen speciale kenmerken nodig volgens de EC richtlijnen.

Voorafgaand aan het gebruik en voor verdere inlichtingen wordt dringend aangeraden het veiligheidsinformatieblad (MSDS) te raadplegen.

BASF Nederland B.V.,
Construction Chemicals

Karolusstraat 2
Postbus 132, NL-4900 AC Oosterhout N.B.
Tel. +31 162 47 66 60. Fax +31 162 42 96 94
e-mail : basf-cc-nl@basf.com
www.master-builders-solutions.basf.nl
B.T.W. NL 001829117B01
HR Arnhem 09022883

EXTRA INFORMATIE

Voor extra informatie en aspecten die niet in dit product informatie blad beschreven zijn verwijzen wij naar ondersteuning bij uw technisch adviseur.

Technische gegevens	
Categorie volgens EN934-2	: SPL EN 934-2 : T3.1/T3.2
	: WRS EN 934-2 : T9
Chloride gehalte in %m	: max. 0,1
Natriumoxide-eq. in %m	: max. 3
Hoofdwerking	: superplastificerend
	: waterdichtingsmiddel in de massa
Volumieke massa kg/l	: 1,100
Droge stofgehalte EN480-8	: 35%
pH	: 5 - 8
Aggregatie toestand	: vloeibaar
Toepassingstemperatuur	: vanaf 5'C
Kleur	: lichtbruin
VHB kleurcode	: grijs
Effectief bestanddeel	: polycarboxylaat ether

De data die in dit technische informatieblad worden vermeld alsmede adviezen en andere ondersteunende activiteiten zijn gebaseerd op onze huidige technische kennis en ervaring. In verband met de vele factoren bij de verwerking en toepassing van onze producten, wordt de koper van onze producten niet ontslagen van zijn verplichting om deze producten zelf te keuren en te testen, specifiek met betrekking tot de geschiktheid van de geleverde goederen voor de geïmplementeerde processen of daaruit voortvloeiende producten. De data garanderen niet bepaalde eigenschappen of de geschiktheid voor een concrete toepassing van het product. Alle bijbehorende beschrijvingen, tekeningen, foto´s, data, verhoudingen, gewichten etc. kunnen zonder voorafgaande kennisgeving worden gewijzigd en vertegenwoordigen niet de overeengekomen contractuele kwaliteit van het product. Het is de verantwoordelijkheid van de ontvanger van onze producten om eventuele Intellectuele eigendomsrechten, bestaande wet- en regelgeving in acht te nemen. Bij herdruk komen voorgaande uitgaven te vervallen.

BUILDING TRUST

TECHNISCHE FICHE
Tixo®

SUPERPLASTIFICEERDER, STERK WATERREDUCEERDER, WATERDICHTINGSMIDDEL IN DE MASSA CONFORM DE NORM NBN EN 934-2 T3.1 – T3.2

PRODUCTBESCHRIJVING

Tixo® is een superplastificeerder, sterke water reduceerder, waterdichtingsmiddel in de massa van de laatste generatie.

TOEPASSINGEN

Tixo® wordt aanbevolen voor beton dat geproduceerd wordt in de betoncentrale en prefab fabrieken.

Dankzij de zeer sterke watervermindering, de uitstekende vloeibaarheid gecombineerd met een sterke cohesie en dankzij de zelfverdichtende kenmerken, wordt Tixo® toegepast bij de volgende beton types:

- zelfverdichtend beton (SCC),
- beton met zwak W/C gehalte,
- beton met hoge weerstand op lange termijn,
- beton met een lang reologie behoud,
- waterdichtbeton.

Wij bevelen het niet aan voor de productie van gepolijst beton.

Tixo® kan gebruikt worden met andere hulpstoffen (ons raadplegen).

EIGENSCHAPPEN / VOORDELEN

Tixo® reageert door middel van verschillende mechanismen. Zijn actie bevindt zich op het absorberend oppervlak van de cementkorrel en de afscheiding van elk van deze korrels. Het beïnvloedt eveneens het hydratatie proces.

Dankzij deze eigenschappen, bekomt men volgende resultaten:

- zelfverdichtend gedrag,
- zeer sterke waterreduceerder,
- zeer grote vloeibaarheid,
- lang behoud van de reologie,
- verhoogt sterk de waterdichtheid,
- vermindert de snelheid van de carbonatatie van beton.

Tixo® bevat geen chloriden of andere producten die de corrosie van staal bevordert. Kan eveneens gebruikt worden zonder beperkingen wat betreft gewapend en voorgespannen beton.

PRODUCTINFORMATIE

VORM

UITERLIJK / KLEUR

Vloeibaar, bruinachtig

VERPAKKING

Vat van 200 kg (verloren verpakking)

Container van 1000 L (met statiegeld)

OPSLAG

OPSLAGCONDITIES / HOUDBAARHEID

12 maanden vanaf de productiedatum indien opgeslagen in de origine verpakking in een lokaal dat beschermd is tegen vorst en hoge temperaturen en bij een temperatuur tussen de +5°C en +35°C.

TECHNISCHE GEGEVENS

CHEMISCHE BASIS

Water gebaseerde polymeeroplossing

DENSITEIT

1,090 kg/l ± 0,020

pH

4,6 ± 1,5

CL^- IONENGEHALTE

Minder dan 0,10 %

DROGESTOF (NBN EN 480-8)

25,0 % ± 1,50

Na_2O EQ.

Maximum 1,0 %

SYSTEEMINFORMATIE

TOEPASSINGSDETAILS

VERBRUIK

De aanbevolen dosering bedraagt

- als superplastificeerder: 0,5 tot 2 % van het cementgewicht.
- als waterdichtingsmiddel: 1 % van het cementgewicht.

Overdoseringen zijn mogelijk. De juiste dosering wordt vastgesteld door proeven uit te voeren, aangezien ze afhangt van da aard van de componenten van het beton, de gewenste kwaliteit en de weersomstandigheden.

In functie van de gebruikte cement kan een bindingsvertraging opgemerkt worden.

TE VERMIJDEN CONTACTEN

Tixo® is een wateroplossing en kan dus bevriezen. Teruggebracht op +20°C en correct gehomogeniseerd, na een intense menging, behaald het product zijn initiale kwaliteiten terug. In dit geval ons raadplegen.

TOEPASSINGSINSTRUCTIES	**TOEPASSINGSMETHODE / GEREEDSCHAP**
	Tixo® wordt na het aanmaakwater, of terzelfder tijd als het water toegevoegd in de menger.
	Voor een optimale watervermindering, raden wij aan om het mengsel vochtig te mengen gedurende minimum 60 seconden.
	Tenslotte om een zo goed mogelijke dichtheid te bekomen, mag het toevoegen van het resterend water alléén gebeuren na 40 seconden mengtijd teneinde alle overtollig water te vermijden.
	Gebruikmakend van Tixo® realiseert men een beton van zeer hoge kwaliteit.
	De regels der kunst voor de productie en het plaatsen van beton moeten eveneens gerespecteerd worden voor de Tixo®
	Vers beton moet altijd beschermd worden tegen uitdroging.
WAARDENBASIS	Alle technische gegevens vermeld in deze Technische Fiche zijn gebaseerd op laboratoria testen.
	Actueel gemeten gegevens kunnen verschillend zijn door omstandigheden buiten onze controle.
LOKALE BEPERKINGEN	Let op dat als gevolg van specifieke plaatselijke voorschriften, de prestaties van dit product van land tot land kunnen variëren. Raadpleeg het lokale productinformatieblad voor de precieze beschrijving en toepassingsmogelijkheden.
VEILIGHEIDS- EN GEZONDHEIDSVOORSCHRIFTEN	Voor informatie en advies over de veilige hantering, opslag en verwijdering van chemicaliën verwijzen wij naar het meest recente veiligheidsinformatieblad die fysische, ecologische, toxicologische en andere veiligheidsgegevens bevat.
HERINNERING	Tixo® wordt ook gebruikt voor het realiseren van zelfverdichtend beton. In dit geval, is een bijzondere samenstelling onontbeerlijk. Ons raadplegen.
	Onze hulpstof kan niet als verantwoordelijk worden gesteld voor een eventuele kleurverandering van het beton in de tijd.
	Onze producten dienen zorgvuldig te worden opgeslagen, aangebracht en gehanteerd.
WETTELIJKE INFORMATIE	De informatie, en met name de aanbevelingen met betrekking tot de toepassing en het eindgebruik van Sika-producten, wordt in goed vertrouwen verstrekt op basis van de huidige kennis en ervaring van Sika met producten die op de juiste wijze zijn opgeslagen, behandeld en toegepast onder normale omstandigheden in overeenstemming met de aanbevelingen van Sika. In de praktijk zijn de verschillen in materialen, onderlagen en werkelijke omstandigheden ter plaatse zodanig dat er geen garantie kan worden ontleend met betrekking tot verhandelbaarheid of geschiktheid voor een bepaald doel, noch enige aansprakelijkheid voortvloeiend uit enige juridische relatie, op basis van deze informatie, of uit enige schriftelijke aanbevelingen of enig ander advies dat wordt gegeven. De gebruiker van het product moet de verenigbaarheid van het product testen voor de beoogde toepassing en doel. Sika behoudt zich het recht om de producteigenschappen te wijzigen. Onze verantwoordelijkheid zou in geen enkel geval in het gedrang kunnen worden gebracht, in de veronderstelling van een uitvoering die niet conform is met onze inlichtingen. De eigendomsrechten van derden dienen te worden gerespecteerd. Alle bestellingen worden aanvaard onder de huidige verkoop- en leveringsvoorwaarden. Gebruikers dienen altijd de meest recente uitgave van het lokale technische informatieblad te raadplegen voor het betreffende product; exemplaren hiervan worden op verzoek verstrekt.

VOOR MEER INFORMATIE OVER DE Tixo® TECHNOLOGIE:

SIKA NV
Concrete
Pierre Dupontstraat 167
1140 Brussel
Belgium
www.sika.be

Tel.: +32 (0)2 726 16 85
Fax: +32 (0)2 726 28 09
E-mail: info@be.sika.com

© 2014 Sika nv België

Construction

Sika® ViscoCrete®-4035 M

Verzögerer/Fliessmittel (VZ/FM)

Beschreibung

Sika® ViscoCrete®-4035 M ist ein Verzögerer/Fliessmittel neuester Generation für Beton.

Anwendung

Sika® ViscoCrete®-4035 M ist besonders für die Herstellung von Beton mit verlängerter Verarbeitungszeit in Baustellenanlagen geeignet.

Sika® ViscoCrete®-4035 M wird vor allem für folgende Anwendungen eingesetzt:
- Für Betonanwendungen im Sommer
- Beton mit verlängerter Verarbeitungszeit
- Beton mit höchster Wasserreduktion
- Hochleistungsbeton

Sika® ViscoCrete®-4035 M enthält weder Chloride noch andere die Stahlkorrosion fördernde Stoffe. Es kann daher unbedenklich bei Stahl- und Spannbetonkonstruktionen eingesetzt werden.

Vorteile

Sika® ViscoCrete®-4035 M kombiniert verschiedene Wirkungsmechanismen.

Durch Adsorption an der Oberfläche und räumliche Trennwirkung der Feinstanteile bei gleichzeitig fortschreitendem Hydratationsprozess werden die folgenden Eigenschaften erzielt:
- Äusserst starke Wasserreduktion (dadurch hohe Dichtigkeiten und Festigkeiten)
- Hohes Fliessvermögen (damit stark reduzierter Verarbeitungs- und Verdichtungsaufwand)
- Stark verbesserte Wasserdichtigkeit
- Verbessertes Kriech- und Schwindverhalten
- Langsamere Karbonatisierung des Betons

Produktdaten

Art

Farbton	Bernsteinfarben
Lieferform	Einweggebinde (Fass) à: 220 kg Kunststoff-Wechselcontainer à: 1000 kg (Eigentum der Sika Schweiz AG)

Construction

Lagerung

Lagerbedingungen / Haltbarkeit	Im ungeöffneten Originalgebinde bei einer Lagertemperatur zwischen +5 °C und +35 °C: 12 Monate ab Produktionsdatum. Vor direkter Sonnenbestrahlung und Frost schützen. Für die Lagerung saubere Tanks verwenden. Diese sollten mindestens einmal pro Jahr gereinigt und desinfiziert werden. Gefrorenes Sika® ViscoCrete®-4035 M kann nach langsamem Auftauen bei Zimmertemperatur und nach intensivem Durchmischen wieder verwendet werden.

Technische Daten

Chemische Basis	Modifiziertes Polycarboxylat in Wasser	
Gleichmässigkeit	Homogen	
Dichte	1.08 ± 0.01 g/cm³	(Relative Dichte bei +20 °C)
pH Wert	4.5 ± 1.0	
Alkaligehalt	≤ 1.0 M-%	(Na_2O-Äquivalent)
Üblicher Feststoffgehalt	35.0 ± 1.0 M-%	
Wasserlöslicher Cl-Gehalt	≤ 0.10 M-%	

Verarbeitungs-hinweise

Dosierung	0.4 - 1.5 % Die Dosierung bezieht sich auf das Zementgewicht.

Verarbeitungsanweisun

Zugabe	Sika® ViscoCrete®-4035 M kann dem Anmachwasser beigemischt oder gleichzeitig mit diesem im Mischer zugegeben werden. Ideal ist eine Dosierung nach 50 - 80 % des Grobwassers. Sika® ViscoCrete®-4035 M sollte nie in die Trockenmischung gegeben werden. Zur optimalen Ausnutzung der starken Wasserreduktion empfehlen wir eine minimale Nassmischzeit von 60 Sekunden bei optimaler Durchmischung. Weiter ist zu beachten, dass die Feinwasserdosierung nach frühestens 2/3 der Nassmischzeit gestartet wird, um Überschusswasser im Beton zu vermeiden.
Wichtige Hinweise	Sika® ViscoCrete®-4035 M darf **nicht** mit Produkten auf Basis von Melamin und/oder Naphthalin kombiniert werden. Vorversuche sind unerlässlich. Zur Sicherstellung einer optimalen Verarbeitung und Nachbehandlung des Betons sind die nötigen Massnahmen gemäss SIA 262 zu treffen.

Messwerte

Alle in diesem Produktdatenblatt aufgeführten technischen Daten stammen aus Laborversuchen. Von uns nicht beeinflussbare Umstände können zu Abweichungen der effektiven Werte führen.

Länderspezifische Daten

Die Angaben in diesem Produktdatenblatt sind gültig für das entsprechende, von der Sika Schweiz AG ausgelieferte Produkt. Bitte berücksichtigen Sie, dass die Angaben in anderen Ländern davon abweichen können, beachten Sie im Ausland das lokale Produktdatenblatt.

Wichtige Sicherheitshinweis

Für detaillierte Angaben konsultieren Sie bitte das aktuelle Sicherheitsdatenblatt unter www.sika.ch.

Construction

Rechtliche Hinweise

Die vorstehenden Angaben, insbesondere die Vorschläge für Verarbeitung und Verwendung unserer Produkte, beruhen auf unseren Kenntnissen und Erfahrungen im Normalfall, vorausgesetzt die Produkte wurden sachgerecht gelagert und angewandt. Wegen der unterschiedlichen Materialien, Untergründen und abweichenden Arbeitsbedingungen kann eine Gewährleistung eines Arbeitsergebnisses oder eine Haftung, aus welchem Rechtsverhältnis auch immer, weder aus diesen Hinweisen, noch aus einer mündlichen Beratung begründet werden, es sei denn, dass uns insoweit Vorsatz oder grobe Fahrlässigkeit zur Last fällt. Hierbei hat der Anwender nachzuweisen, dass er schriftlich alle Kenntnisse, die zur sachgemässen und erfolgversprechenden Beurteilung durch Sika erforderlich sind, Sika rechtzeitig und vollständig übermittelt wurden. Der Anwender hat die Produkte auf ihre Eignung für den vorgesehenen Anwendungszweck zu prüfen. Änderungen der Produktspezifikationen bleiben vorbehalten. Schutzrechte Dritter sind zu beachten. Im Übrigen gelten unsere jeweiligen Verkaufs- und Lieferbedingungen. Es gilt das jeweils neueste Produktdatenblatt, das von uns angefordert werden sollte.

Sika Schweiz AG
Postfach
Tüffenwies 16
CH-8048 Zürich

Tel. 058 436 40 40
Fax 058 436 46 55
www.sika.ch

Appendix B

Amoras project

AMORAS is an acronym for Antwerp Mechanical Dewatering, Recycling and Application of Sludge. The AMORAS project has emerged in 2006 by the Flemish Government, in order to provide a sustainable and permanent solution for the storage and treatment of the maintenance dredging material from the River Scheldt in Antwerp. The project is located within the port area, between canal dock B1 and the motorway A12, on the right bank of the river Scheldt. The AMORAS installation can be subdivided into different sub-processes on three different locations: (A) Location 'Lillobrug', (B) Location 'Bietenveld', (C) Location 'Zandwinningsput' (see Fig. B.1) [66, 135].

A. Location 'Lillobrug'

At location 'Lillobrug', an underwatercel (1) and sand separation installation (2) are located. The underwatercel provides a temporary buffering for the less contaminated dredging material and has a capacity of 300.000 m^3. The contaminated fraction, which is estimated at 20% of the total dredging material, is not stored in the underwatercel, but is immediately pumped to a processing installation offshore. After storage in the underwatercel, the dredging material is pumped to the sand separation installation. To avoid damage to the mechanical installation, all particles larger than 8 mm are first separated by means of two sieves. Thereafter, the dredging material is sent to the sand separation installation, where the sand fraction (particles > 63 µm) is separated from the finer silt fraction (particles < 63 µm) by hydrocyclones. The remaining silt fraction is subsequently pumped to location 'Bietenveld', through pressure pipes (3) [66, 135].



Figure B.1: AMORAS project with subdivision in different locations (A. location 'Lillobrug', B. location 'Bietenveld', C. location 'Zandwinningsput') and sub-processes ((1) underwater cell, (2) sand separation installation, (3) pressure pipes, (4) consolidation ponds with dredging portico, (5) dewatering installation, (6) water treatment installation, (7) storage location), adapted from [66].

B. Location 'Bietenveld'

At location 'Bietenveld', thickening or consolidation of the silt fraction takes place in a specially designed circular buffer pond (4). The buffer pond consists of 4 consolidation ponds, each with a volume of 120.000 m^3. In a relatively short time, the dredging material will consolidate spontaneously until reaching a density approximating its original in-situ density. Dredging of the consolidated material is then done by means of two dredging pumps, housed in a portico. After consolidation and dredging, the consolidated material is pumped to the dewatering installation (5). To facilitate the solid-liquid separation, the dredging material is first mixed with lime milk, ferric chloride or polyelectrolytes, to initiate flake formation. The treated dredging material is subsequently pumped to the membrane chamber filter press, where most of the water is pressed out under pressure and dewatered filter cakes (dry matter content $> 60\%$) are obtained. The membrane chamber filter press consists of 193 filter chambers and the installation makes it possible to treat 600.000 tonnes of dry matter sediment per year. The resulting filtrate water is thereafter temporary buffered, before being treated in the water treatment installation (6). The water treatment installation works with a suspended active sludge system and the process consists of a sequence of physico-chemical pre-treatment and biological

treatment. During the pretreatment, the suspended particles are removed and the pH is corrected. During the biological purification, the organic substances and nitrogen are removed from the water by a sequence of pre-denitrification, nitrification, denitrification and post-aeration [66, 135].

C. Location 'Zandwinningsput'

Finally, the dewatered filter cakes are transported to a storage location (7), location 'Zandwinningsput', where the filter cakes are stored in a controlled manner (see Fig. B.2) [66, 135].



Figure B.2: Storage of the dewatered filter cakes.

Appendix C

Water absorption aggregates

The water absorption of the different aggregates can be found on the technical datasheets of the aggregates (see Appendix A) and is summarised in Table C.1, for both sand and gravel from three different suppliers.

Table C.1: Water absorption of the aggregates according to the technical fiches.

	Sand	Gravel
I	$\leq 0.5\%$	$\leq 1.2\%$
II	0.1%	1.6±0.7%
II	0.4±0.3%	0.7±0.3%

The water absorption of the aggregates can also be measured and calculated according to the European standard EN 1097-6 [82]. This was done only for the sand and gravel from supplier II and the results are summarised in Table C.2. It is concluded that for both the sand and the gravel, the measured water absorption is 0.1% less than the (minimal) water absorption according to the technical fiche.

Table C.2: Measured water absorption of aggregates.

	Sand	Gravel
II	0.0%	0.8%

Considering the amount of sand (640 kg/m^3) and the amount of gravel (1225 kg/m^3) in the concrete mix, the amount of water absorbed by the aggregates can be calculated. By taking into account the upper and lower

limits of the water absorption, as mentioned on the technical datasheets, the water absorption by the aggregates from the different suppliers equals:

- Supplier I: 8.95 ± 8.95 litres water per m^3 concrete (according to the technical datasheet).
- Supplier II: 9.8 litres water per m^3 concrete (measured).
- Supplier III: 11.1 ± 5.6 litres water per m^3 concrete (according to the technical datasheet).

An average value of 10 litres of water per m^3 of concrete [24], thus, well represents the water absorption of the aggregates of the different suppliers. However, due to the heterogeneity of the aggregates, variations are always possible.

Appendix D

Modelling of UPV curves

Mathematical model fitting of the velocity curves results in smoothing of the curves and allows more accurate determination of characteristic points (e.g. inflection points). In literature, different mathematical functions, mostly logistic functions, are proposed to model the P-wave velocity [46, 54, 114, 162, 163, 178, 179].

1 Logistic function. Logistic functions are often used to describe S-shaped curves [114, 178]. Grosse et al. [114] proposed the Boltzmann function (Eq. D.1) to describe the velocity curve.

$$V_P(t) = \frac{v_1 - v_2}{1 + \exp\left(\frac{t - t_0}{dt}\right)} + v_2 \tag{D.1}$$

with v_1 the initial velocity value (at t=-∞), v_2 the final velocity value (at t=∞) and dt the gradient at t_0 (the center point between v_1 and v_2) (see Fig. D.1 (left)).

2 Power logistic function. Since the velocity curves typically show a smaller branch with higher curvature at early ages, a power logistic function (Eq. D.2) was also proposed by Grosse et al. [114] in order to obtain a better fit.

$$V_P(t) = \frac{v_1 - v_2}{1 + \left(\frac{t}{t_0}\right)^p} + v_2 \tag{D.2}$$

with v_1 the initial velocity value (at t=0), v_2 the final velocity value (at t=∞) and p replaces the gradient dt (see Fig. D.1 (right)) [54, 114, 178].

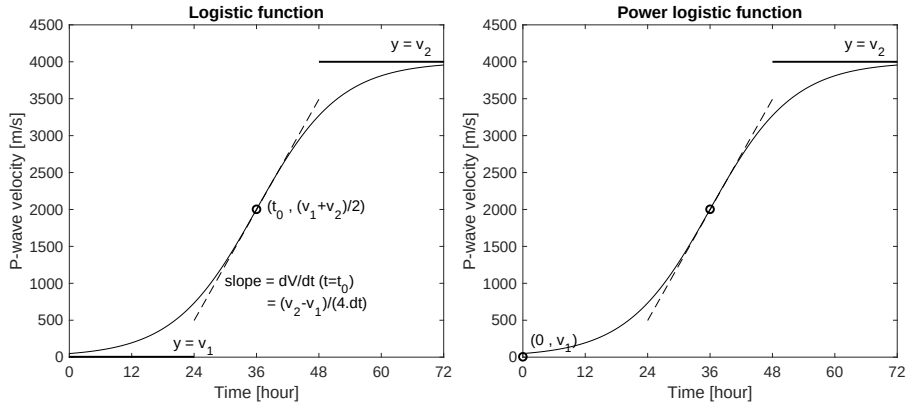

Figure D.1: Sample curve demonstrating the influence of different parameters on the logistic (left) and power logistic function (right), adapted from [114].

3 Bi- or multi-logistic function. Since the P-wave velocity curves actually consist of more than one S-shaped curve, bi-logistic or multi-logistic functions are also often used to describe the process [46, 162, 163, 178, 179]. These functions superpose two or more logistic functions with different gradients, inflection points and end values (see Eq. D.3) and are a generalisation of Eq. D.1 .

$$V_P(t) = \sum_i \frac{v_i}{1 + \exp\left(\frac{t - t_i}{g_i}\right)} + c \tag{D.3}$$

Multi-logistic model fitting results in a better fit due to the higher set of fitting parameters. However, the latter is also the main disadvantage of this type of fitting. The high amount of fitting parameters leaves a lot of opportunity for bad fitting, since the fitting is very unstable and highly depends on the initial parameters. Furthermore, the physical meaning of the parameters is less clear/non-existing for the superposed logistic functions and determination of the initial input parameters is therefore hard.

4 Multi-exponential function. Exponential functions are the most 'easy' functions to describe S-shaped curves and are commonly used to describe the hydration process (by means of heat release). Multi-exponential model fitting could therefore also be used to describe the velocity curves.

$$V_P(t) = \sum_i a_i \cdot \exp\left(-\left(\frac{b_i}{t}\right)^{c_i}\right) + d \tag{D.4}$$

with a_i the amplitude, b_i the time parameter, c_i the shape parameter and d the baseline parameter.

Cement paste

Model fitting of logistic, power-logistic, bi- and tri-logistic and bi- and tri-exponential functions was studied for the different cement paste mixes. Due to instability of the multi-logistic model fitting and the impossible task to accurately determine the initial parameters (for i>3), multi-logistic and multi-exponential (i>3) model functions are not considered. The logistic and power-logistic fitting methods are both independent of the input parameters; the bi- and tri-logistic and bi- and tri-exponential fitting methods are (slightly/strongly) depending on the input parameters. The more fitting parameters used, the less clear their physical meaning and less accurate the determination of their starting values.

The modelling results of the different mathematical functions are shown in Fig. D.2 and Fig. D.3 (respectively for the cement paste mixes with and without addition of superplasticizer), and the corresponding fitting parameters are shown in Tables D.1-D.6, together with the initial starting values used (the asterix* represents cement paste mixes without superplasticizer). The root mean square errors (RMSEs) of all fitting methods for all compositions are shown in Fig. D.4 and D.5 (respectively for the mixes with and without addition of superplasticizer), and are calculated as:

$$\mathrm{RMSE} = \sqrt{\frac{\sum_i \left(\hat{y}_i - y_i\right)^2}{n}} \tag{D.5}$$

with $\hat{y}_i$ the modelled values of the velocity, y_i the experimental values of the velocity and n the amount of data points.

It is observed in Fig. D.2 and Fig. D.3 that the logistic, power-logistic, bi-logistic and bi-exponential functions does not well fit the experimental data. This is also confirmed by the high RMSEs (see Fig. D.4 and Fig. D.5) of these functions. The tri-logistic and tri-exponential functions, on the other hand, better fit the experimental results of the velocity curves. This can be explained by the fact that the logistic, power-logistic, bi-logistic and bi-exponential functions only describe one or two S-shaped curves, while the tri-logistic and tri-exponential describe three S-shaped curves. Since the goal of the model fitting was to more accurately determine the inflection points of the velocity curves, the fitting behaviour at early ages is important. Therefore, the results of the model fitting up to 48 hours for the cement paste mixes with superplasticizer and up to 24 hours for the cement paste mixes without superplasticizer, are shown in Fig. D.6 and Fig. D.7 respectively, for the tri-logistic and tri-exponential

functions only. It is observed in Fig. D.6 that for the mixes with superplasticizer, all tri-exponential functions very well fit the experimental data, while the tri-logistic functions does not well describe the early-age behaviour, especially for the blended cements. The tri-exponential function is therefore retained for the mixes with superplasticizer. For the mixes without superplasticizer, on the other hand, Fig. D.7 shows that both the tri-logistic and tri-exponential functions does not well fit the two superposed S-shaped velocity curves. This will result in distorted values of the inflection points, and wrong determination of the setting times.

In order to be able to better fit the velocity curves of the mixes without superplasticizer at early ages, the tri-logistic and tri-exponential functions were fitted to the experimental data, up to 48 hours only. The results of the model fitting are shown in Fig. D.8 for the tri-logistic and tri-exponential functions. The corresponding fitting parameters and RMSEs are summarised in Tables D.7-D.9. It is observed that both the tri-logistic and tri-exponential functions now much better fit the experimental results of the cement paste mixes without superplasticizer. The tri-logistic functions, however, still show some deviation in the beginning and show (slightly) higher RMSEs compared to the tri-exponential functions. The tri-exponential functions will therefore be retained.

Concrete

The parameter results of the tri-exponential model fitting of the P- and S-wave velocities of the concrete samples are respectively shown in Table D.10 and D.11.

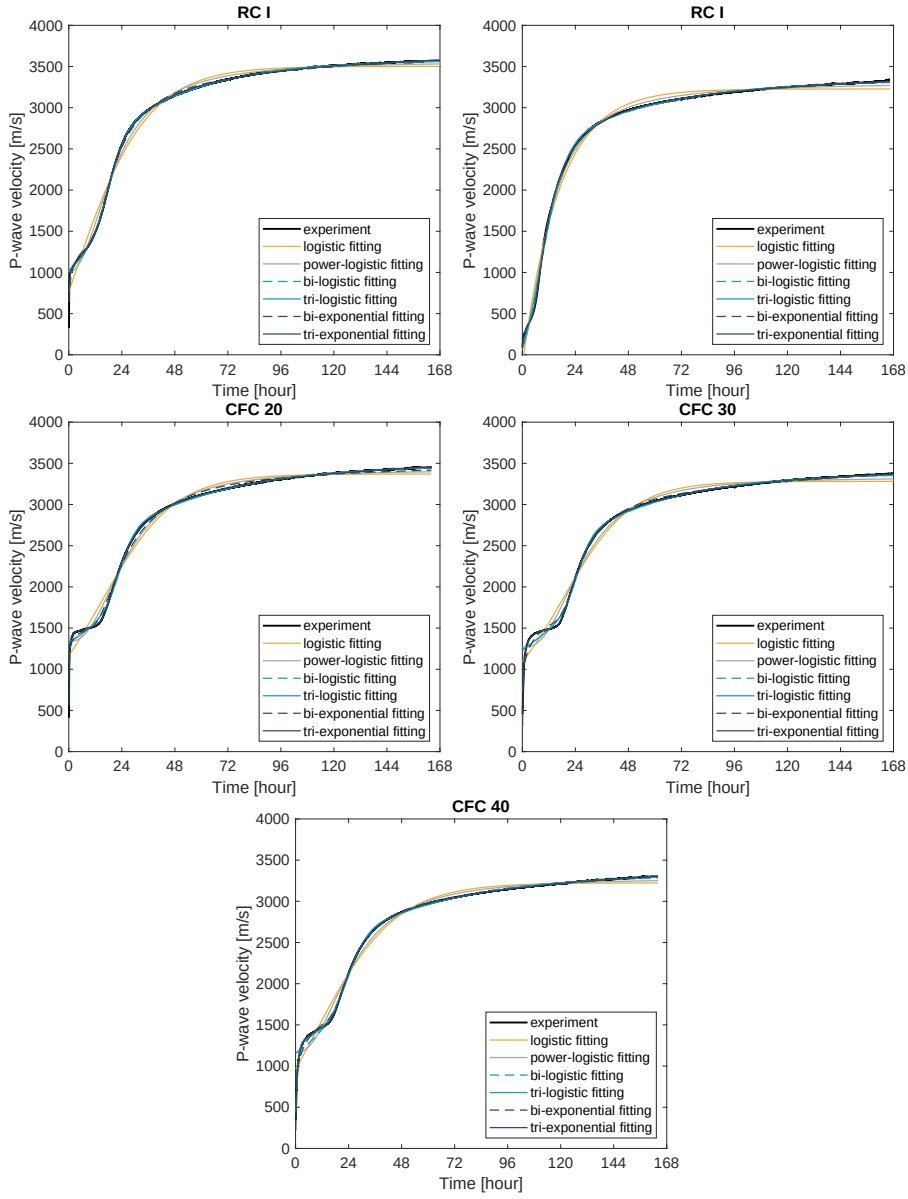

Figure D.2: Comparison of the experimental data with the model fitting of the velocity curves with logistic, power-logistic, bi- and tri-logistic and bi- and tri-exponential functions for the cement paste mixes with superplasticizer up to 7 days.

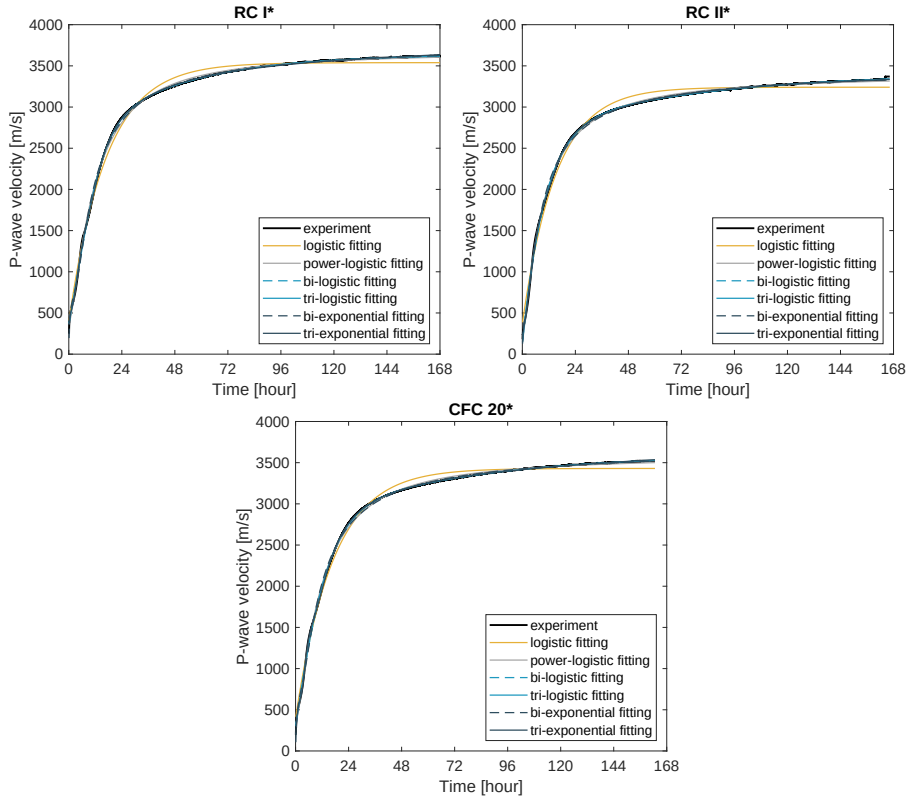

Figure D.3: Comparison of the experimental data with the model fitting of the velocity curves with logistic, power-logistic, bi- and tri-logistic and bi- and tri-exponential functions for the cement paste mixes without superplasticizer up to 7 days.

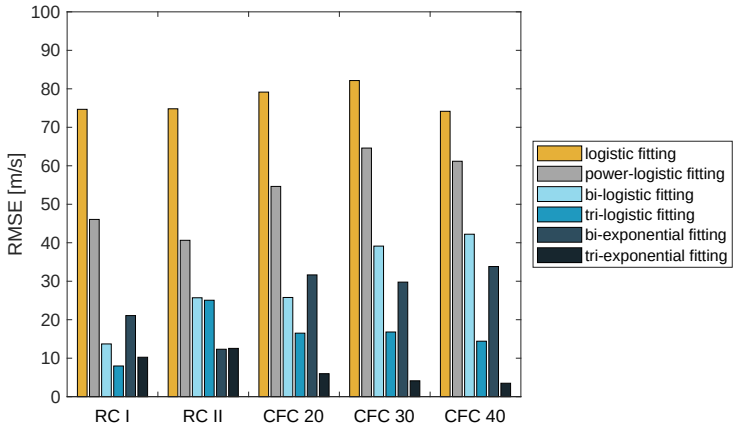

Figure D.4: RMSE of the different model functions for the cement paste mixes with superplasticizer.

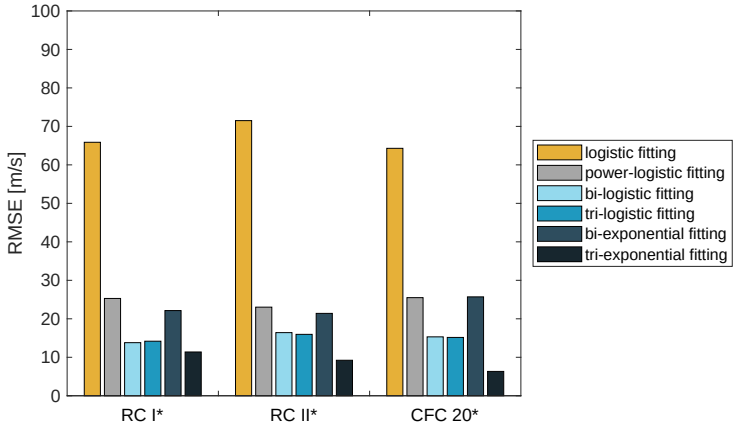

Figure D.5: RMSE of the different model functions for the cement paste mixes without superplasticizer.

Table D.1: Parameters of the logistic model fitting for different cement paste mixes with and without addition of superplasticizer.

	v_1 [m/s]	v_2 [m/s]	t_0 [h]	dt [-]
initial	-2000	3300	-1	16
RC I	-2170.3	3502.8	-1.2	17.5
RC II	-395675	3227.5	-78.3	16.4
CFC 20	257.1	3370.4	14.6	16.5
CFC 30	444.1	3281.1	18.5	15.2
CFC 40	-477.5	3223.8	8.3	18.3
RC I*	-613089	3539.0	-88.3	16.8
RC II*	-1568396	3240.8	-95.4	15.1
CFC 20*	-789835	3430.0	-94.0	16.9

Table D.2: Parameters of the power-logistic model fitting for different cement paste mixes with and without addition of superplasticizer.

	v_1 [m/s]	v_2 [m/s]	t_0 [h]	p [-]
initial	500	3300	21	2
RC I	1005.4	3562.5	21.1	2.1
RC II	101.2	3310.5	12.8	1.7
CFC 20	1337.5	3423.1	26.5	2.4
CFC 30	1268.3	3330.1	27.6	2.6
CFC 40	1162.9	3284.4	26.1	2.3
RC I*	362.4	3680.9	11.4	1.4
RC II*	147.7	3405.0	9.1	1.2
CFC 20*	321.7	3591.3	11.3	1.3

Table D.3: Parameters of the bi-logistic model fitting for different cement paste mixes with and without addition of superplasticizer.

	v_1 [m/s]	v_2 [m/s]	t_1 [h]	t_2 [h]	g_1 [-]	g_2 [-]	c [-]
initial	-1100	4000	21	-40	4	-40	1000
RC I	-1355.6	3024.5	18.1	-13.8	4.1	-34.6	552.0
RC II	-2804.4	2673.7	8.6	-26.4	5.4	-41.0	656.1
CFC 20	-1034.3	2638.9	22.9	-12.6	3.8	-40.2	838.4
CFC 30	-952.3	2939.4	24.8	-14.5	3.5	-36.9	433.7
CFC 40	-1021.9	3018.0	23.0	-19.7	4.5	-38.9	289.7
RC I*	-3768.8	2980.8	3.1	-28.6	6.7	-39.2	655.1
RC II*	-17780.2	3715.4	-16.1	-89.9	9.0	-62.2	-315.3
CFC 20*	-6842.3	2807.7	-4.8	-60.1	9.2	60.8	790.8

Table D.4: Parameters of the tri-logistic model fitting for different cement paste mixes with and without addition of superplasticizer.

	v_1 [m/s]	v_2 [m/s]	v_3 [m/s]	t_1 [h]	t_2 [h]	t_3 [h]	g_1 [-]	g_2 [-]	g_3 [-]	c [-]
initial	-1100	1000	4000	21	-20	-40	4	-20	-40	1000
RC I	-1342.2	825.1	2363.7	18.2	-14.4	-16.6	4.1	-29.9	-36.6	389.7
RC II	-2704.5	973.2	1853.9	8.7	-14.7	-27.1	5.4	-22.2	-49.7	521.4
CFC 20	-997.2	656.2	2377.7	23.0	-16.4	-19.6	3.7	-31.2	-43.0	445.9
CFC 30	-946.1	795.7	2308.3	24.9	-15.2	-17.2	3.5	-27.5	-41.0	278.0
CFC 40	-1113.7	1976.7	2017.4	23.8	-0.1	-3.8	4.5	-0.7	-42.9	-661.7
RC I*	-3485.9	1068.6	2025.8	3.5	-14.5	-27.2	6.4	-22.2	-44.7	549.5
RC II*	-9237.4	1888.9	1490.4	-9.7	0.8	-25.4	6.6	-11.3	-63.2	30.4
CFC 20*	-6789.4	1381.1	1875.5	-6.7	-10.8	-27.9	9.5	-10.2	-57.3	336.2

Table D.5: Parameters of the bi-exponential model fitting for different cement paste mixes with and without addition of superplasticizer.

	a_1 [m/s]	a_2 [m/s]	b_1 [h]	b_2 [h]	c_1 [-]	c_2 [-]	d [-]
initial	1000	2500	3	15	0.5	1.5	5
RC I	8058.1	1674.8	17765.5	18.2	0.1	2.4	0.0
RC II	3081.8	2327.8	341.5	10.3	0.2	1.7	4.5
CFC 20	2210.5	1768.4	0.0	22.9	0.1	2.0	5.1
CFC 30	11638.4	1238.2	410846.5	24.5	0.1	3.4	0.0
CFC 40	9811.2	1111.1	17769.7	23.4	0.1	3.4	0.0
RC I*	1447.3	2457.0	0.9	9.8	0.3	1.2	5.1
RC II*	871.0	2646.4	0.5	7.6	0.4	1.0	5.1
CFC 20*	1540.8	2238.3	1.3	10.1	0.4	1.2	5.1

Table D.6: Parameters of the tri-exponential model fitting for different cement paste mixes with and without addition of superplasticizer.

	a_1 [m/s]	a_2 [m/s]	a_3 [m/s]	b_1 [h]	b_2 [h]	b_3 [h]	c_1 [-]	c_2 [-]	c_3 [-]	d [-]
initial	800	1500	2000	3	15	24	0.5	1.75	3	5
RC I	706.2	1547.3	1735.8	18.1	20.0	0.1	4.9	1.2	0.2	5.1
RC II	2257.8	1828.9	167.0	10.3	41.1	0.0	1.8	0.3	0.2	5.5
CFC 20	1085.6	1188.6	1486.1	20.8	42.9	0.1	3.7	0.9	1.0	5.0
CFC 30	1453.0	492.3	1564.2	23.3	82.8	0.2	3.6	1.7	0.7	5.9
CFC 40	1170.1	1010.8	1613.5	22.3	83.0	0.3	3.6	0.7	0.6	5.9
RC I*	384.2	2448.1	1719.6	13.8	8.0	4.3	4.3	1.0	0.1	4.9
RC II*	1386.9	2267.4	225.2	3.5	6.2	15.4	0.2	1.0	5.9	5.2
CFC 20*	1108.3	775.9	4012.3	14.9	4.4	81.8	2.4	2.9	0.2	8.2

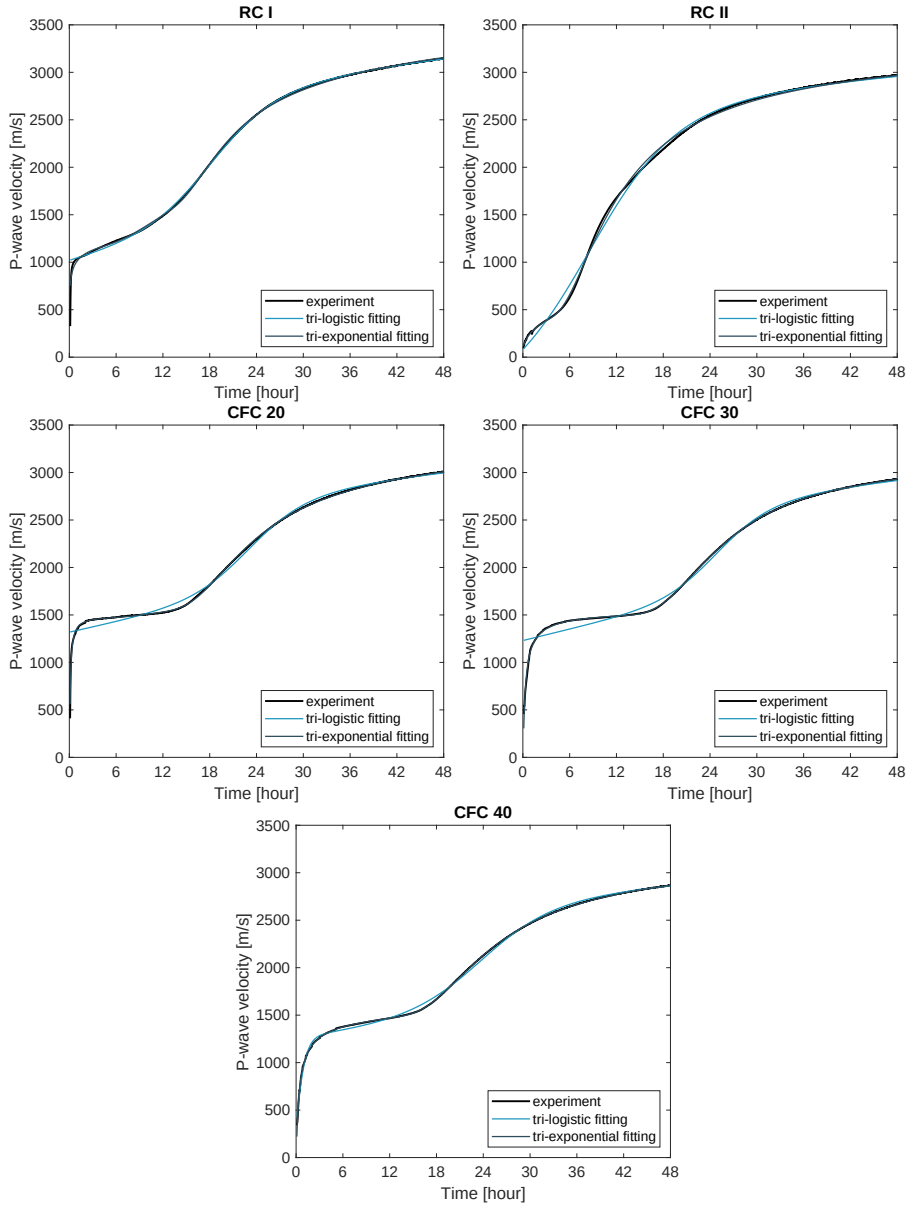

Figure D.6: Comparison of the experimental data with the model fitting of the velocity curves with tri-logistic and tri-exponential functions for the cement paste mixes with superplasticizer up to 48 hours.

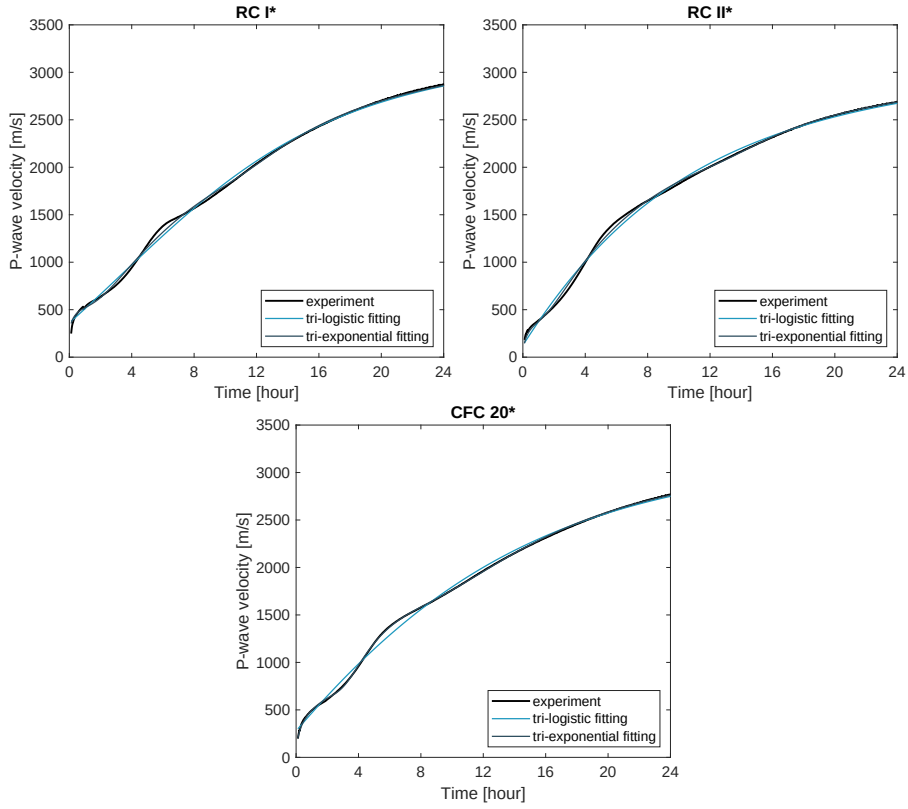

Figure D.7: Comparison of the experimental data with the model fitting of the velocity curves with tri-logistic and tri-exponential functions for the cement paste mixes without superplasticizer up to 24 hours.

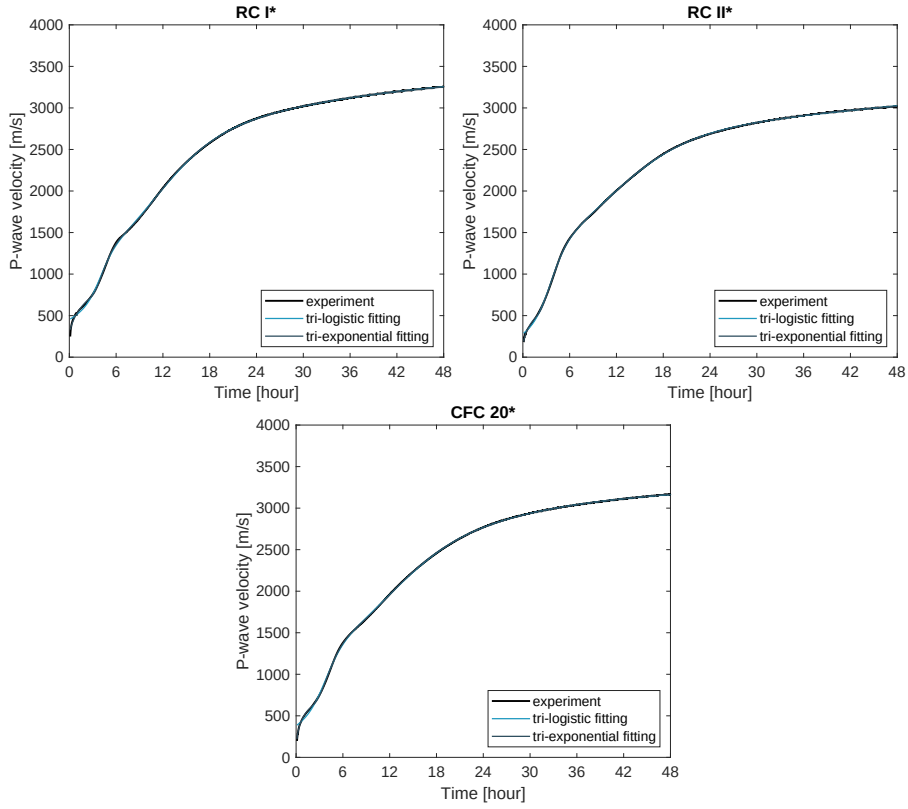

Figure D.8: Comparison of the experimental data with the 48 hours model fitting of the velocity curves with tri-logistic and tri-exponential functions for the cement paste mixes without superplasticizer.

Table D.7: RMSEs of the tri-logistic and tri-exponential 48 hours model fitting for different cement paste mixes without addition of superplasticizer.

	tri-logistic [m/s]	tri-exponential [m/s]
RC I*	12.99	6.88
RC II*	6.94	5.40
CFC 20*	12.29	5.68

Table D.8: Parameters of the tri-logistic 48 hours model fitting for different cement paste mixes without addition of superplasticizer.

	v_1 [m/s]	v_2 [m/s]	v_3 [m/s]	t_1 [h]	t_2 [h]	t_3 [h]	g_1 [-]	g_2 [-]	g_3 [-]	c [-]
RC I*	-1335.4	571.8	2517.2	11.3	4.0	-3.1	3.9	-0.9	-20.3	353.7
RC II*	-1530.4	916.7	3113.5	10.6	3.5	-32.1	5.1	-1.1	-59.1	-365.5
CFC 20*	-1033.9	740.2	2266.9	12.3	3.8	1.9	4.3	-1.1	-15.6	268.0

Table D.9: Parameters of the tri-exponential model fitting for different cement paste mixes without addition of superplasticizer.

	a_1 [m/s]	a_2 [m/s]	a_3 [m/s]	b_1 [h]	b_2 [h]	b_3 [h]	c_1 [-]	c_2 [-]	c_3 [-]	d [-]
RC I*	1138.1	640.5	3414.8	13.2	4.5	54.9	2.7	3.7	0.2	294.2
RC II*	706.4	3583.4	1107.5	14.7	105.9	4.2	2.8	0.2	2.1	128.4
CFC 20*	1111.7	877.4	3571.5	15.2	4.5	67.3	2.4	2.6	0.2	3.4

Table D.10: Parameters of the tri-exponential model fitting of the P-wave velocity of the different concrete mixes.

	a_1 [m/s]	a_2 [m/s]	a_3 [m/s]	b_1 [h]	b_2 [h]	b_3 [h]	c_1 [-]	c_2 [-]	c_3 [-]	d [-]
RC I	1340.6	2170.2	1289.8	2.9	5.6	6.8	0.5	2.5	5.2	5.0
RC II	1228.8	2371.2	1479.1	1.1	5.8	4.3	0.2	2.6	3.0	5.1
CFC 20	889.6	1309.5	2456.3	2.1	5.7	8.2	0.5	2.3	4.2	5.0
CFC 30	1699.9	2067.0	991.7	2.9	7.6	8.0	1.1	2.4	8.3	5.0
CFC 40	1634.4	1973.1	1224.7	2.6	7.4	9.1	1.1	2.4	6.9	5.0

Table D.11: Parameters of the tri-exponential model fitting of the S-wave velocity of the different concrete mixes.

	a_1 [m/s]	a_2 [m/s]	a_3 [m/s]	b_1 [h]	b_2 [h]	b_3 [h]	c_1 [-]	c_2 [-]	c_3 [-]	d [-]
RC I	924.9	1895.6	2.5	4.7	7.9	25.6	1.1	3.1	1.5	5.2
RC II	542.9	2139.0	0.0	3.3	7.3	39.3	1.2	2.5	2.2	5.5
CFC 20	488.5	1997.1	348.6	4.3	9.4	50.8	1.1	3.3	0.5	5.2
CFC 30	701.3	1998.0	0.0	4.4	9.6	25.1	0.9	3.5	0.8	5.1
CFC 40	393.8	2176.7	76.3	5.4	11.5	0.0	1.7	3.1	1.0	4.4

Appendix E

Shrinkage modelling

Parameters empirical shrinkage models

Table E.1: Autogenous shrinkage model parameters (1).

			β-n model		EC 2 model	MC 2010 model	
	t_0	s	$\epsilon_{au,28d}$	$n_{\epsilon au}$	f_{ck}	α_{au}	f_{cm}
RC I	0.36	0.15	82.62	1.32	47.94	1193	49.20
RC II	0.34	0.20	43.16	0.87	36.75	954	37.26
CFC 20	0.42	0.24	54.29	0.36	55.13	717	56.66
CFC 30	0.43	0.24	49.38	0.36	49.08	717	52.12
CFC 40	0.46	0.24	42.36	0.36	49.25	717	51.16

Table E.2: Autogenous shrinkage model parameters (2).

	Bazant B4 model					Rifai model				
	t_0	$\epsilon_{au\infty}$	τ_{au}	α	r_t	y_0	A_1	t_1	A_2	t_2
RC I	0.36	79.32	0.34	0.99	-2.91	93.13	62.98	1.23	34.05	22.03
RC II	0.34	38.01	0.24	1.56	-7.55	37.04	42.84	1.28	0.00	123.96
CFC 20	0.42	50.72	0.72	1.53	-0.57	84.64	40.46	0.60	37.78	109.17
CFC 30	0.43	46.14	0.72	1.53	-0.57	80.41	40.46	0.60	37.78	109.17
CFC 40	0.46	39.63	0.72	1.53	-0.57	74.39	40.46	0.60	37.78	109.17

Table E.3: Drying shrinkage model parameters.

		β-n model			EC 2 model			MC 2010 model		Bazant B4 model	
	t_s	s	$\epsilon_{dr,28d}$	$n_{\epsilon dr}$	f_{cm}	$\alpha_{ds,1}$	$\alpha_{ds,2}$	$\alpha_{ds,1}$	$\alpha_{ds,2}$	$\epsilon_{dr\infty}$	τ_0
RC I	1.11	0.14	313.57	5.46	49.20	5.28	0.09	6.69	0.010	-729.92	0.016
RC II	1.09	0.20	324.82	3.89	37.26	4.96	0.10	6.16	0.010	-720.12	0.014
CFC 30	1.07	0.23	247.22	3.68	52.12	1.62	0.00	2.10	0.000	-630.47	0.020
CFC 40	1.00	0.23	229.01	3.68	51.16	1.62	0.00	2.10	0.000	-583.53	0.020

Table E.4: Total shrinkage model parameters.

		β-n model			EC 2 model			MC 2010 model		Bazant B4 model	
	t_s	s	$\epsilon_{dr,28d}$	$n_{\epsilon dr}$	f_{cm}	$\alpha_{ds,1}$	$\alpha_{ds,2}$	$\alpha_{ds,1}$	$\alpha_{ds,2}$	$\epsilon_{dr\infty}$	τ_0
RC I	1.11	0.14	263.95	6.13	49.20	4.51	0.10	4.75	0.010	-755.17	0.025
RC II	1.09	0.20	299.54	4.11	37.26	4.28	0.11	5.33	0.011	-720.49	0.016
CFC 30	1.07	0.23	227.43	3.94	52.12	0.84	0.00	1.39	0.000	-657.52	0.026
CFC 40	1.00	0.23	211.15	3.94	51.16	0.84	0.00	1.39	0.000	-608.61	0.026

Powers' model

Powers and Brownyard (1948) were the first to propose an empirical model for the phase distribution of hardening cement paste. This model was slightly modified over the years and is now known as Powers' model [133]. The development of the phase distribution in hydrating cement paste according to Powers' model, is shown in Fig. E.1.

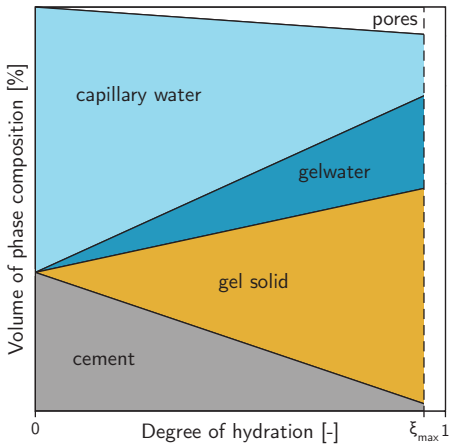

Figure E.1: Volumetric phase distribution of cement paste as a function of the degree of hydration, according to Powers' model (assuming autogenous conditions, i.e. sealed hydration), adapted from [133].

Upon hydration, cement reacts with the free evaporable water, i.e. capillary water, to form cement hydrates, i.e. gel solid. Part of the water is physically bound on the surface of the gel solid by adsorptive forces, i.e. gel water. Due to chemical shrinkage, gas-filled pores are simultaneously formed [133].

The progress of each of the individual phases of the hardening cement paste can be quantified as follows [133, 153]:

- Initial porosity = the volume of capillary water at t=0:

$$p = \frac{w/\rho_w}{w/\rho_w + c/\rho_c} = \frac{w/c}{w/c + \rho_w/\rho_c} \tag{E.1}$$

  with w and c the masses of water and cement, respectively, and ρ_w and ρ_c the densities of water and cement, respectively.

- Unhydrated cement:

$$V_{uc} = \frac{c/\rho_c}{w/\rho_w + c/\rho_c} \cdot (1-\alpha) = (1-p) \cdot (1-\alpha) \tag{E.2}$$

  with α the advancement of the degree of hydration.

- Chemical shrinkage:

$$V_{cs} = \Delta V_{cs} \cdot \rho_c \cdot (1-p) \cdot \alpha \tag{E.3}$$

  with ΔV_{cs} the volume of chemical shrinkage per 100 g of cement reacted.

- Capillary water = the capillary water at t=0 minus the chemically bound water minus the physically bound water (gelwater):

$$V_{cw} = p - w_{gw} \cdot (1-p) \cdot \alpha - w_{cbw} \cdot \frac{\rho_c}{\rho_w} \cdot (1-p) \cdot \alpha \tag{E.4}$$

  with w_{gw} and w_{cbw} the amount of gelwater and chemically bound water, respectively (in g per g reacted cement).

- Gelwater:

$$V_{gw} = w_{gw} \cdot \frac{\rho_c}{\rho_w} \cdot (1-p) \cdot \alpha \tag{E.5}$$

- Gel solid = amount of reacted cement minus the chemical shrinkage plus the chemically bound cater (non-evaporable):

$$V_{gs} = (1-p) \cdot \alpha - \Delta V_{cs} \cdot 10^{-5} \cdot \rho_c \cdot (1-p) \cdot \alpha + w_{cbw} \cdot \frac{\rho_c}{\rho_w} \cdot (1-p) \cdot \alpha \tag{E.6}$$

The water saturation fraction can subsequently be determined as the ratio of the volume of evaporable water content (V_{ew}) and the volume of pores (V_p). The evaporable water content is the sum of the capillary water content and gel water content. The volume of the pores equals the volume of the capillary water, gel water and chemical shrinkage [153].

$$S_w = \frac{V_{ew}(\alpha}{V_p(\alpha)} = \frac{V_{cw}(\alpha) + V_{gw}(\alpha)}{V_{cw}(\alpha) + V_{gw}(\alpha) + V_{cs}(\alpha)} \tag{E.7}$$

$$\Rightarrow S_w = \frac{p - w_{cbw} \cdot \rho_c/\rho_w \cdot (1-p) \cdot \alpha}{p - [w_{cbw} \cdot \rho_c/\rho_w - \Delta V_{cs} \cdot 10^{-5} \cdot \rho_c] \cdot (1-p) \cdot \alpha} \tag{E.8}$$

The only unknowns here are the volume of the chemical shrinkage (ΔV_{cs}) and the amount of chemically bound water (w_{cbw}).

Calculation advancement degree of hydration

The advancement of the degree of hydration α is calculated as:

$$\alpha = \frac{Q}{Q_\infty} \tag{E.9}$$

with Q_∞ the ultimate cumulative heat, calculated by fitting the cement paste cumulative heat results (see Fig. 5.3) to an exponential/S-shaped model:

$$Q(t) = Q_\infty \cdot \exp\left(-\frac{\tau}{t}\right)^\beta \tag{E.10}$$

with τ the hydration time parameter and β the hydration shape parameter, both fitting parameters. The parameter results of the cumulative heat model fitting are given in Tabel E.5. The results of the modelled cumulative heat and the experimentally obtained values are shown in Fig. E.2.

Table E.5: Fitting parameters of the cumulative heat model for cement paste.

	Q_∞ [MJ/m^3]	τ [-]	β [-]
RC I	386.56	1081.05	86.48
RC II	295.76	980.77	78.46
CFC 20	343.00	1115.74	89.26
CFC 30	313.59	1136.91	90.95
CFC 40	291.13	1128.16	90.25

It can be concluded that the results of τ and β correspond well with the values of τ and β obtained on concrete (see Table 5.9).

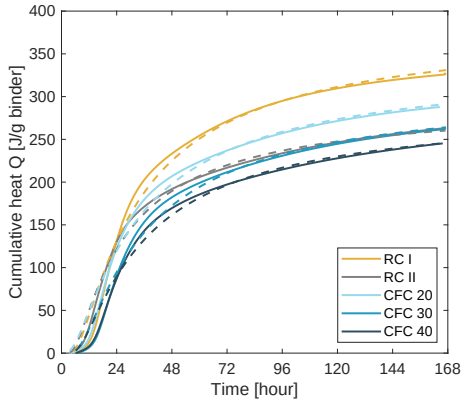

Figure E.2: Modelled cumulative heat (dashed lines) versus experiments (full lines) for the different cement paste samples.

Appendix F

Drying shrinkage microcracks

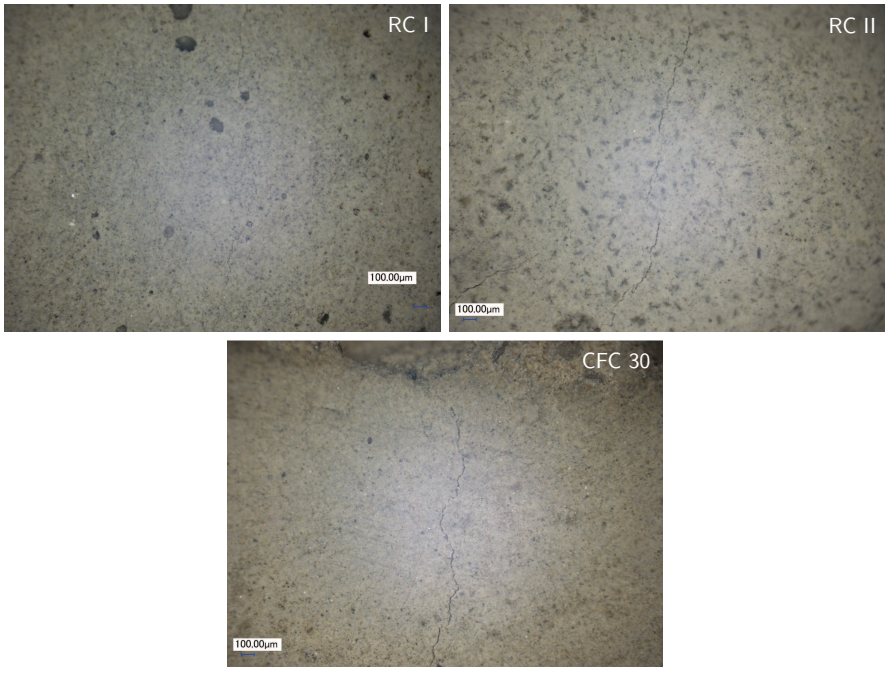

Figure F.1: Microcracks observed on the surfaces of the RC I, RC II and CFC 30 drying shrinkage concrete samples.

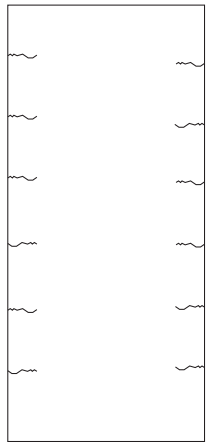

Figure F.2: Drying shrinkage cracking pattern.

Appendix G

Verification of eccentricity of the creep specimens

Due to difficulties in the manual placing of the creep specimen in the frame, the creep specimens are not perfectly centered and the stress development is therefore not uniform over the surface of the concrete sample. Every side of the sample will experience a slightly different stress level, due to the development of two bending moments (M_x and M_y) induced by the eccentricity of the load, see Fig. G.1. The stress at a random point (x,y) on the surface of the creep specimen equals:

$$\sigma_{zz} = \frac{F}{A} + \frac{M_x \cdot y}{I_z} + \frac{M_y \cdot x}{I_z} \tag{G.1}$$

with $M_x = F \cdot e_x$ and $M_y = F \cdot e_y$ and $I_z = \frac{b^4}{12}$ and $A = b^2$. The first term of Eq. G.1 is the stress due to the applied load (F), the second and third term are the additional stresses due to the bending moments.

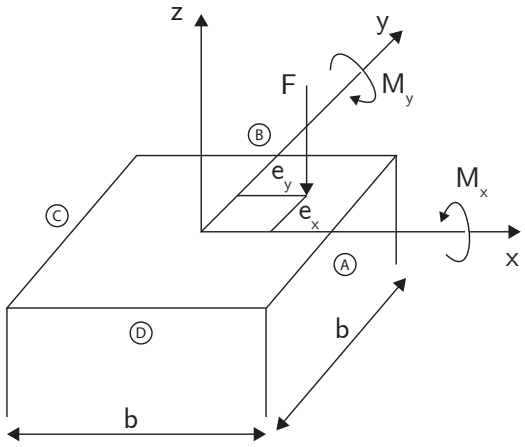

Figure G.1: Eccentricity (e_x and e_y) of the creep load resulting in parasitic bending moments (M_x and M_y).

In order to determine the eccentricities e_x and e_y of each creep specimen, the stress level on the four sides of the specimen is described in function of the applied force (F) and the eccentricities (e_x) and e_y) (see Eq. G.2-G.5). By using the measured deformations (ϵ_{zz}) on each side of the creep specimen, the eccentricities can than be calculated.

Side A (y=0 and x=b/2):

$$\Rightarrow \sigma_{zz}^{A} = E \cdot \epsilon_{zz}^{A} = \frac{F}{A} + \frac{F \cdot e_y}{I_z} \cdot \frac{b}{2} \tag{G.2}$$

Side B (y=b/2 and x=0):

$$\Rightarrow \sigma_{zz}^{B} = E \cdot \epsilon_{zz}^{B} = \frac{F}{A} + \frac{F \cdot e_x}{I_z} \cdot \frac{b}{2} \tag{G.3}$$

Side C (y=0 and x=-b/2):

$$\Rightarrow \sigma_{zz}^{C} = E \cdot \epsilon_{zz}^{C} = \frac{F}{A} - \frac{F \cdot e_y}{I_z} \cdot \frac{b}{2} \tag{G.4}$$

Side D (y=-b/2 and x=0):

$$\Rightarrow \sigma_{zz}^{D} = E \cdot \epsilon_{zz}^{D} = \frac{F}{A} - \frac{F \cdot e_x}{I_z} \cdot \frac{b}{2} \tag{G.5}$$

Solving the first three equations gives:

$$e_x = \frac{\epsilon_{zz}^{B}/\epsilon_{zz}^{C} \cdot (1 - e_y \cdot \alpha) - 1}{\alpha} \tag{G.6}$$

$$e_y = -\frac{1 - \epsilon_{zz}^{A}/\epsilon_{zz}^{C}}{\alpha \cdot (\epsilon_{zz}^{A}/\epsilon_{zz}^{C} + 1)} \tag{G.7}$$

The eccentricities and bending moments of each creep specimen can then be calculated and the results of the basic and drying creep specimens are respectively shown in Table G.1 and Table G.2.

Table G.1: Eccentricities and bending moments of the basic creep specimens.

	M_x [Nm]	e_x [mm]	M_y [Nm]	e_y [mm]
RC I (A)	14.57	0.37	50.55	1.27
RC I (B)	45.96	1.15	-36.68	-0.92
RC II (A)	-34.48	-1.11	-66.9	-2.15
RC II (B)	-123.70	-3.97	-3.93	-0.13
CFC 30 (A)	32.98	0.88	-17.27	-0.46
CFC 30 (B)	-9.13	-0.24	70.51	1.89
CFC 40 (A)	29.63	0.90	23.80	0.72
CFC 40 (B)	-10.56	-0.32	100.75	3.05

Table G.2: Eccentricities and bending moments of the drying creep specimens.

	M_x [Nm]	e_x [mm]	M_y [Nm]	e_y [mm]
RC I (A)	58.68	1.47	-33.43	-0.84
RC I (B)	-0.56	0.01	31.82	0.80
RC II (A)	-75.83	-2.43	6.51	0.21
RC II (B)	37.69	1.21	-63.03	2.02
CFC 30 (A)	55.60	1.49	-36.11	-0.97
CFC 30 (B)	-73.06	-1.96	84.06	2.25
CFC 40 (A)	-62.35	-1.89	-54.18	-1.64

High bending moments could significantly affect the stresses developed at each side of the creep specimen. The observed bending moments, however, are relatively small and only affect the stress level in a minor way. This is confirmed by the small variation in stress level due to the bending moments (see Table G.3 and Table G.4. Overall, the impact of the eccentricity of the creep specimens on the stress level is thus negligible.

Table G.3: Impact of the bending moments on the stress level for the basic creep specimens.

	σ [MPa]	Δσ [MPa]	Δσ [%]
RC I (A)	8.12	0.03	0.4
RC I (B)	8.12	0.04	0.5
RC II (A)	6.36	0.09	1.4
RC II (B)	6.36	0.25	3.9
CFC 30 (A)	7.62	0.02	0.2
CFC 30 (B)	7.62	0.07	0.9
CFC 40 (A)	6.73	0.02	0.1
CFC 40 (B)	6.73	0.16	2.3

Table G.4: Impact of the bending moments on the stress level for the drying creep specimens.

	σ [MPa]	Δσ [MPa]	Δσ [%]
RC I (A)	8.12	0.06	0.7
RC I (B)	8.12	0.01	0.2
RC II (A)	6.36	0.09	1.5
RC II (B)	6.36	0.09	1.4
CFC 30 (A)	7.62	0.06	0.8
CFC 30 (B)	7.62	0.17	2.2
CFC 40 (A)	6.73	0.1	1.5

Bibliography

[1] Abdalhmid, J. M., Ashour, A. F., and Sheehan, T. Long-term drying shrinkage of self-compacting concrete: experimental and analytical investigations. *Construction and Building Materials 202* (2019), 825–837.

[2] Achour, R., Zentar, R., Abriak, N.-E., Rivard, P., and Gregoire, P. Durability study of concrete incorporating dredged sediments. *Case Studies in Construction Materials 11* (2019), e00244.

[3] Agostini, F., Skoczylas, F., and Lafhaj, Z. About a possible valorisation in cementitious materials of polluted sediments after treatment. *Cement and Concrete Composites 29*, 4 (2007), 270–278.

[4] Aili, A., Vandamme, M., Torrenti, J.-M., and Masson, B. Is long-term autogenous shrinkage a creep phenomenon induced by capillary effects due to self-desiccation? *Cement and Concrete Research 108* (2018), 186–200.

[5] Akkaya, Y., Ouyang, C., and Shah, S. P. Effect of supplementary cementitious materials on shrinkage and crack development in concrete. *Cement and Concrete Composites 29*, 2 (2007), 117–123.

[6] Aligizaki, K. K. *Pore structure of cement-based materials: testing, interpretation and requirements.* CRC Press, 2005.

[7] American Concrete Insitutute (A.C.I.). Guide for modeling and calculation shrinkage in hardened concrete, 2008.

[8] Antoni, M., Rossen, J., Martirena, F., and Scrivener, K. Cement substitution by a combination of metakaolin and limestone. *Cement and Concrete Research 42*, 12 (2012), 1579–1589.

[9] Aouad, G., Laboudigue, A., Gineys, N., and Abriak, N. Dredged sediments used as novel supply of raw material to produce Portland cement clinker. *Cement and Concrete Composites 34*, 6 (2012), 788–793.

[10] Asselin, A. Early-age cracking in massive concrete structures: sensitivity analysis and parameters identification. Tech. rep., École Normale Supérieure Paris-Saclay, 2017-2018.

[11] ASTM International. C1218/C1218M Standard test method for water-soluble chloride in mortar and concrete, 2008.

[12] ASTM International. C1698-09 Standard test method for autogenous strain of cement paste and mortar, 2014.

[13] ASTM International. C512/C512M-15 Standard test method for creep of concrete in compression, 2015.

[14] ASTM International. C1608-17 Standard test method for chemical shrinkage of hydraulic cement paste, 2017.

[15] Bažant, Z. P. Prediction of concrete creep and shrinkage: past, present and future. *Nuclear Engineering and Design 203*, 1 (2001), 27–38.

[16] Bažant, Z. P., and Chern, J. Concrete creep at variable humidity: constitutive law and mechanism. *Materials and Structures 18*, 1 (1985), 1.

[17] Bažant, Z. P., Hauggaard, A. B., Baweja, S., and Ulm, F.-J. Microprestress-solidification theory for concrete creep. I: Aging and drying effects. *Journal of Engineering Mechanics 123*, 11 (1997), 1188–1194.

[18] Bažant, Z. P., Jirásek, M., Hubler, M., and Carol, I. RILEM draft recommendation: TC-242-MDC multi-decade creep and shrinkage of concrete: material model and structural analysis. Model B4 for creep, drying shrinkage and autogenous shrinkage of normal and high-strength concretes with multi-decade applicability. *Materials and Structures 48*, 4 (2015), 753–770.

[19] Bažant, Z. P., and Yunping, X. Drying creep of concrete: constitutive model and new experiments separating its mechanisms. *Materials and Structures 27*, 1 (1994), 3–14.

[20] Baquerizo, L. G., Matschei, T., Scrivener, K. L., Saeidpour, M., and Wadsö, L. Hydration states of afm cement phases. *Cement and Concrete Research 73* (2015), 143–157.

[21] Barcelo, L., Moranville, M., and Clavaud, B. Autogenous shrinkage of concrete: a balance between autogenous swelling and self-desiccation. *Cement and Concrete Research 35*, 1 (2005), 177–183.

[22] Baroghel-Bouny, V., Mounanga, P., Khelidj, A., Loukili, A., and Rafaï, N. Autogenous deformations of cement pastes: part II. W/C effects, micro–macro correlations, and threshold values. *Cement and Concrete Research 36*, 1 (2006), 123–136.

[23] Beckstrom, B. D., Leavitt, D. R., Mensinger, M. C., Peck, E., and Stern, E. A. Thermal treatment for reclamation and beneficial use of contaminated sediments. In *Proceedings of the 33rd International Conference on Thermal Treatment Technologies & Hazardous Waste Combustors (2014)*, pp. 1–14.

[24] Belgische BetonGroepering. *Betontechnologie*. Brussel, 2009.

[25] Benboudjema, F. Presentation at the COST action TU1404 Training School on Modelling of cement-based materials and structures at early age - Module 5: Modelling of creep. 2017.

[26] Benboudjema, F., Meftah, F., and Torrenti, J.-M. Interaction between drying, shrinkage, creep and cracking phenomena in concrete. *Engineering Structures 27*, 2 (2005), 239–250.

[27] Benboudjema, F., and Torrenti, J.-M. Early-age behaviour of concrete nuclear containments. *Nuclear Engineering and Design 238*, 10 (2008), 2495–2506.

[28] Bendimerad, A. Z., Roziere, E., and Loukili, A. Plastic shrinkage and cracking risk of recycled aggregates concrete. *Construction and Building Materials 121* (2016), 733–745.

[29] Bentz, D. P., Garboczi, E. J., and Quenard, D. A. Modelling drying shrinkage in reconstructed porous materials: application to porous vycor glass. *Modelling and Simulation in Materials Science and Engineering 6*, 3 (1998), 211.

[30] Berndt, M. Properties of sustainable concrete containing fly ash, slag and recycled concrete aggregate. *Construction and Building Materials 23*, 7 (2009), 2606–2613.

[31] Berodier, E., and Scrivener, K. Evolution of pore structure in blended systems. *Cement and Concrete Research 73* (2015), 25–35.

[32] Bhalla, N., Sharma, S., Sharma, S., and Siddique, R. Monitoring early-age setting of silica fume concrete using wave propagation techniques. *Construction and Building Materials 162* (2018), 802–815.

[33] Bisschop, J. *Drying Shrinkage Microcracking in Cement-based Materials*. PhD thesis, 2002.

[34] Bizzozero, J. *Hydration and dimensional stability of calcium aluminate cement based systems*. PhD thesis, 2014.

[35] Bizzozero, J., Gosselin, C., and Scrivener, K. L. Expansion mechanisms in calcium aluminate and sulfoaluminate systems with calcium sulfate. *Cement and Concrete Research 56* (2014), 190–202.

[36] Bouasker, M., Khalifa, N. E. H., Mounanga, P., and Kahla, N. B. Early-age deformation and autogenous cracking risk of slag–limestone filler-cement blended binders. *Construction and Building Materials 55* (2014), 158–167.

[37] Bouasker, M., Mounanga, P., Turcry, P., Loukili, A., and Khelidj, A. Chemical shrinkage of cement pastes and mortars at very early age: Effect of limestone filler and granular inclusions. *Cement & Concrete Composites 30*, 1 (2008), 13–22.

[38] Bouhamou, N.-E., Mostefa, F., Mebrouki, A., Bendani, K., and Belas, N. Influence of dredged sediment on the shrinkage behavior of self-compacting concrete. *Materiali in Tehnologije 50*, 1 (2016), 127–135.

[39] Boulay, C. Test rig for early age measurements of the autogenous shrinkage of a concrete. In *Proceedings of the RILEM-JCI International Workshop ConCrack 3 (2012)*, pp. 111 – 122.

[40] Briffaut, M., Benboudjema, F., Torrenti, J.-M., and Nahas, G. Concrete early age basic creep: Experiments and test of rheological modelling approaches. *Construction and Building Materials 36* (2012), 373–380.

[41] Briffaut, M., Benboudjema, F., Torrenti, J.-M., and Nahas, G. Effects of early-age thermal behaviour on damage risks in massive concrete structures. *European Journal of Environmental and Civil Engineering 16*, 5 (2012), 589–605.

[42] Brooks, J. J. How admixtures affect shrinkage and creep. *Concrete International 21*, 4 (1999), 35–38.

[43] Brooks, J. J., and Johari, M. A. M. Effect of metakaolin on creep and shrinkage of concrete. *Cement & Concrete Composites 23*, 6 (2001), 495–502.

[44] Bullard, J. W., Jennings, H. M., Livingston, R. A., Nonat, A., Scherer, G. W., Schweitzer, J. S., Scrivener, K. L., and Thomas, J. J. Mechanisms of cement hydration. *Cement and Concrete Research 41*, 12 (2011), 1208–1223.

[45] Burgos-Montes, O., Palacios, M., Rivilla, P., and Puertas, F. Compatibility between superplasticizer admixtures and cements with mineral additions. *Construction and Building Materials 31* (2012), 300–309.

[46] Carette, J. *Towards Early Age Characterization of Eco-Concrete containing blast-furnace slag and limestone filler*. PhD thesis, 2015.

[47] Carette, J., Joseph, S., Cizer, O., and Staquet, S. Decoupling the autogenous swelling from the self-desiccation deformation in early age concrete with mineral additions: micro-macro observations and unified modelling. *Cement and Concrete Composites* (2017).

[48] Carette, J., and Staquet, S. Multi-physical description of the autogenous deformations of concrete with blast-furnace slag. In *Proceedings of the 2nd International RILEM/COST Conference on Early Age Cracking and Serviceability in Cement-based Materials and Structures (2017)*, S. Staquet and D. Aggelis, Eds., vol. 1, pp. 265–270.

[49] Carette, J., and Staquet, S. Monitoring the setting process of mortars by ultrasonic P and S-wave transmission velocity measurement. *Construction and Building Materials 94* (2015), 196–208.

[50] Carette, J., and Staquet, S. Monitoring the setting process of eco-binders by ultrasonic P-wave and S-wave transmission velocity measurement: mortar vs concrete. *Construction and Building Materials 110* (2016), 32–41.

[51] Carette, J., and Staquet, S. Unified modelling of the temperature effect on the autogenous deformations of cement-based materials. *Cement and Concrete Composites 94* (2018), 62–71.

[52] Cervera, M., Oliver, J., and Prato, T. Thermo-chemo-mechanical model for concrete. I: Hydration and aging. *Journal of Engineering Mechanics 125*, 9 (1999), 1018–1027.

[53] Chen, H.-J., Yang, M.-D., Tang, C.-W., and Wang, S.-Y. Producing synthetic lightweight aggregates from reservoir sediments. *Construction and Building Materials 28*, 1 (2012), 387–394.

[54] Chen, W., Li, Y., Shen, P., and Shui, Z. Microstructural development of hydrating Portland cement paste at early ages investigated with non-destructive methods and numerical simulation. *Journal of Nondestructive Evaluation 32*, 3 (2013), 228–237.

[55] Chikouche, M. A., Ghorbel, E., and Bibi, M. The possibility of using dredging sludge in manufacturing cements: optimization of heat treatment cycle and ratio replacement. *Construction and Building Materials 106* (2016), 330–341.

[56] Coussy, O. *Poromechanics*. John Wiley & Sons, 2004.

[57] Coussy, O., Dangla, P., Lassabatère, T., and Baroghel-Bouny, V. The equivalent pore pressure and the swelling and shrinkage of cement-based materials. *Materials and Structures 37*, 1 (2004), 15–20.

[58] Craeye, B., De Schutter, G., Desmet, B., Vantomme, J., Heirman, G., Vandewalle, L., Cizer, O., Aggoun, S., and Kadri, E. Effect of mineral filler type on autogenous shrinkage of self-compacting concrete. *Cement and Concrete Research 40*, 6 (2010), 908–913.

[59] Dang, T. A., Kamali-Bernard, S., and Prince, W. A. Design of new blended cement based on marine dredged sediment. *Construction and Building Materials 41* (2013), 602–611.

[60] Darquennes, A., and Benboudjema, F. Behavior of activated ternary binders under autogenous condition. In *Proceedings of the ACI Symposium (2018)*, vol. 326, pp. 22.1–22.10.

[61] Darquennes, A., Staquet, S., Delplancke-Ogletree, M.-P., and Espion, B. Effect of autogenous deformation on the cracking risk of slag cement concretes. *Cement and Concrete Composites 33*, 3 (2011), 368–379.

[62] Darquennes, A., Staquet, S., and Espion, B. Shrinkage of slag cement concrete in free and restrained conditions. In *Proceedings of the International RILEM Conference on Volume Changes of Hardening Concrete: Testing and Mitigation (2006)*, RILEM Publications SARL, pp. 165–174.

[63] De Schutter, G. Degree of hydration based kelvin model for the basic creep of early age concrete. *Materials and Structures 32*, 4 (1999), 260.

[64] De Weerdt, K., Haha, M. B., Le Saout, G., Kjellsen, K. O., Justnes, H., and Lothenbach, B. Hydration mechanisms of ternary Portland cements containing limestone powder and fly ash. *Cement and Concrete Research 41*, 3 (2011), 279–291.

[65] Delsaute, B., Torrenti, J. M., and Staquet, S. Modeling basic creep of concrete since setting time. *Cement and Concrete Composites 83* (2017), 239–250.

[66] Departement Mobiliteit en Openbare Werken (MOW), Vlaamse Overheid. Amoras. Retrieved from http://www.maritiemetoegang.be/projecten/amoras (2019, November 29).

[67] Deschner, F., Winnefeld, F., Lothenbach, B., Seufert, S., Schwesig, P., Dittrich, S., Goetz-Neunhoeffer, F., and Neubauer, J. Hydration of Portland cement with high replacement by siliceous fly ash. *Cement and Concrete Research 42*, 10 (2012), 1389–1400.

[68] Desmet, B., Atitung, K. C., Sanchez, M. A. A., Vantomme, J., Feys, D., Robeyst, N., Audenaert, K., De Schutter, G., Boel, V., and Heirman, G. Monitoring the early-age hydration of self-compacting concrete using ultrasonic P-wave transmission and isothermal calorimetry. *Materials and Structures 44*, 8 (2011), 1537–1558.

[69] Di Bella, C., Wyrzykowski, M., and Lura, P. Evaluation of the ultimate drying shrinkage of cement-based mortars with poroelastic models. *Materials and Structures 50*, 1 (2017), 52.

[70] Duan, P., Shui, Z., Chen, W., and Shen, C. Effects of metakaolin, silica fume and slag on pore structure, interfacial transition zone and compressive strength of concrete. *Construction and Building Materials 44* (2013), 1–6.

[71] Esping, O. Effect of limestone filler BET (H_2O)-area on the fresh and hardened properties of self-compacting concrete. *Cement and Concrete Research 38*, 7 (2008), 938–944.

[72] European Committee for standardization. B 15-229 Concrete testing - Non-destructive testing - Measurement of sound velocity, 1991.

[73] European Committee for standardization. EN 197-1 Cement - Part 1: Composition, specifications and conformity criteria for common cements, 2000.

[74] European Committee for standardization. EN 206-1 Concrete - Part 1: Specification, performance, production and conformity, 2000.

[75] European Committee for standardization. EN 1990 (Eurocode): Basis of structural design, 2002.

[76] European Committee for standardization. EN 12504-4 Testing concrete - Part 4: Determination of ultrasonic pulse velocity, 2004.

[77] European Committee for standardization. EN 1992-1-1 (Eurocode 2): Design of concrete structures - Part 1-1: General rules and rules for buildings, 2005.

[78] European Committee for standardization. EN 934-2 Admixtures for concrete, mortar and grout - Part 2: Concrete admixtures - definitions, requirements, conformity, marking and labelling, 2009.

[79] European Committee for standardization. EN 12390-6 Testing hardened concrete - Part 6: Tensile splitting strength of test specimens, 2010.

[80] European Committee for standardization. EN 196-6 methods of testing cement- part 6: Determination of fineness, 2010.

[81] European Committee for standardization. EN 933-1 Tests for geometrical properties of aggregates - Part 1: Determination of particle size distribution - sieving method, 2012.

[82] European Committee for standardization. EN 1097-6 Tests for mechanical and physical performance of aggregates - Part 6: Determination of particle density and water absorption, 2013.

[83] European Committee for standardization. EN 12620 aggregates for concrete, 2013.

[84] European Committee for standardization. EN 196-2 Method of testing cement - Part 2 : Chemical analysis of cement, 2013.

[85] European Committee for standardization. EN 12390-13 Testing hardened concrete - Part 13: Determination of secant modulus of elasticity in compression, 2014.

[86] European Committee for standardization. EN 196-1 Methods of testing cement - Part 1: Determination of strength, 2016.

[87] European Committee for standardization. EN 196-3 Methods of testing cement - Part 3: Determination of setting times and soundness, 2016.

[88] European Committee for standardization. EN 12350-2 Testing fresh concrete - Part 2: Slump test, 2019.

[89] European Committee for standardization. EN 12350-5 Testing fresh concrete - Part 5: Flow table test, 2019.

[90] European Committee for standardization. EN 12350-6 Testing fresh concrete - Part 6: Density, 2019.

[91] European Committee for standardization. EN 12350-7 Testing fresh concrete - Part 7: Air content - Pressure methods, 2019.

[92] European Committee for standardization. EN 12390-3 Testing hardened concrete - Part 3: Compressive strength of test specimens, 2019.

[93] European Committee for standardization. EN 12390-5 Testing hardened concrete - Part 5: Flexural strength of test specimens, 2019.

[94] European Committee for standardization. EN 12390-7 Testing hardened concrete - Part 7: Density strength of test specimens, 2019.

[95] Fairbairn, E. M., and Azenha, M. *Thermal Cracking of Massive Concrete Structures: State of the Art Report of the RILEM Technical Committee 254-CMS*. Springer, 2018.

[96] Faure, A. *Capacité d'un sédiment à se substituer à la fraction argileuse de la matière première de l'industrie des liants hydrauliques*. PhD thesis, 2017.

[97] Faure, A., Smith, A., Coudray, C., Anger, B., Colina, H., Moulin, I., and Thery, F. Ability of two dam fine-grained sediments to be used in cement industry as raw material for clinker Production and as pozzolanic additional constituent of portland-composite cement. *Waste and Biomass Valorization 8*, 6 (2017), 2141–2163.

[98] Flatt, R. J., Roussel, N., and Cheeseman, C. R. Concrete: an eco material that needs to be improved. *Journal of the European Ceramic Society 32*, 11 (2012), 2787–2798.

[99] Flatt, R. J., and Scherer, G. W. Thermodynamics of crystallization stresses in DEF. *Cement and Concrete Research 38*, 3 (2008), 325–336.

[100] Fontana, P., and Meng, B. Influence of mix composition on early-age autogenous deformations of cement pastes. In *Proceedings of the International RILEM Conference on Volume Changes of Hardening Concrete: Testing and Mitigation (2006)*, pp. 261–272.

[101] Gamble, B., and Parrott, L. Creep of concrete in compression during drying and wetting. *Magazine of Concrete Research 30*, 104 (1978), 129–138.

[102] Gardner, N., and Lockman, M. Design provisions for drying shrinkage and creep of normal-strength concrete. *Materials Journal 98*, 2 (2001), 159–167.

[103] Gawin, D., Pesavento, F., and Schrefler, B. A. Hygro-thermo-chemo-mechanical modelling of concrete at early ages and beyond. Part I: hydration and hygro-thermal phenomena. *International Journal for Numerical Methods in Engineering 67*, 3 (2006), 299–331.

[104] Gawin, D., Pesavento, F., and Schrefler, B. A. Hygro-thermo-chemo-mechanical modelling of concrete at early ages and beyond. Part II: shrinkage and creep of concrete. *International Journal for Numerical Methods in Engineering 67*, 3 (2006), 332–363.

[105] Ge, Z., Wang, K., Sandberg, P. J., and Ruiz, J. M. Characterization and performance prediction of cement-based materials using a simple isothermal calorimeter. *Journal of Advanced Concrete Technology 7*, 3 (2009), 355–366.

[106] Gedam, B. A., Bhandari, N., and Upadhyay, A. Influence of supplementary cementitious materials on shrinkage, creep, and durability of high-performance concrete. *Journal of Materials in Civil Engineering* (2015), 04015173.

[107] Gilbert, R. *Time effects in concrete structures.* Elsevier Science Publishers, New York, 1988.

[108] Gleize, P. J., Cyr, M., and Escadeillas, G. Effects of metakaolin on autogenous shrinkage of cement pastes. *Cement and Concrete Composites 29*, 2 (2007), 80–87.

[109] Gonçalves, J., Tavares, L., Toledo Filho, R. D., and Fairbairn, E. Performance evaluation of cement mortars modified with metakaolin or ground brick. *Construction and Building Materials 23*, 5 (2009), 1971–1979.

[110] Gonçalves, M. C., and Margarido, F. *Materials for Construction and Civil Engineering.* Springer, 2015.

[111] Granger, L. *Comportement différé du béton dans les enceintes de centrales nucléaires: analyse et modélisation.* PhD thesis, 1995.

[112] Grasley, Z. C., and Leung, C. K. Desiccation shrinkage of cementitious materials as an aging, poroviscoelastic response. *Cement and Concrete Research 41*, 1 (2011), 77–89.

[113] Grasley, Z. C., Scherer, G. W., Lange, D. A., and Valenza, J. J. Dynamic pressurization method for measuring permeability and modulus: II. cementitious materials. *Materials and Structures 40*, 7 (2007), 711–721.

[114] Grosse, C. Ultrasound through-transmission techniques for quality control of fresh concrete. In *Proceedings of the Conference on Advanced testing of fresh cementitious materials (2008)*, pp. 83–93.

[115] Güneyisi, E., Gesoğlu, M., and Mermerdaş, K. Improving strength, drying shrinkage, and pore structure of concrete using metakaolin. *Materials and Structures 41*, 5 (2008), 937–949.

[116] Hamer, K., and Karius, V. Brick production with dredged harbour sediments. An industrial-scale experiment. *Waste Management 22*, 5 (2002), 521–530.

[117] Hansen, W. Drying shrinkage mechanisms in Portland cement paste. *Journal of the American Ceramic Society 70*, 5 (1987), 323–328.

[118] Hauggaard, A. B., Damkilde, L., and Hansen, P. F. Transitional thermal creep of early age concrete. *Journal of Engineering Mechanics 125*, 4 (1999), 458–465.

[119] Havlásek, P., and Jirásek, M. Multiscale modeling of drying shrinkage and creep of concrete. *Cement and Concrete Research 85* (2016), 55–74.

[120] Heirman, G., Vandewalle, L., Van Gemert, D., Boel, V., Audenaert, K., De Schutter, G., Desmet, B., and Vantomme, J. Time-dependent deformations of limestone powder type self-compacting concrete. *Engineering Structures 30*, 10 (2008), 2945–2956.

[121] Hewlett, P. *Lea's chemistry of cement and concrete*. Elsevier, 2003.

[122] Hilaire, A. *Etude des déformations différées des bétons en compression et en traction, du jeune au long terme: application aux enceintes de confinement*. PhD thesis, 2014.

[123] Holt, E. E. *Early age autogenous shrinkage of concrete*. Technical Research Centre of Finland (VTT), 2001.

[124] Hu, X., Shi, C., Shi, Z., Tong, B., and Wang, D. Early age shrinkage and heat of hydration of cement-fly ash-slag ternary blends. *Construction and Building Materials 153* (2017), 857–865.

[125] Hu, Z., Wyrzykowski, M., Scrivener, K., and Lura, P. Prediction of autogenous shrinkage of cement pastes as poro-visco-elastic deformation. *Cement and Concrete Research 126* (2019), 105917.

[126] Hua, C., Acker, P., and Ehrlacher, A. Analyses and models of the autogenous shrinkage of hardening cement paste: I. modelling at macroscopic scale. *Cement and Concrete Research 25*, 7 (1995), 1457–1468.

[127] Huang, H., and Ye, G. Examining the "time-zero" of autogenous shrinkage in high/ultra-high performance cement pastes. *Cement and Concrete Research 97* (2017), 107–114.

[128] Imbabi, M. S., Carrigan, C., and McKenna, S. Trends and developments in green cement and concrete technology. *International Journal of Sustainable Built Environment 1*, 2 (2012), 194–216.

[129] International Federation for Structural Concrete (fib). Model Code 2010, 2010.

[130] Japan Society of Civil Engineers (JSCE). JSCE Guidelines for concrete, standard specifications for concrete structures - 2007 "Design", 2010.

[131] Jensen, O. M. Influence of cement composition on autogenous deformation and change of the relative humidity. *Proc. Shrinkage* (2000), 143–153.

[132] Jensen, O. M., and Hansen, P. F. Autogenous deformation and RH-change in perspective. *Cement and Concrete Research 31*, 12 (2001), 1859–1865.

[133] Jensen, O. M., and Hansen, P. F. Water-entrained cement-based materials: I. principles and theoretical background. *Cement and Concrete Research 31*, 4 (2001), 647–654.

[134] Jiang, C., Yang, Y., Wang, Y., Zhou, Y., and Ma, C. Autogenous shrinkage of high performance concrete containing mineral admixtures under different curing temperatures. *Construction and Building materials 61* (2014), 260–269.

[135] Jonckheere, E. AMORAS stelt toekomst Antwerpse haven veilig. *Engineeringnet.be 105* (2012), 2–4.

[136] Juenger, M. C., and Siddique, R. Recent advances in understanding the role of supplementary cementitious materials in concrete. *Cement and Concrete Research 78* (2015), 71–80.

[137] Juenger, M. C. G., Snellings, R., and Bernal, S. A. Supplementary cementitious materials: new sources, characterization, and performance insights. *Cement and Concrete Research 122* (2019), 257–273.

[138] Juilland, P., Gallucci, E., Flatt, R., and Scrivener, K. Dissolution theory applied to the induction period in alite hydration. *Cement and Concrete Research 40*, 6 (2010), 831–844.

[139] Kanstad, T., Hammer, T. A., Bjøntegaard, Ø., and Sellevold, E. J. Mechanical properties of young concrete: Part II: Determination of model parameters and test program proposals. *Materials and Structures 36*, 4 (2003), 226–230.

[140] Keating, J., Hannant, D., and Hibbert, A. Comparison of shear modulus and pulse velocity techniques to measure the build-up of structure in fresh cement pastes used in oil well cementing. *Cement and Concrete Research 19*, 4 (1989), 554–566.

[141] Khatri, R. P., Sirivivatnanon, V., and Gross, W. Effect of different supplementary cementitious materials on mechanical properties of high performance concrete. *Cement and Concrete Research 25*, 1 (1995), 209–220.

[142] Klemczak, B., Batog, M., and Pilch, M. Assessment of concrete strength development models with regard to concretes with low clinker cements. *Archives of Civil and Mechanical Engineering 16*, 2 (2016), 235–247.

[143] Klemczak, B., and Żmij, A. Reliability of standard methods for evaluating the early-age cracking risk of thermal-shrinkage origin in concrete walls. *Construction and Building Materials 226* (2019), 651–661.

[144] Kmack, R. M., Kurtis, K. E., Jacobs, L. J., and Kim, J.-Y. Assessment of air entrainment in fresh cement paste using ultrasonic nondestructive testing. *Journal of ASTM International 7*, 1 (2009), 1–18.

[145] Kovler, K., and Zhutovsky, S. Overview and future trends of shrinkage research. *Materials and Structures 39*, 9 (2006), 827–847.

[146] Lafhaj, Z., Samara, M., Agostini, F., Boucard, L., Skoczylas, F., and Depelsenaire, G. Polluted river sediments from the north region of france: Treatment with novosol® process and valorization in clay bricks. *Construction and Building Materials 22*, 5 (2008), 755–762.

[147] Lee, K., Lee, H., Lee, S., and Kim, G. Autogenous shrinkage of concrete containing granulated blast-furnace slag. *Cement and Concrete Research 36*, 7 (2006), 1279–1285.

[148] Li, J., and Yao, Y. A study on creep and drying shrinkage of high performance concrete. *Cement and Concrete Research 31*, 8 (2001), 1203–1206.

[149] Li, Z. Drying shrinkage prediction of paste containing meta-kaolin and ultrafine fly ash for developing ultra-high performance concrete. *Materials Today Communications 6* (2016), 74–80.

[150] Liu, Z., and Hansen, W. Aggregate and slag cement effects on autogenous shrinkage in cementitious materials. *Construction and Building Materials 121* (2016), 429–436.

[151] Lothenbach, B., Le Saout, G., Gallucci, E., and Scrivener, K. Influence of limestone on the hydration of Portland cements. *Cement and Concrete Research 38*, 6 (2008), 848–860.

[152] Lothenbach, B., Scrivener, K., and Hooton, R. Supplementary cementitious materials. *Cement and Concrete Research 41*, 12 (2011), 1244–1256.

[153] Lura, P., Jensen, O. M., and van Breugel, K. Autogenous shrinkage in high-performance cement paste: an evaluation of basic mechanisms. *Cement and Concrete Research 33*, 2 (2003), 223–232.

[154] Lura, P., van Breugel, K., and Maruyama, I. Effect of curing temperature and type of cement on early-age shrinkage of high-performance concrete. *Cement and Concrete Research 31*, 12 (2001), 1867–1872.

[155] Mailvaganam, N. P., Rixom, M., Manson, D. P., and Gonzales, C. *Chemical admixtures for concrete*. CRC Press, 1999.

[156] Martin, L. H. J., Winnefeld, F., Tschopp, E., Müller, C. J., and Lothenbach, B. Influence of fly ash on the hydration of calcium sulfoaluminate cement. *Cement and Concrete Research 95* (2017), 152–163.

[157] Maruyama, I. Origin of drying shrinkage of hardened cement paste: hydration pressure. *Journal of Advanced Concrete Technology 8*, 2 (2010), 187–200.

[158] Matschei, T., Lothenbach, B., and Glasser, F. P. The AFm phase in Portland cement. *Cement and Concrete Research 37*, 2 (2007), 118–130.

[159] Mazloom, M., Ramezanianpour, A. A., and Brooks, J. J. Effect of silica fume on mechanical properties of high-strength concrete. *Cement and Concrete Composites 26*, 4 (2004), 347–357.

[160] Mechtcherine, V.; Dudziak, L. *Effects of Superabsorbent Polymers on Shrinkage of Concrete: Plastic, Autogenous, Drying*. Springer, 2012.

[161] Mermerdaş, K., and Arbili, M. M. Explicit formulation of drying and autogenous shrinkage of concretes with binary and ternary blends of

silica fume and fly ash. *Construction and Building Materials 94* (2015), 371–379.

[162] Meyer, P. S., Yung, J. W., and Ausubel, J. H. A primer on logistic growth and substitution: the mathematics of the loglet lab software. *Technological Forecasting and Social Change 61*, 3 (1999), 247–271.

[163] Mohamed, M. S., Carette, J., Delsaute, B., and Staquet, S. Applicability of ultrasonic measurement on the monitoring of the setting of cement pastes: effect of water content and mineral additions. *Advances in Civil Engineering Materials 6*, 2 (2017), 84–99.

[164] Mokarem, D. W., Weyers, R. E., and Lane, D. S. Development of a shrinkage performance specifications and prediction model analysis for supplemental cementitious material concrete mixtures. *Cement and Concrete Research 35*, 5 (2005), 918–925.

[165] Mounanga, P., Bouasker, M., Pertue, A., Perronnet, A., and Khelidj, A. Early-age autogenous cracking of cementitious matrices: physico-chemical analysis and micro/macro investigations. *Materials and Structures 44*, 4 (2011), 749–772.

[166] Neville, A. *Properties of Concrete*. Pearson Education, Essex, 2012.

[167] Olivier, K. *Etude expérimentale et modélisation de l'auto-cicatrisation des matériaux cimentaires avec additions minérales*. PhD thesis, 2016.

[168] Paris, J. M., Roessler, J. G., Ferraro, C. C., DeFord, H. D., and Townsend, T. G. A review of waste products utilized as supplements to Portland cement in concrete. *Journal of Cleaner Production 121* (2016), 1–18.

[169] Poon, C.-S., Kou, S., and Lam, L. Compressive strength, chloride diffusivity and pore structure of high performance metakaolin and silica fume concrete. *Construction and Building Materials 20*, 10 (2006), 858–865.

[170] Puertas, F., Santos, H., Palacios, M., and Martínez-Ramírez, S. Polycarboxylate superplasticiser admixtures: effect on hydration, microstructure and rheological behaviour in cement pastes. *Advances in Cement Research 17*, 2 (2005), 77–89.

[171] Qian, X., and Li, Z. The relationships between stress and strain for high-performance concrete with metakaolin. *Cement and Concrete Research 31*, 11 (2001), 1607–1611.

[172] Ramachandran, V. S. *Concrete admixtures handbook: properties, science and technology*. William Andrew, 1996.

[173] Rao, G. A. Long-term drying shrinkage of mortar — influence of silica fume and size of fine aggregate. *Cement and Concrete Research 31*, 2 (2001), 171–175.

[174] Reinhardt, H., and Grosse, C. Continuous monitoring of setting and hardening of mortar and concrete. *Construction and Building Materials 18*, 3 (2004), 145–154.

[175] Richardson, I. The calcium silicate hydrates. *Cement and Concrete Research 38*, 2 (2008), 137–158.

[176] Rifai, F. *Immobilisation de déchets magnésiens dans un matériau alcali-activé: étude expérimentale et numérique*. PhD thesis, 2017.

[177] Rizwan, S. A., and Bier, T. A. Early volume changes of high performance self-compacting cementitious systems containing pozzolanic powders. In *Proceedings of the International RILEM Conference on Volume Changes of Hardening Concrete: Testing and Mitigation (2006)*, RILEM Publications SARL, pp. 283–292.

[178] Robeyst, N., Gruyaert, E., and De Belie, N. Ultrasonic monitoring of setting and hardening behaviour of concrete and mortar with blast furnace slag cement. In *Proceedings of the 12th International congress on the Chemistry of Cement (2007)*.

[179] Robeyst, N., Gruyaert, E., Grosse, C. U., and De Belie, N. Monitoring the setting of concrete containing blast-furnace slag by measuring the ultrasonic P-wave velocity. *Cement and Concrete Research 38*, 10 (2008), 1169–1176.

[180] Rougelot, T., Skoczylas, F., and Burlion, N. Water desorption and shrinkage in mortars and cement pastes: experimental study and poromechanical model. *Cement and Concrete Research 39*, 1 (2009), 36–44.

[181] Rozas, F., Castillo, A., Martínez, I., and Castellote, M. Guidelines for assessing the valorization of a waste into cementitious material: dredged sediment for production of self compacting concrete. *Materiales de Construcción 65*, 319 (2015), 057.

[182] Sabir, B. B., Wild, S., and Bai, J. Metakaolin and calcined clays as pozzolans for concrete: a review. *Cement & Concrete Composites 23*, 6 (2001), 441–454.

[183] Saha, A. K. Effect of class F fly ash on the durability properties of concrete. *Sustainable Environment Research 28*, 1 (2018), 25–31.

[184] Samara, M., Lafhaj, Z., and Chapiseau, C. Valorization of stabilized river sediments in fired clay bricks: factory scale experiment. *Journal of Hazardous Materials 163*, 2 (2009), 701–710.

[185] Samouh, H., Rozière, E., and Loukili, A. Influence of specimen size and measurements duration on the long-term extrapolation of drying shrinkage. *Construction and Building Materials 150* (2017), 276–286.

[186] Sant, G., Lura, P., and Weiss, J. Measurement of volume change in cementitious materials at early ages: review of testing protocols and interpretation of results. *Transportation Research Record: Journal of the Transportation Research Board*, 1979 (2006), 21–29.

[187] Sayers, C., and Grenfell, R. Ultrasonic propagation through hydrating cements. *Ultrasonics 31*, 3 (1993), 147–153.

[188] Schindler, A. K. Prediction of concrete setting. In *Proceedings of the RILEM International Symposium on Advances in Concrete through Science and Engineering (2004)*, J. Weiss, K. Kovler, J. Marchand, and S. Mindess, Eds., RILEM Publications SARL.

[189] Schneider, M. The cement industry on the way to a low-carbon future. *Cement and Concrete Research 124* (2019), 105792.

[190] Schneider, M., Romer, M., Tschudin, M., and Bolio, H. Sustainable cement production - present and future. *Cement and Concrete Research 41*, 7 (2011), 642–650.

[191] Schöler, A. *Hydration of multi-component cements containing clinker, slag, type-V fly ash and limestone.* PhD thesis, 2016.

[192] Sciumè, G., Benboudjema, F., De Sa, C., Pesavento, F., Berthaud, Y., and Schrefler, B. A multiphysics model for concrete at early age applied to repairs problems. *Engineering Structures 57* (2013), 374–387.

[193] Scrivener, K., Snellings, R., and Lothenbach, B. *A practical guide to microstructural analysis of cementitious materials.* CRC Press, 2016.

[194] Scrivener, K. L. *The development of microstructure during the hydration of Portland cement.* PhD thesis, 1984.

[195] Scrivener, K. L., Crumbie, A. K., and Laugesen, P. The interfacial transition zone (ITZ) between cement paste and aggregate in concrete. *Interface Science 12*, 4 (2004), 411–421.

[196] Scrivener, K. L., John, V. M., and Gartner, E. M. Eco-efficient cements: Potential economically viable solutions for a low-CO_2 cement-based materials industry. *Cement and Concrete Research 114* (2018), 2–26.

[197] Scrivener, K. L., Lothenbach, B., De Belie, N., Gruyaert, E., Skibsted, J., Snellings, R., and Vollpracht, A. TC 238-SCM: hydration and microstructure of concrete with SCMs. *Materials and Structures 48*, 4 (2015), 835–862.

[198] Sellier, A., Multon, S., Buffo-Lacarrière, L., Vidal, T., Bourbon, X., and Camps, G. Concrete creep modelling for structural applications: non-linearity, multi-axiality, hydration, temperature and drying effects. *Cement and Concrete Research 79* (2016), 301–315.

[199] Shariq, M., Prasad, J., and Abbas, H. Creep and drying shrinkage of concrete containing GGBFS. *Cement and Concrete Composites 68* (2016), 35–45.

[200] Siddique, R., and Khan, M. I. *Supplementary cementing materials*. Springer Science & Business Media, 2011.

[201] Siham, K., Fabrice, B., Edine, A. N., and Patrick, D. Marine dredged sediments as new materials resource for road construction. *Waste Management 28*, 5 (2008), 919–928.

[202] Skibsted, J., and Snellings, R. Reactivity of supplementary cementitious materials (SCMs) in cement blends. *Cement and Concrete Research 124* (2019), 105799.

[203] Smerda, Z., and Kristek, V. *Creep and Shrinkage of Concrete Elements and Structures*. Elsevier, Amsterdam, 1988.

[204] Snellings, R. *Mineralogical study of the pozzolanic properties of natural zeolites*. PhD thesis, 2011.

[205] Snellings, R., Cizer, O., Horckmans, L., Durdziński, P. T., Dierckx, P., Nielsen, P., Van Balen, K., and Vandewalle, L. Properties and pozzolanic reactivity of flash calcined dredging sediments. *Applied Clay Science 129* (2016), 35–39.

[206] Snellings, R., Horckmans, L., Durdzinski, P., Van Bunderen, C., Vandewalle, L., Van Balen, K., Dockx, J., Vandekeybus, J., and Cizer, O. Calcined dredged sediments as supplementary cementitious materials: properties and pozzolanic reactivity. In *Proceedings of the International RILEM Conference on Materials, Systems and Structures in Civil Engineering (Segment on Concrete with Supplementary Cementitious Materials) (2016)*, O. M. Jensen, K. Kovler, and N. De Belie, Eds., pp. 205–212.

[207] Snellings, R., Horckmans, L., Van Bunderen, C., Vandewalle, L., and Cizer, O. Flash-calcined dredging sediment blended cements: effect on cement hydration and properties. *Materials and Structures 50*, 6 (2017), 241.

[208] Snellings, R., and Kamyab, H. Valorisatie van fijne slibfracties als cementtoeslagstof. Tech. rep., VITO, 2018.

[209] Snellings, R., Mertens, G., and Elsen, J. Supplementary cementitious materials. *Reviews in Mineralogy and Geochemistry 74*, 1 (2012), 211–278.

[210] Suntharalingam, S., and Takahashi, Y. Experimental study on autogenous shrinkage behaviors of different portland blast furnace slag cements. *Construction and Building Materials 230* (2020), 116980.

[211] Tangtermsirikul, S. Effect of chemical composition and particle size of fly ash on autogenous shrinkage of paste. In *Proceedings of the International Workshop on the Autogenous Shrinkage of Concrete (1999)*, E&FN Spon, pp. 175–185.

[212] Taylor, H. F. *Cement chemistry*. Thomas Telford, 1997.

[213] Tazawa, E.-i., and Miyazawa, S. Influence of cement and admixture on autogenous shrinkage of cement paste. *Cement and Concrete Research 25*, 2 (1995), 281–287.

[214] Teklay, A., Yin, C., Rosendahl, L., and Kohler, L. L. Experimental and modeling study of flash calcination of kaolinite rich clay particles in a gas suspension calciner. *Applied Clay Science 103* (2015), 10–19.

[215] Termkhajornkit, P., Nawa, T., Nakai, M., and Saito, T. Effect of fly ash on autogenous shrinkage. *Cement and Concrete Research 35*, 3 (2005), 473–482.

[216] Thomas, M. *Supplementary cementing materials in concrete*. CRC Press, 2013.

[217] Trtnik, G., and Turk, G. Influence of superplasticizers on the evolution of ultrasonic P-wave velocity through cement pastes at early age. *Cement and Concrete Research 51* (2013), 22–31.

[218] Trtnik, G., Turk, G., Kavcic, F., and Bosiljkov, V. B. Possibilities of using the ultrasonic wave transmission method to estimate initial setting time of cement paste. *Cement and Concrete Research 38*, 11 (2008), 1336–1342.

[219] Trtnik, G., Valic, M. I., Kavcic, F., and Turk, G. Comparison between two ultrasonic methods in their ability to monitor the setting process of cement pastes. *Cement and Concrete Research 39*, 10 (2009), 876–882.

[220] Ulm, F.-J., and Coussy, O. Couplings in early-age concrete: from material modeling to structural design. *International Journal of Solids and Structures 35*, 31 (1998), 4295–4311.

[221] United Nations. Bigger climate action emerging in cement industry (2019). Retrieved from https://unfccc.int/news/bigger-climate-action-emerging-in-cement-industry (2019, July 25).

[222] Van Bunderen, C. *Invloed van het gecombineerd gebruik van (super)plastificeerder en luchtbelvormer in wegenbeton op het korte termijngedrag.* MSc thesis, 2015.

[223] Van Bunderen, C., Snellings, R., Horckmans, L., Vandewalle, L., and Cizer, O. Mixture proportions of concrete with dredging sediments as novel SCM. In *Proceedings of the 10th ACI/RILEM International Conference on Cementitious Materials and Alternative Binders for Sustainable Concrete (2017)*, A. Tagnit-Hamou, Ed., vol. 1, pp. 27.1–27.10.

[224] Van Bunderen, C., Snellings, R., Vandewalle, L., and Cizer, O. Early-age hydration and autogenous deformation of cement paste containing flash calcined dredging sediments. *Construction and Building Materials 200* (2019), 104–115.

[225] Vandewalle, L. *Ontwerp van constructiecomponenten: beton deel 1.* CuDi VTK vzw, Heverlee, 2012.

[226] Vlahinić, I., Jennings, H. M., and Thomas, J. J. A constitutive model for drying of a partially saturated porous material. *Mechanics of Materials 41*, 3 (2009), 319–328.

[227] Wang, L., Yang, H. Q., Zhou, S. H., Chen, E., and Tang, S. W. Mechanical properties, long-term hydration heat, shinkage behavior and crack resistance of dam concrete designed with low heat portland (LHP) cement and fly ash. *Construction and Building Materials 187* (2018), 1073–1091.

[228] Wild, S., Khatib, J., and Roose, L. Chemical shrinkage and autogenous shrinkage of portland cement—metakaolin pastes. *Advances in Cement Research 10*, 3 (1998), 109–119.

[229] Wu, L., Farzadnia, N., Shi, C., Zhang, Z., and Wang, H. Autogenous shrinkage of high performance concrete: A review. *Construction and Building Materials 149* (2017), 62–75.

[230] Wyrzykowski, M., Di Bella, C., and Lura, P. Prediction of drying shrinkage of cement-based mortars with poroelastic approaches - a critical review. In *Proceedings of the 6th Biot Conference on Poromechanics (2017)*.

[231] Ye, H. Creep mechanisms of calcium–silicate–hydrate: an overview of recent advances and challenges. *International Journal of Concrete Structures and Materials 9*, 4 (2015), 453–462.

[232] Yu, C., Sun, W., and Scrivener, K. Mechanism of expansion of mortars immersed in sodium sulfate solutions. *Cement and Concrete Research 43* (2013), 105–111.

[233] Zentar, R., Dubois, V., and Abriak, N. E. Mechanical behaviour and environmental impacts of a test road built with marine dredged sediments. *Resources, Conservation and Recycling 52*, 6 (2008), 947–954.

[234] Zhang, J., Hou, D., and Chen, H. Experimental and theoretical studies on autogenous shrinkage of concrete at early ages. *Journal of Materials in Civil Engineering 23*, 3 (2011), 312–320.

[235] Zhang, J., Hou, D., and Gao, Y. Integrative studies on autogenous and drying shrinkages of concrete at early-age. *Advances in Structural Engineering 15*, 7 (2012), 1041–1051.

[236] Zhang, J., Qin, L., and Li, Z. Hydration monitoring of cement-based materials with resistivity and ultrasonic methods. *Materials and Structures 42*, 1 (2009), 15–24.

[237] Zhang, T., Gao, P., Luo, R., Guo, Y., Wei, J., and Yu, Q. Measurement of chemical shrinkage of cement paste: comparison study of ASTM C 1608 and an improved method. *Construction and Building Materials 48* (2013), 662–669.

[238] Zhang, W., Zhang, Y., Liu, L., Zhang, G., and Liu, Z. Investigation of the influence of curing temperature and silica fume content on setting and hardening process of the blended cement paste by an improved ultrasonic apparatus. *Construction and Building Materials 33* (2012), 32–40.

[239] Zhang, Y., and Kong, X. Correlations of the dispersing capability of NSF and PCE types of superplasticizer and their impacts on cement hydration with the adsorption in fresh cement pastes. *Cement and Concrete Research 69* (2015), 1–9.

[240] Zhang, Y., Zhang, W., She, W., Ma, L., and Zhu, W. Ultrasound monitoring of setting and hardening process of ultra-high performance cementitious materials. *NDT & E International 47* (2012), 177–184.

[241] Zhao, Z., Benzerzour, M., Abriak, N.-E., Damidot, D., Courard, L., and Wang, D. Use of uncontaminated marine sediments in mortar and concrete by partial substitution of cement. *Cement and Concrete Composites 93* (2018), 155–162.

[242] Zhu, J., Kee, S.-H., Han, D., and Tsai, Y.-T. Effects of air voids on ultrasonic wave propagation in early age cement pastes. *Cement and Concrete Research 41*, 8 (2011), 872–881.

[243] Zingg, A., Winnefeld, F., Holzer, L., Pakusch, J., Becker, S., Figi, R., and Gauckler, L. Interaction of polycarboxylate-based superplasticizers with cements containing different C_3A amounts. *Cement and Concrete Composites 31*, 3 (2009), 153–162.

[244] Zreiki, J., Bouchelaghem, F., and Chaouche, M. Early-age behaviour of concrete in massive structures, experimentation and modelling. *Nuclear Engineering and Design 240*, 10 (2010), 2643–2654.

Curriculum vitae

Céline Van Bunderen
° 30 December 1992, Sint-Niklaas (Belgium)

Education

2015-2020	PhD in Engineering Science, Civil Engineering KU Leuven, Leuven, Belgium
2013-2015	Master in Engineering Science, Civil Engineering KU Leuven, Leuven, Belgium
2010-2013	Bachelor in Engineering Science, Civil Engineering KU Leuven, Leuven, Belgium
2004-2010	High school, Latin-Mathematics Onze-Lieve-Vrouw-Presentatie, Sint-Niklaas, Belgium

Experience

2015-2020	PhD researcher KU Leuven, Leuven, Belgium *International PhD level courses, participation to international scientific conferences, regular doctoral seminars*
2015-2020	Teaching assistant KU Leuven, Leuven, Belgium *Guiding Master's theses, supervising exercise sessions (Probability Theory & Statistics, Continuous Mechanics & Strength of Materials), coaching problem solving and design (P&O: Civil Engineering 2)*

Awards and grants

Research Foundation Flanders (FWO), Flanders, Belgium. *Travel grant for long stay abroad* (2019).

DTU-COST-RILEM Doctoral Training school on Service life of cement-based materials and structures, Lyngby, Denmark. *Poster award, bronze price in recognition of exceptional technical content* (2016).

Research stays abroad

ENS Paris-Saclay, Cachan, France. 15/01/2019 - 15/04/2019

List of publications

Articles in internationally peer-reviewed scientific journals

- **Van Bunderen, C.**, Benboudjema, F., Snellings, R., Vandewalle, L. and Cizer, Ö. Experimental analysis and modelling of mechanical properties and shrinkage of concrete recycling flash calcined dredging sediments. *Cement and Concrete Composites.* (under review)
- **Van Bunderen, C.**, Snellings, R., Vandewalle, L. and Cizer, Ö. Early-age hydration and autogenous shrinkage of cement paste containing flash calcined dredging sediments. *Construction and Building Materials 200* (2019), 104-115.
- Snellings, R., Horckmans, L., **Van Bunderen, C.**, Vandewalle, L. and Cizer, Ö. Flash-calcined dredging sediment blended cements: effect on cement hydration and properties. *Materials and Structures 50*, 6 (2017), 241.

Articles presented at international conferences and symposia

- **Van Bunderen, C.**, Snellings, R., Horckmans, L., Vandewalle, L. and Cizer, Ö. Early-age structural development of cement blended with flash calcined dredging sediments. In Serdar, M., Stirmer, N. and Provis, J. (Eds.), *Proceedings of the International Conference on Sustainable Materials, Systems and Structures – New Generation of Construction Materials* (2019), pp. 164-171, Rovinj, Croatia.

- **Van Bunderen, C.**, Snellings, R., Horckmans, L., Vandewalle, L. and Cizer, Ö. Mixture proportions of concrete with dredging sediments as novel SCM. In Arzki, T.-H. (Ed.), *Proceedings of the 10th ACI/RILEM International Conference on Cementitious Materials and Alternative Binders for Sustainable Concrete* (2017), pp. 27.1-27.10, Montreal, Canada.

- Cizer, Ö., **Van Bunderen, C.**, Vandewalle, L., Horckmans, L. and Snellings, R. Effect of flash-calcined dredging sediments on cement hydration and microstructure. In Staquet, S. and Aggelis, D. (Eds.), *Proceedings of the 2nd International RILEM/COST Conference on Early Age Cracking and Serviceability in Cement-based Materials and Structures* (2017), pp. 55-62, Brussels, Belgium.

- **Van Bunderen, C.**, Snellings, R., Horckmans, L., Vandewalle, L. and Cizer, Ö. Autogenous deformation of paste containing calcined clay-rich dredging sediments as SCM. In Staquet, S. and Aggelis, D. (Eds.), *Proceedings of the 2nd International RILEM/COST Conference on Early Age Cracking and Serviceability in Cement-based Materials and Structures* (2017), pp. 215-220, Brussels, Belgium.

- **Van Bunderen, C.**, Snellings, R., Horckmans, L., Dockx, J., Vandekeybus, J., Vandewalle, L. and Cizer, Ö. Concrete with Flash-Calcined Dredging Sediments as a Novel Supplementary Cementitious Material. In Hordijk, D. A. and Lukovic, M. (Eds.), *Proceedings of the 2017 fib Symposium High Tech Concrete: Where Technology and Engineering Meet* (2017), pp. 109-116, Maastricht, The Netherlands.

- **Van Bunderen, C.**, Snellings, R., Horckmans, L., Dockx, J., Vandekeybus, J., Van Balen, K., Vandewalle, L. and Cizer, Ö. Durability properties of concrete recycling clay-rich dredging sediments as a novel supplementary cementitious material. In De Schutter, G., De Belie, N., Janssens, A. and Van Den Bossche, N. (Eds.), *Proceedings of the 14th DBMC International Conference on Durability of Building Materials and Components* (2017), pp. 119-120, Ghent, Belgium.

- Snellings, R., Horckmans, L., Durdzinski, P., **Van Bunderen, C.**, Vandewalle, L., Van Balen, K., Dockx, J., Vandekeybus, J. and Cizer, Ö. Calcined dredged sediments as supplementary cementitious materials: properties and pozzolanic reactivity. In Jensen, O. M., Kovler, K. and De Belie, N. (Eds.), *Proceedings of the International RILEM Conference Materials, Systems and Structures in Civil Engineering, Segment on Concrete with Supplementary Cementitious Materials* (2016), pp. 317-324, Lyngby, Denmark.

- **Van Bunderen, C.**, Snellings, R., Horckmans, L., Dockx, J., Vandekeybus, J., Van Balen, K., Vandewalle, L. and Cizer, Ö. Properties of concrete recycling clay-rich dredging sediments as a novel supplementary cementitious material. In Ahzena, M., Gabrijel, I., Schlicke, D., Kanstad, T. and Jensen, O. M. (Eds.), *Proceedings of the International RILEM Conference Materials, Systems and Structures in Civil Engineering, Segment on Service Life of Cement-Based Materials and Structures* (2016), Vol 1, pp. 317-324, Lyngby, Denmark.

Scientific outreach

- **Van Bunderen, C.**, Snellings, R., Horckmans, L., Dockx, J., Vandekeybus, J., Van Balen, K., Vandewalle L. and Cizer, Ö. BINDAMOR: Hergebruik van AMORAS-filterkoek als cementvervanger in beton. *Bouwkroniek: Weekblad voor Bouw en Industrie*, Betongids (2016), pp. 51-53.

Master thesis

- **Van Bunderen, C.**, Beeldens, A. (sup.) and Vandewalle, L. (co-sup.), *Invloed van het gecombineerd gebruik van (super)plastificeerder en luchtbelvormer in wegenbeton op het korte termijngedrag.* MSc thesis, Department of Civil Engineering, KU Leuven, 2015.



FACULTY OF ENGINEERING SCIENCE
DEPARTMENT OF CIVIL ENGINEERING
BUILDING MATERIALS AND BUILDING TECHNOLOGY
Kasteelpark Arenberg 40, box 2448
B-3001 Leuven
http://www.bwk.kuleuven.be